



The Search for Long-lived Particles with the FASER Experiment at the LHC

A thesis submitted in accordance with the requirements of the
University of Liverpool for the degree of Doctor of Philosophy

Charlotte Cavanagh

Supervised by

Professor Monica D'Onofrio

Professor Carl Gwilliam

Department of Physics

Oliver Lodge Laboratory

University of Liverpool

December 2024



Abstract

This thesis documents the results of analyses searching for long-lived particles (LLPs) using the FASER experiment at the Large Hadron Collider. The results of the search for dark photons, A' , at FASER with coupling to SM particles with the signature $A' \rightarrow e^+e^-$ are presented. This analysis uses proton-proton collision data at a centre of mass energy of $\sqrt{s} = 13.6$ TeV corresponding to an integrated luminosity of 27.0 fb^{-1} collected by the FASER experiment in 2022. The search provides sensitivity to dark photons with couplings $4 \times 10^{-6} < \epsilon < 2 \times 10^{-4}$ and with masses $10 \text{ MeV} < m_{A'} < 80 \text{ MeV}$, resulting in world-leading exclusion limits for dark photon masses $17 \text{ MeV} < m_{A'} < 70 \text{ MeV}$ and couplings $2 \times 10^{-5} < \epsilon < 1 \times 10^{-4}$ [1]. The results of this analysis are also reinterpreted for the $B - L$ gauge boson model.

The results of the search for axion-like particles (ALPs), a , with coupling to the $SU(2)_L$ gauge boson with the decay signature $a \rightarrow \gamma \gamma$ are also presented. This analysis uses proton-proton collision data at a centre of mass energy of $\sqrt{s} = 13.6$ TeV corresponding to an integrated luminosity of 57.7 fb^{-1} collected by the FASER experiment in 2022 and 2023. This search provides sensitivity to ALPs with coupling $10^{-5} \text{ GeV}^{-1} < g_{aWW} < 10^{-3} \text{ GeV}^{-1}$ and masses $60 \text{ MeV} < m_a < 500 \text{ MeV}$, providing world-leading exclusion limits for ALP masses $100 < m_a < 250 \text{ MeV}$, with coupling $3 \times 10^{-5} \text{ GeV}^{-1} < g_{aWW} < 5 \times 10^{-4} \text{ GeV}^{-1}$ [2, 3].

Additionally, models where ALPs interact either exclusively with photons or with gluons are considered for interpretation using the selection outlined in the search for ALPs with coupling to the $SU(2)_L$ gauge boson. In the case of the ALP coupling to photons, ALP masses up to $m_a \sim 80 \text{ MeV}$ are excluded and previously unexplored parameter space around $g_{a\gamma\gamma} \sim 10^{-4} \text{ GeV}^{-1}$ is probed. In the case of the ALP coupling to gluons, FASER probes unconstrained regions around the π mass and η meson mass where production rate is enhanced due to resonant mixing. The analysis is also reinterpreted for the $U(1)B$ gauge boson, the up-philic scalar, the Type-I two Higgs doublet model, and the dark photon.

The results of the 2021 calorimeter test beam are also discussed, as well as the planned preshower detector upgrade and the resulting impact on future ALP searches.

Declaration

I confirm that this thesis is my own work, except where explicit reference is made to other works. This work has not previously been submitted to any institute, including this one.

Lottie Cavanagh

Acknowledgements

The people I must thank first and foremost are my supervisors Monica and Carl. Without their support this work would not have been possible, the knowledge and skills I have gained in the last four years are the direct result of their patience, kindness and dedication to maintaining a supportive and productive working environment. They have set an incredibly high bar and I understand just how incredibly lucky I have been to find myself in such a team. I will greatly miss my time as part of the LivFASER group and I very much hope that we continue to collaborate long into the future.

Monica, I have an incredible respect for you as a researcher and scientist. I have so much admiration for your approach to supervision and your ability to share your vast knowledge and insight. Thank you for seeing the potential in me even at times when I struggled to see it myself.

Carl, your support and advice has been so valuable to me over the years. You are a coding wizard and I am grateful that even a fraction of your skills has managed to rub off on me. Thank you for always offering your guidance and listening to my stories.

And of course I must thank my friends and family for their endless support in all aspects. I must thank my Liverpool friends for their unwavering belief in my scientific endeavours over the last 8 years. Conor, thank you for being by my side since our very first days of undergrad. I'm so grateful that we have been able to share this journey together. To my CERN friends and colleagues, thank you for all the plentiful coffee discussions.

Happy First Birthday Dash, I have a feeling it will be a while until your parents are able to visit me in Geneva again, especially as you don't have your passport yet. Luckily there is plenty of time, I can't wait to turn you into a physics nerd.

To Liv, I would be nowhere without you.

Contents

| | |
|-----------------|------|
| List of Figures | xxiv |
|-----------------|------|

| | |
|----------------|--------|
| List of Tables | xxviii |
|----------------|--------|

| | |
|-----------------------|----------|
| 1 Introduction | 1 |
|-----------------------|----------|

| | |
|-------------------------------|----------|
| 2 Theoretical Overview | 4 |
|-------------------------------|----------|

| | |
|------------------------------------------------------|---|
| 2.1 The Standard Model of Particle Physics | 4 |
|------------------------------------------------------|---|

| | |
|---------------------------------------------------------------------|---|
| 2.1.1 Quantum Electrodynamics and Electroweak Unification | 6 |
|---------------------------------------------------------------------|---|

| | |
|----------------------------------------|---|
| 2.1.2 Quantum Chromodynamics | 7 |
|----------------------------------------|---|

| | |
|-----------------------------------------------|---|
| 2.1.3 The Standard Model Lagrangian | 8 |
|-----------------------------------------------|---|

| | |
|--------------------------------------------------|---|
| 2.2 Shortcomings of the Standard Model | 8 |
|--------------------------------------------------|---|

| | |
|-----------------------------|---|
| 2.2.1 Dark Matter | 9 |
|-----------------------------|---|

| | |
|---------------------------------------------------|----|
| 2.2.2 Baryon Asymmetry and CP Violation | 11 |
|---------------------------------------------------|----|

| | |
|---------------------------------------|----|
| 2.2.3 The Hierarchy Problem | 12 |
|---------------------------------------|----|

| | |
|-----------------------------------------------------|----|
| 2.3 Motivating the Search for Dark Matter | 12 |
|-----------------------------------------------------|----|

| | |
|-----------------------------------|----|
| 2.3.1 Detection Methods | 12 |
|-----------------------------------|----|

| | |
|-------------------------------------------------|----|
| 2.3.2 WIMPs and Thermal Relic Density | 13 |
|-------------------------------------------------|----|

| | |
|------------------------------------|----|
| 2.3.3 Dark Sector Models | 15 |
|------------------------------------|----|

| | |
|------------------------------------------------------|----|
| 2.4 Motivating a Forward Search at the LHC | 16 |
|------------------------------------------------------|----|

| | |
|-------------------------------|----|
| 2.5 The Dark Photon | 17 |
|-------------------------------|----|

| | |
|--------------------------------------------------|----|
| 2.5.1 Dark Photon Production and Decay | 18 |
|--------------------------------------------------|----|

| | |
|---------------------------------------------------------|----|
| 2.5.2 The Parameter Space and Existing Limits | 20 |
|---------------------------------------------------------|----|

| | | |
|----------|---------------------------------------------------------------------|-----------|
| 2.6 | Axion-like Particles | 22 |
| 2.6.1 | ALPs Coupling to Photons | 23 |
| 2.6.2 | ALPs Coupling to Gluons | 24 |
| 2.6.3 | ALPs Coupling to the $SU(2)_L$ Gauge Boson | 25 |
| 3 | The FASER Experiment | 31 |
| 3.1 | The LHC | 31 |
| 3.1.1 | Luminosity | 34 |
| 3.2 | The FASER Detector | 35 |
| 3.3 | Detector Components | 38 |
| 3.3.1 | FASER ν Emulsion Detector | 40 |
| 3.3.2 | Scintillators | 41 |
| 3.3.3 | Tracking Spectrometer | 45 |
| 3.3.4 | Electromagnetic Calorimeter | 49 |
| 3.4 | Trigger and Data Acquisition | 51 |
| 4 | Event and Object Reconstruction | 56 |
| 4.1 | Event Reconstruction | 57 |
| 4.1.1 | Track Reconstruction | 57 |
| 4.1.2 | PMT Waveform Reconstruction | 59 |
| 4.2 | Calorimeter Response | 60 |
| 4.2.1 | Energy Response | 63 |
| 4.2.2 | Corrections and Local Effects | 64 |
| 4.2.3 | Energy Resolution | 67 |
| 4.3 | The 2021 Calorimeter Test Beam | 69 |
| 4.3.1 | Test Beam Simulation | 69 |
| 4.3.2 | Preshower Correction | 72 |
| 4.3.3 | Test Beam Results | 73 |
| 5 | The Modelling of Physical Processes and Statistical Analysis | 76 |
| 5.1 | Monte Carlo Simulation and Event Generators | 76 |

| | | |
|----------|-----------------------------------------------------------------|------------|
| 5.1.1 | MC Event Generators | 78 |
| 5.1.2 | FORESEE: The Forward Experiment Sensitivity Estimator | 80 |
| 5.2 | Modelling of the Dark Photon and ALP Signal | 81 |
| 5.3 | Overview of MC Background Samples | 83 |
| 5.3.1 | Modelling of Far-Forward Neutrino Interactions | 83 |
| 5.3.2 | FLUKA and Large-angle Muon Simulations | 84 |
| 5.4 | Statistical Analysis | 85 |
| 5.4.1 | The HistFitter Framework | 86 |
| 5.4.2 | The CL_s Method and Fit Configuration | 88 |
| 6 | The Search for Dark Photons | 91 |
| 6.1 | Dataset and Simulation Samples | 91 |
| 6.2 | Event Selection | 94 |
| 6.3 | Background Estimation | 96 |
| 6.3.1 | Neutrino Background | 97 |
| 6.3.2 | Neutral Hadrons | 98 |
| 6.3.3 | Inefficiency of the Veto Scintillators | 99 |
| 6.3.4 | Large-angle Muons | 100 |
| 6.3.5 | Non-collision Backgrounds | 104 |
| 6.3.6 | Summary of Total Expected Background | 106 |
| 6.4 | Systematic Uncertainties | 107 |
| 6.4.1 | Signal Theory Uncertainties | 107 |
| 6.4.2 | Experimental Uncertainties | 109 |
| 6.4.3 | A Summary of Systematic Uncertainties | 111 |
| 6.5 | Results | 113 |
| 6.5.1 | Reinterpretation: The $B - L$ Gauge Boson | 116 |
| 7 | The Search for Axion-like Particles | 117 |
| 7.1 | Dataset and Simulation Samples | 117 |
| 7.2 | Event Selection | 120 |
| 7.3 | Background Estimation | 126 |

| | | |
|----------|----------------------------------------------------------------------|------------|
| 7.3.1 | Neutrino Background | 127 |
| 7.3.2 | Neutral Hadrons | 134 |
| 7.3.3 | Inefficiency of the Veto Scintillators | 136 |
| 7.3.4 | Large-angle Muons | 136 |
| 7.3.5 | Non-collision Backgrounds | 142 |
| 7.3.6 | Summary of Total Expected Background | 144 |
| 7.4 | Systematic Uncertainties | 145 |
| 7.4.1 | Theory Uncertainties | 145 |
| 7.4.2 | Experimental Uncertainties | 146 |
| 7.4.3 | A Summary of Systematic Uncertainties | 152 |
| 7.5 | Results | 155 |
| 7.5.1 | ALPs Coupling to Photons | 159 |
| 7.5.2 | ALPs Coupling to Gluons | 159 |
| 7.5.3 | Reinterpretations | 160 |
| 8 | The Preshower Detector Upgrade and Future Outlook | 166 |
| 8.1 | High-Precision Tungsten-Silicon Preshower Detector Upgrade | 166 |
| 8.1.1 | Sub-detector Layout | 167 |
| 8.1.2 | Monolithic Readout Chip | 168 |
| 8.1.3 | Prototype Tests for Pre-production | 169 |
| 8.1.4 | Tests of Production Chips | 170 |
| 8.1.5 | Implications for Future ALPs Search | 172 |
| 8.2 | Outlook | 174 |
| 9 | Conclusion | 177 |
| | Glossary | 178 |
| | Bibliography | 185 |
| | Appendices | 203 |

| | | |
|----------|-------------------------------------------------|------------|
| A | FASER’s EM Calorimeter | 204 |
| A.1 | Calorimeter Corrections | 204 |
| A.2 | Calorimeter Energy Uncertainty | 204 |
| B | ALP Signal Selection: Tracking Variables | 208 |

List of Figures

| | | |
|-----|----------------------------------------------------------------------------------------------------------------------------------------------------------------------------------------------------------------------------------------------------------------------------------------------------------------------------------------------------------------------------------------------------------------------------------------------------------------------------------------------------------------------------------------------------------------------------------------------------------------------|----|
| 2.1 | The observed galactic rotation curve (data points) for the M33 galaxy showing the contributions from the stellar disc and gaseous disc and the dark matter halo contribution needed to match the data. Figure from Ref. [4]. | 10 |
| 2.2 | A composite image taken from Ref. [5] (X-ray: NASA/CXC/CfA/M.Markevitch et al.; Optical: NASA/STScI; Magellan/U.Arizona/D.Clowe et al.; Lensing Map: NASA/STScI; ESO WFI; Magellan/U.Arizona/D.Clowe et al.) showing the galaxy cluster 1E 0657-56, regions of hot gas are shown in pink, regions where most of the mass density lies are shown in blue. | 11 |
| 2.3 | Thermal freeze-out of dark matter for different annihilation cross sections. The comoving number density Y and resulting thermal relic density Ω_χ of a 100 GeV dark matter particle as a function of temperature T . The solid line represents the dark matter cross section that yields the correct relic density, the coloured bands show the density for cross section variation of order 10, 10^2 and 10^3 from $\Omega_\chi \sim 0.23$. The dashed line shows the number density of a particle that did not “freeze-out” but remained in thermal equilibrium. Figure from Ref. [6]. | 14 |
| 2.4 | The different portals involved in dark sector dark matter models. The four main portal types are highlighted: Vector, Scalar, Neutrino, Axion, grouped by those that require renormalisable coupling and those that require higher operators. | 16 |
| 2.5 | Feynman diagrams for LLP production processes: dark photon production from pion decay (left), dark photon production via dark bremsstrahlung (right). The red circle indicates the kinetic mixing parameter ϵ . Figure from Ref. [7]. | 18 |

| | | |
|------|----------------------------------------------------------------------------------------------------------------------------------------------------------------------------------------------------------------------------------------------------------------------------------------------------------------------------------------------------------------------------------------------------------------------------|----|
| 2.6 | Inelastic dark photon production cross section (per ϵ^2) as a function of mass. The total cross section and the far-forward cross section are shown. Figure from Ref. [8]. | 19 |
| 2.7 | (Top) The decay length of the dark photon in the parameter space that FASER is sensitive to. (Bottom) The branching fractions of the dark photon into leptonic and hadronic final states, as a function of dark photon mass. Figure from Ref. [7]. | 20 |
| 2.8 | Existing experimental constraints in the parameter space probed in FASER's search for dark photons. Includes existing limits from the BaBar collaboration, the KLOE experiment, the LHCb collaboration, NA62, NA64, NA48, E141, Orsay, NuCal, E137, CHARM. | 21 |
| 2.9 | (a) ALP with coupling to photons (ALP-photon) production via the Primakoff process in which a photon is converted into an ALP when colliding with a nucleus, N . In the context of FASER, N would be LHC infrastructure, most likely the TAN (neutral particle absorber). (b) The production rate of ALPs from the Primakoff process within an angular acceptance $\theta < 0.2$ mrad with energy $E > 1$ TeV. | 23 |
| 2.10 | ALP-photon decay to two highly energetic photons. Figure from Ref. [3]. | 24 |
| 2.11 | (Top) The decay length of the ALP-photon in the parameter space that FASER is sensitive to. (Bottom) The branching fractions of the ALP-photon into $\gamma\gamma$, with a sub-leading contribution from $ee\gamma$ s, as a function of ALP mass. Figure from Ref. [7]. | 25 |
| 2.12 | (a) ALP with coupling to gluons (ALP-gluon) production via pion mixing. (b) The production rate of ALP-gluon from $\pi^0 \rightarrow a$, $\eta \rightarrow a$ and $\eta' \rightarrow a$ within an angular acceptance $\theta < 0.2$ mrad with energy $E > 1$ TeV. | 26 |
| 2.13 | ALP-gluon decay to two highly-energetic photons, using pion mixing. Figure from Ref. [3]. | 26 |
| 2.14 | ALP production via top loop, involving B meson decay to kaon and a W boson. . . | 27 |
| 2.15 | The production rate of ALPs from B meson and Kaon decays in the mass range of interest in this analysis. There are four production modes relevant to this ALP model: $B^0 \rightarrow X_s a$, $B^\pm \rightarrow X_s a$, $B_s \rightarrow X_s a$ and $K \rightarrow \pi a$. The shaded bands indicate the uncertainty associated with these production modes. | 28 |

| | | |
|------|-------------------------------------------------------------------------------------------------------------------------------------------------------------------------------------------------------------------------------------------------------------------------------------------------------------------------------------------------------------------------------------------------------------------------------------------------------------------------------------------------------------------------------------------------------------------------------------------------------------------------------------------------------------------------------------------------|----|
| 2.16 | A typical ALP decay signature to two highly collimated and highly energetic photons in the case of the ALP-W model. The red circle indicates the ALP coupling constant g_{aWW} . | 28 |
| 2.17 | Existing experimental constraints in the parameter space probed in FASER's search for axion-like particles with coupling to the W boson. Includes existing limits from NuCal, NA62/64, beam dumps, KTEV, KOTO, E949, CDF, BaBar, E137, NA62, SN1987, NA62, E949, LHCb and LEP. | 29 |
| 3.1 | A diagram of the CERN accelerator complex, modified from Ref. [9] to include FASER in the TI12 tunnel that connected the LHC and the SPS in the time of LEP. | 32 |
| 3.2 | Schematic diagram of the octants of the LHC. It shows the 4 interaction points where the largest experiments are situated. Figure modified from Ref. [10]. | 33 |
| 3.3 | The instantaneous luminosity measured at IP1 and the total and coincidence trigger rate recorded by FASER for 2 LHC fills in May 2024. The instantaneous luminosity is provided by ATLAS and shown in blue, the total trigger output rate is shown in green. The output rate of a coincidence trigger requiring a signal the veto scintillator and the preshower scintillator, is shown in red. Figure from Ref. [11]. | 35 |
| 3.4 | The total luminosity delivered during LHC stable beams as of July 2024 (measurement by ATLAS) (yellow). The total luminosity recorded by FASER (blue). | 36 |
| 3.5 | FASER's location in service tunnel TI12, 480m east of the ATLAS IP. Figure adapted from Ref. [12]. | 36 |
| 3.6 | Schematic view of the far-forward region downstream of ATLAS and various particle trajectories as they make their way through the LHC infrastructure towards FASER. The upper panel shows the 480 metres between the IP and FASER, the beam collision axis is shown with a dotted line, and several components of the LHC, which have a large influence on the particle flux seen at FASER, are highlighted. The lower left of the Figure shows various high energy particles that can be produced at the IP. LLPs travel through the LHC infrastructure without interacting, the lower right of the figure shows LLPs arriving at FASER, 480 m after they are produced. Figure from Ref. [13]. | 37 |

| | | |
|------|----------------------------------------------------------------------------------------------------------------------------------------------------------------------------------------------------------------------------------------------------------------------------------------------------------------------------------------|----|
| 3.7 | FASER in TI12 in January 2023, viewed from the calorimeter towards FASER ν . . . | 39 |
| 3.8 | The components and coordinate system of the FASER detector, adapted from Ref. [14] | 40 |
| 3.9 | The four scintillator stations used in FASER, taken from Ref. [14] | 42 |
| 3.10 | Charge deposited in the first layer of the VetoNu scintillator in front of FASER ν in data. Using a 40 pC threshold (indicated by the dotted red line), the measured MIP detection efficiency is 99.99976(2). | 44 |
| 3.11 | The timing distribution of the top timing scintillator with a timing resolution of 423.0 ± 0.5 ps. Figure from Ref. [11]. | 45 |
| 3.12 | The current FASER preshower detector, January 2023. | 46 |
| 3.13 | A schematic of the current preshower detector: 50 mm graphite blocks, 20 mm plastic scintillator layers, 3.18 mm tungsten absorber. | 46 |
| 3.14 | The ratio of charge deposited in the two preshower scintillator layers for a 200 GeV π^- , a 150 GeV μ^- and a 200 GeV e^- from test beam data. Calculated in terms of the equivalent number of MIPs. Figure adapted from Ref. [15]. | 47 |
| 3.15 | The hit efficiency as a function of a) the applied hit threshold (in fC) and b) the applied bias voltage (in V) for the FASER silicon strip (SCT) tracker. The nominal settings are indicated as as a dashed line, and yields an average hit efficiency across the full tracker of $99.64 \pm 0.10\%$. Figure from Ref. [11]. | 48 |
| 3.16 | SCT barrel module inside an aluminium test-box. Figure from Ref. [11]. | 48 |
| 3.17 | A tracker plane with all eight SCT barrel modules. Figure from Ref. [11]. | 49 |
| 3.18 | Arrangement of the 4 FASER calorimeter modules in a 2×2 configuration before additional shielding and dual readout PMTs were added. Figure from Ref. [14]. . . . | 50 |
| 3.19 | Design of the LHCb outer ECAL modules used for FASER. Figure from Ref. [16]. . . | 50 |
| 3.20 | A FASER calorimeter Hamamatsu R7899-20 PMT. Figure from Ref. [14]. | 50 |
| 3.21 | Dual readout upgrade for the calorimeter PMTs in YETS 2023. PMT 1 has a “low” energy range of 0.1 to 300 GeV. PMT 2 has a “high” energy range of 3 to 3000 GeV. The region of overlap is useful for cross calibrations. | 51 |
| 3.22 | A diagram of the FASER TDAQ architecture showing the underground and surface elements. The number in brackets is the number of channels used for readout. Figure from Ref. [17]. | 52 |

| | | |
|------|----------------------------------------------------------------------------------------------------------------------------------------------------------------------------------------------------------------------------------------------------------------------------------------------------------------------------------------------------------------------------------------------------------------------------------------------------------------------------------------------------------------------------------------------------------------------------------------------------------------------------------------------------------------------------------------------------------------------------------------------------------------------------------------------------------------------------------------------------------------------------|----|
| 3.23 | FASER recorded trigger rate for individual items and total recorded rate (black) for LHC Fill 8143 on 19th August 2022. Trigger items: timing scintillator (green), signal in any veto or preshower scintillators (orange), coincidence trigger between FASER ν veto and preshower (red), calorimeter (blue). Figure from Ref. [11]. | 54 |
| 3.24 | Photograph of DAQ electronics in TI12, January 2023. | 55 |
| 4.1 | An event display showing a collision event of a muon traversing the FASER detector. The measured track momentum is 21.9 GeV. The waveforms are shown for signals in scintillator counters and calorimeter modules and are fitted using a Crystal Ball function. All PMT waveforms are consistent with a muon passing through the scintillators and one of the calorimeter modules. The event has been triggered by modules in the VetoNu scintillator station, veto scintillator station and timing scintillator station with pulses above 25 mV, and by modules in the preshower station with pulses above above 3 mV. The detected hits in the SCT modules are shown with blue lines and the reconstructed track is shown with a red line. In the title of the waveform plots, left and right is defined facing the downstream direction. Figure from Ref. [11]. | 59 |
| 4.2 | An example of a typical PMT raw waveform signal coming from the digitiser. Waveforms have a window of 1200 ns, with 2 ns bins and a negative amplitude of ADC counts. Figure from Ref. [18]. | 60 |
| 4.3 | (a) The distribution of ADC counts for a PMT waveform (b) A Gaussian fit of the zoomed in ADC histogram range. Figure from Ref. [18]. | 61 |
| 4.4 | (a) A example of a typical PMT raw waveform signal coming from the digitiser. Waveforms have a window of 1200 ns, with 2 ns bins and a negative amplitude of ADC counts. (b) An example of a saturated waveform pulse. Figure from Ref. [18]. | 61 |
| 4.5 | A example of a reconstructed waveform in the bottom right ECAL module. | 62 |
| 4.6 | The energy loss for positive muons according to the Bethe-Bloch formula (shown between the second and third grey band. The rest of the plot shows other models). Figure from Ref. [19]. | 63 |

| | | |
|------|-------------------------------------------------------------------------------------------------------------------------------------------------------------------------------------------------------------------------------------------------------------------------------------------------------------------------------------------------------------------------------------------------------------------------------------------------------------------------------------------------------------|----|
| 4.7 | Fitted MC distribution for (a) a 100 GeV electron fitted with a CB function (b) a 100 GeV muon fitted with a Landau distribution simulated in FASER's ECAL . . . | 65 |
| 4.8 | Non-uniformity in calorimeter response across the ECAL cell for (a) a 50 GeV electron in LHCb data [20] (b) a 200 GeV electron in FASER data. The dashed blue line on the LHCb plot shows the centre of the ECAL cell, the solid blue lines indicate the edges. The FASER plot shows data collected from two areas of the ECAL cell: away from the WLS fibres (green) and close to the WLS fibres (red), showing the position-dependent response, in addition to the change in response at the cell edge. . | 66 |
| 4.9 | Simulation of the (a) energy response and (b) energy resolution of electrons in the outer ECAL module LHCb test beam [20]. | 68 |
| 4.10 | The simulated calorimeter energy resolution in (a) the original test beam MC and (b) the updated test beam MC that includes the most up-to-date material description and implementation of the studied local effects in the calorimeter. Compared with the parameterisation of LHCb test beam results in green. | 68 |
| 4.11 | A photograph of the test beam setup in Experimental Hall North (EHN1) at CERN | 70 |
| 4.12 | A diagram of the components used in the test beam. The coordinate system is also shown. | 70 |
| 4.13 | The different scan point positions used in the test beam. Scan point 8 represents the centre of the top middle ECAL module. | 71 |
| 4.14 | An event display showing the simulated hits of a 100 GeV electron in the test beam MC geometry | 71 |
| 4.15 | The calibrated EM energy in the calorimeter of MC simulation compared to test beam response of each of the six ECAL modules. Figure from Ref. [18]. | 72 |
| 4.16 | The energy deposited in the calorimeter modules vs the preshower scintillator layers in test beam simulation (100 GeV electron). | 73 |
| 4.17 | The effect of the preshower correction on the charge deposited by a 100 GeV electron in test beam data. The preshower corrected charge (red) shows a reduced and improved energy resolution. | 74 |
| 4.18 | Calorimeter energy resolution measurement in test beam data (blue) and simulation (red), compared to a parameterisation of LHCb test beam results. | 74 |

| | | |
|-----|---------------------------------------------------------------------------------------------------------------------------------------------------------------------------------------------------------------------------------------------------------------------------------------------------------------------------------------------------------------------------------------------------------------------------------------------------------------------------------------------------------------------------------------------------------------------------------------------------------------------------------------------------------------|----|
| 5.1 | The distribution of (a) π^0 mesons and (b) B^0 mesons in the forward (θ, p) plane. Where θ is the angle with respect to beam axis and p is the meson's momentum. The predicted spectra is obtained assuming 14 TeV pp collision energy. The angular acceptance of FASER is indicated. Figure from Ref. [21]. | 81 |
| 5.2 | Predictions for the production of B -mesons with POWHEG+Pythia prescription used for the ALP signal MC (NLO+NLL PDF + P8), compared to the POWHEG+HERWIG and LHCb data. The blue band shows the large scale uncertainties. Figure from Ref. [22]. | 82 |
| 5.3 | The predicted energy distribution of (a) electron neutrinos and (b) muon neutrinos from CC interactions in FASER ν for an integrated luminosity of 250 fb^{-1} . The component from light (charm) hadron decays is shown in red (blue). The shaded regions show the corresponding uncertainties associated with the flux. The light hadron component includes neutrinos produced in π , K and Λ decays, simulated using the EPOS-LHC, QGSJET, SIBYLL and PYTHIA generators. The charm hadron component includes neutrinos produced in D and Λ_c decays, simulated using POWHEG + PYTHIA. Figure from Ref. [23]. | 84 |
| 5.4 | (a) The p -value can be visualised as the integral of a PDF from the observed value to the end of the probability density function. This is shown in Figure 5.4a. (b) The relation between the p -value and significance Z . Figure from Ref. [24]. | 88 |
| 6.1 | Reconstructed good tracks normalised by the corresponding luminosity for the runs used in this analysis. A good track is defined as having a momentum of at least 20 GeV, a χ^2/NDF of less than 25 and at least 12 hits on track within a 95 mm radius once extrapolated back to the scintillator station. | 92 |
| 6.2 | Reconstructed events normalised by the corresponding luminosity for the runs used in this analysis. Plot shows the total yield of events with calorimeter energy greater than 100 GeV. | 93 |

| | | |
|------|---------------------------------------------------------------------------------------------------------------------------------------------------------------------------------------------------------------------------------------------------------------------------------------------------------------------------------------------------------------------------------------------------------------------------------------------------------------------------------------------------------------------------|-----|
| 6.3 | Dark photon MC signal points spanning the 2D parameter space as a function of dark photon mass and coupling. Included are existing constraints from previous experiments (grey) and projected sensitivity of future experiments (dashed lines). In yellow is the predicted FASER reach assuming various benchmark amounts of recorded luminosity. | 93 |
| 6.4 | A typical dark photon (A') signal event traversing FASER. The neutral A' (dotted line) enters the detector from the left and deposits no charge in any of the veto scintillator stations. It decays within FASER's decay volume to a highly-energetic e^+e^- pair (dashed lines) which leave charge deposits in the timing scintillator, as well as two tracks within the tracking spectrometer. Energy deposits in the preshower and calorimeter are consistent with an EM shower. Figure from Ref. [1]. | 94 |
| 6.5 | Charge deposited in the timing scintillator in data (black), populated mainly by muon events, compared to a representative dark photon MC signal sample (green). The dotted line indicates the 70 pC charge selection used in this analysis. | 95 |
| 6.6 | The calorimeter EM energy distribution of the GENIE neutrino MC sample after the signal region selections have been applied. The dashed line indicates the calorimeter energy requirement above 500 GeV, above this point there are 1.5×10^{-3} expected neutrino events. | 97 |
| 6.7 | The ABCD background estimation method showing the control regions, validation regions and signal regions used to validate the large-angle muon estimate in the dark photon analysis. | 102 |
| 6.8 | An example of the regions considered for the ABCD configuration carried out in the first entry in Table 6.6. | 103 |
| 6.9 | The calorimeter energy distribution of cosmic muon events with various track requirements. Zero events with tracks survive selections. No events survive the requirement of at least one good track. | 105 |
| 6.10 | The calorimeter energy distribution of beam 1 background events with various track requirements. Zero events with tracks survive the veto scintillator selection. | 106 |

- 6.11 The energy spectrum of a dark photon signal with mass 50 MeV and coupling $\epsilon = 3 \times 10^{-5}$ produced in meson decays whose production is modelled by the EPOS-LHC (blue), QGSJET (orange) and SIBYLL (green) generators. The production due to bremsstrahlung is shown in grey, with a factor of two variation in the p_T cutoff. The bottom panel shows the ratio of the different generator estimates with the parameterisation of the uncertainty as a function of signal energy. Figure from Ref. [1]. 108
- 6.12 (a) The E/p distribution for photon conversion events with $75 \text{ GeV} < p < 175 \text{ GeV}$ for data and FLUKA MC. (b) The fitted E/p peak values for various momentum ranges: $20 \text{ GeV} < p < 30 \text{ GeV}$, $35 \text{ GeV} < p < 75 \text{ GeV}$, $75 \text{ GeV} < p < 125 \text{ GeV}$, $125 \text{ GeV} < p < 175 \text{ GeV}$. The E/p ratio is centred around one, and the agreement between data and MC is well within the 6.06% uncertainty across the momentum range. 110
- 6.13 Top panel: The two track reconstruction efficiency as a function of track separation for single, overlaid tracks in both data and FLUKA MC. Shown in red is the track separation of e^+e^- tracks in a representative A' signal sample. Bottom panel: The ratio of the reconstruction efficiency of these overlaid events in data and MC. 112
- 6.14 Calorimeter EM energy distributions showing three representative A' signal samples with (a) all data events with at least one good track (b) data events with at least one good track which also survive the veto scintillator selections outlined in the selection. 114
- 6.15 Calorimeter EM energy distributions showing three representative A' signal samples showing data events with 2 good tracks that pass all the signal selections. Zero events survive these requirements. 114
- 6.16 Interpretation of the signal region yield as A' exclusion limits with the assumption of 2×10^{-3} background events and zero data events. The expected limit with 90% CL is shown by the dashed line and yellow uncertainty band. The observed limit is shown by the blue line. Existing constraints are shown in grey. The thermal relic density target is shown in red, 115

| | | |
|------|-------------------------------------------------------------------------------------------------------------------------------------------------------------------------------------------------------------------------------------------------------------------------------------------------------------------------------------------------------------------------------------------------------------------------------------------------------------------------------------------------------------------------------------------------------------------------------------------------------------------------------------------------------------------------------------------------------------------------------------------------------------|-----|
| 6.17 | Interpretation of the signal region yield as $B - L$ gauge boson exclusion limits. The expected limit with 90% CL is shown by the dashed line and green uncertainty band. The observed limit is shown by the blue line. Existing constraints are shown in grey. | 116 |
| 7.1 | Calorimeter trigger efficiency in 2022 vs 2023 data. The calo turn-on curve vs total energy for a large run in 2022 (red) and 2023 (blue). | 118 |
| 7.2 | Reconstructed events per unit luminosity that pass data quality requirements in the 2022 dataset. Plot shows the total yield of events with calorimeter energy greater than 100 GeV. The large error band seen in run 8752 is due to low statistics for this run (10.3 pb ⁻¹ recorded). | 119 |
| 7.3 | Reconstructed events per unit luminosity that pass data quality requirements in the 2023 dataset. Plot shows the total yield of events with calorimeter energy greater than 100 GeV. | 119 |
| 7.4 | ALP-W signal points generated across the parameter space that FASER is sensitive to. Previous limits set by existing experiments are indicated in grey. The projected expected limits in red and blue were produced for 27 fb ⁻¹ , which is equivalent to the dataset used in the dark photon analysis, and 60 fb ⁻¹ , which was the initial prediction for the combined 2022 and 2023 dataset used in the ALP search, and close to the final 57.7 fb ⁻¹ that was recorded. These projections are shown for a zero-background case with a 500 GeV calorimeter energy selection. This is not the case for this analysis, which has a non-zero background expectation and applies a stricter calorimeter energy requirement. | 121 |
| 7.5 | A typical ALP signal event traversing FASER. The neutral ALP (dotted line) enters the detector from the left and deposits no charge in any of the veto scintillator stations. It decays within FASER's decay volume to two highly energetic photons (dashed lines) which also do not leave any charge deposits in the timing scintillator. However, energy deposits will be seen in both preshower layers and in the calorimeter, as the EM shower develops. Figure from Ref. [3]. | 122 |

| | | |
|------|-----------------------------------------------------------------------------------------------------------------------------------------------------------------------------------------------------------------------------------------------------------------------------------------------------------------------------------------------------------------------------------------------------------------------------------------------------------------------------------|-----|
| 7.6 | Charge deposited in the top timing scintillator layer. Comparison between data (black) and a representative ALP signal point (blue) with mass 200 GeV and coupling 1×10^{-4} . Shown for (a) the 2022 dataset and (b) the 2023 dataset. | 124 |
| 7.7 | Calorimeter EM energy distributions for ALP signal models with (a) $m_a = 100$ MeV (b) $m_a = 200$ MeV for a range of different couplings. The calorimeter EM energy threshold of 1.5 TeV is indicated by the dashed line. | 124 |
| 7.8 | Significance studies on initial ALP-W signal sample. The significance of selections on the calorimeter EM energy (left) assuming 100% (red), 50% (blue) and 20% (green) background uncertainty. For two different ALP MC samples. | 126 |
| 7.9 | Distributions in r - z of the neutrino interaction vertex (blue/red) and ALP decay vertex (yellow) within the FASER detector with (a) calorimeter energy above 100 GeV (b) calorimeter energy above 100 GeV and preshower ratio > 4.5 | 127 |
| 7.10 | Plot showing the magnet region, calorimeter region and preshower region. The three different regions for targeting neutrino interactions, in the plane of the preshower layer 1 and preshower ratio variables. The preshower region becomes the signal region for this analysis at high calorimeter energies. | 128 |
| 7.11 | Number of MIPs in the second preshower layer against calorimeter energy for electron neutrinos (red) and muon neutrinos (blue) as well as a representative ALP signal (yellow). The neutrinos are categorised in terms of their interaction vertex: (a) neutrinos interacting in the magnet, (b) neutrinos interacting in the calorimeter, (c) neutrinos interacting in the preshower. The green dashed line shows the threshold used in this analysis: PS1 nMIP > 10 | 130 |
| 7.12 | Preshower ratio against calorimeter energy for electron neutrinos (red) and muon neutrinos (blue) as well as a representative ALP signal (yellow). The neutrinos are categorised in terms of their interaction vertex: (a) neutrinos interacting in the magnet, (b) neutrinos interacting in the calorimeter, (c) neutrinos interacting in the preshower. The green dashed line shows the threshold used in this analysis: PS ratio > 4.5 | 130 |

| | | |
|------|--------------------------------------------------------------------------------------------------------------------------------------------------------------------------------------------------------------------------------------------------------------------------------------------------------------------------------------------------------------------------------------------------------------------------------------------------------------------------------------------------|-----|
| 7.13 | The preshower ratio distribution of the neutrino background MC in (a) the magnet region and (b) the calorimeter region. The neutrino background is shown in terms of light and charm components. The uncertainty band includes MC statistical uncertainties and systematic uncertainties on the neutrino background flux. | 131 |
| 7.14 | The preshower layer 1 nMIP distribution of the neutrino background MC in (a) the magnet region and (b) the calorimeter region. The neutrino background is shown in terms of light and charm components. The uncertainty band includes MC statistical uncertainties and systematic uncertainties on the neutrino background flux. | 131 |
| 7.15 | The calorimeter energy distribution in the magnet region for a representative ALP signal and the MC neutrino background in terms of (a) light and charm components and (b) neutrino type. The green dashed line indicates the region that was unblinded at the beginning of the unblinding procedure. | 132 |
| 7.16 | The calorimeter energy distribution in the calorimeter region for a representative ALP signal and the MC neutrino background in terms of (a) light and charm components and (b) neutrino type. The green dashed line indicates the region that was unblinded at the beginning of the unblinding procedure. | 132 |
| 7.17 | The calorimeter energy distribution in the preshower region for a representative ALP signal and the MC neutrino background in terms of (a) light and charm components and (b) neutrino type. The ALP signal has mass 120 GeV and coupling $1 \times 10^{-4} \text{ GeV}^{-1}$. The preshower region becomes the signal region for this analysis at high calorimeter energy. The green dashed line indicates the region that was unblinded at the beginning of the unblinding procedure. | 133 |
| 7.18 | The first ABCD configuration considered to target large-angle muons. Using an inversion of the timing scintillator charge selection used in this analysis, and the calorimeter energy. The unblinded regions are indicated in pink. The regions where the timing charge requirement is inverted are indicated by the dashed blue lines to show where large-angle muons would be expected to populate data. | 138 |

| | | |
|------|-------------------------------------------------------------------------------------------------------------------------------------------------------------------------------------------------------------------------------------------------------------------------------------------------------------------------------------------------------------------------------------------------------------------|-----|
| 7.19 | ABCD configuration of the two configurations considered to target muons. Using an inversion of the veto scintillator charge requirement used in this analysis, and the calorimeter energy as the ABCD variables. The regions where the veto charge requirement is inverted are highlighted in blue to show where forward-going muons are expected to populate data. | 141 |
| 7.20 | Timing in the calorimeter of beam 1 background events (red) and collision events (blue). Placing a threshold at -5 ns removes all components of beam 1 background. | 144 |
| 7.21 | (a) Photon conversion in TI12 data and MC. A correction factor for the preshower variables is derived based on the difference between the two. (b) The difference in test beam data and 100 GeV electron MC in the geometry description matching that used to generate the ALP signal, used to estimate the uncertainty assigned to the preshower variables. | 149 |
| 7.22 | The agreement between data and MC measured as a function of momentum in studies of photon conversion events, resulting in correction factors for the preshower variables to be applied in MC for (a) PS1 nMIP (1.20) and (b) PS Ratio (1.13). | 149 |
| 7.23 | Calorimeter EM energy distributions in the preshower and signal regions, showing the composition of the neutrino background expectation separated (a) in terms of neutrino type and (b) in terms of light/charm production. The final energy bin above 1.5 TeV shows the signal region and is indicated by the green arrow. | 156 |
| 7.24 | An event display of the data event seen in the ALP analysis. Run 8834, eventID 44421456. This event is in time with a collision event and shows signal in the timing scintillator, second preshower layer and the bottom right calorimeter module. | 156 |
| 7.25 | Reconstructed PMT waveworms from ALPtrino event (Run 8834, eventID 44421456) in: (a) the top layer of the timing scintillator with a peak of 12.9 mV and an integrated charge of 1.9 pC. (b) the second preshower scintillator layer with a peak of 1907.8 mV and an integrated charge of 653.3 pC. (c) the bottom right calorimeter module with a peak of 970.4 mV and an integrated charge of 364.3 pC. | 157 |

- 7.26 Interpretation of the signal region yield as exclusion limits for the ALP with coupling to the $SU(2)_L$ gauge boson (ALP-W), with the assumption of 0.44 neutrino background events. The expected limit with 90% CL is shown by the dashed line and yellow uncertainty band. The observed limit is shown by the blue line. Existing constraints are shown in grey. 158
- 7.27 Interpretation of the signal region yield as exclusion limits for the ALP with coupling to photon (ALP-photon), with the assumption of 0.44 neutrino background events. The expected limit with 90% CL is shown by the dashed line and yellow uncertainty band. The observed limit is shown by the blue line. Existing constraints are shown in grey. 159
- 7.28 Interpretation of the signal region yield as exclusion limits for the ALP with coupling to gluons (ALP-gluon), with the assumption of 0.44 neutrino background events. The expected limit with 90% CL is shown by the dashed line and yellow uncertainty band. The observed limit is shown by the blue line. Existing constraints are shown in grey. 160
- 7.29 Interpretation of the signal region yield as exclusion limits for the $U(1)B$ gauge boson model. The expected limit with 90% CL is shown by the dashed line and yellow uncertainty band. The observed limit is shown by the blue line. Existing constraints are shown in grey. Certain models require the introduction of new, heavier fields which can have phenomenological implications, constraints using such models are indicated by the blue dashed line. The yellow (expected limit) band is not visible in some regions, such as the upper part of the exclusion curves, due to overlap with the blue (observed limit) line and because the expected band is smaller than the thickness of the observed line. 162
- 7.30 Interpretation of the signal region yield as exclusion limits for the up-philic scalar model. The expected limit with 90% CL is shown by the dashed line and yellow uncertainty band. The observed limit is shown by the blue line. Existing constraints are shown in grey. 163

| | | |
|------|------------------------------------------------------------------------------------------------------------------------------------------------------------------------------------------------------------------------------------------------------------------------------------------------------|-----|
| 7.31 | Interpretation of the signal region yield as exclusion limits for the Type-I two-Higgs doublet model. The expected limit with 90% CL is shown by the dashed line and yellow uncertainty band. The observed limit is shown by the blue line. Existing constraints are shown in grey. | 164 |
| 7.32 | Interpretation of the signal region yield as dark photon exclusion limits. The expected limit with 90% CL is shown by the dashed line and yellow uncertainty band. The observed limit is shown by the blue line. Existing constraints are shown in grey, including FASER's previous results. | 165 |
| 8.1 | CAD view of the preshower detector upgrade, showing the six preshower detector planes. | 167 |
| 8.2 | (a) A preshower planes with 12 modules mounted on a 20×20 cm ² , 5 mm thick cooling plate. (b) CAD diagram of the components that make up each preshower module. Figure from Ref. [25]. | 168 |
| 8.3 | An example of one of the ASIC chips, the structure of the super-columns and 13 super pixels are indicated in blue, with a diagram of a single SP on the right-hand side, pads run along the bottom of the chip for probing (red). | 169 |
| 8.4 | (a) FASER pre-production probe card used to probe the pre-production chips. (b) Marks from the probe card needles left on the pre-production chip pads after establishing a good contact. | 170 |
| 8.5 | LV test to configure pre-production chip. In blue is the LV current I_0 , in orange is the threshold current I_{thr} and green is the current pulled by the FPGA. | 171 |
| 8.6 | HV test to characterise pre-production chip. The current pulled by the HV I_{hv} is shown in blue, the current pulled by the LV I_0 is shown in orange. | 171 |
| 8.7 | A wafer containing multiple chips being loaded into the probe station. | 172 |
| 8.8 | The predicted physics reach with the upgraded preshower detector in the ALP-W parameter space. Figure from Ref. [25]. | 173 |
| 8.9 | FASER's projected sensitivity to the ALP-W model with the combined Run 3 (250 fb ⁻¹) and Run 4 (680 fb ⁻¹) datasets. The bottom panel shows the branching fraction to the various final states as a function of mass. Figure from Ref. [26]. | 175 |

| | | |
|------|---------------------------------------------------------------------------------------------------------------------------------------------------------------------------------------------------------------------------------------------------------------------------------------------------------------------------------------------------------------------|-----|
| 8.10 | FASER's projected sensitivity to the dark photon model with the combined Run 3 (250 fb^{-1}) and Run 4 (680 fb^{-1}) datasets. The bottom panel shows the branching fraction to the various final states as a function of mass. Figure from Ref. [26]. | 176 |
| 8.11 | Proposed layout of the FPF experimental cavern. The coloured boxes indicated possible experiments and their dimensions. This includes FASER2 for studying LLPs and FASER ν 2 for studying neutrinos. Figure from Ref. [27]. | 176 |
| A.1 | The change in energy loss in the calorimeter due to the implementation of (a) Birks' Law correction (red) and (b) non-uniformity correction (blue). The green represents the simulation setup without the correction, FTFP BERT ATL refers to the physics list used in the simulation. | 205 |
| A.2 | The change in fraction of deposited energy due to the addition of Tyvek paper into the ECAL simulation, compared to the setup without Tyvek (black). Two different Tyvek densities were investigated 0.95 g/cm^3 (red) and 2.265 g/cm^3 (green). | 205 |
| A.3 | The average of the calibrated energies of each of the six test beam calorimeter modules as a function of beam energy in data and MC. The average linear fit in each case shows the extrapolation process to higher energy (500 GeV) to evaluate the uncertainty at this point. The fits results in a difference of 2.46% at 500 GeV. Figure from Ref. [18]. | 207 |
| B.1 | (a) Number of clusters and (b) Number of spacepoints in 7 ALP-W MC signal samples compared with GENIE neutrino MC. Histograms represent the signal samples, the blue markers show the neutrino MC. | 209 |
| B.2 | Number of track segments in 7 ALP-W MC signal samples compared with GENIE neutrino MC. Histograms represent the signal samples, the blue markers show the neutrino MC. | 209 |

List of Tables

| | | |
|-----|--------------------------------------------------------------------------------------------------------------------------------------------------------------------------------------------------------------------------------------------------------------------------------------------------------------------------------------------------------------------------------------------------------------------|-----|
| 2.1 | An overview of the three generations of fermions and bosons that make up the Standard Model of particle physics. | 5 |
| 3.1 | The independent efficiencies of each of the five veto scintillators using the 2022 dataset. Veto layer 0 belongs to the first module of the veto scintillator station, veto layers 1 and 2 belong to the second module of the veto scintillator station. | 43 |
| 3.2 | The definitions of the eight trigger outputs used in FASER. | 53 |
| 3.3 | Trigger items that combine the eight trigger outputs. | 53 |
| 4.1 | Descriptions of the different steps used in the reconstruction of full tracks within FASER’s tracking spectrometer. | 58 |
| 6.1 | MC cutflow for representative dark photon signal points with mass 25.1 MeV and coupling $\epsilon = 3 \times 10^{-5}$ and mass 50.1 MeV and coupling $\epsilon = 1 \times 10^{-5}$, showing number of signal events entering and passing each selection, along with the efficiency of that selection and the cumulative efficiency to that point. The signal yield is scaled for 27.0 fb^{-1} | 96 |
| 6.2 | Summary of the MC estimate for the neutrino background for 27.0 fb^{-1} in the signal region. Included are uncertainties from flux variations, and those derived from MC statistics, respectively. The total estimate is $(1.5 \pm 1.9(\text{syst.})) \pm 0.5(\text{stat.}) \times 10^3$ events. | 98 |
| 6.3 | Summary of the neutral hadron estimate method targeting two and three-track events. | 99 |
| 6.4 | Cutflow for large-angle muon background in the case of a veto signal (top) and no veto signal (bottom). | 100 |

| | | |
|-----|-----------------------------------------------------------------------------------------------------------------------------------------------------------------------------------------------------------------------------------------------------------------------------------------------------------------------------------------------------------------------------------------------------------------------------------------------------------------------------------------------------------------------------|-----|
| 6.5 | Event yields in the various regions. Note: number of events as found using a 30 pC charge requirement for a single track. | 104 |
| 6.6 | Calculations and predictions for intermediate validation regions and for the final signal regions. In the former case, various ranges are used as test. For the SR, only the integrated 10-500 GeV region is used for the predictions. The uncertainty in 100% due to the Veto region in the range 100-500 GeV having only 1 event. Post-unblinding: in bold, the observed events (0) in both validation and signal regions. | 104 |
| 6.7 | Summary of the different sources of background considered in this analysis and the total estimate, with uncertainty. | 107 |
| 6.8 | Summary of the track scale, and resolution variations in MC and compared to data. | 112 |
| 6.9 | Summary of the various sources of signal uncertainty, the size of the uncertainty and the range of the effect of this uncertainty on the signal yield across the parameter space. For the latter, the numbers in parenthesis indicate the effect on signals in the new exclusion reach with this analysis. The error on the MC statistics is calculated using the standard deviation of the sum of the weights (W) of each sample. The systematic uncertainty is dominated by the uncertainty on the signal generators. . . | 113 |
| 7.1 | Requirements on data to target physics events and ensure good quality data. . . . | 120 |
| 7.2 | Event selection for the ALPs analysis signal region. | 125 |
| 7.3 | MC cutflow for representative ALP-W signal points with mass 120 MeV and coupling $g_{aWW} = 3 \times 10^{-4} \text{ GeV}^{-1}$ and mass 100 MeV and coupling $g_{aWW} = 6 \times 10^{-5} \text{ GeV}^{-1}$, showing number of signal events entering and passing each selection, along with the efficiency and the cumulative efficiency to that point. The signal yield is scaled for 57.7 fb^{-1} | 125 |
| 7.4 | MC cutflow for the neutrino background MC prediction. The background yield is scaled for 57.7 fb^{-1} | 125 |

| | | |
|------|----------------------------------------------------------------------------------------------------------------------------------------------------------------------------------------------------------------------------------------------------------------------------------------------------------------------------------------------------------------------------------------------------------------------------------------------------------------------------|-----|
| 7.5 | Neutrino MC predictions in the calorimeter, magnet and preshower validation regions compared to data. Broken down in terms of neutrino flavour and with the uncertainties from flux variations, experimental uncertainties associated with the preshower and calorimeter, and those derived from MC statistics, respectively. | 135 |
| 7.6 | Summary of the MC estimate for the neutrino background for 57.7 fb^{-1} in the signal region. Included are uncertainties from flux variations, experimental uncertainties associated with the preshower and calorimeter, and those derived from MC statistics, respectively. | 135 |
| 7.7 | MC cutflow for FLUKA muon sample. | 136 |
| 7.8 | MC cutflow specifically for studying ALP large-angle muon background. | 137 |
| 7.9 | The events in ABCD regions defined above, after the baseline selection. The central MC neutrino estimate in the different regions is subtracted from data events to give a picture of the component of large-angle muons captured by this method. In bold is the negative large-angle muon estimate which proves this method unsuitable for targeting this background. | 139 |
| 7.10 | The events in ABCD regions defined above, after the baseline selection and the preshower requirements used in this analysis (PS ratio > 4.5 , PS1 nMIP > 10). The central MC neutrino estimate in the different regions is subtracted from data events to give a picture of the component of large-angle muons captured by this method. In bold is the negative large-angle muon estimates which proves this method unsuitable for targeting this background. | 139 |
| 7.11 | Data and neutrino yields in the different ABCD regions and the prediction for the large-angle muon estimate for the two preshower selections. To calculate the prediction in region A, the expected MC neutrino background is first subtracted from the data in region C. The uncertainty on the neutrino MC includes flux and experimental sources and is propagated to the final estimate. | 142 |
| 7.12 | Final estimates of the large-angle muon background in the two configurations. | 142 |
| 7.13 | Cutflow of events passing selections for the evaluation of cosmic ray muon background. | 143 |
| 7.14 | Summary of events passing selections and calorimeter timing requirement for the evaluation of beam 1 background. | 144 |

| | | |
|------|------------------------------------------------------------------------------------------------------------------------------------------------------------------------------------------------------------------------------------------------------------------------------------------------------------------------------------------------------------------------------------|-----|
| 7.15 | Summary of the different sources of background considered in this analysis and the total estimate, with uncertainty. | 145 |
| 7.16 | The percentage change in yield up and down due to systematic uncertainty on generator type. Uncertainty from each generator are added in quadrature, including the additional 20% uncertainty arising from modeling of B hadrons in the ALP-W model. | 147 |
| 7.17 | The percentage change in yield up and down due to systematic uncertainty on PS1 nMIP. A correction factor of 1.20 is applied, with an uncertainty of 20%. | 150 |
| 7.18 | The percentage change in yield up and down due to systematic uncertainty on the PS Ratio (preshower1/preshower0). A correction factor of 1.13 was applied, with an uncertainty of 13%. | 151 |
| 7.19 | The percentage change in yield for representative signal MC samples in the case of the 6% calorimeter energy systematic uncertainty implemented in this analysis. . . . | 153 |
| 7.20 | An investigation into the percentage change in signal yield for representative signal MC samples with 10% and 20% calorimeter energy systematic uncertainty. | 154 |
| 7.21 | Systematic uncertainties implemented in the statistical analysis framework. | 154 |
| 7.22 | Summary of the various sources of signal uncertainty, the effect of this uncertainty on the signal yield across the parameter space is shown. Numbers in parenthesis indicate the effect on signals in the new exclusion reach with this analysis. The error on the MC statistics is calculated using the standard deviation of the sum of the weights (W) of each sample. | 155 |
| A.1 | Summary and description of each of the sources of uncertainty on the calorimeter energy threshold, leading to a total uncertainty of 6%. | 206 |

Chapter 1

Introduction

This thesis¹ introduces the Forward Search Experiment (FASER) and its role in searches for physics beyond the Standard Model, specifically searching for long-lived particles produced in the far-forward region at the ATLAS Interaction Point at the LHC.

With the exception of gravity, the Standard Model (SM) of particle physics provides a consistent description of the natural world. However, it is unable to address several key questions, suggesting the need for physics beyond the Standard Model (BSM). One of the strongest pieces of evidence for BSM physics is dark matter (DM) which, according to cosmological measurements [28], dominates the matter density in the universe. Its existence could also imply the existence of a dark or hidden sector that mirrors the complexities of the Standard Model of ordinary matter. The two models primarily explored in this work are dark photons, A' , with coupling to the SM photon, and axion-like particles (ALPs), a , with various couplings to SM particles.

The structure of this thesis is as follows: Chapter 2 outlines the current understanding of particle physics and defines the Lagrangian of each of the models discussed. The motivations for searching for dark matter are explored. Theory surrounding the dark photon model is described, in addition to the production and decay modes that are relevant to the parameter space probed with this model. The same is described for the three axion-like particle models discussed: ALPs with coupling to the $SU(2)_L$ gauge boson, ALPs coupling to photons and ALPs coupling to gluons.

Following this is a brief introduction to the LHC and an in-depth description of the components of the FASER detector are given. Also included in this chapter is a description of FASER's trigger

¹The convention $\hbar = c = 1$ is used throughout this thesis

system and data acquisition.

Chapter 4 introduces the processes of event and object reconstruction, with specific focus on calorimetry. The study of the energy response and resolution of the EM calorimeter (ECAL) has been a large focus of the author’s work, specifically with respect to implementing the Monte Carlo (MC) simulation of the ECAL. The results of the 2021 calorimeter test beam are also presented in this chapter. Chapter 5 details the MC simulations used in the analyses discussed in this thesis, it also describes the framework used in the statistical interpretation of the results presented.

This is followed by an analysis chapter describing the search for dark photons. This analysis uses LHC Run 3 data at a centre of mass energy of $\sqrt{s} = 13.6$ TeV corresponding to an integrated luminosity of 27.0 fb^{-1} collected by the FASER experiment in 2022. The search sets world-leading exclusion limits for dark photons with masses $17 \text{ MeV} < m_{A'} < 70 \text{ MeV}$ and couplings $2 \times 10^{-5} < \epsilon < 1 \times 10^{-4}$. Reinterpretation of these results for the $B - L$ gauge boson is also presented. In this analysis, the author contributed to estimation of the SM background processes, validation of these estimates using data-driven techniques and the estimate of the systematic uncertainties associated with the calorimeter.

A second analysis chapter describes the search for axion-like particles. This analysis also uses LHC Run 3 data, corresponding to an integrated luminosity of 57.7 fb^{-1} collected by the FASER experiment in 2022 and 2023. This search sets world-leading exclusion limits for ALPs with masses $100 < m_a < 250 \text{ MeV}$ and couplings $3 \times 10^{-5} < g_{aWW} < 5 \times 10^{-4} \text{ GeV}^{-1}$. The exclusion limits for ALPs coupling to photons and ALPs coupling to gluons are also presented, in addition to further reinterpretation with the $U(1)B$ gauge boson model, the up-philic scalar model, the Type-I two Higgs doublet model, and the dark photon model. The author led analysis efforts, covering numerous aspects including the definition and optimisation of the signal selection, the estimation of the SM background using both MC and data-driven approaches, the estimation of signal systematic uncertainties related to the MC generation, the estimation of the experimental systematic uncertainties related to the calorimeter, and the statistical interpretation of the final results.

The final chapter before the conclusion describes the hardware tests performed in preparation for the preshower detector upgrade in 2024. The author had significant involvement in the pre-production and production level tests of the chips used in the high-precision W-Si preshower

detector upgrade. The implications of this detector upgrade on future ALP searches are explored in addition to the outlook of the FASER experiment for the remainder of Run 3 and Run 4.

Chapter 2

Theoretical Overview

This chapter details the theoretical motivation for searching for LLPs with FASER, specifically dark photons and ALPs. It provides an overview of the Standard Model of particle physics, shortcomings that contribute towards the motivation for a search for dark matter, and details of the particular models that are targeted in the analyses discussed in this thesis.

2.1 The Standard Model of Particle Physics

The Standard Model provides an elegant description of all known elementary particles and their interactions. It has been extremely successful in describing experimental measurements in high energy particle physics [29] and describes three of the four fundamental forces: the weak force, the strong force, and electromagnetism. An overview of the structure of the SM is given in Table 2.1; the information presented is taken from Ref. [30] with the exception of the upper limit given on the mass of the electron neutrino, which is taken from Ref. [31]. The SM is made up of fermions, particles of half-integer spin that obey Fermi-Dirac statistics, and bosons, particles with integer spin that obey Bose-Einstein statistics. The fermions can be divided into two categories: quarks and leptons. The bosons can be divided into gauge bosons, with spin 1, and scalar bosons, with spin 0.

There are three “generations” of fermions with increasing mass within the SM, into which the 6 quarks and 6 leptons are arranged. The gauge bosons: W and Z bosons, the photon and the gluon, are the vector bosons responsible for the weak, electromagnetic, and strong interactions,

Table 2.1: An overview of the three generations of fermions and bosons that make up the Standard Model of particle physics.

| The Standard Model | | | | | |
|--------------------|-------------------|------------|----------------|---------------|-----------|
| Fermions | | | | | |
| Generation | Name | Symbol | Charge (e) | Spin | Mass |
| I | Up quark | u | $+\frac{2}{3}$ | $\frac{1}{2}$ | 2.2 MeV |
| | Down quark | d | $-\frac{1}{3}$ | $\frac{1}{2}$ | 4.7 MeV |
| | Electron | e | -1 | $\frac{1}{2}$ | 0.511 MeV |
| | Electron neutrino | ν_e | 0 | $\frac{1}{2}$ | <0.8 eV |
| II | Charm quark | c | $+\frac{2}{3}$ | $\frac{1}{2}$ | 1.275 GeV |
| | Strange quark | s | $-\frac{1}{3}$ | $\frac{1}{2}$ | 95 MeV |
| | Muon | μ | -1 | $\frac{1}{2}$ | 105.7 MeV |
| | Muon neutrino | ν_μ | 0 | $\frac{1}{2}$ | <0.19 MeV |
| III | Top quark | t | $+\frac{2}{3}$ | $\frac{1}{2}$ | 173 GeV |
| | Bottom quark | b | $-\frac{1}{3}$ | $\frac{1}{2}$ | 4.18 GeV |
| | Tau | τ | -1 | $\frac{1}{2}$ | 1.78 GeV |
| | Tau neutrino | ν_τ | 0 | $\frac{1}{2}$ | <18.2 MeV |
| Bosons | | | | | |
| Force | Name | Symbol | Charge (e) | Spin | Mass |
| Electromagnetic | Photon | γ | 0 | 1 | 0 |
| Strong | Gluon | g | 0 | 1 | 0 |
| Weak | W^+ | W^+ | +1 | 1 | 80.4 GeV |
| | W^- | W^- | -1 | 1 | 80.4 GeV |
| | Z | Z^0 | 0 | 1 | 91.2 GeV |
| - | Higgs | h | 0 | 0 | 125.2 GeV |

respectively. Gravity is not incorporated into the SM although it should have a force carrier, the graviton, with spin 2 [32]. Additionally, there is the Higgs boson [33, 34], a scalar boson that, via the spontaneous electroweak symmetry breaking (EWSB) of the Higgs field, gives mass to the fundamental fermions and the W and Z bosons [35]. This process is known as the Higgs mechanism.

Leptons experience three of the fundamental interactions: the weak interaction, gravity and, if charged, electromagnetism. The three types are: electron e , muon μ , and tau τ ; the muon and tau leptons are unstable particles which decay to lighter particles via the weak interaction. The neutrinos, which come in these three flavours, are also classed as leptons. Neutrinos can oscillate between flavours; they are neutral particles that interact very rarely and are considered nearly massless [36].

Quarks are the only particles in the SM to experience all four fundamental forces, they carry colour charge which allows them to experience the strong interaction. Quarks come in six flavours: up and down, charm and strange, top and bottom. Free quarks cannot exist in nature, at least not at the current temperature and state of our universe due to colour confinement [37]: only gauge invariant objects, i.e. colourless particles can be observed. Quarks are confined within hadrons, a particle class that includes mesons and baryons. Mesons consist of a quark-antiquark pair, for example, the pion π . The π^+ meson is made up of an up and an anti-down quark $u\bar{d}$, its antiparticle, the π^- meson, is made up of an anti-up quark and a down quark $\bar{u}d$. The neutral pion, the π^0 meson, is considered to be a combination of $u\bar{u}$ and $d\bar{d}$. Baryons consist of three quarks, for example the proton is a baryon made up of uud . Additionally, exotic hadrons with more than three quarks have been predicted since the formation of the quark model [38]. Tetraquark and pentaquark candidates have been observed [39], consisting of four and five quarks, respectively, where “quarks” refers to both the particle and its antiparticle.

2.1.1 Quantum Electrodynamics and Electroweak Unification

Quantum Electrodynamics (QED) is the quantum field theory of electromagnetic interactions. The photon, γ , is the force carrier of the electromagnetic interaction. QED acts between photons and electrically-charged fermions. It is an abelian gauge theory, meaning that all elements within the group are commutable, described by the symmetry group $U(1)$.

The weak interaction is responsible for radioactive decay, its force carriers are the W^\pm and Z bosons. The weak force is the only fundamental force to break CP symmetry [40]. Unification between electromagnetism and the weak interaction results in a $SU(2)_L \times U(1)_Y$ group. The $SU(2)_L$ group has three associated gauge fields: $W_\mu^{(1)}$, $W_\mu^{(2)}$ and $W_\mu^{(3)}$, the $U(1)_Y$ group has a neutral gauge field B_μ which couples to hypercharge ($Y = 2(Q - T_3)$ where Q is the electric charge and T_3 is the third component of weak isospin). The W bosons can be written as a combination of $W_\mu^{(1)}$ and $W_\mu^{(2)}$:

$$W^\pm = \frac{1}{\sqrt{2}}(W_\mu^{(1)} \mp W_\mu^{(2)}). \quad (2.1)$$

The electroweak gauge bosons γ and Z are written as combinations of B_μ and $W_\mu^{(3)}$, connected

through the weak mixing angle θ_W [41]:

$$A_\mu = +B_\mu \cos \theta_W + W_\mu^{(3)} \sin \theta_W, \quad (2.2)$$

$$Z_\mu = -B_\mu \sin \theta_W + W_\mu^{(3)} \cos \theta_W, \quad (2.3)$$

where A_μ and Z_μ are the corresponding neutral fields of the photon and Z boson, respectively. Gauge bosons in the SM are required to be massless, however, the masses of the W and Z bosons are acquired through the Higgs mechanism, implying EWSB [41]. The coupling of the Higgs field to fermions (quarks and charged leptons) occurs via Yukawa coupling [42].

2.1.2 Quantum Chromodynamics

Quantum Chromodynamics (QCD) is the quantum field theory of strong interactions. The gluon is the force carrier for the strong interaction, which acts on quarks and gluons. Like electric charge in QED, the QCD charge carried by quarks and gluons is colour, which comes in three types: red, blue and green. There are eight gluons due to these colour combinations, corresponding to eight fields G_μ^a where $a = 1, \dots, 8$ [41].

The coupling strength, α_s , of QCD is dependent on the energy scale [43]; α_s is large at low energies, requiring a non-perturbative QCD description where quarks and gluons behave according to colour confinement; α_s is small at higher energy, requiring a perturbative QCD description where quarks and gluons have asymptotic freedom. At higher orders of perturbation theory, loop corrections arise leading to ultraviolet (UV) divergences, which requires the introduction of the renormalisation scale, μ_R , at which α_s can be calculated. QCD is a non-abelian gauge theory, meaning that gluons are able to self-interact. It has the symmetry group $SU(3)_C$ which describes rotation in colour space.

2.1.2.1 The Strong CP Problem

An unsolved puzzle in the Standard Model is the lack of CP violation in strong interactions [44], an observation that should be possible according to QCD [45]. Weak interactions are known to violate CP symmetry, but in strong interactions, which also contain a CP-violating term in their

Lagrangian, this remains unobserved [46].

2.1.3 The Standard Model Lagrangian

The SM is a quantum field theory in which Lagrangian formalism is used to describe the field associated with each kind of particle. The symmetries in the SM are described by local phase transformations of the symmetry groups $SU(3)_C \times SU(2)_L \times U(1)_Y$. A compact form of the Lagrangian can be written as shown in Equation 2.4.

$$\begin{aligned} \mathcal{L} = & -\frac{1}{4}F^{\mu\nu}F_{\mu\nu} \\ & + \bar{\Psi}(i\gamma^\mu D_\mu)\Psi + h.c. \\ & + \Psi_i y_{ij} \Psi_j \Phi + h.c. \\ & + |D_\mu \Phi|^2 - V(\Phi). \end{aligned} \tag{2.4}$$

Within this equation are the kinetic terms of the three fundamental forces described in the SM that correspond to the $SU(3)_C \times SU(2)_L \times U(1)_Y$ gauge invariance. $\bar{\Psi}(i\gamma^\mu D_\mu)\Psi$ is the gauge covariant derivative term which encompasses the interactions between the fermions and the forces and expresses how fields vary based on their position within a reference frame, where Ψ is the wavefunction. The remaining terms refer to the contributions to the SM from the Higgs boson field (Φ): $\Psi_i y_{ij} \Psi_j \Phi$ describes the Yukawa terms related to fermion masses, $|D_\mu \Phi|^2$ dictates how the Higgs couples through the gauge covariant derivative to particles, $V(\Phi)$ describes the interactions of the Higgs with the vacuum expectation value, and “+*h.c.*” refers to the addition of the Hermitian conjugate. The $-\frac{1}{4}F^{\mu\nu}F_{\mu\nu}$ term is the kinetic energy term, where $F_{\mu\nu}$ can be written in terms of the field tensors for the electroweak and strong force:

$$F^{\mu\nu}F_{\mu\nu} = B^{\mu\nu}B_{\mu\nu} + W^{(i)\mu\nu}W_{\mu\nu}^{(i)} + G^{a\mu\nu}G_{\mu\nu}^a. \tag{2.5}$$

2.2 Shortcomings of the Standard Model

Excluding gravity, the Standard Model provides a consistent description of all known fermionic particles and their interactions up to the Planck scale $\mathcal{O}(10^{19})$ GeV [6]. However, there are several

physical phenomena that the SM cannot explain, pointing at the existence of physics beyond the Standard Model (BSM).

2.2.1 Dark Matter

One of the strongest arguments that the SM does not yet provide a complete picture is dark matter (DM) which dominates the matter density in the universe. Although the origin and properties of DM remain a mystery, the existence of DM in the universe is inferred from gravitational and visible effects [47] that will be discussed in this section. Other pieces of evidence of DM include the temperature fluctuations [48] of the cosmic microwave background (CMB) which show anisotropies that can be used to measure the mean density of dark matter, which is roughly five times larger than the baryonic matter density of the universe. Ordinary matter makes up only 5% of the matter in our universe, the rest falls under the umbrella of dark matter and dark energy [28]. Dark energy contributes to 68% of the energy content of the current universe, it is necessary to explain the accelerating expansion of the universe. Unlike dark matter, it has a very low density and is uniform across all space.

2.2.1.1 Galactic Rotation Curves

The first evidence of dark matter was in the measurement of galaxy rotation curves [49] and the formation and growth of galactic halos. It has been found that the stellar rotational velocity within a galaxy remains constant or “flat” regardless of how distant a star is from the galactic centre. This observation goes against expectation, Newton’s law of gravity demonstrates that rotational velocity of stars should decrease with distance from the centre of the galaxy according to $v \propto 1/\sqrt{r}$ [41]. Figure 2.1, adapted from Ref. [4], shows the observed rotational velocity curve of the M33 galaxy, compared with the best fitting model that includes the contributions from the dark matter halo, stellar disc and gaseous disc. The shape of the observed rotational velocity at higher radius motivates the idea that the galactic halo of dark matter must be contributing to these observations.

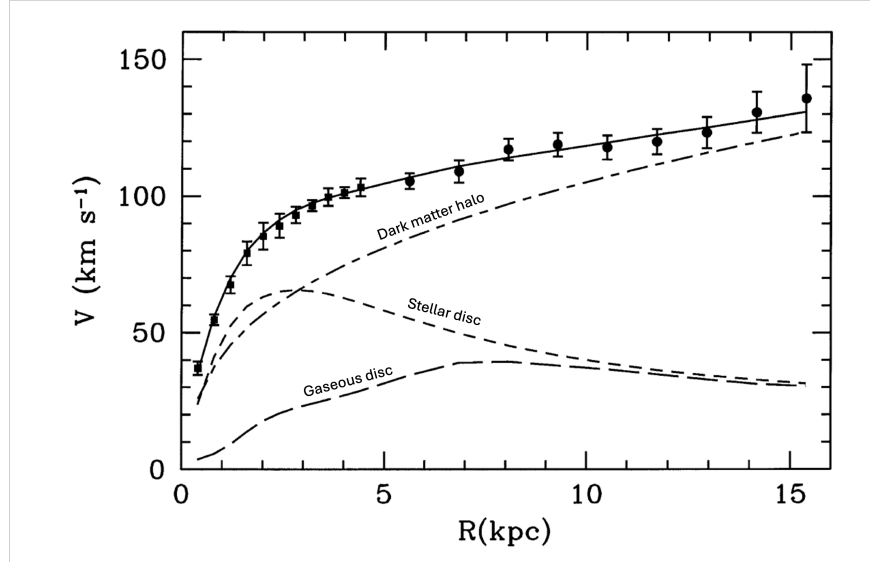


Figure 2.1: The observed galactic rotation curve (data points) for the M33 galaxy showing the contributions from the stellar disc and gaseous disc and the dark matter halo contribution needed to match the data. Figure from Ref. [4].

2.2.1.2 Bullet Cluster

The most energetic event known to have occurred since the Big Bang is the formation of galaxy cluster 1E 0657-56 from the collision of two large clusters of galaxies. Figure 2.2 [5] shows this “Bullet Cluster”. The Figure shows a composite image which combines data from NASA’s Chandra X-ray Observatory [50] and optical data from the Hubble Space Telescope and Magellan Telescope with a gravitational lensing map [5]. The two pink regions in the Figure represent hot gas containing most of the “normal” matter. The blue regions show where most of the mass of the cluster is concentrated; clear separation from normal matter leads to the conclusion that the majority of the mass of the galaxy clusters comes from dark matter. The Bullet Cluster also provides an opportunity for gravitational lensing studies, gravitational lensing is the visible effect of the bending of space-time near any gravitating mass [51], causing the deflection of passing light. The lensing of distant objects without anything visible in the foreground to cause such lensing, provides a potential piece of evidence for invisible gravitational dark matter, which would explain the distortion and magnification of images of background galaxies.



Figure 2.2: A composite image taken from Ref. [5] (X-ray: NASA/CXC/CfA/M.Markevitch et al.; Optical: NASA/STScI; Magellan/U.Arizona/D.Clowe et al.; Lensing Map: NASA/STScI; ESO WFI; Magellan/U.Arizona/D.Clowe et al.) showing the galaxy cluster 1E 0657-56, regions of hot gas are shown in pink, regions where most of the mass density lies are shown in blue.

2.2.2 Baryon Asymmetry and CP Violation

The matter-antimatter asymmetry problem is the apparent imbalance of baryonic and anti-baryonic matter in the universe. According to assumptions made in the Big Bang, the universe should be neutral and equal amounts of matter and antimatter should have been created at the time of the Big Bang. This is not the case, the universe looks to be dominated by matter.

Sakharov [52] proposed three conditions that must be fulfilled in order for any amount of matter-antimatter asymmetry to exist. These are as follows: the violation of baryon number conservation, charge-parity (CP) violation, and non-thermal equilibrium.

One source of CP violation is the Cabibbo-Kobayashi-Maskawa (CKM) matrix that describes quark mixing [44]. Neutrinos could also contribute to CP violation; with the inclusion of neutrino masses, another source arises from the weak interaction in leptonic mixing [53]. However, with existing sources of CP violation in the SM, the baryon asymmetry generated as a result is not currently sufficient to explain the current levels of matter-antimatter asymmetry.

2.2.3 The Hierarchy Problem

The Planck mass provides the Planck scale $\mathcal{O}(10^{19})$ GeV [6]; the limit of the Planck scale is determined by the magnitudes of the four universal constants: the speed of light c , the Planck constant h , Newton’s gravitational constant G_N , and the Boltzmann constant k_B . The Hierarchy problem arises in relation to the Higgs mass, which has two terms: the bare Higgs mass and the mass that comes from the sum of loop corrections from particles that couple to the Higgs. Due to the Higgs’ coupling to fermions and the W and Z bosons, m_H is proportional to the fermion and boson masses. As a result of loop corrections, one would expect the mass of the physical Higgs boson to approach that of the Planck scale. However, the Higgs mass lies around the weak scale ($m_W \sim 100$ GeV – 1 TeV) and, as mentioned, the Higgs mechanism occurs via spontaneous EWSB. An unphysical amount of “fine-tuning” in the SM is necessary to obtain a Higgs mass at the correct value.

2.3 Motivating the Search for Dark Matter

DM can be framed as an unknown particle produced in the early universe [47], this modelling explores the idea that DM has a weak coupling to baryonic matter in an attempt to place the question of dark matter into the context of known cosmology and particle physics [54].

2.3.1 Detection Methods

There are three main methods to search for dark matter candidates: indirect detection, direct detection and collider searches [55]. Indirect dark matter detection methods search for the products of dark matter annihilation, this is usually done with space-based experiments such as the Fermi Large Area Telescope which looks for an excess of gamma rays from the centre of the Milky Way [56]. Direct dark matter detection looks for the direct interaction of DM with atomic nuclei [57], requiring large experiments such as the LZ experiment [57] at Sandford Underground Research Facility in South Dakota, US. The experiment consists of a dual-phase time projection chamber (TPC) containing seven tonnes of liquid xenon [58]. Another example of a direct detection dark matter experiment is DarkSide [59] in Gran Sasso, Italy; this experiment uses argon-based TPCs.

Traditional searches for dark matter in high-energy collisions at particle colliders rely on the idea of missing transverse energy from electrically neutral, invisible particles and the detection of visible components such as hadron jets and charged leptons [60]. This is distinct from far-forward experiments at colliders, such as FASER, which do not exploit the transverse plane. Collider searches offer a probe to dark matter but only direct or indirect DM searches can confirm a signal is dark matter, since there are existing weakly-interacting particles that can produce missing transverse energy such as neutrinos.

2.3.2 WIMPs and Thermal Relic Density

Dark matter could be a thermal relic of the Big Bang [6]. The thermal relic density is the constant number density of dark matter in the event of thermal freeze out [61]. In the high temperatures of the early universe thermal equilibrium is achieved, as the universe cools and the temperature falls below the mass of the dark matter particles, the number of dark matter particles falls exponentially. In addition to cooling, the universe is also expanding which prevents the dark matter density from falling completely to zero. The distribution of gaseous dark matter particles at this point is spread such that annihilation cannot happen. This is the point at which thermal freeze out occurs, the number density of dark matter asymptotically approaches a constant value. Thermal freeze out is shown in Figure 2.3 [6] for a dark matter particle with the correct relic density to be a remnant of the Big Bang.

Weakly interacting massive particles (WIMPs) are the most well studied candidates for dark matter of a particulate nature [6]. They typically have a mass in the range of the weak scale and naturally have the correct relic density to serve as dark matter candidates. If a dark matter particle χ has mass $m_\chi \sim 100$ GeV and a coupling to the hidden sector $g_\chi \sim 0.6$ around the weak scale, this results in a thermal relic density [62]:

$$\Omega_\chi h^2 \sim \frac{m_\chi^2}{g_\chi^4} h^2 \sim 0.12 \quad (2.6)$$

which corresponds to the density of non-baryonic dark matter evident in the CMB, $\Omega_{DM} \sim 0.227 \pm 0.014$ [28], where h here is Hubble constant in units of $100 \text{ kms}^{-1} \text{ Mpc}^{-1}$, $h = 0.6727 \pm 0.0066$.

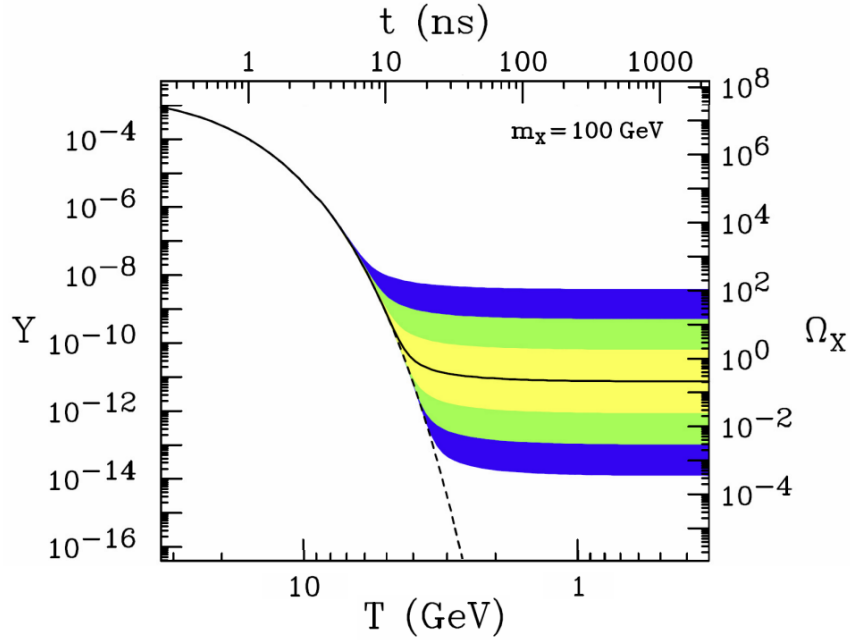


Figure 2.3: Thermal freeze-out of dark matter for different annihilation cross sections. The comoving number density Y and resulting thermal relic density Ω_χ of a 100 GeV dark matter particle as a function of temperature T . The solid line represents the dark matter cross section that yields the correct relic density, the coloured bands show the density for cross section variation of order 10, 10^2 and 10^3 from $\Omega_\chi \sim 0.23$. The dashed line shows the number density of a particle that did not “freeze-out” but remained in thermal equilibrium. Figure from Ref. [6].

2.3.3 Dark Sector Models

The absence of interactions between DM and ordinary matter motivates the idea that potential DM particles χ would be neutral under SM forces G_{SM} . The same logic dictates that all SM particles are neutral under an extended SM by a non-abelian gauge group G_ν [63]. However, these potential light, long-lived DM particles could be charged under new forces that have not yet been discovered [54]. Such new forces could exist in a dark sector or hidden-sector, which is more complex than a single DM particle; the dark matter candidates could belong to an entire new sector that mirrors the complexities of the Standard Model.

This thesis will focus on hidden-sector dark matter. Constraints from SM symmetries allow several types of “portal” interactions between dark sectors and the SM. The mass range of hidden-sector DM lies in the vicinity of Standard Model mass scales $\mathcal{O}(100 \text{ TeV})$ down to below keV masses. FASER has sensitivity to long-lived particles with masses around $m \sim 100 \text{ MeV}$ [7] and renormalisable portal interactions between the SM and the dark sector: dark photons and the $B - L$ gauge boson, dark Higgs, and heavy neutral leptons (HNLs). There is also sensitivity to pseudoscalar axion-like particles (ALPs) coupled to photons through non-renormalisable operators [7]. The different models are introduced in Figure 2.4, showing the four portal types to which FASER is sensitive.

There is the “vector” portal mediated by the dark photon and the “axion” portal mediated by ALPs coupling to photons (ALP-photon), gluons (ALP-gluon) and the $SU(2)_L$ gauge boson (ALP-W). Additionally, although not explored here, there is the “Higgs” portal mediated by dark scalars and the “neutrino” portal mediated by heavy neutral leptons (HNLs).

Three of these four models are considered benchmark models defined by the CERN Physics Beyond Colliders (PBC) [64] study group: dark photons (BC1) [65], ALP-photon (BC9) and ALP-gluon (BC11) [66]. The ALP-W model [67, 68] is not considered a PBC benchmark, however, ALPs with coupling to the $SU(2)_L$ gauge boson provide a more natural UV completion of the ALP-photon model.

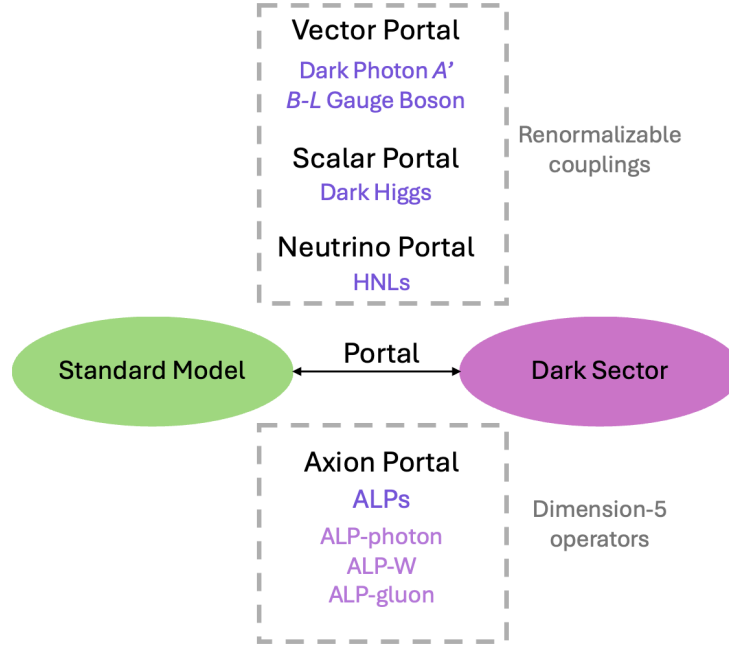


Figure 2.4: The different portals involved in dark sector dark matter models. The four main portal types are highlighted: Vector, Scalar, Neutrino, Axion, grouped by those that require renormalisable coupling and those that require higher operators.

2.4 Motivating a Forward Search at the LHC

In the setting of the LHC, such light, weakly interacting, long-lived candidates for dark matter are predominantly produced along the line of sight (LOS), in the far-forward region from the interaction points. The particles may travel hundreds of metres without interacting, before they decay to visible particles [7]. They are produced parallel to the beam line [69], in an inherent blind spot that the large LHC experiments are unable to access due to where the LHC beam pipe lies in relation to their experimental setup, and their focus on studying the transverse plane. FASER is ideally situated to exploit this blind spot, lying on the beam collision axis 480 m downstream of the ATLAS interaction point (IP1). More details about the location and experimental setup of FASER are given in Chapter 3.

2.5 The Dark Photon

As introduced before, the dark photon, A' , is a hypothetical particle that could provide a “vector” portal to a dark sector that contains a $U(1)'$ electromagnetic force [1]. The renormalisable interaction between $U(1)'$ and the SM results in the dark photon that kinetically mixes with the SM photon [70]. The Lagrangian which describes the dark photon is obtained from an extension of the Standard Model Lagrangian through the addition of a $U(1)'$ gauge boson A'^μ such that the Lagrangian [71] can be written as:

$$\mathcal{L} = -\frac{1}{4}F_{\mu\nu}F^{\mu\nu} - \frac{\epsilon'}{2}F_{\mu\nu}F'^{\mu\nu} - \frac{1}{4}F'_{\mu\nu}F'^{\mu\nu} - eJ_\mu A^\mu - e'J_\mu A'^\mu + \frac{1}{2}m_{A'}^2 A'^2 \quad (2.7)$$

where A^μ and A'^μ denote the gauge bosons associated with $U(1)$ hypercharge and new $U(1)'$ gauge group, respectively. $-\frac{\epsilon'}{2}F_{\mu\nu}F'^{\mu\nu}$ is the kinetic term connecting $F_{\mu\nu}$, the electromagnetic field strength tensor associated with the Standard Model $U(1)$, and $F'^{\mu\nu}$, the tensor associated with $U(1)'$ and the dark sector. $m_{A'}$ is the mass of the dark photon and the hypercharge current is written as $J_\mu = \sum_f \bar{f} A' \gamma f$, where the sum is over all SM fermions, f . e and e' are the electric charge and the charge associated with the dark sector, respectively.

The detection of the dark photon is made possible by its kinematic mixing with the Standard Model photon, the strength of the coupling between the SM and the dark sector is governed by a mixing parameter ϵ . After redefining the fields and rotating to the mass eigenstates [71], the new gauge boson acquires a coupling to the $U(1)$ hypercharge that is proportional to ϵ' . The coupling can be expressed as $\epsilon = \epsilon' \cos \theta_W$, where θ_W is the weak mixing angle. The Lagrangian [1] for the dark photon can therefore be written:

$$\mathcal{L} \supset \frac{1}{2}m_{A'}^2 A'^2 - \epsilon e \sum_f q_f \bar{f} A' \gamma f. \quad (2.8)$$

where $m_{A'}$ is the mass of the dark photon, ϵ is the kinetic mixing parameter that defines the parameter space of the dark photon model, and q_f is the normalised electric charge.

The size of the kinetic mixing parameter, ϵ , determines the strength of the interaction and the lifetime of the dark photon. The kinetic mixing parameter can be anything between 10^{-11}

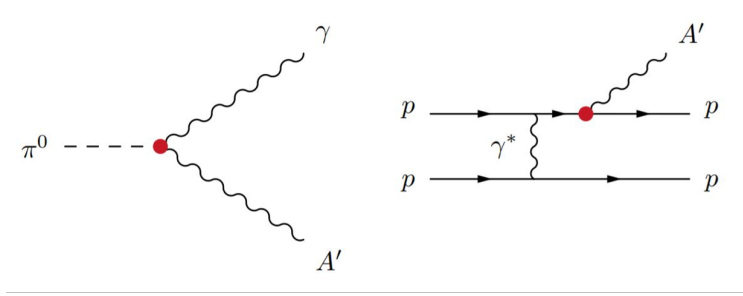


Figure 2.5: Feynman diagrams for LLP production processes: dark photon production from pion decay (left), dark photon production via dark bremsstrahlung (right). The red circle indicates the kinetic mixing parameter ϵ . Figure from Ref. [7].

and 10^{-2} . The lower the kinematic coupling, the lower the decay rate to SM particles, which is proportional to ϵ^2 , and hence the longer lived the particle. The kinetic mixing of the dark photon needs to be small to motivate that such a particle has not yet been observed.

2.5.1 Dark Photon Production and Decay

Dark photon production in the very forward region takes place predominantly via light meson decays and dark bremsstrahlung. Dark bremsstrahlung is the emission of a dark photon from proton scattering [7]. These processes produce highly-energetic dark photons along the LOS with a decay length compatible with the location of FASER. The Feynman diagrams for dark photon production via neutral pion decay and dark bremsstrahlung are shown in Figure 2.5 [7]. For light meson decays the example of π^0 decay is shown as it is the dominant signal contribution, however, there is also a significant contribution from η decay which is a comparable production mode for $m_{A'} \sim 100$ MeV, occurring via the same mechanism.

Dark photon production via neutral pion decay $\pi^0 \rightarrow A' \gamma$ is accessible for $m_{A'} < m_{\pi^0} \approx 135$ MeV, with a branching fraction of $B(\pi^0 \rightarrow A' \gamma) = 2 \epsilon^2 (1 - m_{A'}^2/m_{\pi^0}^2)^3 B(\pi^0 \rightarrow \gamma \gamma)$ where $B(\pi^0 \rightarrow \gamma \gamma) \approx 0.99$ [1, 72]. Production via eta meson decay $\eta \rightarrow A' \gamma$ is accessible for $m_{A'} < m_\eta \approx 548$ MeV, with a branching fraction of $B(\eta \rightarrow A' \gamma) = 2 \epsilon^2 (1 - m_{A'}^2/m_\eta^2)^3 B(\eta \rightarrow \gamma \gamma)$ where $B(\eta \rightarrow \gamma \gamma) \approx 0.39$ [1, 72]. Production via dark bremsstrahlung $pp \rightarrow pp A'$ is accessible for $m_{A'}$ up to $\mathcal{O}(2 \text{ GeV})$ [73].

Dark photon production can occur through other mechanisms involving the decays of heavier mesons such as through η' meson decay or through direct Drell-Yan production in which a quark-

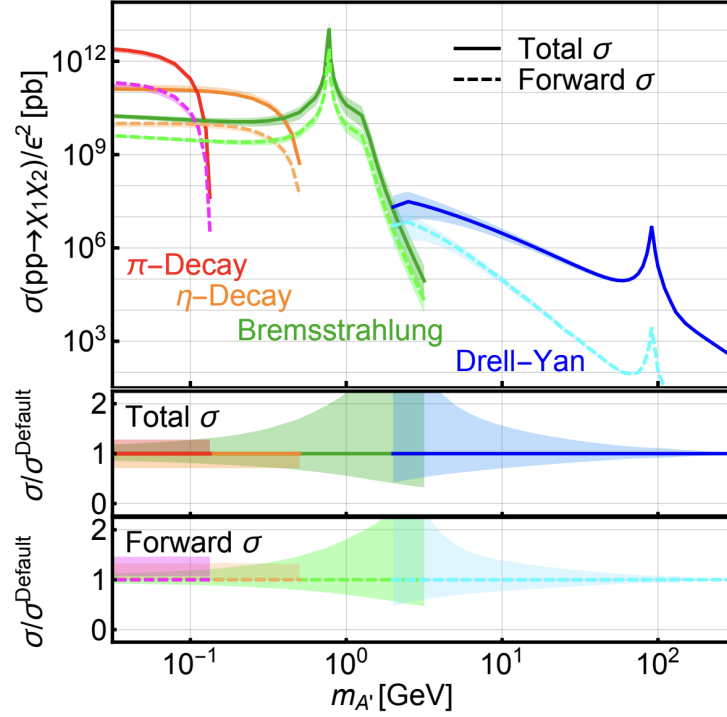


Figure 2.6: Inelastic dark photon production cross section (per ϵ^2) as a function of mass. The total cross section and the far-forward cross section are shown. Figure from Ref. [8].

antiquark pair annihilate to produce a dark photon $q\bar{q} \rightarrow A'$ [74]. These production mechanisms have very small cross sections at the dark photon mass range of interest, hence they can be considered sub-dominant and their contributions neglected. An overview of the total and far-forward production cross section for dark photons is shown in Figure 2.6 [8]. The highest dark photon mass considered in the search for dark photons described in this thesis is $m_{A'} = 112$ MeV, the Drell-Yan production mechanism becomes relevant at masses above $m_{A'} \sim 1$ GeV.

In the case where $E_{A'} \gg m_{A'} \gg m_e$ where $E_{A'}$ is the energy of A' , dark photons typically have a mass $m_{A'} \sim 100$ MeV and coupling $\epsilon \sim 10^{-5}$ with a decay length [65]:

$$L = c\tau\gamma\beta \sim (80 \text{ m}) \left[\frac{10^{-5}}{\epsilon} \right]^2 \left[\frac{E_{A'}}{\text{TeV}} \right] \left[\frac{100 \text{ MeV}}{m_{A'}} \right]^2 \quad (2.9)$$

where τ is the lifetime of the dark photon, travelling at speed $\beta = v/c$ where c is the speed of light. Dark photons with this mass and coupling have $\mathcal{O}(\text{TeV})$ energy and a decay length of the order of 80 m, this is well within the range of FASER's sensitivity to LLPs. The dark photon decay length and the branching fraction into different leptonic and hadronic final states is shown

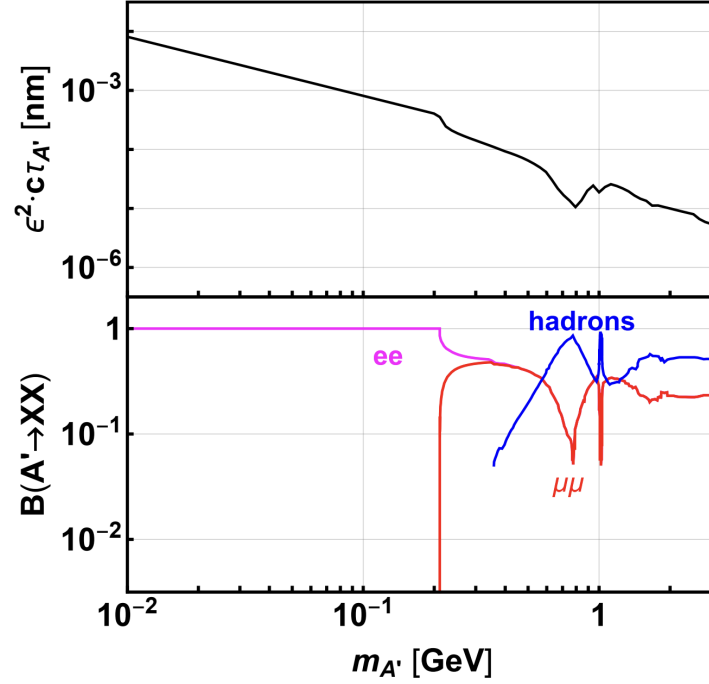


Figure 2.7: (Top) The decay length of the dark photon in the parameter space that FASER is sensitive to. (Bottom) The branching fractions of the dark photon into leptonic and hadronic final states, as a function of dark photon mass. Figure from Ref. [7].

in Figure 2.7 [7]. Dark photons with masses in the range $2m_e < m_{A'} < 2m_\mu \simeq 211$ MeV decay to e^+e^- pairs with a branching fraction of 100%.

2.5.2 The Parameter Space and Existing Limits

Figure 2.8 gives a picture of the dark photon parameter space and the existing limits from experiments that have also searched for a massive dark photon with kinetic mixing between $U(1)'$ and hypercharge. The dark photon model allows for the correct thermal relic density to be obtained [1], as discussed in Section 2.3.2, in the scenario where the dark photon couples to a light dark matter field, χ . The thermal relic density is shown with the red line, in order for the dark photon model to correspond to $\Omega_\chi h^2 = 0.12$, the line assumes that the mass ratio between the dark matter candidate and the dark photon is equal to $m_\chi/m_{A'} = 0.6$ and the dark photon coupling constant to dark matter has a fixed value of $\alpha_{DM} = 0.1$ [1]. These constraints ensure that the dark matter primarily annihilates to SM final states via $\chi\chi \rightarrow A' \rightarrow ff$ since it is assumed that $m_{A'} < 2m_\chi$ [71].

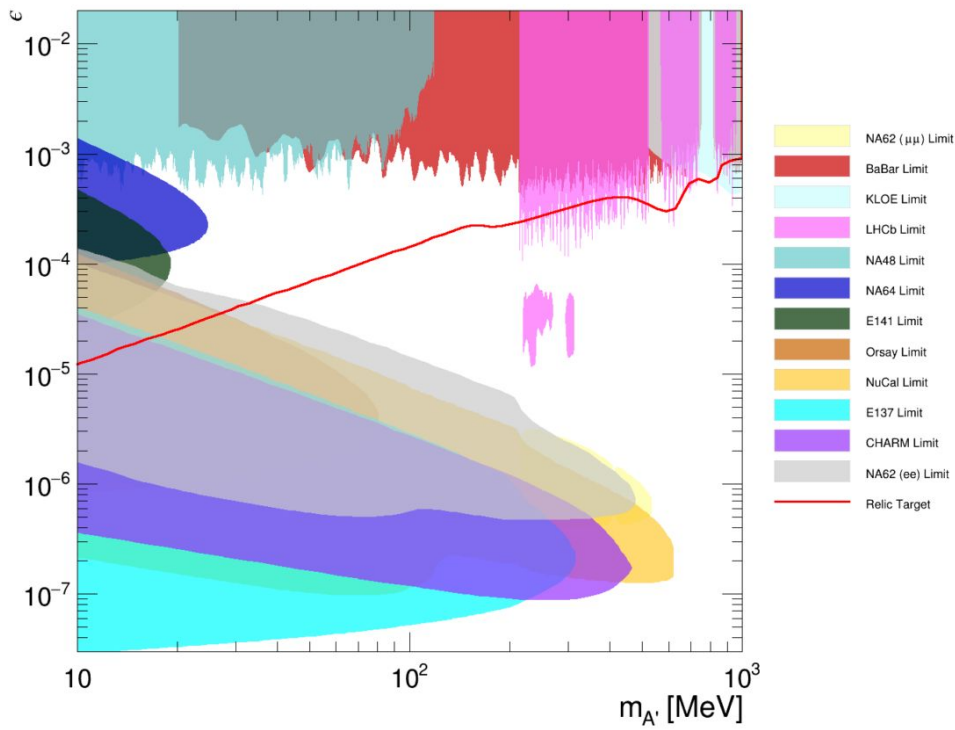


Figure 2.8: Existing experimental constraints in the parameter space probed in FASER’s search for dark photons. Includes existing limits from the BaBar collaboration, the KLOE experiment, the LHCb collaboration, NA62, NA64, NA48, E141, Orsay, NuCal, E137, CHARM.

Existing experimental constraints in the parameter space probed by FASER’s search for dark photons include limits set by: BaBar [75], KLOE [76], LHCb [77], NA62 [78, 79], NA64 [80], NA48 [81], E141 [82], Orsay [83], NuCal [84], E137 [85] and CHARM [86]. The different experimental efforts can be divided into results from: electron beam dumps [87], proton beam dumps [88], e^+e^- colliders, pp collisions, meson decays and electron fixed-target experiments [89].

Limits set by electron beam dump experiments tend to be in the low mass region across a broad range of couplings, for example NA64, E141 and E137 all show results from electron beam dumps. Extending to slightly higher mass range and in a region of relatively low coupling are the results from proton beam dumps, for example the Orsay, NuCal and CHARM limits [90]. Across most of the mass range in the parameter space FASER is sensitive to, at higher coupling than the electron and proton beam dump experiments ($\epsilon > 10^{-3}$), are the results from e^+e^- colliders such as BaBar and KLOE. Results from pp collisions target parameter space at high coupling and with dark photon mass towards $\mathcal{O}(1 \text{ GeV})$, for example the limit in pink set by LHCb which searched for dark photon decays with $\mu^+\mu^-$ final states. FASER’s search for dark photons particularly targets the region of unexplored parameter space with $\epsilon \sim 10^{-5} - 10^{-4}$ and with masses $m_{A'} \sim 10 \text{ MeV} - 100 \text{ MeV}$.

2.6 Axion-like Particles

Solutions to the strong CP problem have been proposed in many forms [91, 92], one of the most successful solutions is the Peccei-Quinn Mechanism [68]. The global $U(1)$ symmetry (the PQ symmetry) is spontaneously broken by the QCD axion a [93]. Its coupling to ordinary matter is proportional to $1/f_a$, where f_a is the scale at which electroweak symmetry breaking occurs. The physical mechanism that leads to the axion is model dependent and also allows for other axion-like particles [91].

ALPs are defined as pseudoscalar particles coupled to SM particles by dimension-5 couplings to gauge bosons or derivative interactions to fermions [94]. ALPs can naturally serve as the source of dark matter in the universe, providing an “axion” portal to the dark sector.

This section will look at three ALP models: ALPs with coupling to the SM photon, referred to in this work as the ALP-photon model, ALPs with coupling to the gluon, referred to as ALP-gluon model and ALPs with coupling to the $SU(2)_L$ gauge boson, referred to as the ALP-W model. All

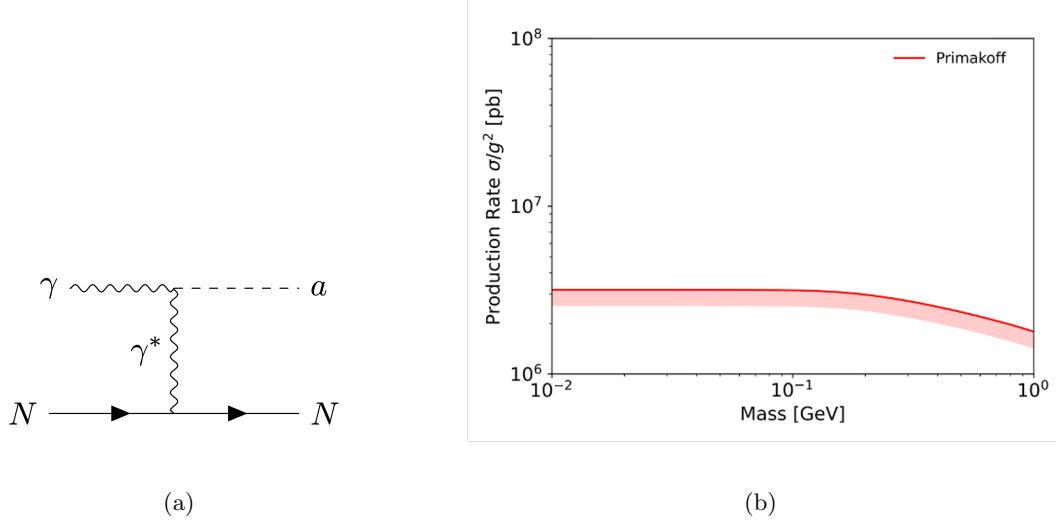


Figure 2.9: (a) ALP with coupling to photons (ALP-photon) production via the Primakoff process in which a photon is converted into an ALP when colliding with a nucleus, N . In the context of FASER, N would be LHC infrastructure, most likely the TAN (neutral particle absorber). (b) The production rate of ALPs from the Primakoff process within an angular acceptance $\theta < 0.2$ mrad with energy $E > 1$ TeV.

the models considered decay to SM final states, resulting in a highly-energetic di-photon signature.

2.6.1 ALPs Coupling to Photons

ALPs with coupling only to SM photons is a benchmark model [7] for which the relevant Lagrangian is:

$$\mathcal{L} \supset \frac{1}{2}m_a^2 a^2 - \frac{1}{4}g_{a\gamma\gamma}aF_{\mu\nu}\tilde{F}^{\mu\nu} \quad (2.10)$$

where m_a is the mass of the ALP and, at low energy scales (below the scale of EWSB), the di-photon coupling $g_{a\gamma\gamma} = 1/f_\gamma$ [7].

In the far forward region, ALPs with coupling to photons are highly-energetic and produced predominantly via the Primakoff process [7]. In the Primakoff process the photon is converted into an ALP when it collides with a nucleus, this is illustrated in Figure 2.9a [7]. There are additional processes that produce ALPs at FASER but these contributions to the signal are considered subdominant for this model. The production rate via the Primakoff process is shown in Figure 2.9b.

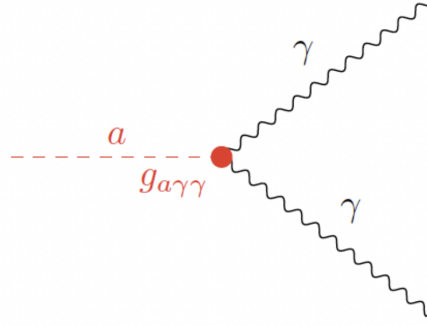


Figure 2.10: ALP-photon decay to two highly energetic photons. Figure from Ref. [3].

FASER targets ALPs which have mass $m_a \sim 50$ MeV and coupling $g_{a\gamma\gamma} \sim 10^{-4}$, which typically have momentum in the TeV range. The decay length is of the order of several hundred metres, according to Equation 2.11 [66]:

$$L = c\tau\gamma\beta \sim 630 \text{ m} \left[\frac{10^{-4} \text{ GeV}^{-1}}{g_{a\gamma\gamma}} \right]^2 \left[\frac{p_a}{\text{TeV}} \right] \left[\frac{50 \text{ MeV}}{m_a} \right]^4, \quad (2.11)$$

where p_a is the momentum of the ALP, τ is the lifetime of the ALP, travelling at speed $\beta = v/c$ where c is the speed of light. The ALP decay length is within the range of FASER's sensitivity to LLPs.

ALPs coupling to photons predominantly decay to a highly-energetic di-photon pair as is shown in Figure 2.10. The ALP-photon decay length and the branching fraction is shown in Figure 2.11 [7]. There is a sub-leading decay channel in which one of the photons is produced off-shell and converts into an e^+e^- pair, this has a branching fraction of around 1% [66].

2.6.2 ALPs Coupling to Gluons

As discussed in this chapter, the concept of axions and axion-like particles was introduced in an attempt to solve the strong CP problem [45, 95]. The mass of the QCD axion is set by its coupling to gluons and so a model in which axion-like particles couple only to gluons can be considered. This is also a PBC benchmark case, the Lagrangian describing the ALP-gluon model is:

$$\mathcal{L} \supset -\frac{1}{2}m_a^2 a^2 - \frac{g_s^2}{8} g_{agg} G_{\mu\nu}^a \tilde{G}^{a\mu\nu} \quad (2.12)$$

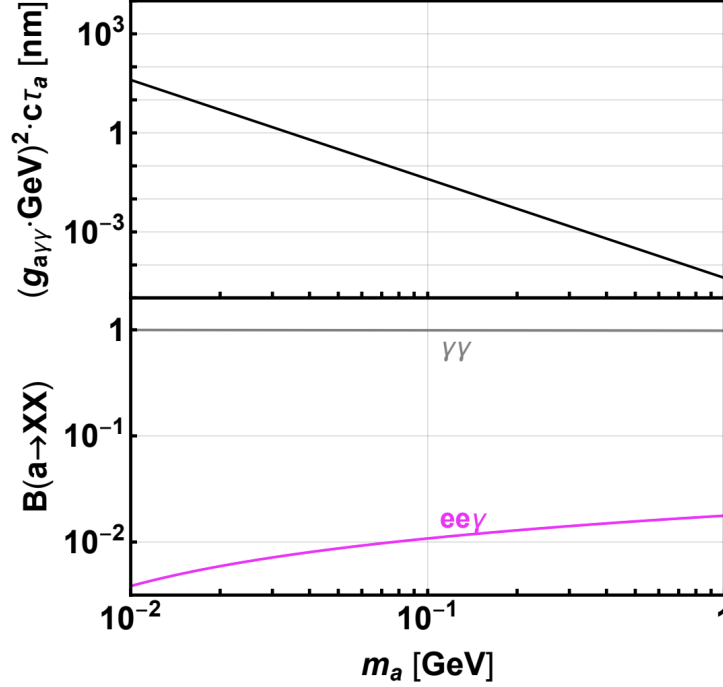


Figure 2.11: (Top) The decay length of the ALP-photon in the parameter space that FASER is sensitive to. (Bottom) The branching fractions of the ALP-photon into $\gamma\gamma$, with a sub-leading contribution from $ee\gamma$ s, as a function of ALP mass. Figure from Ref. [7].

where g_{agg} is the ALP coupling constant. ALPs in this model can be produced in flavour-changing neutral-current (FCNC) B -meson decays, however, this element is loop suppressed and sub-leading. The dominant production modes in the ALP-gluon case are $\pi^0 \rightarrow a$, $\eta \rightarrow a$ and $\eta' \rightarrow a$. ALP production via π^0 mixing is shown in Figure 2.12a and an overview of production rate for these various modes is shown in Figure 2.12b.

The dominant decay mode for ALP-gluon interactions at low masses is to two photons, depicted in Figure 2.13. At $m_a > 3m_\pi$ decays via $a \rightarrow 3\pi^0$ and $a \rightarrow \pi^+ \pi^- \pi^0$ become accessible [96], each of these modes has a similar decay rate.

2.6.3 ALPs Coupling to the $SU(2)_L$ Gauge Boson

ALPs can couple to the SM field strength tensor $W_{\mu\nu}^a$ from the $SU(2)$ gauge group [67], this is a possible UV completion of the ALP with photon couplings, the Lagrangian for this coupling is:

$$\mathcal{L} \supset -\frac{1}{2}m_a^2 a^2 - \frac{g_{aWW}}{4} a W_{\mu\nu}^a \tilde{W}_{\mu\nu}^a \quad (2.13)$$

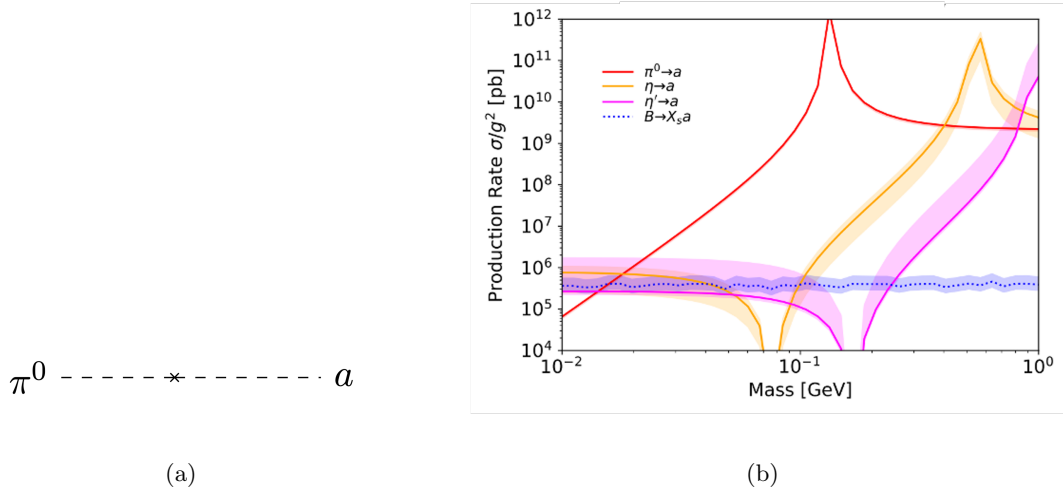


Figure 2.12: (a) ALP with coupling to gluons (ALP-gluon) production via pion mixing. (b) The production rate of ALP-gluon from $\pi^0 \rightarrow a$, $\eta \rightarrow a$ and $\eta' \rightarrow a$ within an angular acceptance $\theta < 0.2$ mrad with energy $E > 1$ TeV.

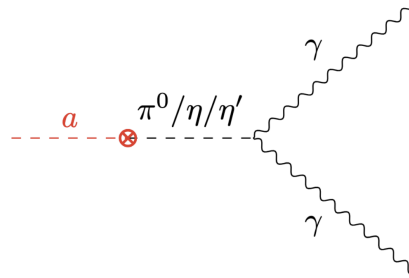


Figure 2.13: ALP-gluon decay to two highly-energetic photons, using pion mixing. Figure from Ref. [3].

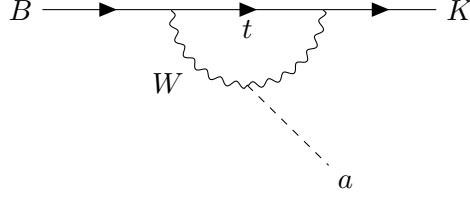


Figure 2.14: ALP production via top loop, involving B meson decay to kaon and a W boson.

where g_{aWW} is the coupling constant with dimensions GeV^{-1} .

The coupling to the $SU(2)_L$ gauge boson occurs before electroweak symmetry breaking; after EWSB additional couplings of the ALP to $\gamma\gamma$, ZZ and $Z\gamma$ open up [67], the strengths of these additional ALP couplings are dictated by the weak mixing angle. The production of ALPs in Z decays is rare and can be neglected; the production of ALPs with coupling to photons through the Primakoff process provides a sub-leading contribution to the ALP event rate in this case.

In the ALP- W model, the ALP is primarily produced in B meson decays, although the coupling to the W boson also gives rise to kaon decays at a sub-dominant rate. Figure 2.14 shows an example Feynman diagram for ALP production in $B \rightarrow X_s a$ in the case where the strange hadron, X_a , is a kaon. The loop diagram is facilitated by flavour-changing down-type quark-decay, or flavour changing neutral-current (FCNC) decay.

The leading production processes are $B^0 \rightarrow X_s a$ and $B^\pm \rightarrow X_s a$. Decays of other B mesons including B_s still have sub-dominant contributions to the production rate. Kaon decay also contributes at a lower rate, with a sharp cut-off in mass range compared to the other modes considered. The production rate in the mass range $10 \text{ MeV} < m_a < 1 \text{ GeV}$ relevant for the ALP- W search is shown in Figure 2.15 for $B^0 \rightarrow X_s a$, $B^\pm \rightarrow X_s a$, $B_s \rightarrow X_s a$ and $K \rightarrow \pi a$. The production via B meson decay is dominant across the entire parameter space.

The ALP decays to a highly-energetic di-photon pair, shown in Figure 2.16. There is also the possibility of a radioactively induced decay that includes a converted photon: $a \rightarrow \gamma ee$, this decay channel contributes only at the level of a few percent and is neglected in this search.

2.6.3.1 The Parameter Space and Existing Limits

Figure 2.17 shows the parameter space of interest to FASER with this ALP search with coupling to the W boson. Existing constraints in this parameter space have been set by: NuCal,

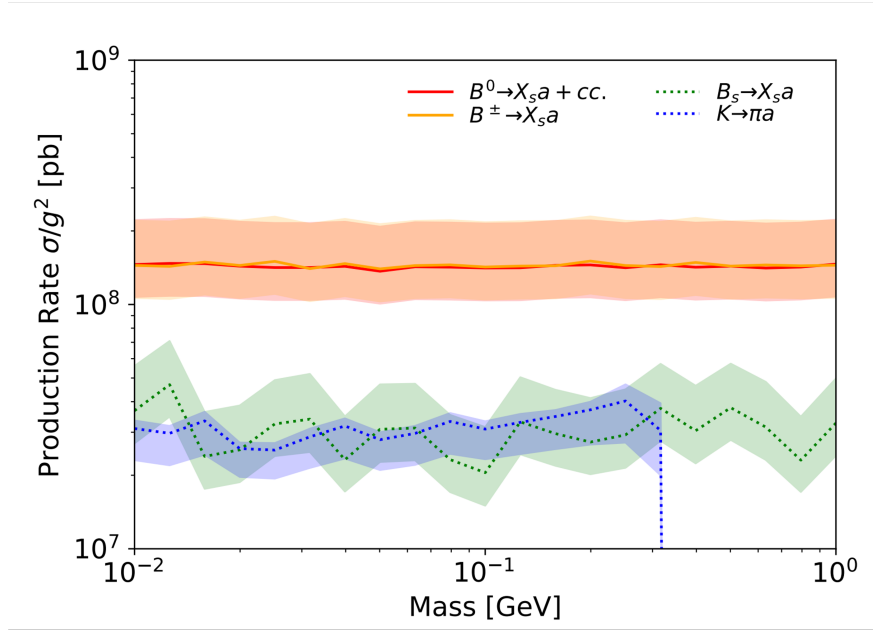


Figure 2.15: The production rate of ALPs from B meson and Kaon decays in the mass range of interest in this analysis. There are four production modes relevant to this ALP model: $B^0 \rightarrow X_s a$, $B^\pm \rightarrow X_s a$, $B_s \rightarrow X_s a$ and $K \rightarrow \pi a$. The shaded bands indicate the uncertainty associated with these production modes.

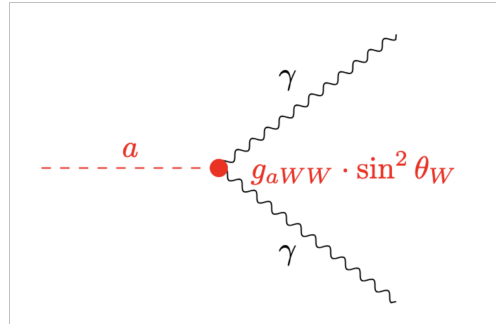


Figure 2.16: A typical ALP decay signature to two highly collimated and highly energetic photons in the case of the ALP-W model. The red circle indicates the ALP coupling constant g_{aWW} .

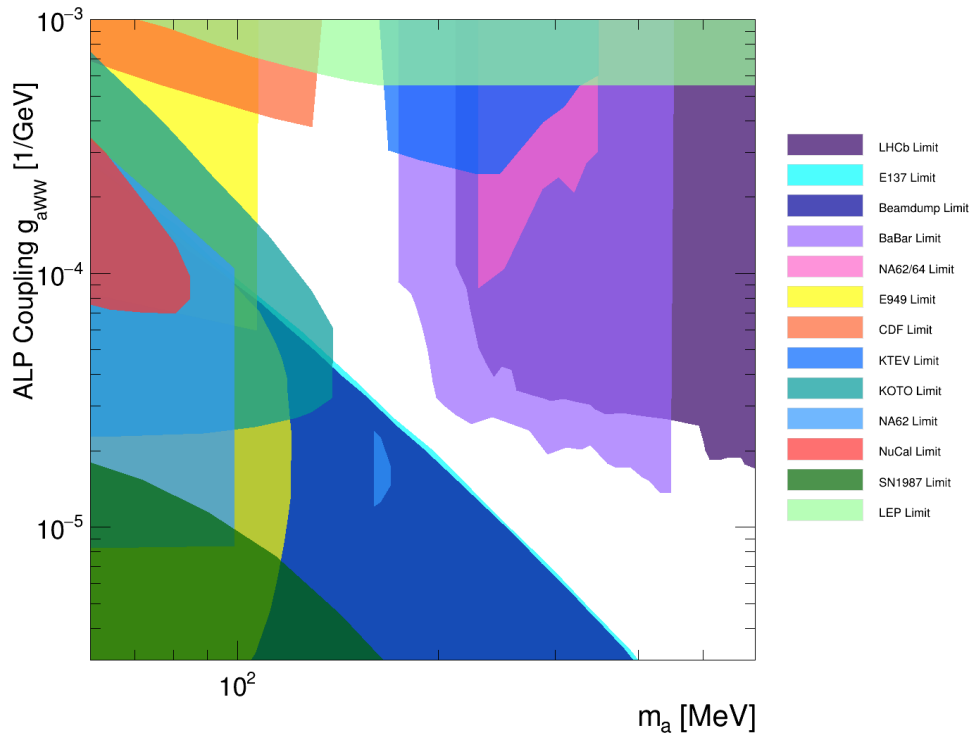


Figure 2.17: Existing experimental constraints in the parameter space probed in FASER's search for axion-like particles with coupling to the W boson. Includes existing limits from NuCal, NA62/64, beam dumps, KTEV, KOTO, E949, CDF, BaBar, E137, NA62, SN1987, NA62, E949, LHCb and LEP.

NA62/64 [97], beam dumps, KTEV [98], KOTO [99], E949 [100, 101], CDF [102], BaBar [103], E137 [85], SN1987 [104], NA62 [105], E949, LHCb and LEP [106].

Experimental results from the BaBar collaboration come from studying B^\pm decays in $B\bar{B}$ meson pairs at SLAC. The experiment probes a similar parameter space to FASER, at a slightly higher ALP mass. Experiments with sensitivity at weaker coupling include results from SN1987, which search for ALPs emitted during supernova. At stronger couplings the parameter space is probed by LEP in searches for ALPs produced in Z decays. Experimental results from the KOTO collaboration show “possible observation of three anomalous events in the search for $K_L \rightarrow \pi^0 \nu\bar{\nu}$ ” [67], this observation would indicate a branching fraction that exceeds the SM prediction by two orders of magnitude. A potential explanation for this discrepancy would be the introduction of a new light (so that it can be produced in kaon decays), weakly-interacting, long-lived particle with a mass of the order of a few MeV, such as the ALP. FASER has the possibility to answer the questions raised by this neutral kaon anomaly, benefiting particularly from its sensitivity to a much higher amount of high-energy LLP decay events with very low SM background [67].

Chapter 3

The FASER Experiment

This chapter provides an overview of the CERN accelerator complex and LHC infrastructure in the context of the FASER experiment. The concept of luminosity is introduced and a detailed description of the components of the FASER detector is given.

3.1 The LHC

The Large Hadron Collider (LHC) is the largest and most powerful particle accelerator in the world. It consists of a 27 km ring of superconducting magnets and was switched on for the first time on 10th September 2008. The LHC is capable of creating both proton-proton collisions and lead ion collisions; this thesis will focus on *pp* collisions.

The CERN accelerator complex is shown in Figure 3.1, modified from Ref. [9]. The protons accelerated in the LHC are fed into a chain of accelerators starting from a single source of hydrogen gas which is ionised to produce negative hydrogen ions. LINAC4 accelerates the negative hydrogen ions to 160 MeV [107] and the ions are stripped of their two electrons during injection into the Booster. Within the Booster the protons reach an energy of 2 GeV in preparation for injection into the Proton Synchrotron (PS). Within the PS the protons reach an energy of 26 GeV and are accelerated to 450 GeV in the Super Proton Synchrotron (SPS), the final stage before the proton beam enters the LHC. The LHC accelerates each proton to an energy of 6.8 TeV, resulting in a centre of mass energy $\sqrt{s} = 13.6$ TeV.

Each proton beam is split up into 2835 bunches of 10^{11} protons, separated in time by 25 ns [10].

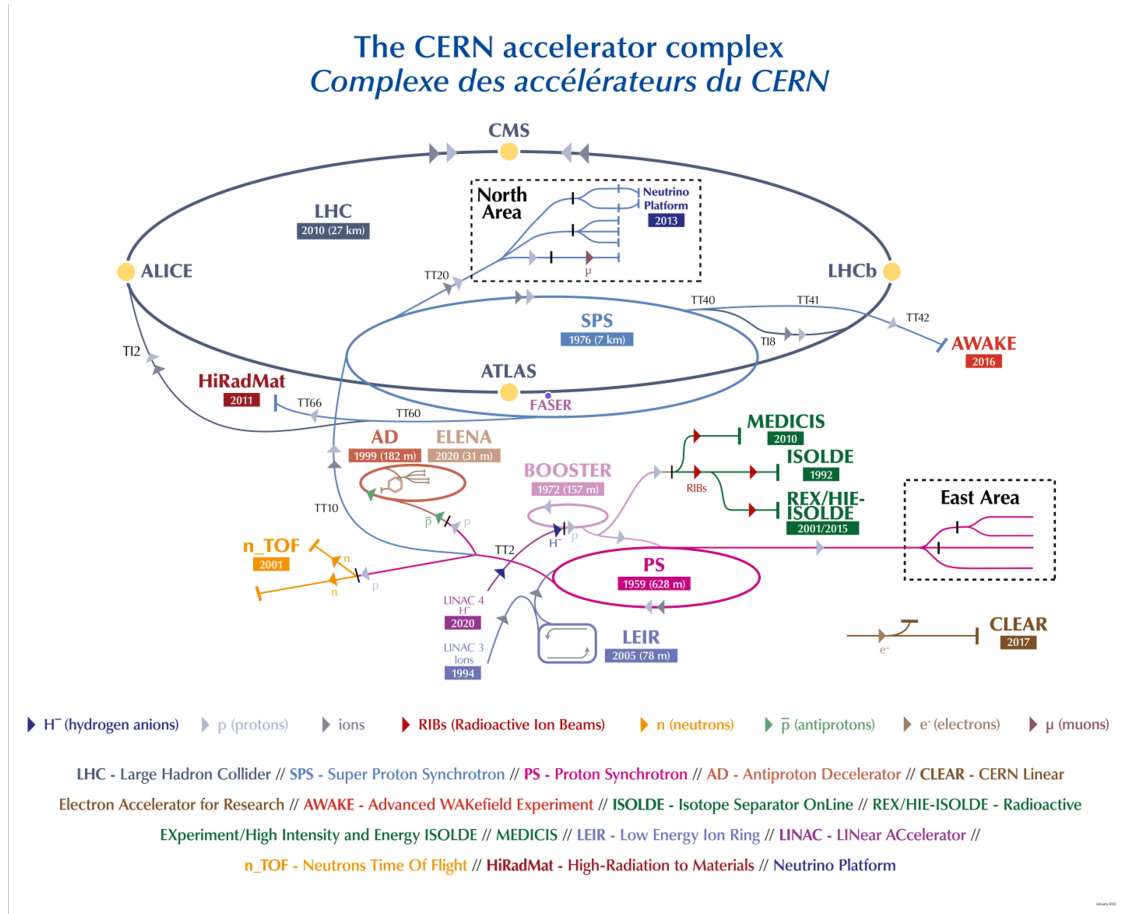


Figure 3.1: A diagram of the CERN accelerator complex, modified from Ref. [9] to include FASER in the TI12 tunnel that connected the LHC and the SPS in the time of LEP.

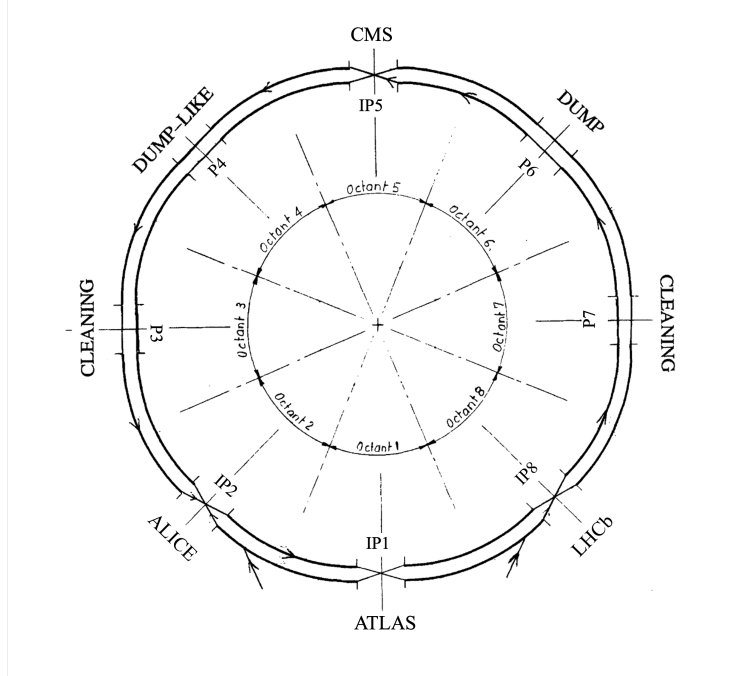


Figure 3.2: Schematic diagram of the octants of the LHC. It shows the 4 interaction points where the largest experiments are situated. Figure modified from Ref. [10].

The bunches are accelerated using 16 radiofrequency (RF) cavities housed in 4 cryomodules along the LHC ring, the field within the RF cavities oscillates at such a frequency that the structure of the proton bunches is maintained. Figure 3.2 [10] shows the octants that form the LHC ring. There are 8 arcs separated by 8 straight sections with a total of 1232 dipole magnets, for bending the beam, and 392 quadrupole magnets, for focusing the beam. The injection of proton bunches into the LHC machine is referred to as a “fill”.

The two proton beams are accelerated in opposite directions and collisions occur at dedicated interaction points located around the LHC ring. The four large experiments at the LHC are positioned to correspond to these crossing points. The ATLAS experiment is located at Interaction Point (IP) 1, ALICE at IP2, CMS at IP5 and LHCb at IP8.

In addition to FASER, there are four other small experiments at the LHC: SND@LHC, LHCf, MoEDAL and TOTEM. SND@LHC is an experiment designed to detect collider neutrinos, it has a complimentary neutrino program to FASER and is located on the opposite side of the ATLAS IP in the forward region. LHCf is an astroparticle physics experiment designed to study particles in the forward region to determine the origin of ultra-high-energy cosmic rays, it is comprised of

two independent detectors that sit 140 m either side of the ATLAS IP. MoEDAL is an experiment designed to directly search for the magnetic monopole, located at the LHCb IP. Finally, TOTEM is an experiment aimed at measuring the proton-proton interaction cross section, elastic scattering and diffraction processes at the LHC, it is located at the CMS IP.

LHC operations are divided into Runs, when beam circulates in the LHC and physics data taking commences, and Long Shutdowns (LS), when the machine is switched off and maintenance and upgrades are carried out. Run 1 began in 2009 until 2013, followed by 2 years of LS1. Run 2 began in 2015 until 2018, followed by 5 years of LS2. Run 3 began in March 2022; as of 2024 Run 3 is ongoing with LS3 planned to start in 2026. The LHC does not run in the winter months, from November to February there is a Year End Technical Stop (YETS) for smaller scale maintenance and planned access to the LHC tunnel.

3.1.1 Luminosity

The instantaneous luminosity delivered in a particle collider is defined as the rate of collisions between particles in the two beams; the integrated luminosity is the total number of collisions that occur in a particular area over a particular period of time. The total number of expected events is calculated from the cross section of the interaction and the instantaneous luminosity. The cross section of an interaction is a measure of the probability of a particular process and is defined in Chapter 5.1. The cross section is typically written as σ and measured in barns (b); a barn is a unit of area corresponding to 10^{-28} m^2 .

In the case of process X, the expected number of events can be calculated as:

$$N_{Events}(pp \rightarrow X) = \sigma_{(pp \rightarrow X)} L \quad (3.1)$$

where L is the integrated luminosity which is measured in inverse barns (b^{-1}) and can be written as the integral of the instantaneous luminosity with respect to time, $L = \int \mathcal{L} dt$. The instantaneous luminosity [108] is defined as:

$$\mathcal{L} = \frac{N_b^2 n_b f_{rev} \gamma_r}{4\pi \epsilon_n \beta^*} F \quad (3.2)$$

where N_b^2 is the number of particles per bunch, f_{rev} is the revolution frequency, γ_r is the relativistic

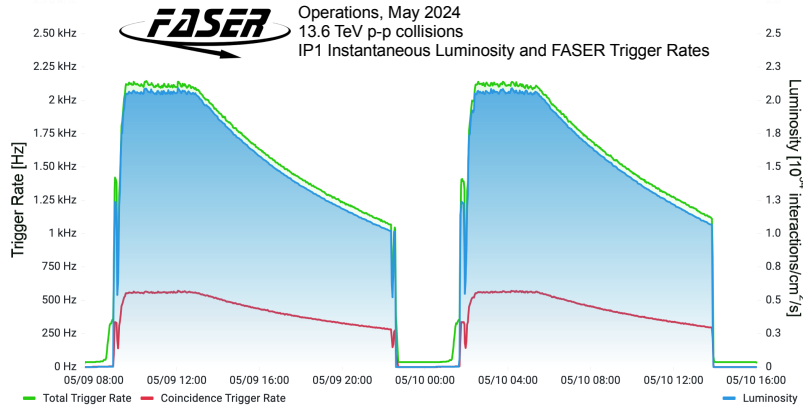


Figure 3.3: The instantaneous luminosity measured at IP1 and the total and coincidence trigger rate recorded by FASER for 2 LHC fills in May 2024. The instantaneous luminosity is provided by ATLAS and shown in blue, the total trigger output rate is shown in green. The output rate of a coincidence trigger requiring a signal the veto scintillator and the preshower scintillator, is shown in red. Figure from Ref. [11].

gamma factor, ϵ_n is the normalised transverse beam emission at the IP, β^* is the optical beta function at the collision point, and F is the geometric luminosity reduction factor [108] due to the crossing angle at the IP. The crossing angle is the full angle between the orbits of beam 1 and beam 2 in the LHC [10]. The beta function describes the “squeezing” of the beam; a low β^* represents a narrow beam and a higher value of β^* describes a wider, straight beam.

Figure 3.3 [11] shows the instantaneous luminosity measured at IP1 and delivered to FASER during two LHC fills in May 2024. Figure 3.4 [11] shows the total integrated luminosity versus time delivered to FASER during stable beams for pp collisions at 13.6 TeV centre-of-mass energy in 2022, 2023 and 2024. The luminosity information shown is provided by the ATLAS Collaboration [109] using their latest calibration. In 2022 FASER recorded 27.0 fb^{-1} suitable for the analyses discussed in this thesis; in 2023 a further 30.7 fb^{-1} was recorded. As of July 2024, over 110 fb^{-1} has been delivered to FASER; Run 3 aims to achieve a total integrated luminosity of $L = 250 \text{ fb}^{-1}$ [26].

3.2 The FASER Detector

The FASER experiment sits in the TI12 tunnel, 480 m downstream of the ATLAS Interaction Point (IP1) [69] positioned in the far-forward region along the beam collision axis line of sight (LOS). The location of the detector in relation to the ATLAS IP and the LHC is shown in Figure 3.5.

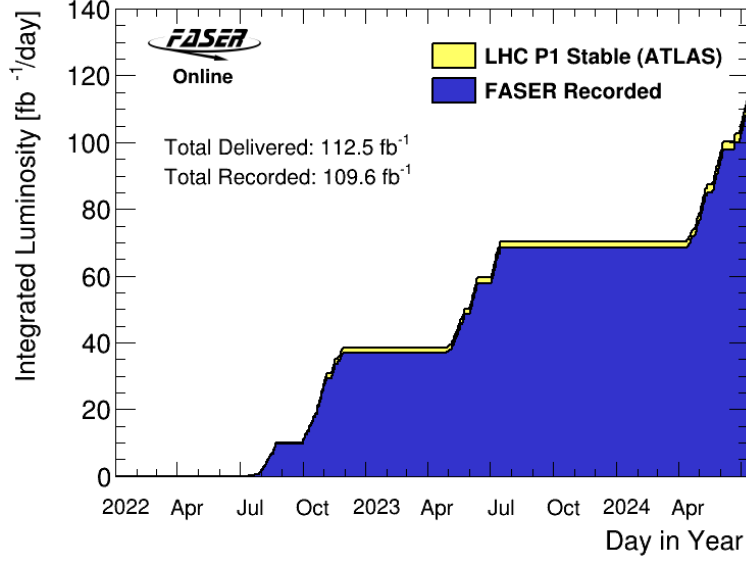


Figure 3.4: The total luminosity delivered during LHC stable beams as of July 2024 (measurement by ATLAS) (yellow). The total luminosity recorded by FASER (blue).

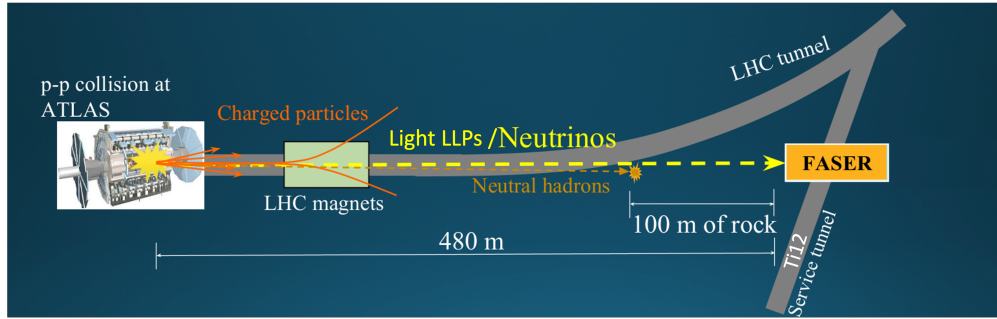


Figure 3.5: FASER's location in service tunnel TI12, 480m east of the ATLAS IP. Figure adapted from Ref. [12].

TI12 is a former service tunnel that connected the LHC tunnel to the SPS in the time of LEP. The tunnel slopes slightly upwards, to connect to the shallower SPS, this was something that was taken into account to make sure FASER sits on the beam collision axis which passes along the floor of TI12 [7]. A 45 cm deep trench was dug to lower the floor, the exact position of the LOS is determined by the beam crossing angle and polarity at IP1, the position of the FASER experiment can be adjusted to account for a possible shift in these parameters [110]. The 480 m between IP1 and FASER consists of a 270 m long straight insertion section before the beam enters an arc and bends away from the beam collision axis. The remaining distance includes ~ 10 m of concrete and 90 m of rock.

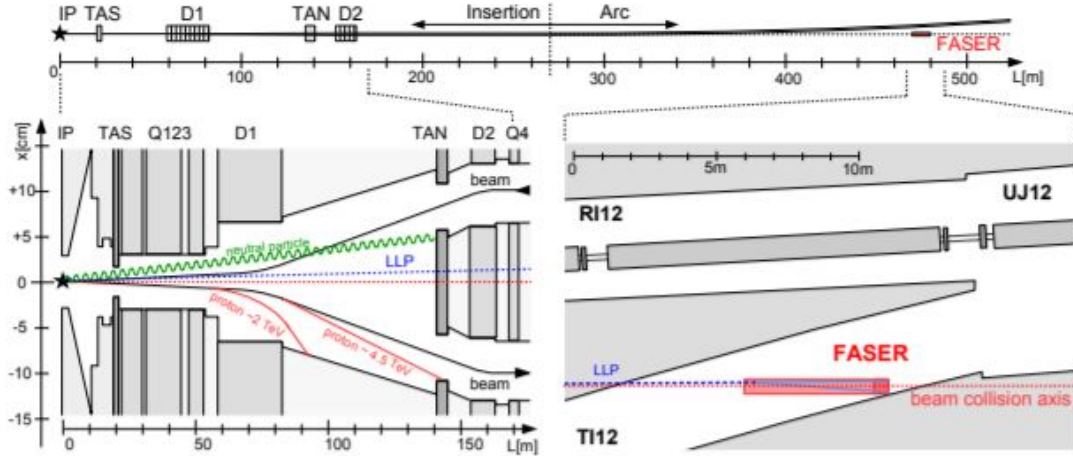


Figure 3.6: Schematic view of the far-forward region downstream of ATLAS and various particle trajectories as they make their way through the LHC infrastructure towards FASER. The upper panel shows the 480 metres between the IP and FASER, the beam collision axis is shown with a dotted line, and several components of the LHC, which have a large influence on the particle flux seen at FASER, are highlighted. The lower left of the Figure shows various high energy particles that can be produced at the IP. LLPs travel through the LHC infrastructure without interacting, the lower right of the figure shows LLPs arriving at FASER, 480 m after they are produced. Figure from Ref. [13].

A schematic of FASER in relation to the LHC infrastructure between the ATLAS IP and TI12 can be seen in Figure 3.6 [13]. After the interaction point, the two proton beams reside in a single beam pipe following the collision. After the TAS (Target Absorber for Secondary particles), the beam is separated by the inner beam separation dipole magnet [10] which also deflects other charged particles from the collision. At a distance of around 140 m from the IP, the TAN (Target Absorber for Neutral particles) absorbs neutral particles produced at the IP and the proton beams are transitioned into individual beam pipes, the horizontal separation between the beams is 96 mm [111]. At around 160 m downstream, the proton beam passes the outer beam separation dipole magnet, this gives the beams a horizontal separation of 194 mm and ensures they are parallel. At 270 m downstream of ATLAS the LHC magnets start to deflect the beam and the tunnel curves away from the collision axis. Charged particles produced in the far-forward region are deflected away from FASER by the LHC magnets. The majority of neutral hadrons are stopped by the TAS and the TAN or in the rock preceding FASER. The only standard model particles capable of reaching FASER with large fluxes are muons and neutrinos.

An understanding of neutrinos and how they interact in and around FASER [112] is vital for

understanding the LLP signal and potential background. The flux of neutrinos in the forward region of the LHC can be considered in three categories: prompt neutrinos, those produced in the decays of short-lived particles, particularly charm hadrons; displaced neutrinos, produced in the decay of long-lived light hadrons in the LHC beam pipe before interaction with any material, this refers to mainly pions and kaons; secondary neutrinos, produced from downstream hadronic showers which result from interactions of primary hadrons with material upstream of FASER. These are discussed in more detail in the context of Monte Carlo generators in Chapter 5.

3.3 Detector Components

A recent photograph of FASER in TI12 can be seen in Figure 3.7 and a schematic of the detector components is shown in Figure 3.8, adapted from Ref. [14]. The FASER detector is described in detail in Ref. [14]. Particles produced at IP1 enter the detector from the right of the diagram in Figure 3.8. FASER is 7 m long and has an active radius of 10 cm. The FASER detector uses a cartesian coordinate system with the z -axis pointing along the beam collision axis on the LOS away from IP1, the y -axis pointing vertically upwards, and the x -axis pointing horizontally towards the LHC machine. The origin (0,0) of the coordinate system is aligned with the centre of the magnets in the transverse x - y plane and conventionally at the front surface of the second tracker station in the z plane. The angular acceptance of FASER is $\theta \lesssim 1$ mrad, where θ is the angle with respect to the beam collision axis. The pseudorapidity, η , is often used instead of θ when discussing angular acceptance, this is defined as $\eta = -\ln(\tan\theta/2)$ where $\eta = 0$ would correspond to an angle perpendicular to the beam collision axis.

The first component of the detector is the “VetoNu” scintillator system, to veto charged particles before they enter the detector, this scintillator sits in front of the FASER ν emulsion detector (red), described later. The FASER ν box is followed by Interface Tracker (IFT), a single tracking station (orange) that enables muon tracks in the emulsion to be linked to tracks in the electronic detector. The next component is the “Veto” scintillator station (yellow) to veto charged particles produced in the FASER ν detector. The veto scintillator layers are followed by a 0.57 T permanent dipole magnet (blue) which acts as a decay volume for incoming particles. It has a 10 cm aperture radius and is 1.5 m long; the magnets bend charged particle tracks in the y direction. In the case of



Figure 3.7: FASER in TI12 in January 2023, viewed from the calorimeter towards FASER ν .

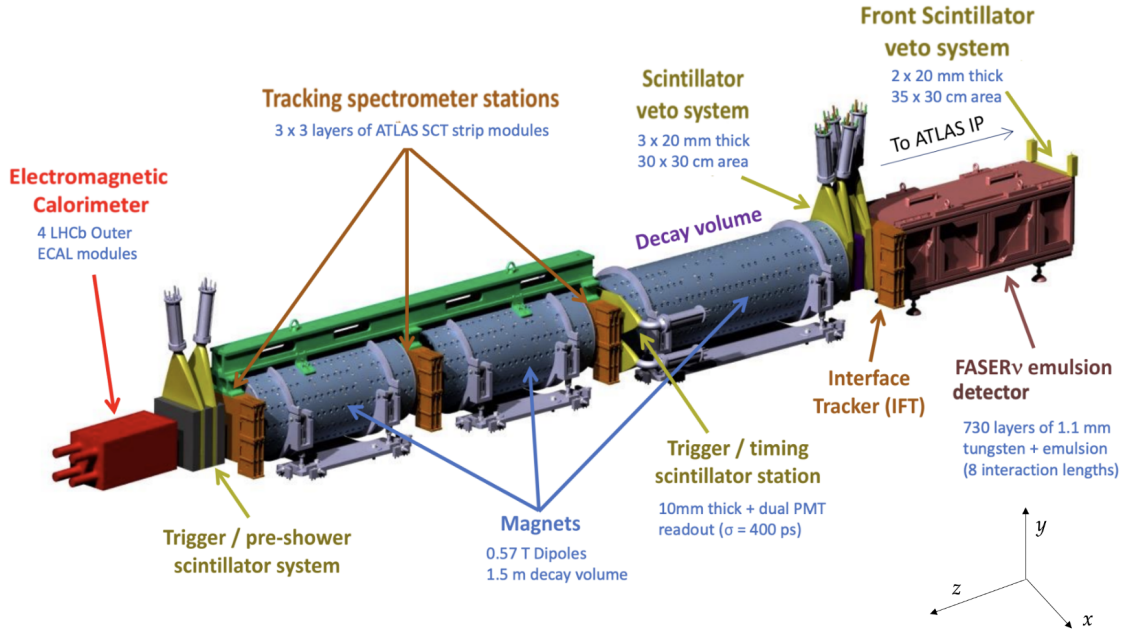


Figure 3.8: The components and coordinate system of the FASER detector, adapted from Ref. [14]

highly collimated particle tracks, the magnet provides a horizontal kick to separate tracks to a detectable distance. There is a third scintillator station for timing and triggering (yellow); this scintillator, larger in area than the Veto and VetoNu scintillators, is referred to as the timing scintillator or timing station and sits in front of the tracking spectrometer. FASER's tracker consists of three tracking stations (orange) and two 1 m long 0.57 T permanent dipole magnets. The role of the tracking spectrometer is to observe the characteristic signal of two oppositely charged particles pointing back to the IP, and measure their momentum. Immediately following the tracking spectrometer is the preshower detector and scintillator system (yellow), also used for triggering. The final component is a sampling electromagnetic calorimeter (red) to measure the total electromagnetic energy of incoming particles.

3.3.1 FASER ν Emulsion Detector

FASER ν is a passive emulsion-based neutrino detector. It is made up of emulsion films interleaved with 770 1 mm-thick tungsten plates which act as a target for neutrino interactions. The FASER ν detector has a target mass of 1.1 tonnes and has a transverse size of $25 \times 30 \text{ cm}^2$.

The tungsten acts as a target for neutrino interactions and the emulsion films record the trajectories of all charged particles that enter the FASER ν box with excellent position and angular resolution. It can be used to identify leptons produced in charged-current (CC) neutrino interactions, for example muons are easily characterised by their long tracks that can penetrate up to the eight interaction lengths that make up the FASER ν detector [14]. FASER ν has measured the interaction cross section for ν_e and ν_μ , detailed in Ref. [113]. FASER ν also has sensitivity to ν_τ , the expected number of charged-current ν_τ interactions in FASER ν during LHC Run 3 is 28 events [23]. Due to the nature of emulsion, FASER ν is a passive detector that must be removed from the TI12 tunnel for read out, it is necessary to exchange the box before track multiplicity becomes so high that the ability to distinguish and reconstruct track vertices in the emulsion is degraded.

The FASER ν emulsion detector is not used in either of the analyses discussed in this thesis. However, whilst the tungsten plates do play a role in suppressing potential background, they also act as a target for neutrino interactions.

3.3.2 Scintillators

The four scintillator stations within FASER are vital to achieve high detection efficiency. The scintillators are used for the vetoing of charged particles and also for triggering purposes. The light in each scintillator is transmitted to PMTs (Photomultiplier tubes) through wavelength shifting (WLS) rods or plastic light guides, the exact design and setup depends on the location and role of the specific scintillator. Each scintillator module, consisting of the scintillator plane, WLS rod/light guide and PMT, is wrapped in 0.5 mm-thick foil to avoid light leakage. In front of each PMT is an open-ended optical fibre for injecting light pulses for calibration purposes. The arrangement of each of the four scintillator stations can be seen in Figure 3.9 [14].

The first scintillator station is placed in front of FASER ν in order to veto charged particles as they enter the detector. VetoNu is made up of two scintillator layers and its design is unique compared to the other stations, due to the limited space available in the FASER ν trench. The two scintillator modules are positioned back to back and each include a 30×35 cm EJ-200 plastic scintillator which is 2 cm thick and connected via a $1.5 \times 1.5 \times 37.5$ cm EJ-280 plastic WLS rod [114] to a Hamamatsu H11934-300 PMT [115]. This PMT is a 12 dynode-stage head-on PMT with a 23 mm sensitive photocathode [14].

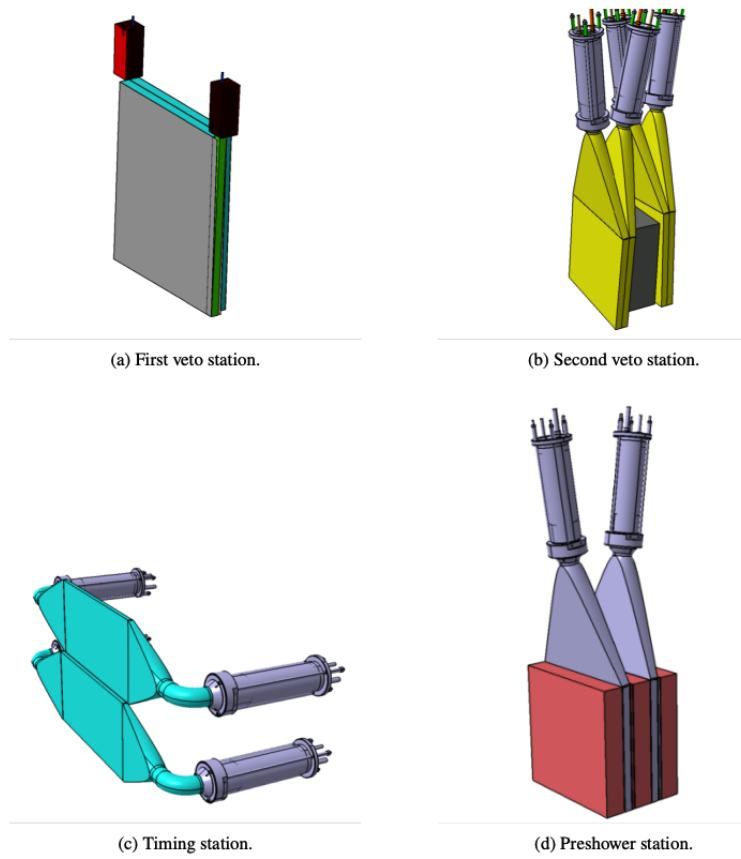


Figure 3.9: The four scintillator stations used in FASER, taken from Ref. [14]

Table 3.1: The independent efficiencies of each of the five veto scintillators using the 2022 dataset. Veto layer 0 belongs to the first module of the veto scintillator station, veto layers 1 and 2 belong to the second module of the veto scintillator station.

| Scintillator | Efficiency (%) |
|----------------|----------------|
| VetoNu Layer 0 | 99.99976(2) |
| VetoNu Layer 1 | 99.99974(2) |
| Veto Layer 0 | 99.99994(1) |
| Veto Layer 1 | 99.999976(7) |
| Veto Layer 2 | 99.999982(6) |

The second scintillator station is placed in front of the FASER decay volume, this veto station has four scintillator layers which form two pairs of modules. Each module in a pair is again placed back-to-back for increased efficiency. EJ-200 plastic scintillator plates are used, connected via light guides to Hamamatsu H6410 PMTs [116], these are large 12 dynode-stage head-on PMTs with a 47 mm sensitive aperture. Two layers of permalloy tube protection surround the PMTs to protect from magnetic fields [14]. The primary role of this second scintillator station is to suppress high energy muons. To avoid high energy photons due to muon bremsstrahlung entering the FASER volume undetected, a 10 cm-thick lead block is placed between the two veto scintillator modules to act as an absorber. The lead block can also act as a target for neutrino interactions. Each veto scintillator plane is larger than FASER’s active transverse size in order to more effectively veto charged particles, even those that could enter FASER at large angles. The total size of the 2 cm-thick scintillator plane in each module is 30×30 cm. The light guide and PMT are positioned vertically and at slight angles to avoid interference between the neighbouring PMTs.

FASER sees a rate of 0.4 Hz cm^{-2} muons from IP1. This has been confirmed with in-situ measurements of the muon flux in TI12 and simulated by FLUKA [117]. The efficiency of the veto system composed of five scintillator planes has been measured, with each plane showing a muon veto inefficiency below 10^{-5} using a 40 pC threshold. Within a fiducial selection of 100 mm in the extrapolated track x and y positions, the inefficiency of the entire veto scintillator system is 10^{-27} . The normalised charge distribution of single track events in the first VetoNu scintillator layer is shown in Figure 3.10 [11] and the efficiency of each individual veto scintillator layer is shown in Table 3.1.

The third scintillator station is the timing scintillator station which provides trigger and timing

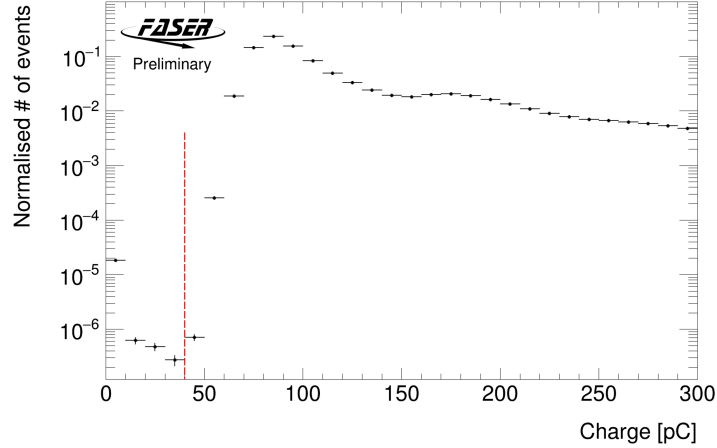


Figure 3.10: Charge deposited in the first layer of the VetoNu scintillator in front of FASER ν in data. Using a 40 pC threshold (indicated by the dotted red line), the measured MIP detection efficiency is 99.99976(2).

information to FASER, it is located after the decay volume magnet and before the first tracking station. The timing scintillator station is used to precisely measure the arrival time of physics signals with respect to the pp collisions at IP1, this information can be used to suppress non-collision backgrounds. This station has a larger area than the veto scintillator planes, in order to cover the magnet surface and to detect muons that may enter FASER at a large angle after the veto scintillators. The timing station is made up of two 1 cm-thick 40×20 cm scintillator layers which are stacked vertically with a 5 mm overlap and referred to as the top and bottom timing scintillators. Each layer is connected to a Hamamatsu H6410 PMT via light guides that are bent at 90° to minimize size due to limited space in the trench. The total charge deposited in the timing scintillator is a combination of the charge deposited in each of the two layers. The timing distribution of the top timing scintillator is shown in Figure 3.11 [11]; the top timing station has a timing resolution of 423.0 ± 0.5 ps, the resolution of the bottom timing scintillator is similar.

The fourth and final scintillator station is part of the preshower detector; it can be used as an additional trigger station and can also provide coincidence triggering to reduce the rate of non-physics triggers [14]. The preshower detector is located after the final tracking station and before the calorimeter and is shown in Figure 3.12. It is made up of two 20 mm-thick scintillator planes which form the active sensor component. Each scintillator layer is preceded by a 3.18 mm-thick sheet of tungsten that acts as an absorber and aids the development of particle showers. The

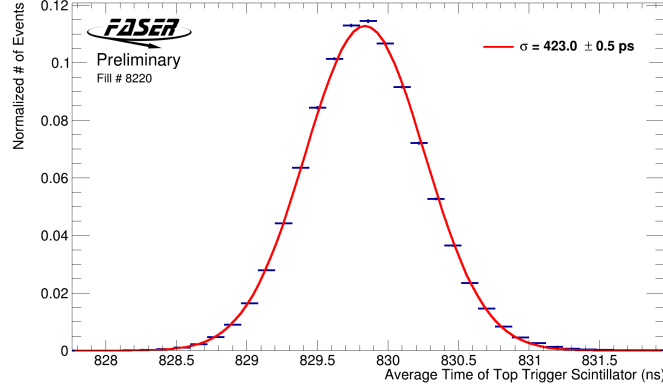


Figure 3.11: The timing distribution of the top timing scintillator with a timing resolution of 423.0 ± 0.5 ps. Figure from Ref. [11].

absorbers correspond to roughly one radiation length. Graphite blocks are interleaved before and after the preshower layers to minimise the back-splash of activity in the calorimeter leaving signal in the preshower scintillators or the final layer of the tracker. The geometry of the preshower detector is shown in Figure 3.13; in total, the preshower detector has around 2.5 radiation lengths of material. The two preshower scintillator layers are referred to as preshower layer 0 and preshower layer 1. Preshower layer 0 is the first and most upstream scintillator. The role of the preshower is to cause showering of electromagnetic interactions that otherwise would not be distinguishable from other similar signals in the calorimeter, which lacks spatial resolution. In addition, the ratio of the charge deposited in preshower layer 0 and preshower layer 1 can be used for particle identification (PID). Figure 3.14 [15] shows the ratio of charge deposited in preshower layers for a 200 GeV π^- , a 150 GeV μ^- and a 200 GeV e^- from test beam data.

There is a planned upgrade of the preshower detector, to be installed in TI12 in the 2024 YETS. Details of the upgraded preshower detector are given in Chapter 8.

3.3.3 Tracking Spectrometer

FASER has four tracking stations, with three layers per station. There are three stations situated downstream that make up the tracking spectrometer and one station upstream that is the Interface Tracker (IFT) used to link to FASER ν . The FASER tracking stations have three planes which each have eight double-sided silicon microstrip modules with a resolution ($x \times y$) of $580\mu\text{m} \times 17\mu\text{m}$. The



Figure 3.12: The current FASER preshower detector, January 2023.

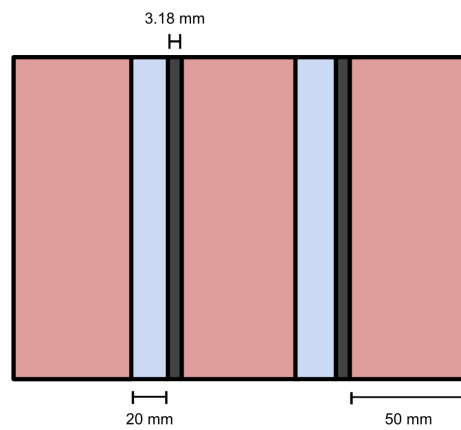


Figure 3.13: A schematic of the current preshower detector: 50 mm graphite blocks, 20 mm plastic scintillator layers, 3.18 mm tungsten absorber.

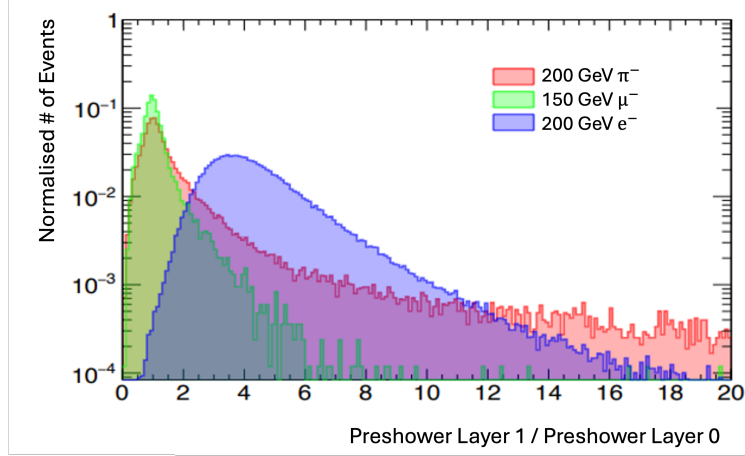


Figure 3.14: The ratio of charge deposited in the two preshower scintillator layers for a 200 GeV π^- , a 150 GeV μ^- and a 200 GeV e^- from test beam data. Calculated in terms of the equivalent number of MIPs. Figure adapted from Ref. [15].

average hit efficiency across the full tracker is 99.64 ± 0.10 %, this is shown in Figure 3.15 [11] as a function of applied hit threshold and as a function of applied bias voltage. The nominal settings for threshold and voltage in the tracker are 1 fC and 150 V, respectively.

The modules used in the tracker are spare barrel SCT (Semiconductor Tracker) modules from ATLAS [118] and consist of four single-sided silicon microstrip sensors that are glued in pairs on each side of the central baseboard, resulting in the double-sided module. On top of one of the sensors in the pair is a copper/polyimide hybrid that provides the readout electronics. Each sensor is 64×63.6 mm² and has 768 readout strips. The silicon strips are the sensitive element of the SCT sensor, readout of the 128 strip channels is done by ATLAS ASIC readout chips [119]. Figure 3.16 [118] shows an SCT barrel module inside an aluminium test-box. Spatial resolution of 17 μ m perpendicular to the strips, and 580 μ m parallel to the strips is provided by the 40 mrad stereo angle between the front and back pairs of sensors.

The eight SCT modules are shown in Figure 3.17 [118] for a single tracker plane, they are held in place by an aluminium frame and arranged with four modules on each side. The modules are oriented with the strip perpendicular to the y -axis so that the momentum of charged particles that are separated by the magnetic field can be measured. The distance between the modules is 2.4 mm to achieve an active area overlap of 2 mm in order to avoid gaps. The overall active area of the tracker plane is 240×240 mm, which covers the 200 mm-diameter magnet aperture of FASER.

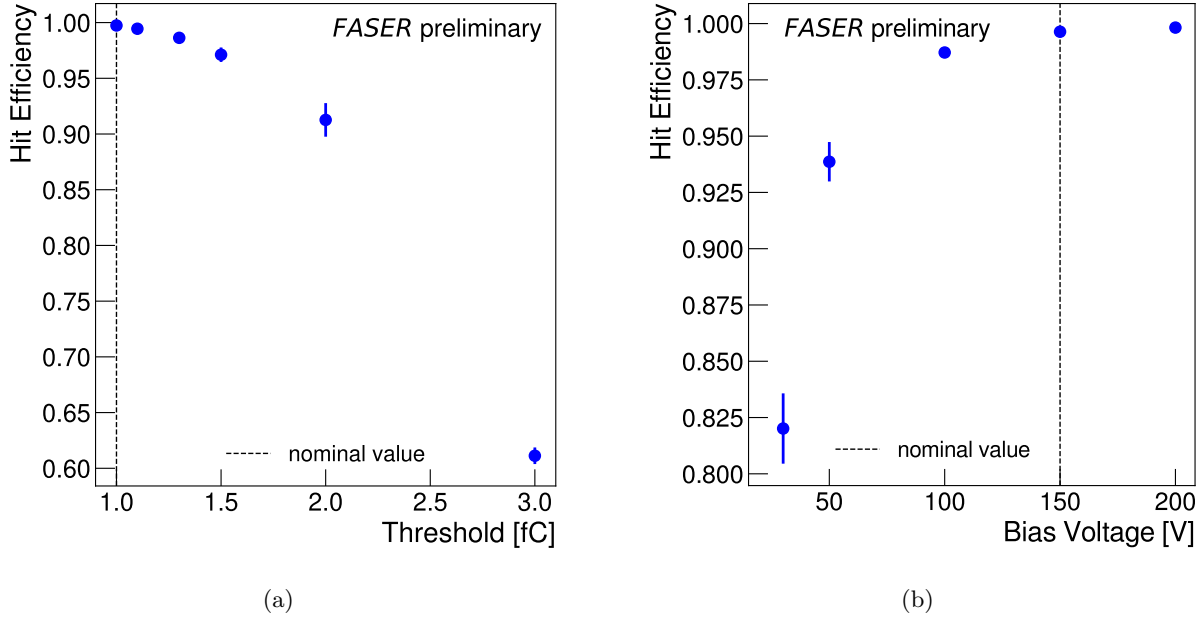


Figure 3.15: The hit efficiency as a function of a) the applied hit threshold (in fC) and b) the applied bias voltage (in V) for the FASER silicon strip (SCT) tracker. The nominal settings are indicated as as a dashed line, and yields an average hit efficiency across the full tracker of $99.64 \pm 0.10\%$. Figure from Ref. [11].

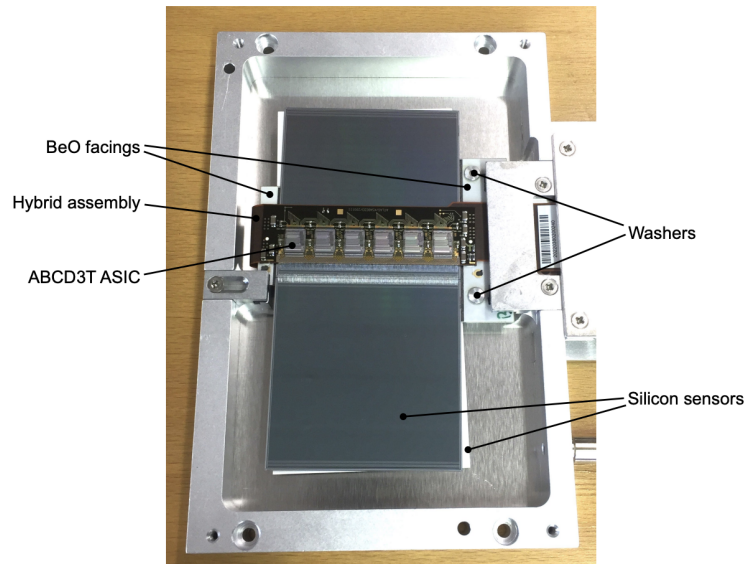


Figure 3.16: SCT barrel module inside an aluminium test-box. Figure from Ref. [11].

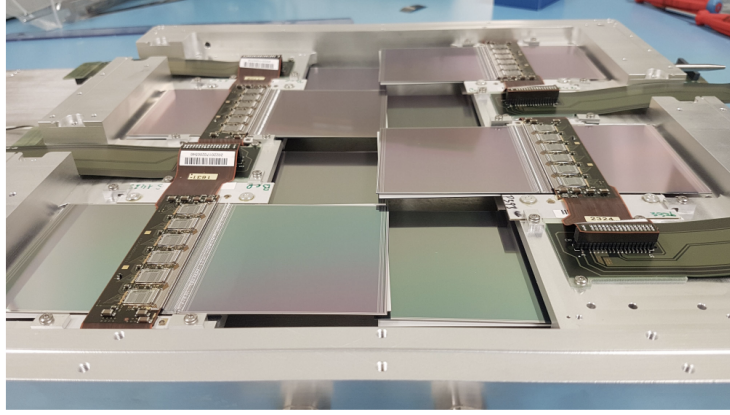


Figure 3.17: A tracker plane with all eight SCT barrel modules. Figure from Ref. [11].

3.3.4 Electromagnetic Calorimeter

The FASER sampling EM calorimeter is made of four spare LHCb outer ECAL modules arranged as shown in Figure 3.18 [14]. Each module is 754 mm long, including the PMT and has a transverse size of 121.2×121.2 mm. The four modules are separated by a gap of 0.2 mm between the top and bottom modules and approximately 1.2 mm between the left and right modules. There is a 50 mrad tilt to the calorimeter in the horizontal plane towards the positive x direction. This tilt is to ensure particles are entering the ECAL modules rather than the gap. Each module features 66 alternating layers of 2 mm lead absorber and 4 mm plastic scintillator, this is shown in Figure 3.19 [16]. Between the lead and scintillator is a very thin layer of Tyvek paper ($120 \mu\text{m}$), in total each cell corresponds to 25 radiation lengths.

The ECAL modules are “Shashlik-type” modules with WLS fibres that penetrate the entire module. These WLS fibres deliver light to a single Hamamatsu R7899-20 PMT [120] at the rear centre of the calorimeter modules. This PMT is a ten dynode-stage head-on PMT custom built for FASER with a voltage-divider to ensure good linearity in the case of large pulses [14]. The voltage divider and PMT sit in a steel tube, shown in Figure 3.20 [14], with additional permalloy protection surrounding it to reduce the effect of magnetic fields. In front of the tube is a 32×8 mm polystyrene light mixer which reduces the non-uniformity of the PMT response. In addition, optical filters can be placed in front of the PMTs to reduce their transmission efficiency to 10%; this allows for the calorimeter to be operated at a higher gain where the non-linearity is reduced, without causing saturation of $\mathcal{O}(\text{TeV})$ signals. In fact, to overcome the compromise between running in

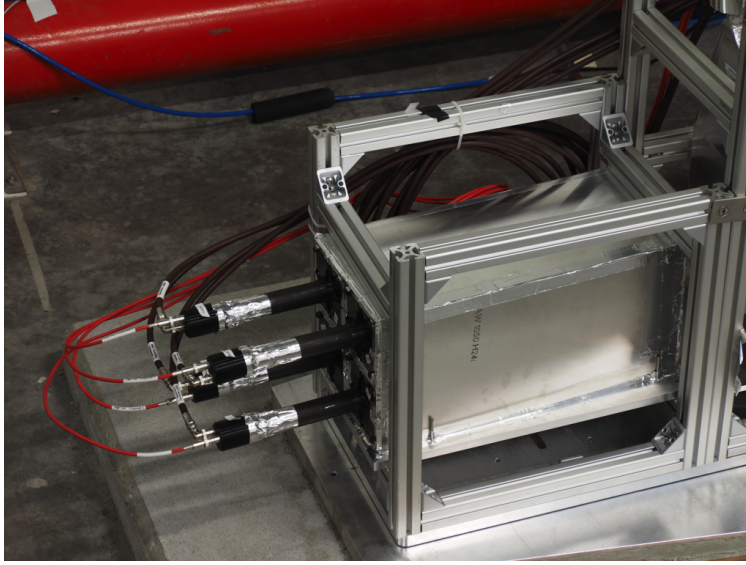


Figure 3.18: Arrangement of the 4 FASER calorimeter modules in a 2×2 configuration before additional shielding and dual readout PMTs were added. Figure from Ref. [14].

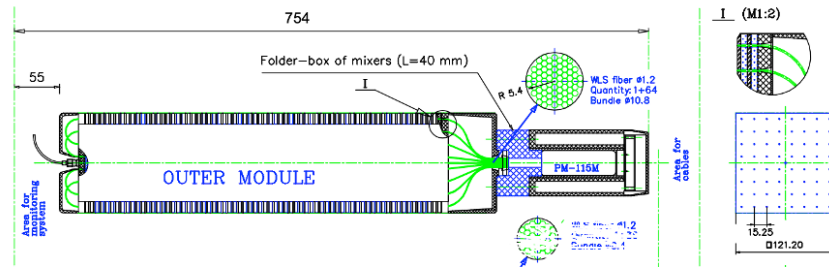


Figure 3.19: Design of the LHCb outer ECAL modules used for FASER. Figure from Ref. [16].

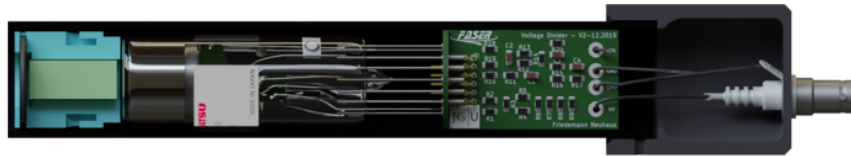


Figure 3.20: A FASER calorimeter Hamamatsu R7899-20 PMT. Figure from Ref. [14].

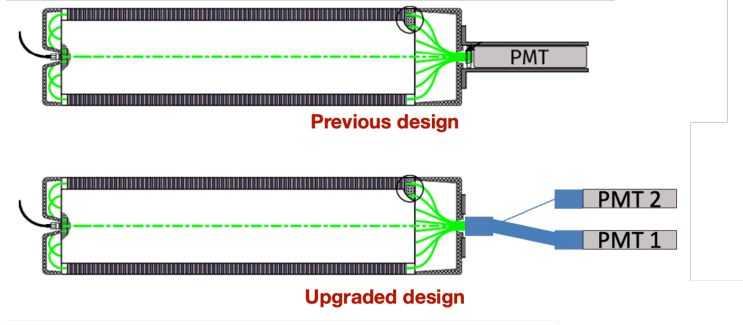


Figure 3.21: Dual readout upgrade for the calorimeter PMTs in YETS 2023. PMT 1 has a “low” energy range of 0.1 to 300 GeV. PMT 2 has a “high” energy range of 3 to 3000 GeV. The region of overlap is useful for cross calibrations.

low or high gain mode, the calorimeter PMTs were upgraded in December 2023 to allow for dual readout. A schematic of this new setup, which allows for measurements to be taken in both high and low gain, and requires an additional digitiser to provide enough channels, is shown in Figure 3.21 (adapted from Ref. [14]). However, the analyses discussed in this thesis, only use data taken with the calorimeter in low gain mode.

3.4 Trigger and Data Acquisition

The trigger and data acquisition (TDAQ) system is designed to maximise robustness and stability during data-taking to ensure that data is recorded with high efficiency [17]. For nominal physics running FASER records data from runs taken with optical filters installed in the calorimeter, as described in Section 3.3.4 and with the calorimeter readout in low gain mode. This is to ensure that high energy deposits do not saturate the calorimeter. Due to its location on the LOS, FASER is designed to be operated completely remotely since there is significant amount of time during data taking that TI12 is inaccessible. FASER does not have a dedicated experimental cavern or physical control room, therefore, monitoring that gives a detailed overview and control of all detector systems, in addition to reliable recording of FASER’s raw data, is vital. FASER employs a operations schedule with a weekly run manager to coordinate detector operations, plan access to TI12 and perform calibrations of the tracker and calorimeter. A weekly shifter monitors the performance of each component of the detector, checks the cooling systems and reports any fluctuations outside of nominal running.

Table 3.2: The definitions of the eight trigger outputs used in FASER.

| Trigger Output | Digitiser Logic Definition |
|----------------|--------------------------------------------------------------------------------------|
| VetoNu | VetoNu PMT 1 and VetoNu PMT 2 |
| 1stVeto | First Veto Layer PMT 1 (PMT 2 not connected to digitiser) |
| 2ndVeto | Second Veto Layer PMT 1 and Second Veto Layer PMT 2 |
| TimingTop | Timing Layer Top Left PMT and Timing Layer Top Right PMT |
| TimingBottom | Timing Layer Bottom Left PMT and Timing Layer Bottom Right PMT |
| Preshower | First Preshower Layer PMT and Second Preshower Layer PMT |
| CaloBottom | Calorimeter Bottom PMT 1 (Module 0) or Calorimeter Bottom Module PMT 2 (Module 1) |
| CaloTop | Calorimeter Top PMT 1 (Module 2) or Calorimeter Top Module PMT 2 (Module 3) |

Table 3.3: Trigger items that combine the eight trigger outputs.

| Trigger Item | Trigger Output Combination |
|----------------------|----------------------------------------------|
| Scintillator Trigger | VetoNu OR 1stVeto OR 2ndVeto OR Preshower |
| Timing Trigger | TimingTop OR TimingBottom |
| Calo Trigger | CaloTop OR CaloBottom |
| Coincidence Trigger | (VetoNu OR 1stVeto OR 2ndVeto) AND Preshower |

available channels. A second digitiser was added to the TDAQ system in 2024 and both PMTs are now connected.

The triggers outputs received by the TLB are combined into four triggers items that generate a Level 1 Accept signal [17]. These trigger items are defined in Table 3.3 and also shown in Figure 3.23 [11]. Figure 3.24 shows the DAQ electronics in TI12.

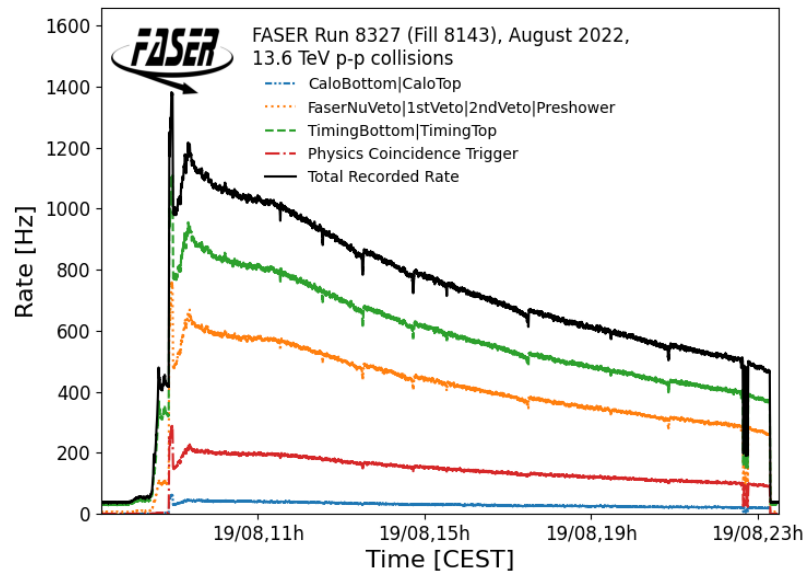


Figure 3.23: FASER recorded trigger rate for individual items and total recorded rate (black) for LHC Fill 8143 on 19th August 2022. Trigger items: timing scintillator (green), signal in any veto or preshower scintillators (orange), coincidence trigger between FASER ν veto and preshower (red), calorimeter (blue). Figure from Ref. [11].

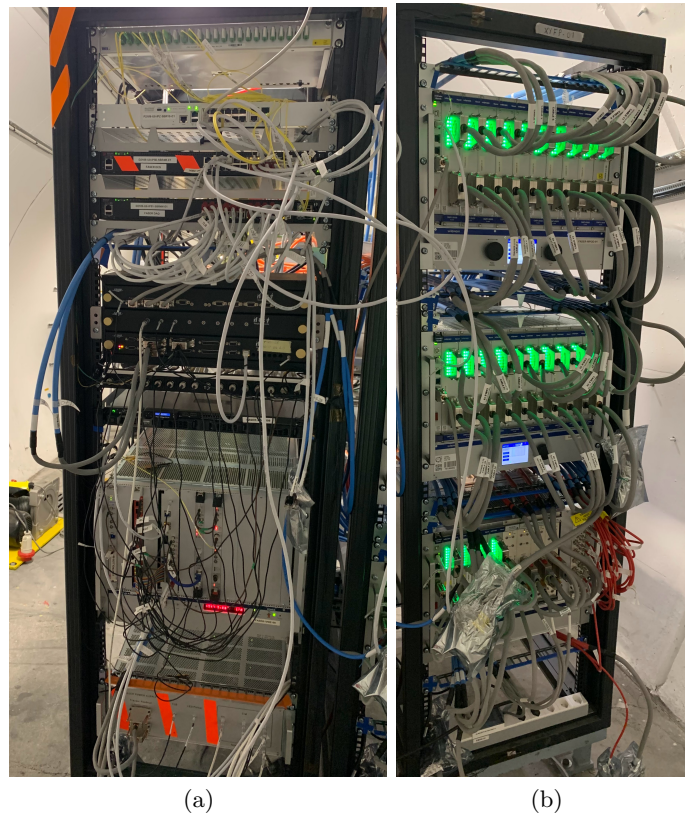


Figure 3.24: Photograph of DAQ electronics in TI12, January 2023.

Chapter 4

Event and Object Reconstruction

This chapter provides details of the steps required for event reconstruction. 27.0 fb^{-1} of reconstructed data recorded in 2022 is used in the dark photon analysis, where track reconstruction is vital to distinguish a highly-collimated electron-positron pair. 57.7 fb^{-1} of reconstructed data recorded throughout 2022 and 2023 is used in the ALP analysis. Reconstructed waveforms in the calorimeter and preshower play an important role in distinguishing ALP signal from background.

This chapter discusses calorimetry and important methods regarding measurement of the energy response and resolution. This is in relation to the author’s work on simulating the ECAL and studying local effects in the calorimeter. The details the 2021 calorimeter test beam [15] are also presented. The test beam campaign was carried out in order to calibrate the calorimeter modules. In addition to an electron energy scan, the uniformity of the muon response was measured, and a pion scan was performed to study the hadronic response. The isolated energy response and resolution of the ECAL was measured and compared to LHCb data [20]. Understanding the calorimeter response is vital to FASER’s simulation of the ECAL: MC description has improved in various iterations as a result of the test beam studies, leading to a more accurate simulation which agrees well with data. The author was involved in generating the initial FASER test beam MC and, using the results of the test beam studies, worked to improve the simulation to better match LHCb data.

4.1 Event Reconstruction

Event reconstruction takes the raw data read from the tracking spectrometer, scintillator PMTs and calorimeter module PMTs and makes the data available for physics analysis. Charged particles will deposit some amount of charge in the VetoNu, Veto and timing scintillator layers, leave tracks in the spectrometer and energy deposits in the preshower scintillators and calorimeter. Neutral particles will leave no signal in the upstream scintillators or the spectrometer but still deposit energy in the preshower and calorimeter. Event reconstruction, as well as simulation and digitisation, is performed in FASER's Calypso offline software framework [121] based on the ATLAS Athena [122] and LHCb GAUDI [123] frameworks.

4.1.1 Track Reconstruction

The detection and reconstruction of tracks within the tracking spectrometer is vital in suppressing potential backgrounds and for identifying certain LLP signals in physics analyses, for example in the case of the dark photon. Track reconstruction also plays a vital role in the rejection of background, especially considering the large flux of muons which traverse FASER. Successful reconstruction of particle tracks from the raw data collected in the SCT strips is performed in a number of steps which take the hits in the tracker and finally form full tracks. The stages in track reconstruction are defined in Table 4.1. A reminder of FASER's coordinate system: the z -axis points along the LOS away from IP1, the y -axis points vertically upwards, and the x -axis points horizontally towards the LHC machine.

A hit in the tracker is recorded when the amount of charge deposited in a single strip is above a certain threshold. A cluster can therefore be defined as adjacent strips on one side of the SCT module, since clusters can only form on a single side of a module the cluster position is only based on the precision local coordinate \hat{y} (perpendicular to the strip). The position of a cluster is defined by the charge-weighted position of the hits. A spacepoint defines the global 3D position of a track, providing the local \hat{x} position of clusters on two sides of a module using the stereo angle between them and combining this with the global position of the SCT module in the aligned geometry. All spacepoints in the three individual layers within a given SCT module are linearly fitted to form track segments that could potentially form a full track within the full tracking spectrometer. The

Table 4.1: Descriptions of the different steps used in the reconstruction of full tracks within FASER’s tracking spectrometer.

| Name | Definition | Description |
|------------|-------------------------------------------------------------------|-------------------------------------------------------------------------------------------------------------------------------------------------------------------------------------|
| Hit | Charge deposits in a single SCT strip above a threshold | A signal detected in the sensitive element of the SCT module sensors |
| Cluster | Adjacent hits in neighbouring SCT modules | Clusters give the total charge of groups of SCT strips that see a signal |
| Spacepoint | The global 3D position of clusters on both sides of an SCT module | Using the stereo-angle between clusters on the front and back of a module and combining with the global position of the SCT module in the aligned geometry |
| Segment | Partially reconstructed track in a single tracking station | A fit of all spacepoints in individual tracking layers in an SCT module. Segments must have an x -angle ≤ 0.08 rad, indicating a track passing through the full spectrometer |
| Full Track | A fully reconstructed track that traverses the full spectrometer | The track segments are used as seeds in a Kalman filter within the ACTS library |

maximum x -angle that a track segment can have and still be considered part of a track capable of traversing the full spectrometer is 0.08 rad. Any track segment with an x -angle above this threshold is discarded. If a track segment shares over 60% of its clusters with another segment, only the track segment with the smallest χ^2 is kept. This requirement avoids overlapping segments. The track segments are used as seeds in a combinatorial Kalman filter [124] within the tracking reconstruction algorithm library [125], FASER uses ACTS (a common tracking software), which takes into account the detector material and the effect of the magnetic field in the spectrometer.

Figure 4.1 [11] shows an event display of the full FASER detector geometry, it shows a reconstructed track from a muon traversing FASER. The hits in the SCT modules are represented by the horizontal blue lines, the reconstructed full track is shown with the red line, traversing all three tracking stations in the spectrometer. This muon has a track momentum of 21.9 GeV. The reconstructed PMT waveforms are also shown, the event was triggered by pulses in the VetoNu scintillator, Veto scintillator and timing scintillator above 25 mV, and by pulses in the preshower station above 3 mV.

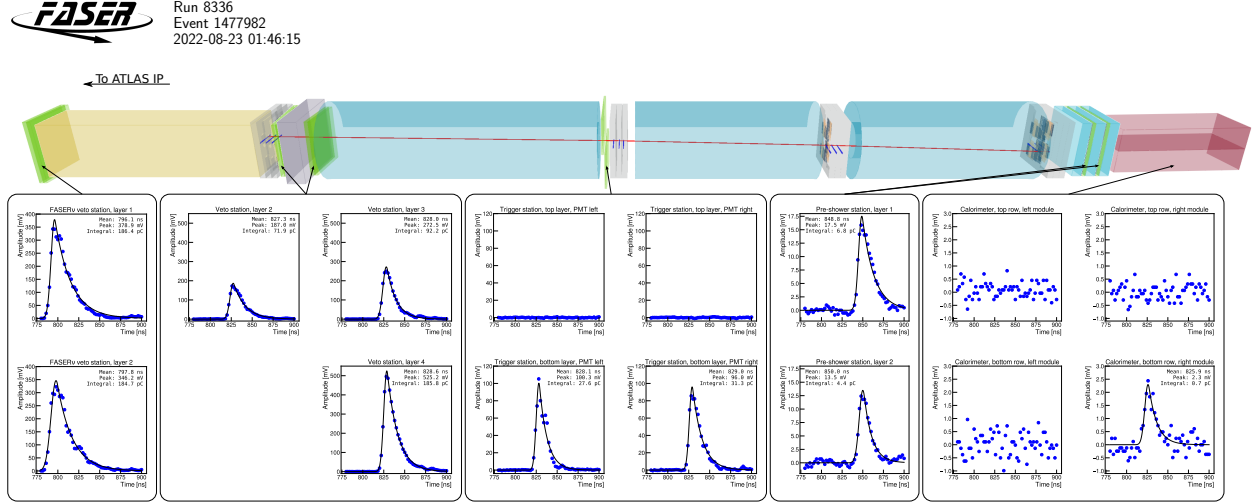


Figure 4.1: An event display showing a collision event of a muon traversing the FASER detector. The measured track momentum is 21.9 GeV. The waveforms are shown for signals in scintillator counters and calorimeter modules and are fitted using a Crystal Ball function. All PMT waveforms are consistent with a muon passing through the scintillators and one of the calorimeter modules. The event has been triggered by modules in the VetoNu scintillator station, veto scintillator station and timing scintillator station with pulses above 25 mV, and by modules in the preshower station with pulses above 3 mV. The detected hits in the SCT modules are shown with blue lines and the reconstructed track is shown with a red line. In the title of the waveform plots, left and right is defined facing the downstream direction. Figure from Ref. [11].

4.1.2 PMT Waveform Reconstruction

Physics data readout from FASER’s scintillators and calorimeter are in the form of digitised information produced by analog-to-digital converters (ADCs). An ADC converts a physics signal, for example the integrated charge readout by a PMT, into a finite number of bits that represent the size/amplitude of said physics signal. Steps must be taken, including subtracting the baseline noise of the signal and inverting the raw waveform, to produce reconstructed waveforms that are prepared for physics analysis. The figures from this section, demonstrating the steps involved in waveform reconstruction, are from Appendix A of Ref. [126].

The first step of the offline reconstruction process involves pedestal subtraction of the baseline noise and inversion of the negative ADC pulse. An example of a raw PMT waveform readout from the digitiser is shown in Figure 4.2 [126]. The digitiser has a 2 V range with a 14 bit readout, resulting in a 0.122 mV/ADC conversion factor. For the baseline subtraction, the distribution of the ADC counts is fitted with a Gaussian fit to obtain the most common value, this process is

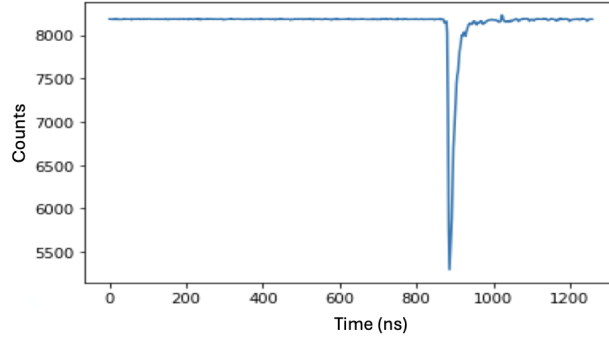


Figure 4.2: An example of a typical PMT raw waveform signal coming from the digitiser. Waveforms have a window of 1200 ns, with 2 ns bins and a negative amplitude of ADC counts. Figure from Ref. [18].

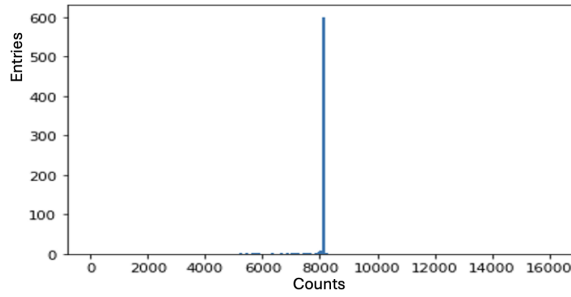
shown in Figure 4.3 [126]. The length of the waveform is large in comparison to the signal pulse, therefore, the most common value obtained from the fit corresponds to the baseline noise. The measured baseline mean is subtracted from the raw waveform and then the signal inverted, in order to get a baseline-subtracted positive pulse which can be used in reconstruction.

Figure 4.4a [126] shows the resulting waveform, within a 120 ns reconstruction window either side of the expected trigger time, fitted with a Crystal Ball function. The CB fit is defined in Section 4.2.1. This allows extraction of the mean, peak and integral of the distribution. This is converted into deposited charge according to the ADC conversion 0.122 mV/ADC. Figure 4.4b [126] shows a failed fit of a saturated waveform pulse, in this case it is preferable to use the fitted value extracted from the distribution rather than the raw charge. Otherwise, the raw value of the charge is always used. Figure 4.5 shows a reconstructed waveform of a high energy signal in the bottom right calorimeter module.

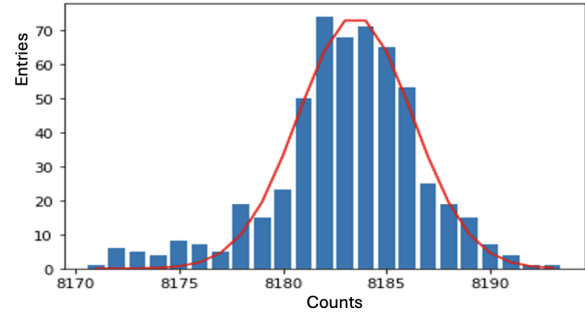
4.2 Calorimeter Response

This section discusses the response and simulation of FASER’s calorimeter, including investigations into the most realistic setup and corrections applied to the material description and geometry. The energy resolution of a calorimeter is discussed in the context of the ECAL simulation, using results from the FASER 2021 calorimeter test beam. Full details of the test beam are presented in Section 4.3.

Sampling EM calorimeters, such as FASER’s, are designed to absorb high-energy electrons and

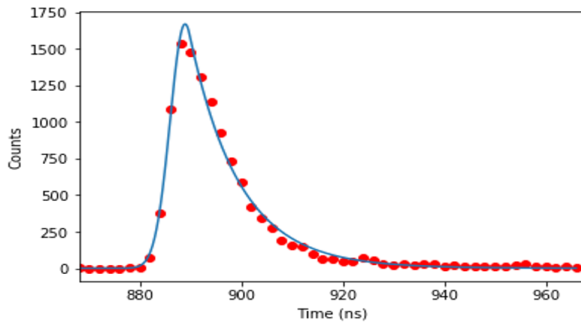


(a)

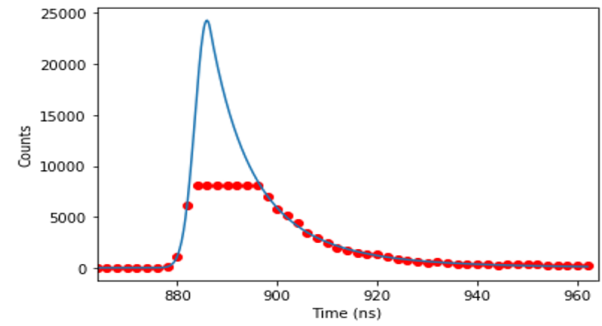


(b)

Figure 4.3: (a) The distribution of ADC counts for a PMT waveform (b) A Gaussian fit of the zoomed in ADC histogram range. Figure from Ref. [18].



(a)



(b)

Figure 4.4: (a) A example of a typical PMT raw waveform signal coming from the digitiser. Waveforms have a window of 1200 ns, with 2 ns bins and a negative amplitude of ADC counts. (b) An example of a saturated waveform pulse. Figure from Ref. [18].

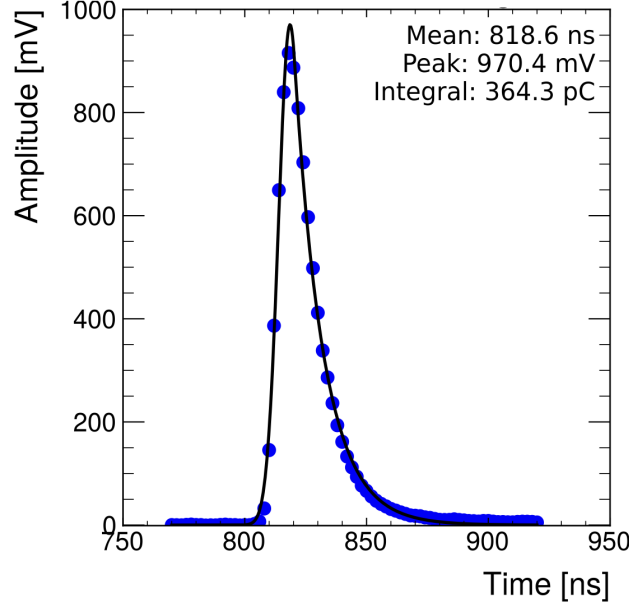


Figure 4.5: A example of a reconstructed waveform in the bottom right ECAL module.

photons and measure their energies through electromagnetic interactions such as bremsstrahlung and pair production. This is a destructive process which does not apply to muons or neutrinos that can penetrate significant amounts of material.

When the charged particles such as electrons or neutral particles such as photons interact with the EM calorimeter, the resulting EM showers are relatively compact and have a short shower depth, ideal for a detector the size of FASER. The size and shape of the shower is governed by the radiation length, defined as the mean length (in cm) to reduce the energy of an electron interacting with the EM calorimeter by a factor of $1/e$ [127] and depends on the material of the calorimeter, the density, and the energy loss of the incoming interacting particles. Charged particles lose energy by ionisation according to the Bethe-Bloch equation [30]:

$$\left\langle -\frac{dE}{dx} \right\rangle = Kz^2 \frac{Z}{A} \frac{1}{\beta^2} \left[\frac{1}{2} \ln \frac{2m_e c^2 \beta^2 \gamma^2 W_{max}}{I^2} - \beta^2 - \frac{\delta(\beta\gamma)}{2} \right] \quad (4.1)$$

where W_{max} is the maximum energy transfer possible in a single collision, I is the mean excitation energy, $\beta = v/c$, e is electron charge and m_e is the electron rest mass, $K = 4\pi N_A r_e^2 m_e c^2$, z is the charge number q/e , Z is the atomic number of the absorber, A is the atomic mass of the absorber. N_A is Avogadro's number and r_e is the classical electron radius.

Muons are considered minimum ionising particles (MIPs) which do not lose much energy in

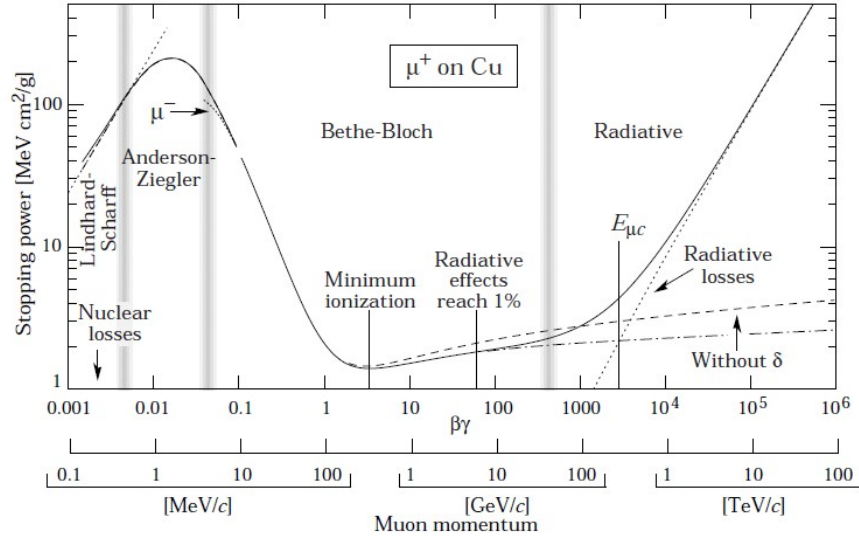


Figure 4.6: The energy loss for positive muons according to the Bethe-Bloch formula (shown between the second and third grey band. The rest of the plot shows other models). Figure from Ref. [19].

the calorimeter. Figure 4.6 [19] illustrates the energy loss of muons according to the Bethe-Bloch formula, ionisation dominates in the MeV to TeV energy range.

4.2.1 Energy Response

The energy response of a calorimeter is the average signal per unit of deposited energy. Not all the energy of an incident particle is deposited in the calorimeter, as there are also absorber layers which degrade the signal. The fraction of energy effectively reconstructed by the calorimeter needs to be estimated and then corrected to achieve the total calorimeter EM energy of an event.

One of the functions believed to best reflect the behaviour of an electron depositing energy in a calorimeter, and therefore best fit the spectrum of deposited energy, is the Crystal Ball (CB) function. The CB function was developed to describe the distribution of energy deposited by electrons or photons.

The CB is made up of a Gaussian peak and a power-law tail, giving it an asymmetry compared

to the standard Gaussian. The CB function is given by [128]:

$$f_{CB}(x : \mu, \sigma, \alpha, n) = N \begin{cases} e^{-\frac{(x-\mu)^2}{2\sigma^2}}, & \text{for } \frac{x-\mu}{\sigma} > -\alpha \\ A \left(\frac{n}{|\alpha|} - |\alpha| - \frac{x-\mu}{\sigma} \right)^{-n}, & \text{for } \frac{x-\mu}{\sigma} \leq -\alpha \end{cases} \quad (4.2)$$

where $A = \left(\frac{n}{|\alpha|} \right)^n e^{-\frac{|\alpha|^2}{2}}$ and where μ and σ are the mean and standard deviation of the Gaussian peak, n is the exponent of the tail function, α represents the connecting point of the Gaussian and power-law tail function, and N is the normalization factor. The μ and σ CB parameters are typically used to study the energy scale and energy resolution of a calorimeter.

The distribution best believed to describe the fluctuations of energy loss due to a minimum ionising particle (MIP), such as a muon, passing through matter is the Landau distribution [129]. This distribution resembles a Gaussian with a long upper tail and gives the probability that the particle loses energy δ whilst traversing x :

$$f_l(x, \delta) = \frac{\phi(\lambda)}{\zeta} \quad (4.3)$$

where $\phi(\lambda)$ is the Landau function and λ is Landau's universal variable. The energy loss corresponding to the maximum of $f_l(x, \delta)$ is the mean most probable energy loss, referred to as the most probable value (MPV).

Figure 4.7 shows a fitted MC distribution for a 100 GeV electron fitted with a CB function and a 100 GeV muon fitted with a Landau distribution, simulated in FASER's ECAL. As expected for a MIP, a very small fraction of the muon's total energy is deposited in the calorimeter. An electron is expected to deposit roughly 16.5% of its total energy in FASER's calorimeter.

4.2.2 Corrections and Local Effects

Since FASER uses outer ECAL modules from LHCb, comparison with their results is useful, particularly when comparing the energy response and local calorimeter effects. Understanding these effects is necessary to implement a realistic simulation. In addition, accurate simulation of the exact material used in FASER can have a large impact on the simulated energy response. This section will explore the impact of implementing Birks' law correction [130] and non-uniformities in light-

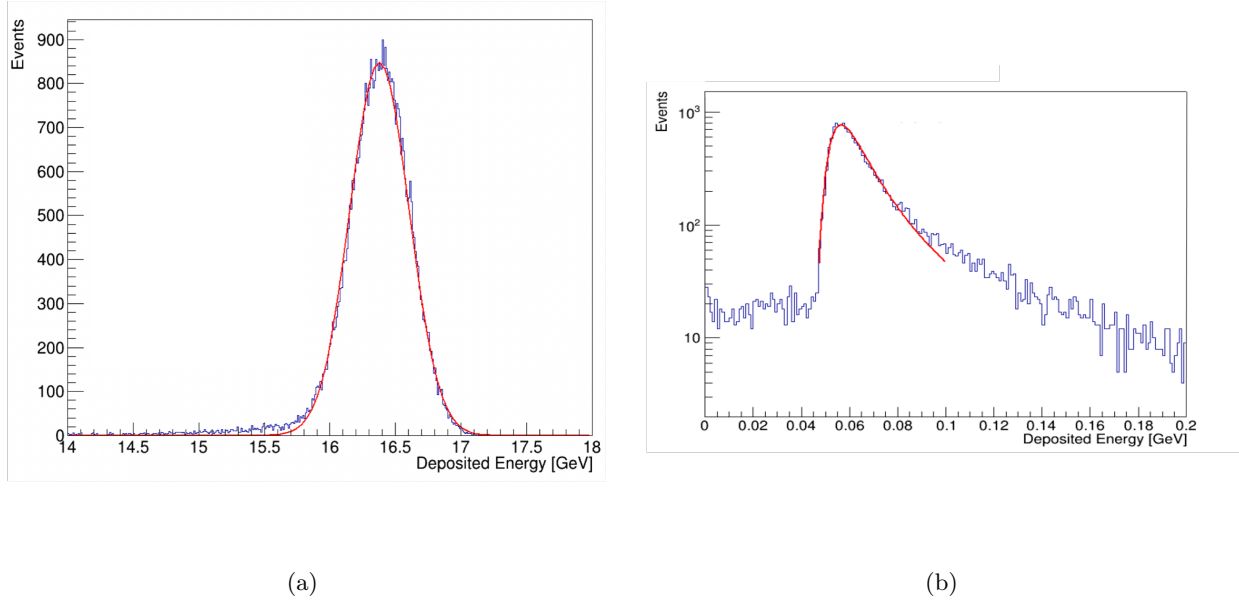


Figure 4.7: Fitted MC distribution for (a) a 100 GeV electron fitted with a CB function (b) a 100 GeV muon fitted with a Landau distribution simulated in FASER's ECAL

collection efficiency in order to build a realistic simulation of FASER's ECAL. There were many effects and aspects of the geometry that were not implemented in the first version of FASER's ECAL simulation, the author studied these effects in order to understand the impact on the detector simulation. The effects have since been implemented into the MC description, leading improvements in the simulated response.

Birks' Law is an empirical formula for the light yield per path length as a function of energy loss per path length, for a particle traversing a scintillator. It is not linear at high loss rates and decreases the energy deposited by around 3%. The correction factor applied to the energy loss, dL/dx , is given by:

$$\frac{dL}{dx} = \frac{1}{1 + \left(c_1 * \frac{dE}{dx} / \rho + c_2 * \left(\frac{dE}{dx} / \rho \right)^2 \right)} \quad (4.4)$$

where $c_1 = 0.013 \text{ gMeV}^{-1}\text{cm}^{-2}$ and $c_2 = 9.6 \times 10^{-6} \text{ g}^2\text{MeV}^{-2}\text{cm}^{-4}$ these constants are obtained from LHCb data. ρ is the density in gcm^{-3} and dE/dx is the average energy loss in MeVcm^{-1} according to the Bethe-Bloch formula in Equation 4.1.

In addition to this, there are also non-uniformities in the ECAL due to light collection efficiency and energy reflection at the edges [131]. Figure 4.8a [20] shows the variation seen at the ECAL

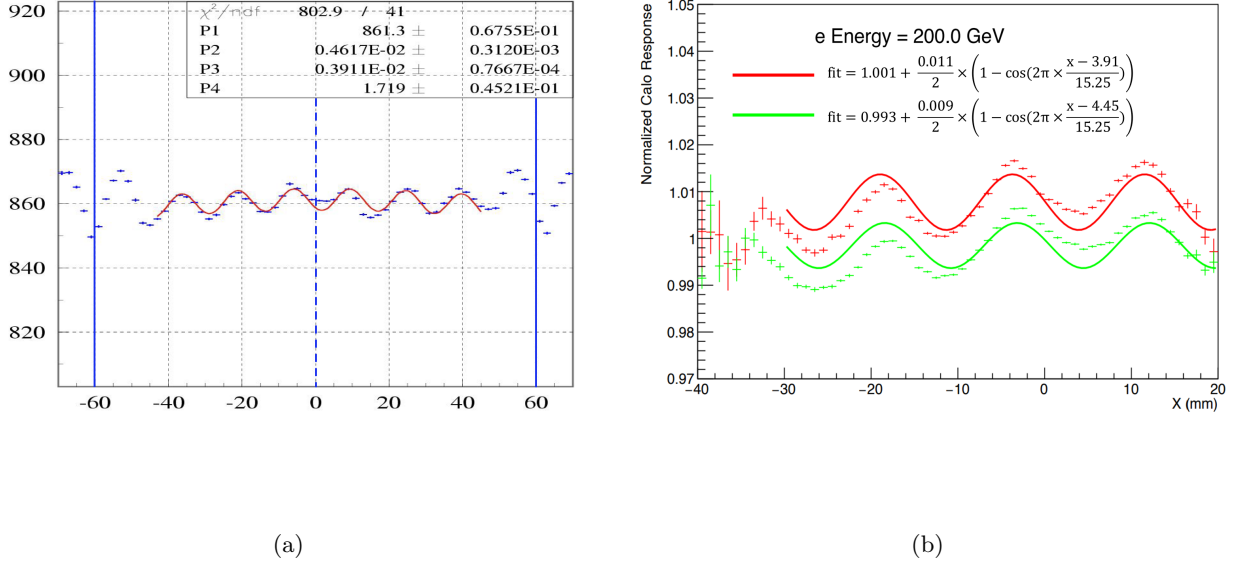


Figure 4.8: Non-uniformity in calorimeter response across the ECAL cell for (a) a 50 GeV electron in LHCb data [20] (b) a 200 GeV electron in FASER data. The dashed blue line on the LHCb plot shows the centre of the ECAL cell, the solid blue lines indicate the edges. The FASER plot shows data collected from two areas of the ECAL cell: away from the WLS fibres (green) and close to the WLS fibres (red), showing the position-dependent response, in addition to the change in response at the cell edge.

cell edges of the LHCb outer modules in the case of 50 GeV electrons. The dashed blue line indicates the centre of the ECAL cell and the solid vertical lines indicate the edges. Figure 4.8b shows the variation in calorimeter response as a function of position in FASER data. It also shows the difference in the response based on the position within the ECAL cell; the red fit uses data collected close to the WLS fibres in the ECAL module, light collection improves close to these fibres. Implementing these non-uniformities into the simulation results in an increase in deposited energy of $\sim 3\%$.

Finally, the layer of Tyvek paper between the alternating plastic scintillator and lead layers in the calorimeter was not initially considered in the FASER MC geometry. Since this material was not included in LHCb's simulation of the ECAL, the author carried out investigations to determine the most suitable density of Tyvek. The results indicated that a Tyvek density of 2.265 g/cm^3 gave the most accurate description of the ECAL modules. The addition of the material into the simulation of the calorimeter geometry decreased the energy deposited in the calorimeter by around

6%. Plots showing the change in energy deposition with the implementation of these effects and corrections can be found in Appendix A.1.

4.2.3 Energy Resolution

The measurement of energy with an EM calorimeter is based on the principle that the energy deposited by a charged particle shower is proportional to the energy of the incident particle. The energy resolution, σ/E , of a realistic calorimeter is defined as [132]:

$$\sigma_E/E = a/\sqrt{E} \oplus b/E \oplus c \quad (4.5)$$

where σ is the width of the CB distribution, \oplus indicates quadratic sum. The a/\sqrt{E} term is the stochastic term that describes fluctuations related to the physical development of the particle shower; b/E is the noise term which describes electronic noise of the readout chain; c represents the constant term that is independent of the particle energy.

LHCb test beam simulation using the same ECAL modules [20] found an energy resolution with a stochastic term of $(9.4 \pm 0.4)\%$ and a constant term of $(0.83 \pm 0.02)\%$. The energy response and resolution of the ECAL modules in LHCb simulation are shown in Figure 4.9 [20]. The energy resolution found in FASER test beam simulation is $(9.73 \pm 0.08)\%$ with a constant term of $(0.97 \pm 0.01)\%$, the comparison of the two results is shown in Figure 4.10 with and without the improvements to the FASER MC resulting from the implementation of non-uniformities, local effects and updated modelling and material description following test beam investigations. The fit of the simulation in Figure 4.10 does not include a noise term since the measurement of the resolution was performed on MC before any digitisation steps to mimic realistic detector noise. The results show that the calorimeter energy resolution is $\mathcal{O}(1\%)$ in the high energy range relevant to the analyses discussed in this thesis. This level of energy resolution in the calorimeter is more than sufficient for physics analysis.

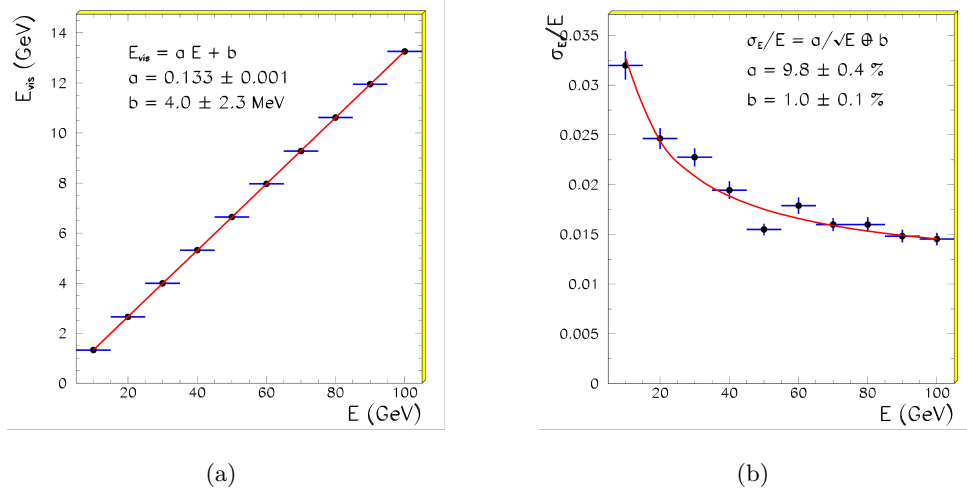


Figure 4.9: Simulation of the (a) energy response and (b) energy resolution of electrons in the outer ECAL module LHCb test beam [20].

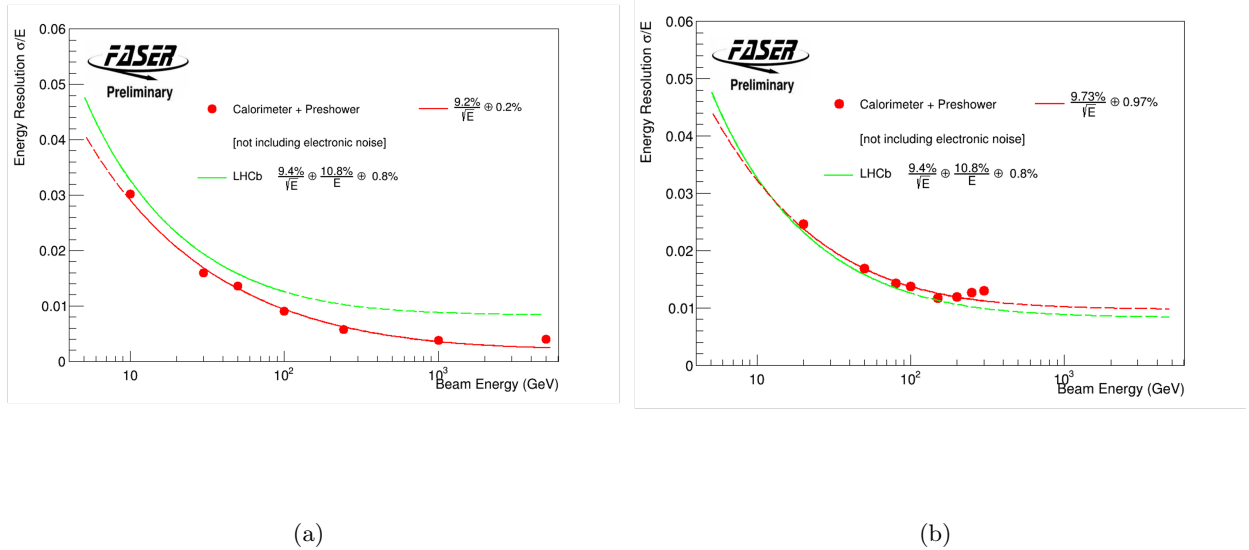


Figure 4.10: The simulated calorimeter energy resolution in (a) the original test beam MC and (b) the updated test beam MC that includes the most up-to-date material description and implementation of the studied local effects in the calorimeter. Compared with the parameterisation of LHCb test beam results in green.

4.3 The 2021 Calorimeter Test Beam

This section details the 2021 electromagnetic calorimeter test beam carried out in order to characterise the calorimeter and tracker of the FASER detector. In order to characterise the ECAL modules an electron energy scan was carried out, in addition, the uniformity of the muon response was measured. A pion scan was performed to study the hadronic response. The isolated energy response and resolution of the ECAL was measured and compared to LHCb data [20]. Understanding the calorimeter response is vital to FASER’s simulation of the ECAL: MC description has improved in various iterations as a result of the test beam studies, leading to a more accurate simulation which agrees well with data. The author was involved in generating the initial FASER test beam MC and, using the results of the test beam studies, worked to improve the simulation to better match LHCb data.

The test beam was carried out using the H2 beamline [133] in Experimental Hall North 1 (EHN1) at CERN, the experimental setup is shown in Figure 4.11. The experimental setup includes: two veto scintillators from TI12 which act as trigger scintillators, the IFT tracking station, the preshower detector, and six ECAL modules, which includes the four chosen for use in TI12 and two spare modules. The entire setup was placed on top of a large scissor table so that the equipment could be moved relative to the beam, in order to test the response at various points across the calorimeter modules. A sketch of the setup is shown in Figure 4.12, the different scan points are shown in Figure 4.13.

4.3.1 Test Beam Simulation

FASER’s test beam MC was initially generated with single-particle events at a fixed energy, the Geant4 package [134] is used to simulate the propagation of particles and energy deposition through the test beam geometry. LHCb test beam results using the same ECAL modules were used for comparison when building the simulation and studying the energy response and resolution, before it could be validated by FASER’s own test beam data. At this stage, the simulation takes the hits directly from the Geant4 simulation and sums their energy, it does not include any digitisation. Digitisation is a step which mimics the detector response, converting the simulation output into an output similar to the PMT pulses of real data. A dedicated geometry was developed for the

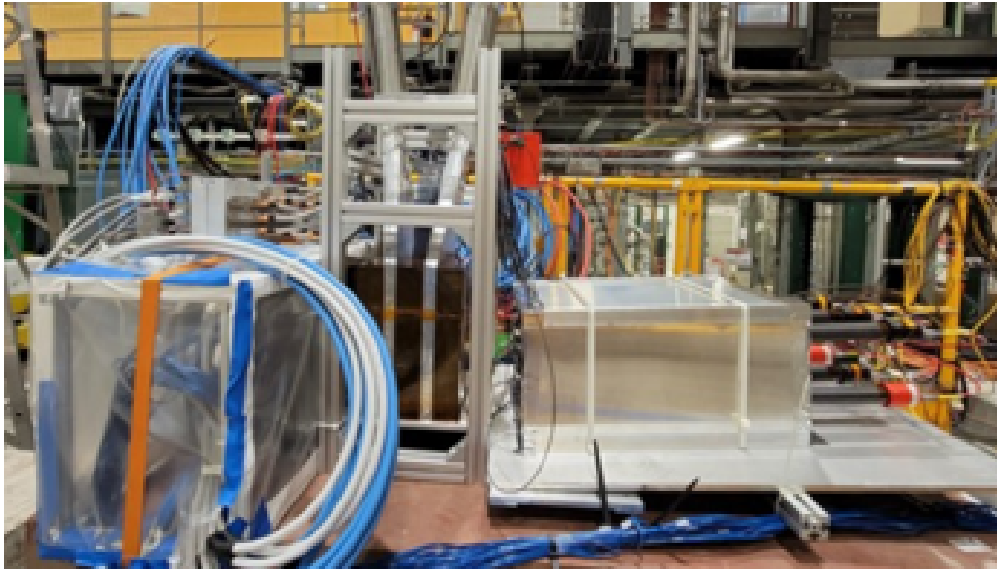


Figure 4.11: A photograph of the test beam setup in Experimental Hall North (EHN1) at CERN

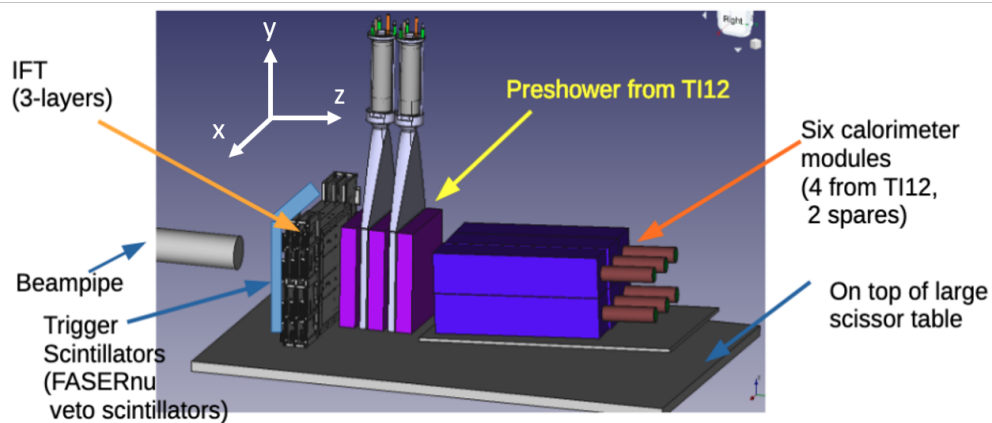


Figure 4.12: A diagram of the components used in the test beam. The coordinate system is also shown.



Figure 4.13: The different scan point positions used in the test beam. Scan point 8 represents the centre of the top middle ECAL module.

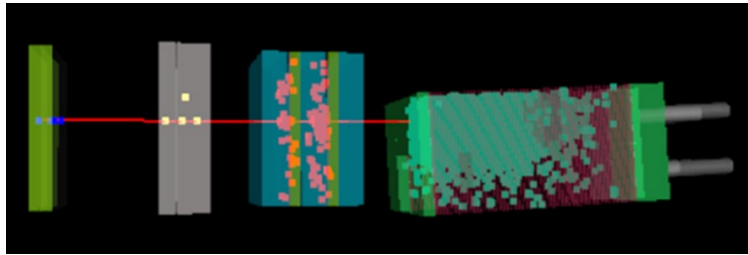


Figure 4.14: An event display showing the simulated hits of a 100 GeV electron in the test beam MC geometry

test beam simulation, shown in an event display produced based on ATLAS VP1 software [135] in Figure 4.14.

This initial simulation showed some discrepancy compared to the test beam data, the difference in the simulated calorimeter response compared to data taken across the calorimeter up to 150 GeV is shown in Figure 4.15 [126]. Applying a correction factor of 8.8% to the calibrated MC calorimeter energy improved the agreement between data and MC, particularly for higher energies. The calorimeter response at every scan point was measured in the case of 100 GeV electron beam. The correction factor is obtained by comparing the average calibrated energy in each of the six ECAL modules to the calibrated energy in MC at 100 GeV. The calibrated EM energy is used in the analyses discussed in this thesis, where the FASER MC geometry implements the same material description and local calorimeter effects as included in the test beam studies.

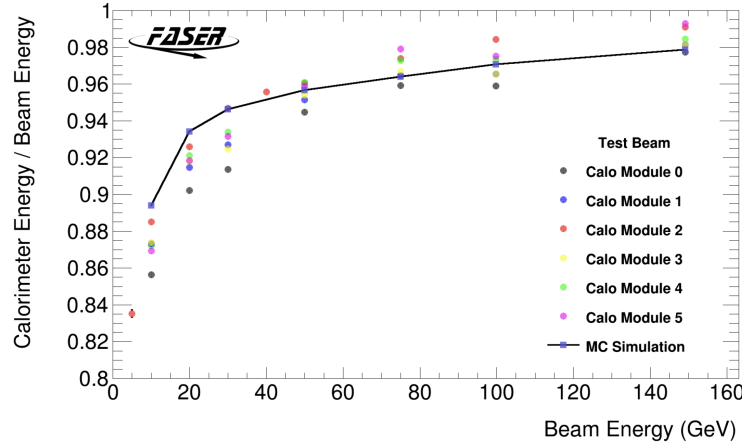


Figure 4.15: The calibrated EM energy in the calorimeter of MC simulation compared to test beam response of each of the six ECAL modules. Figure from Ref. [18].

The reason for the discrepancy in test beam data and MC arises primarily from differences in the material description in the MC geometry compared to the actual setup. The inclusion of Tyvek paper has a large impact on the simulated response. The accurate description of the various local calorimeter effects discussed in Chapter 4.2.2 also affects response and resolution. Another important factor concerning the accuracy of the test beam MC is the realistic simulation of the particle beam and the setup specific to the H2 beamline used in EHN1. Figure 4.10 shows the improved agreement in energy resolution compared to previous LHCb test beam results as a result of updating the material description in FASER MC geometry, implementing the local corrections and non-uniformities discussed previously, and using the most realistic simulation of the H2 beamline. The calculation of calorimeter energy resolution is defined in Chapter 4.2.1 and an example of the fitted energy distribution is shown in Figure 4.7a.

4.3.2 Preshower Correction

In order to study the isolated response of the calorimeter in the test beam, it is necessary to apply a correction factor to the measured energy response to account for the energy lost by a particular particle as it traverses the preshower in the test beam setup. The preshower “steals” a portion of the EM shower from the calorimeter, as a direct result of the two radiation lengths of tungsten radiator. This effect can be seen by the negative slope in Figure 4.16, which shows the total deposited energy in the preshower station compared to the total deposited energy in the calorimeter for a 100 GeV

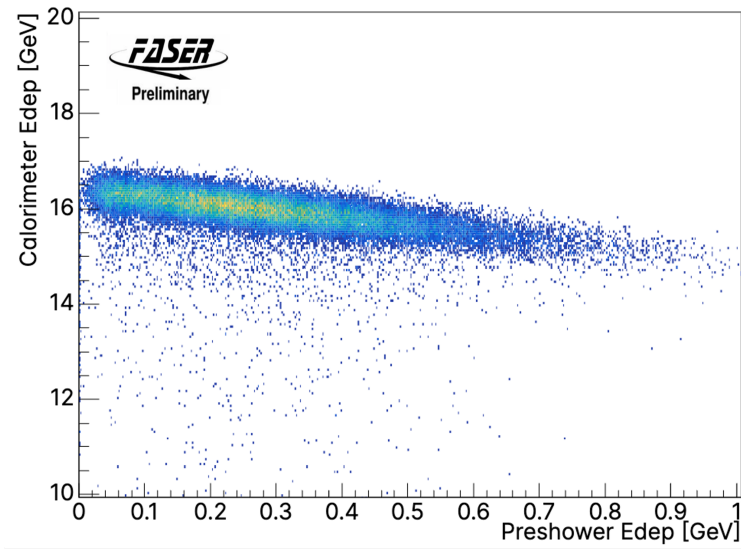


Figure 4.16: The energy deposited in the calorimeter modules vs the preshower scintillator layers in test beam simulation (100 GeV electron).

electron in test beam MC. The effect varies on an event-by-event basis and degrades the energy resolution. This is corrected for in order to obtain the most accurate calorimeter energy resolution measurement.

A preshower correction was derived to mimic the absence of a preshower station, taking into account the deposited charge in the calorimeter and preshower station:

$$Q_{corrected} = Q_{calo} + (m * Q_{preshower}),$$

where Q is the total deposited charge and m is the gradient derived from the fit of the deposits in the preshower vs calorimeter. The preshower correction is applied in both data and MC, resulting in an increased energy response and a reduced energy resolution from $\sim 2.3\%$ to $\sim 1.9\%$ for a 100 GeV electron. The change in response and resolution is due to more charge deposits in the calorimeter and less degradation of signal, this is shown in Figure 4.17 [15] in the case of data.

4.3.3 Test Beam Results

The measurement of energy resolution from the final test beam MC compared to test beam data is shown in Figure 4.18, where both data and MC have been corrected to account for the preshower. The energy resolution shows generally good agreement with some differences that are understood.

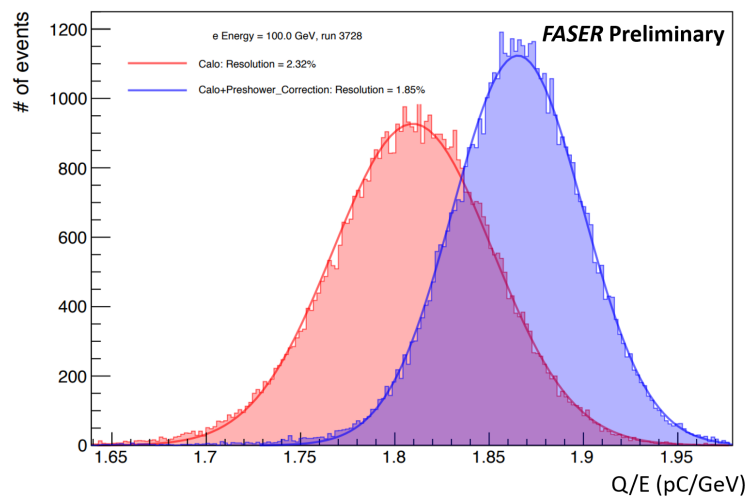


Figure 4.17: The effect of the preshower correction on the charge deposited by a 100 GeV electron in test beam data. The preshower corrected charge (red) shows a reduced and improved energy resolution.

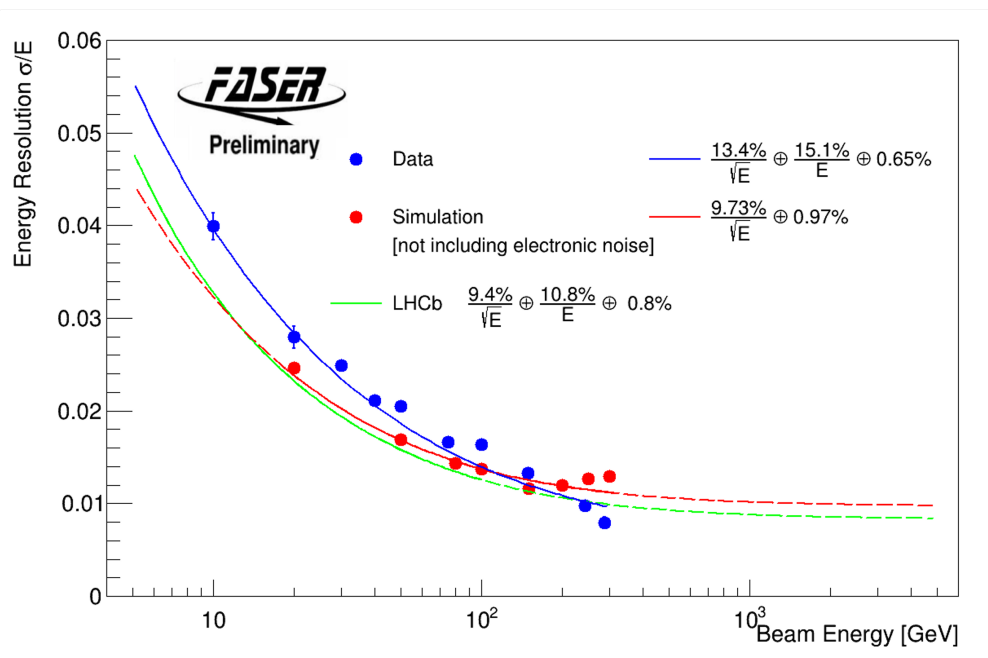


Figure 4.18: Calorimeter energy resolution measurement in test beam data (blue) and simulation (red), compared to a parameterisation of LHCb test beam results.

The test beam MC agrees well with parameterised results from LHCb, differences in data and MC at higher energies are related to the lack of electronic noise implemented in the MC at this stage of the analysis.

Chapter 5

The Modelling of Physical Processes and Statistical Analysis

The realistic modelling of hadron-hadron collisions and the resulting parton interactions is important in particle physics analysis. The generation of dedicated Monte Carlo (MC) simulations is necessary to study potential new physics signals and in order to estimate background processes. This chapter describes the MC samples used in generating the dark photon and ALP signals for the two analyses discussed in this thesis. It includes discussion of the systematic uncertainties that arise due to variations in the generator predictions and descriptions of the samples used in background estimation. This chapter also details the statistical framework used to interpret the results of the dark photon and ALP searches, where MC predicted signal yields are used in combination with background predictions to set the exclusion limits presented in this work.

5.1 Monte Carlo Simulation and Event Generators

The modelling of pp collisions, and the resulting interactions, requires an understanding of parton interactions. Protons cannot be dealt with as point-like particles, but rather their interactions can be described in terms of their constituent, point-like quarks and gluons.

Calculations in the Standard Model used to simulate realistic physics interactions depend on factorisation theorems [136]. Factorisation allows for the separate treatment of different processes. Hard scattering processes at high energy in the LHC, where constituent partons of the incoming

beams interact and produce a relatively small amount of highly-energetic outgoing particles, can be perturbatively calculated [137]. In softer processes, at lower energies typically around 1 GeV, incoming partons are confined within the proton and interact non-perturbatively to produce outgoing particles. Soft processes cannot be calculated from first principles but instead need to be modelled [138].

The Parton Distribution Function (PDF) can be considered the probability of finding a parton a with a momentum fraction x in a hadron h . The PDF is independent of the particular process and cannot be calculated using perturbation theory, it must be determined using experimental data. It contains all unresolved emission below the factorisation scale μ_F . The factorisation scale can be considered as the separation between perturbative and non-perturbative processes.

The cross section for a scattering process $ab \rightarrow n$ in a hadronic collision [137] can be calculated through:

$$\begin{aligned} \sigma &= \sum_{a,b} \int_0^1 dx_a dx_b \int f_a^{h1}(x_a, \mu_F) f_b^{h2}(x_b, \mu_F) d\hat{\sigma}_{ab \rightarrow n}(\mu_F, \mu_R) \\ &\quad \sum_{a,b} \int_0^1 dx_a dx_b \int d\phi_n f_a^{h1}(x_a, \mu_F) f_b^{h2}(x_b, \mu_F) \\ &\quad \times \frac{1}{2\hat{s}} |\mathcal{M}_{ab \rightarrow n}|^2(\phi_n; \mu_F, \mu_R) \end{aligned} \quad (5.1)$$

where:

- $f_a^h(x_a, \mu_F)$ is the parton distribution function (PDF) that depends on the momentum fraction x (the Bjorken variable) of a parton a compared to the parent hadron h and the factorisation scale μ_F .
- $\hat{\sigma}_{ab \rightarrow n}$ is the production cross section of process $ab \rightarrow n$. This parton-level cross section depends on the momenta given by the final-state phase space ϕ_n , the factorisation scale, and the renormalisation scale μ_R .
- $|\mathcal{M}_{ab \rightarrow n}|^2(\phi_n; \mu_F, \mu_R)$ is the matrix element describing the hard scattering processes, averaged over initial-state spin and colour degrees of freedom. The matrix element can be considered as the sum over all the Feynman diagrams for a given process.
- $\frac{1}{2\hat{s}}$ describes the parton flux, $\frac{1}{2\hat{s}} = \frac{1}{2x_a x_b s}$ where s is the hadronic centre-of-mass energy squared.

Standard event generators used in particle physics are typically based on the parton model and employ Leading Order (LO) or Next-to-Leading-Order (NLO) matrix elements to compute simulations [138]. NLO QCD computations have become the typical tools employed at hadron colliders, tests have been carried out by comparing NLO results with experimental measurements. LO calculations include dominant QCD effects at leading logarithmic level, but do not have the same accuracy that NLO enforces. To provide a precision measurement requires the merging of LO and NLO calculations.

A problem with merging NLO calculations with PS simulations is the risk of over-counting. Double-counting occurs when the first emission from the PS and NLO correction is counted in each case. Matching matrix elements and parton showers resolves the issue of double counting when it comes to including NLO calculations in addition to LO [139]. Another method is the POWHEG [140] method to successfully incorporate NLO into the parton shower. An unavoidable feature of subtraction methods is the negative weights, the treatment of these is also handled by POWHEG.

5.1.1 MC Event Generators

Listed here are the event generators and simulation packages used in the production of signal and background processes in MC used in the analyses discussed in this thesis. This is, of course, not an exhaustive list of all event generators and there are other methods used for matrix and PS matching.

PYTHIA The PYTHIA [141] event generator, named after the Ancient Greek Pythic oracle, is used for the generation of high-energy physics collision events. The structure of the PYTHIA event generator can be split into three main parts [142]: the process level which includes the hard scattering processes, described perturbatively; the parton level which includes initial and final state radiation, the simulation of various shower models and beam remnants; the hadron level which deals with QCD confinement, the decay of unstable hadrons and hadron rescattering, described non-perturbatively using modelling and tuning of parameters. In this thesis, PYTHIA8 is used both with the default Monash tune [143] and a dedicated forward tune (PYTHIAForward). The Monash tune is based on physics data from central experiments; PYTHIAForward is based on forward LHCf measurements [144]. PYTHIA is used to model the Parton Shower (PS) matched to

NLO generators such as POWHEG.

POWHEG The POWHEG event generator applies NLO accuracy to the simulation of hadron-hadron collisions. This is achieved through matrix element generation that is interfaced with generators such as PYTHIA in order to simulate the parton shower. POWHEG is used in this thesis with the NNPDF3.1sx+LHCb PDF set [145, 146] to model the production of B -mesons at NLO+NLL x^{-1} [148] accuracy, matched with PYTHIA8 [2] to model the parton shower and hadronisation.

EPOS-LHC The EPOS-LHC [149] event generator is designed for minimum bias hadronic interactions, used for both heavy ion interactions and cosmic ray air shower simulations. EPOS-LHC is used to generate the flux of light hadrons in the forward region, including forward π^0 and η production. EPOS-LHC, SIBYLL, QGSJET and DPMJET are all part of the CRMC program [150].

SIBYLL The SIBYLL [151] event generator is used for cosmic ray and extensive air shower simulations. SIBYLL is used to model hadronic interactions at fixed target and collider experiments, it is based on the Dual Parton Model, Lund Monte Carlo Model and minijet model. In this thesis it is used to calculate the uncertainty on the light hadron flux.

QGSJET The QGSJET [152] event generator is another cosmic ray event generator which is used to model light hadrons, QGSJET is based on the quark gluon string model. The prediction from this generator is also taken into account when calculating the light hadron flux uncertainty.

DPMJET The DPMJET [153] event generator is a cosmic ray event generator based on the Dual Parton Model, it is often used to simulate the production of charmed hadrons.

GENIE GENIE [154] is a neutrino event generator and simulation package that aims to model all types of neutrino interactions with any neutrino flavour and target type. The framework uses a

¹NLL x refers to the computation of next-to-leading logarithmic corrections which deal with small- x resummations due to scaling variations [147].

large number of physics models including nuclear physics models, hadronization models and cross section models which provide accurate calculations of the differential and total cross section of interacting neutrinos. It is used to model the interactions in each of the neutrino MC samples used in this thesis.

FLUKA FLUKA [117] is a simulation package for particle transport and interactions with matter. FASER uses FLUKA to simulate the transport of muons coming from the IP through the machine optics and rock to FASER. It is used in several high-statistic muon MC samples in this thesis.

5.1.2 FORESEE: The Forward Experiment Sensitivity Estimator

Properly modelling the far-forward spectra of mesons which could produce BSM signatures is vital to understand and predict FASER’s sensitivity to LLPs. As discussed above, there are many event generators that can be used to produce MC simulation of hadronic interactions. However, these event generators do not provide predictions of the fluxes of the resulting LLPs at FASER.

The Forward Experiment Sensitivity Estimator (FORESEE) [21] is the package used by FASER that provides the spectra of an extensive list of light mesons, baryons, photons, charmed hadrons, bottom hadrons and heavy gauge bosons and predicts the resulting LLP spectra specific to the FASER location [21]. Figure 5.1a [21] shows the forward spectra predicted by EPOS-LHC in the case of neutral pions, a primary source of dark photons. Figure 5.1b [21] shows the forward spectra predicted by PYTHIA8 with the Monash tune in the case of neutral B -mesons, a primary source of ALPs. The angular acceptance of FASER is to the left of the dashed line in each case. The characteristic transverse momentum of each meson is indicated by the diagonal dashed line. In FORESEE these distributions are used to generate the forward LLP flux due to these meson decays.

FORESEE allows the user to obtain the expected sensitivity reach for particular BSM models. FORESEE takes the generated production of particles from the ATLAS IP using various generators, performs the parameterised LLP production and decay and produces the required four-vectors in HEPMC [155] format used as input to the FASER Geant4 [156] simulation. The package can be used for an extensive range of BSM models with experimental geometries specific to FASER and with the option to apply basic cuts to the visible signal [21]. Three different LLP production modes

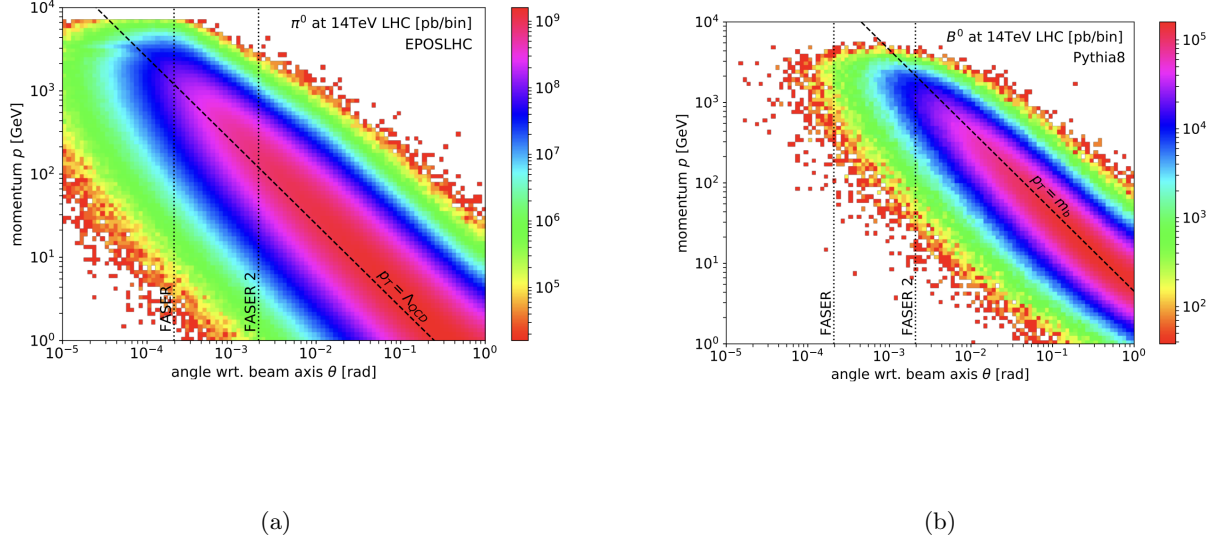


Figure 5.1: The distribution of (a) π^0 mesons and (b) B^0 mesons in the forward (θ, p) plane. Where θ is the angle with respect to beam axis and p is the meson's momentum. The predicted spectra is obtained assuming 14 TeV pp collision energy. The angular acceptance of FASER is indicated. Figure from Ref. [21].

are considered within the framework; the main production mode of LLPs in most models is from the decay of SM particles. LLPs may also be produced in three-body decays, where mixing with SM particles occurs. Finally, LLPs can be produced directly, for example as in A' production via Bremsstrahlung or Drell-Yan production as discussed in Chapter 2. FORESEE generates neutral pions using the EPOS-LHC generator and generates B -mesons using PYTHIA with various tuning parameters including the Monash tune [143] as discussed in the above section.

5.2 Modelling of the Dark Photon and ALP Signal

The production of dark photons in the far-forward region is modelled in FORESEE using the EPOS-LHC generator. Details of the production mechanisms are given in Section 2.5.1. The production of ALPs mainly occurs in FCNC decays of kaons and B -mesons. The modelling of light hadrons that produce the ALP is done using the EPOS-LHC event generator. The simulation of the forward B -mesons comes from recommendations outlined in Ref. [22] using POWHEG with the NNPDF3.1sx+LHCb PDF set [145, 146] to model the B -meson production at NLO+NLLx [148]

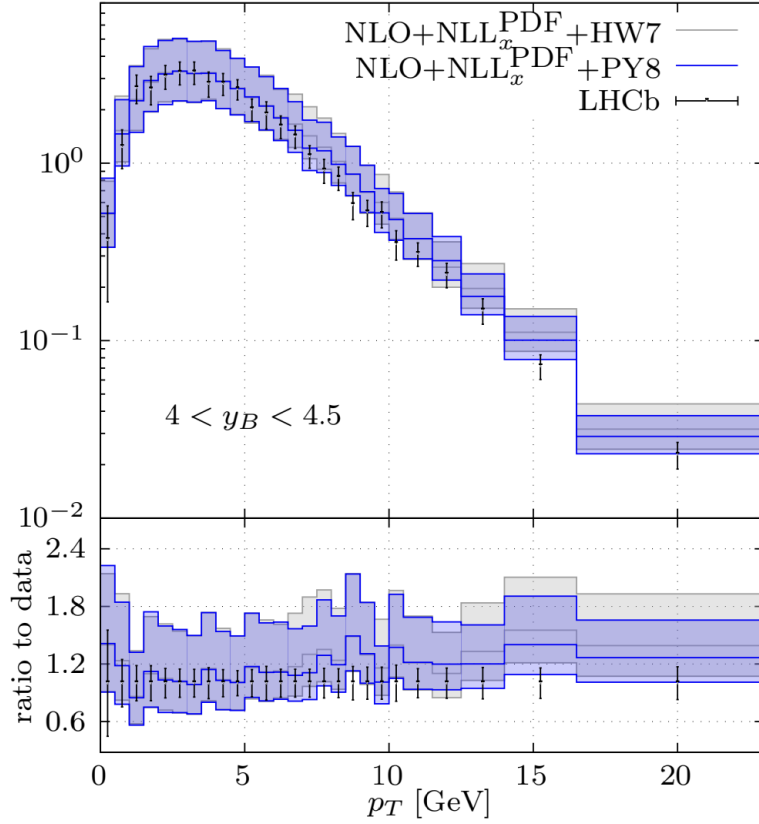


Figure 5.2: Predictions for the production of B -mesons with POWHEG+Pythia prescription used for the ALP signal MC (NLO+NLL PDF + P8), compared to the POWHEG+HERWIG and LHCb data. The blue band shows the large scale uncertainties. Figure from Ref. [22].

accuracy, matched with PYTHIA8 [2]. The NLO calculation is performed in a fixed-flavour scheme with massive heavy quarks and the hadronisation of these heavy quarks is modelled using PYTHIA8. Figure 5.2 [22] shows how the modelling of the production of B -mesons with the prescription chosen for the ALP analysis agrees well with forward LHCb data [22], although with large uncertainties.

The uncertainty on the light hadron component of the ALP signal comes from the spread of the generator predictions provided by SIBYLL, QGSJET, PYTHIA and PYTHIAForward². The uncertainty associated with the charm hadron component comes from the POWHEG+PYTHIA minimum and maximum predictions, which use variation factorisation and renormalisation scales. The central factorisation and renormalisation scales are set to $\mu_F = \mu_R = (m_Q^2 + p_{T,Q}^2)^{1/2}$ where m_Q and $p_{T,Q}$ are the quark mass and transverse momentum, defined in Ref. [22]. The minimum and

²A dedicated forward tune of PYTHIA discussed in Ref. [144].

maximum prediction is obtained by varying μ_F and μ_R by a factor of 2 and a factor of $\frac{1}{2}$. There is an additional 20% uncertainty in the modelling of the B hadrons, recommended following discussion with the FASER theory group, due to the large uncertainties that can be seen in Figure 5.2 [22].

For the generation of the ALP signal, the weights of the different generators are taken into account in the simulation stage before digitisation and reconstruction. With the generation of the A' signal, the uncertainty is derived using a parameterisation of the signal yields from EPOS-LHC, QGSJET and SIBYLL, this is described in Chapter 6.

5.3 Overview of MC Background Samples

This section gives an overview of the MC samples used to evaluate background predictions and systematic uncertainties. This includes the MC samples used to: predict the neutrino background; study photon conversion events; predict the muon flux at FASER; investigate the muon flux specifically reaching FASER at large angles.

5.3.1 Modelling of Far-Forward Neutrino Interactions

Simulation of the total flux of neutrinos at FASER is vital to the dark photon and ALP searches. The total background estimation from neutrinos in both of the analyses is reliant on MC prediction and the neutrino interactions are modelled with GENIE.

In the dark photon analysis, where the component of neutrino background is negligible, a 300 ab^{-1} MC sample of neutrino interactions is used. Modelled in GENIE, this sample uses EPOS-LHC, QGSJET, DPMJET³, SIBYLL and PYTHIA, according to Ref. [157].

In the ALPs analysis the component of neutrino background is not negligible and is modelled according to updated recommendations in Ref. [22]. There are two primary components of the far-forward neutrino flux: light, displaced hadron decays and decays of prompt charmed hadrons. The component of neutrino flux coming from light hadrons is simulated using the EPOS-LHC generator. An envelope of the EPOS-LHC, SIBYLL, QGSJET and PYTHIAForward generators is used to derive the uncertainty. The charm hadron component comes from the POWHEG+PYTHIA prediction with uncertainty derived from scale and tuning variations in the same way as the ALP

³DPMJET has not been tuned to charm production data [157] and is not validated for charm production, it was not included in the generation of neutrino MC for the ALP analysis.

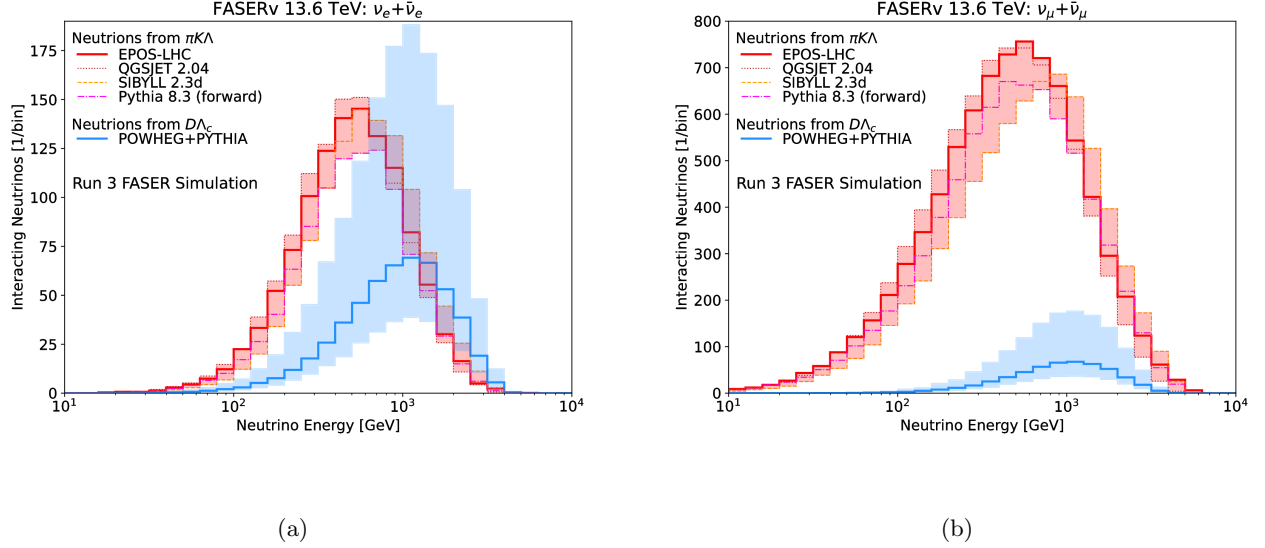


Figure 5.3: The predicted energy distribution of (a) electron neutrinos and (b) muon neutrinos from CC interactions in FASER ν for an integrated luminosity of 250 fb^{-1} . The component from light (charm) hadron decays is shown in red (blue). The shaded regions show the corresponding uncertainties associated with the flux. The light hadron component includes neutrinos produced in π , K and Λ decays, simulated using the EPOS-LHC, QGSJET, SIBYLL and PYTHIA generators. The charm hadron component includes neutrinos produced in D and Λ_c decays, simulated using POWHEG + PYTHIA. Figure from Ref. [23].

signal MC. To combine the light and charm uncertainties to give the symmetric uncertainties on the ν_e and ν_μ component, the maximum deviation from the nominal yield is calculated and then added in quadrature. The neutrino flux produced from the different MC event generators is shown in Figure 5.3 [23] for both ν_e and ν_μ , the large uncertainties particularly associated with the POWHEG+PYTHIA charm hadron component are clear from the large error bands. The contribution from ν_τ expected in the electronic detector considered for the analyses explored in this thesis is negligible. The uncertainty arising from GENIE modelling is negligible.

For each of the MC samples used for the neutrino background estimation, 10 ab^{-1} are simulated and scaled to the size of the dataset used in the ALP search.

5.3.2 FLUKA and Large-angle Muon Simulations

In both analyses, the component of background from muons that may miss the veto scintillators must be evaluated. The use of tracking variables in the signal selection for the dark photon

search, which looks for two closely-spaced charged tracks from an e^+e^- pair makes rejecting muon background simple. However, there is still a possibility that large-angle muons which miss the veto scintillators could enter FASER and produce signal-like topology. It is more difficult to reject this type of background in the ALP search, where no requirements are placed on tracks, therefore, different MC samples are used to evaluate this backgrounds to more specifically target the large-angle muons.

For the purposes of background estimation in the dark photon analysis, two MC samples of high energy muons are used, sampled from the 2D FLUKA energy and angular spectra [117, 158, 159]. The first sample simulates 2×10^7 muon events entering FASER from the direction of IP1. The second sample contains 8×10^5 events generated to study muon events that could miss the veto scintillators. These events are generated at a large angle before the VetoNu detector ($z = -3.75$ m) at a radius of 15-30 cm spanning the edge of the VetoNu acceptance. These samples are used to study photon conversion events and to evaluate the component of large-angle muon background present in the dark photon analysis, see Chapter 6.3.4.

The first MC sample considered in the ALPs search is generated from a FLUKA sample consisting of 200 million pp collisions, resulting in 15×10^6 muon events. This sample includes a realistic spectrum of muons entering from all directions, therefore giving an idea of the number of such large-angle muon events that survive analysis selections, it is also used to estimate the neutral hadron background in Chapter 7.3.2. It provides more statistics than previous samples used in the dark photon search. To properly evaluate the large-angle muon component, there is an additional, dedicated large-angle muon MC sample also used to study this type of muon background. In this sample 4×10^5 muons are simulated at a large angle and radius ($9 \text{ cm} < r < 25 \text{ cm}$) with the FLUKA energy spectrum. The full method for estimating the component of large-angle muon background is explored in Chapter 7.3.4.

5.4 Statistical Analysis

Data analyses rely on prediction for the various signal and background components in the data to aid the interpretation of observations, where the signal component describes the process of interest. If no excess is observed in the data, exclusion limits may be set within a grid of potential physics

scenarios, excluding a subset of the tested parameter space. The statistical interpretation of the results is done using the statistical analysis framework HistFitter [160], described in the following section.

5.4.1 The HistFitter Framework

The HistFactory package is used to build a parametric model to describe the data which is provided as histograms of the MC signal model and associated background. A Probability Density Function (PDF) is constructed to perform fits on the data. The framework performs a profile-likelihood fit, with a general likelihood of an analysis represented by the product of a Poisson distribution of the number of events in control regions (CRs) and signal regions (SRs), and additional Gaussian distributions which constrain the uncertainties. The likelihood, which can be thought of as the probability of a particular outcome of an experiment, is given in Equation 5.2 [160]:

$$\begin{aligned} L(n, \theta^0 | \mu_{sig}, b, \theta) &= P_{SR} \times P_{CR} \times C_{syst} \\ &= P(n_S | \lambda_S(\mu_{sig}, b, \theta)) \times \prod_{i \in CR} P(n_i | \lambda_i(\mu_{sig}, b, \theta)) \times C_{syst}(\theta^0, \theta) \end{aligned} \quad (5.2)$$

where n_S and n_i are the Poisson measurements of the number of events in the signal region and control region i , θ is the nuisance parameter that describes each systematic uncertainty, θ^0 is the central value around which θ can be varied, b is the background prediction, λ_S and λ_i represent the Poisson prediction of the number of events in the SR and CRs. μ_{sig} is the signal-strength parameter, a hypothesised signal rate on which limits can be set.

C_{syst} is the systematic uncertainty term, a probability density function constructed with the product of the Gaussian distributions of each systematic variation [160]. The nominal value of the nuisance parameters describing the systematic uncertainties is varied and a maximum likelihood procedure is performed:

$$C_{syst}(\theta^0, \theta) = \prod_{j \in systs} G(\theta_j^0 - \theta_j) \quad (5.3)$$

where G is the Gaussian width.

HistFitter performs statistical tests based on interpolation and extrapolation algorithms which describe the parameterised PDFs for all values of nuisance parameters θ_j . The likelihood function

in Equation 5.2 is used to construct a profile likelihood ratio in order to test hypothesised values of μ_{sig} [24].

The first step is performing a profile likelihood ratio [24] to test hypothesised values of μ_{sig} given by a test statistic $t_{\mu_{sig}}$ defined in Equation 5.4. In the search for new physics, the test statistic can be used to assess the level of agreement between expected and observed signal yields. A high value of $t_{\mu_{sig}}$ represents incompatibility between the data and μ_{sig} .

$$t_{\mu_{sig}} = -2 \ln \left(\frac{L(\mu_{sig}, \hat{\hat{\theta}})}{L(\hat{\mu}_{sig}, \hat{\theta})} \right). \quad (5.4)$$

$\hat{\theta}$ represents the value of θ that maximises L in Equation 5.2 for a particular value of μ_{sig} [24].

In the search for new physics there are two hypotheses to consider: a *background-only* hypothesis assumes no BSM signal, only contributions from the Standard Model are taken into account; a *signal+background* hypothesis assumes that a BSM signal is present in the dataset in addition to the SM expectation. The distribution of the test statistic is evaluated for each of these hypotheses. When the signal strength is set to $\mu_{sig} = 0$ the signal component is turned off, for $\mu_{sig} = 1$ the signal expectation is set to the nominal value of the model under consideration [160].

Given a hypothesis H_0 , the p -value can estimate the significance of a discrepancy between data and the assumption made in H_0 [30]. Equation 5.5 [24] defines the p -value in terms of test statistic:

$$p = \int_{t_{\mu_{sig}, obs}}^{\inf} f(t_{\mu_{sig}} | \mu_{sig}) dt_{\mu_{sig}}, \quad (5.5)$$

where $t_{\mu_{sig}, obs}$ is the value of the test statistic observed in data, $f(t_{\mu_{sig}} | \mu_{sig})$ represents the PDF of t_{μ} . The p -value can be visualised as the integral of a PDF from the observed value to the end of the probability density function, this is shown in Figure 5.4a [24]. In particle physics searches the usual convention is to convert the p -value to a significance Z , the relation between the p -value and significance is shown in Figure 5.4b [24] and defined according to the quantile Φ^{-1} of a Gaussian distribution in Equation 5.6.

$$Z = \Phi^{-1}(1 - p) \quad (5.6)$$

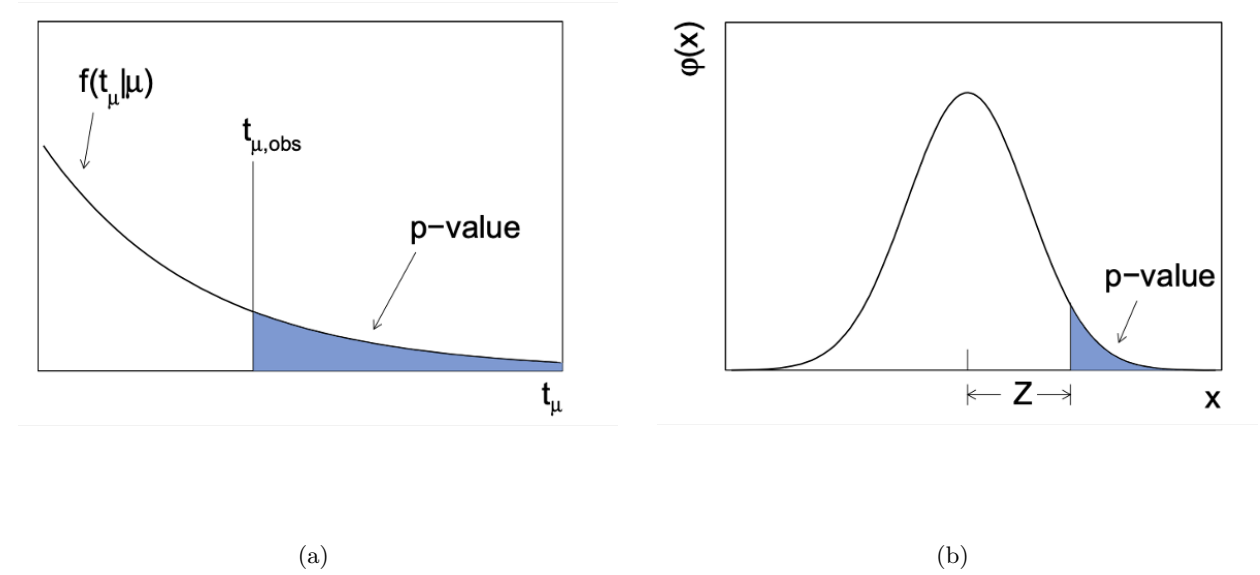


Figure 5.4: (a) The p -value can be visualised as the integral of a PDF from the observed value to the end of the probability density function. This is shown in Figure 5.4a. (b) The relation between the p -value and significance Z . Figure from Ref. [24].

5.4.2 The CL_s Method and Fit Configuration

The results presented in this thesis use the CL_s method [161] to set upper limits at a 90% confidence level. If the p -value is found below a particular threshold, α , typically $\alpha = 0.05$, but in this case in order to be consistent with other experimental constraints $\alpha = 0.1$, then the value of μ_{sig} is said to be excluded at a confidence level of $1 - \alpha$. The confidence level can be written as either: the probability of being consistent with the *signal+background* hypothesis, $p_{s+b} = p_1$, obtained by setting $\mu_{sig} = 1$, or the probability of being consistent with the *background-only* hypothesis, $p_b = p_0$, obtained by setting $\mu_{sig} = 0$.

Depending on whether one wants to quantify the observation of new physics or set a limit to exclude a signal model, there are two approaches. To quantify an observation of signal, data needs to be inconsistent with the *background-only* hypothesis. To set a limit on the signal, the data needs to be inconsistent with the *signal+background* hypothesis [162]. Therefore, exclusion of a signal is dependent on the confidence level of the signal, CL_s , which can be defined in Equation 5.7 in terms of the confidence level in the *signal+background* hypothesis, CL_{s+b} , and the confidence

level in the *background-only* hypothesis, CL_b . Using 90% confidence levels means the probability of falsely excluding a true signal is less than 10%.

$$CL_s = \frac{CL_{s+b}}{CL_b} = \frac{p_{s+b}}{p_b} \quad (5.7)$$

Histfitter has various fit configurations in order to investigate the *background-only* and *signal+background* hypothesis:

Model-independent fit A model-independent fit compares the background prediction with the expectation from the signal. It measures the significance of any observed excess in the SR, independent of any particular signal model. This fitting procedure uses the *background-only* hypothesis; the purpose of this fit is to set upper limits on the number of events above what is expected in the SR.

Model-dependent fit In the case of no excess in data in the SR, a model-dependent fit is used to set exclusion limits. In the case of excess, the model-dependent fit measures the signal strength. This fitting procedure uses the *signal+background* hypothesis; the purpose of this fit is to study a specific signal model.

This thesis presents two searches for BSM physics in the form of LLPs: the dark photon and the axion-like particle. These searches resulted in the observation of no excess in data, leading to the setting of exclusion limits in the respective parameter space. A model-dependent fit is repeated for each point on a grid of potential signal MC scenarios, assessing the confidence level of each point and therefore probing the phase space of the signal model.

The fit configuration used in both analyses uses a signal region with a single bin. There are no control regions or validation regions used in this configuration. Taking the example of the ALP-W analysis, the signal and background yields are fed into the fit configuration, in addition to the various sources of systematic uncertainty. The experimental systematic uncertainties related to the calorimeter and preshower variables used in the signal selection are correlated between the signal and background samples. The uncertainties due to the MC generation of the signal and neutrino

background are uncorrelated as the uncertainty is derived differently in the two cases. Also included in the fit is the uncertainty due to the limited MC statistics of the samples, and the uncertainty on the luminosity measurement from ATLAS, which is implemented as a measurement uncertainty within the framework. More details on the treatment of systematic uncertainties used in the ALP analysis are given in Chapter 7.4.

Chapter 6

The Search for Dark Photons

This chapter describes FASER’s search for dark photons with 27.0 fb^{-1} of the 2022 Run 3 dataset [1, 163]. This analysis searches for a highly-collimated and highly-energetic electron-positron pair that is characteristic of a dark photon decay within FASER’s decay volume. The search provides sensitivity to dark photons with couplings $4 \times 10^{-6} < \epsilon < 2 \times 10^{-4}$ and with masses $10 \text{ MeV} < m_{A'} < 80 \text{ MeV}$. This is a blinded analysis that uses signal and background yields in the defined signal region.

This chapter will describe: the dataset and signal MC simulation samples used in the analysis; the event selection applied to data and MC in order to identify the dark photon signal; the methods of SM background estimation, including a prediction of the total background processes present in the dataset; the evaluation of the various sources of systematic uncertainties; the statistical interpretation of the results of the analysis. The author contributed to the estimation of the SM background and validation of these estimates using data-driven techniques, and the evaluation of the systematic uncertainties associated with the calorimeter.

6.1 Dataset and Simulation Samples

This analysis uses Run 3 data at a centre of mass energy of $\sqrt{s} = 13.6 \text{ TeV}$ corresponding to an integrated luminosity of 27.0 fb^{-1} collected by the FASER experiment in 2022. The luminosity values are evaluated by the ATLAS Collaboration with an uncertainty of 2.2% [164, 109, 165].

The data used for the dark photon analysis are required to belong to a colliding BCID, pass

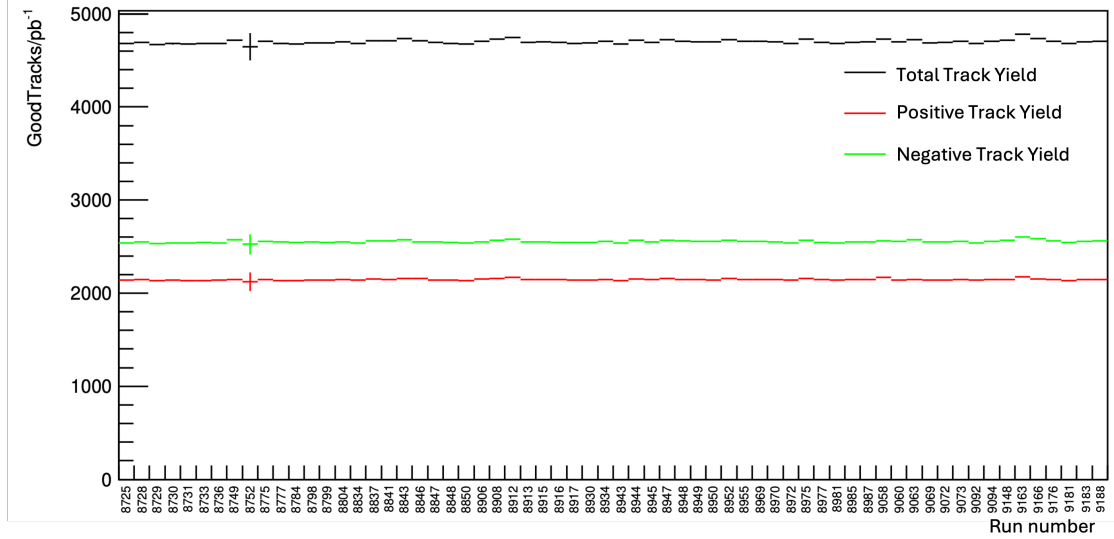


Figure 6.1: Reconstructed good tracks normalised by the corresponding luminosity for the runs used in this analysis. A good track is defined as having a momentum of at least 20 GeV, a χ^2/NDF of less than 25 and at least 12 hits on track within a 95 mm radius once extrapolated back to the scintillator station.

the timing trigger and contain events which have track clusters in all three tracking stations in the spectrometer. In addition, all events must have an EM energy in the calorimeter of at least 100 GeV in order to avoid inefficiency in the calorimeter trigger. Figures 6.1 and 6.2 show the stability of the yields as a function of run number for events with reconstructed good tracks and a calorimeter energy of at least 100 GeV. The yield of events normalised to corresponding luminosity is stable across all data used in this analysis.

The dark photon signal points are generated spanning a 2D parameter space across a range of couplings $\epsilon \sim 10^{-6} - 10^{-4} \text{ GeV}^{-1}$ and with masses $m_{A'} \sim 10 \text{ MeV} - 100 \text{ MeV}$. The modelled parameter space covers the expected region of sensitivity and is shown as a function of mass and coupling in Figure 6.3. The dark photon MC signal samples are modelled in FORESEE [21], the corresponding luminosity varies by signal point on the MC grid but is of the order of several inverse attobarns (ab^{-1}) before it was scaled to a luminosity of 27.0 fb^{-1} and additional simulation samples are used in background estimation and studies of the systematic uncertainties. More details on the simulation of the dark photon signal and background processes are given in Chapter 5.

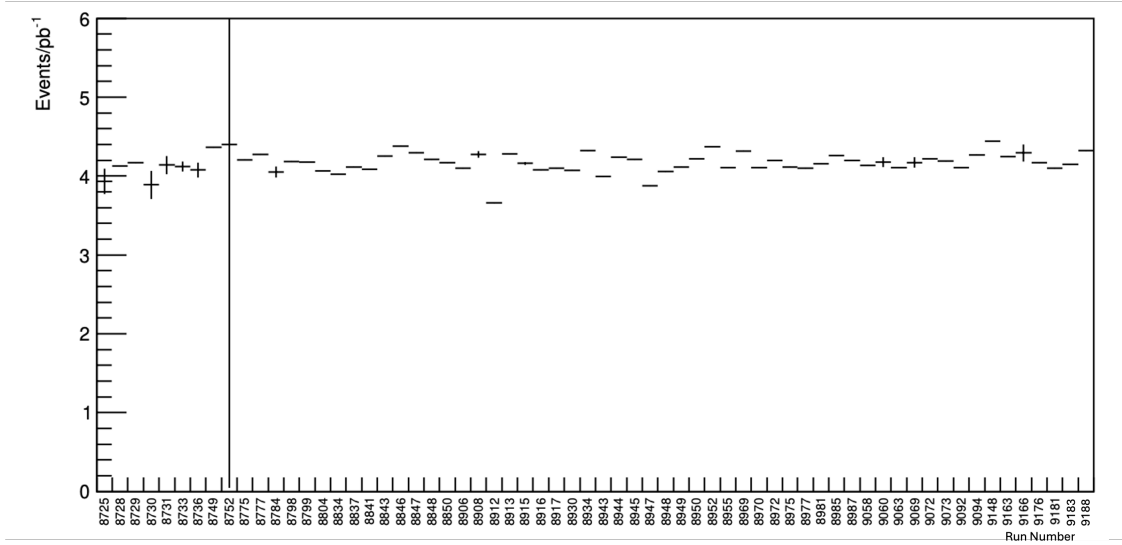


Figure 6.2: Reconstructed events normalised by the corresponding luminosity for the runs used in this analysis. Plot shows the total yield of events with calorimeter energy greater than 100 GeV.

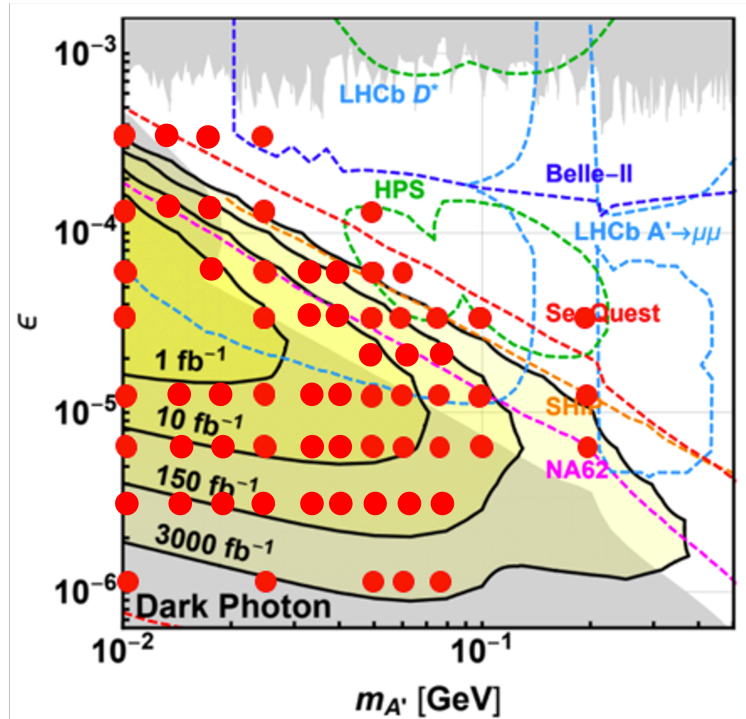


Figure 6.3: Dark photon MC signal points spanning the 2D parameter space as a function of dark photon mass and coupling. Included are existing constraints from previous experiments (grey) and projected sensitivity of future experiments (dashed lines). In yellow is the predicted FASER reach assuming various benchmark amounts of recorded luminosity.

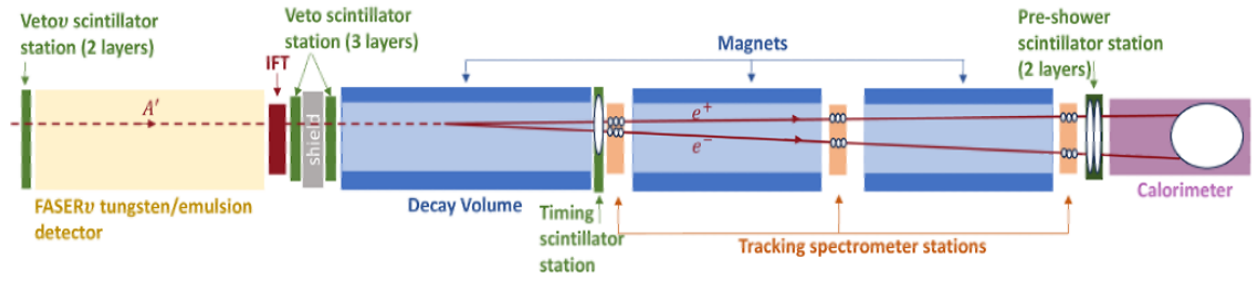


Figure 6.4: A typical dark photon (A') signal event traversing FASER. The neutral A' (dotted line) enters the detector from the left and deposits no charge in any of the veto scintillator stations. It decays within FASER’s decay volume to a highly-energetic e^+e^- pair (dashed lines) which leave charge deposits in the timing scintillator, as well as two tracks within the tracking spectrometer. Energy deposits in the preshower and calorimeter are consistent with an EM shower. Figure from Ref. [1].

6.2 Event Selection

The dark photon signature is shown in Figure 6.4 [1] in which a neutral A' particle enters the detector and deposits no charge in any of the veto scintillator stations. It decays within the FASER decay volume to a highly-energetic e^+e^- pair which leave charge deposits in the timing scintillator as well as two highly-collimated tracks within the tracking spectrometer. In addition, there will be energy deposits in the preshower and calorimeter consistent with an EM shower.

To avoid any bias affecting the outcome of the analysis, a blinding strategy is initially applied to avoid looking at any event with less charge deposited in the veto scintillators than consistent with a MIP, and with more than 100 GeV EM energy deposited in the calorimeter.

The event selection applied to the signal region in this analysis is as follows:

- The event time is consistent with a colliding BCID
- The event passes the timing trigger
- No charge is deposited in any of the five veto scintillator stations
 - Placing a requirement at a threshold of 40 pC is roughly equivalent to half a MIP signal. This requirement removes over 99% of the muon background in this analysis, as shown in Figure 3.10 in Section 3.3.2.
- The charge in the timing scintillators is equivalent to or larger than two MIPs

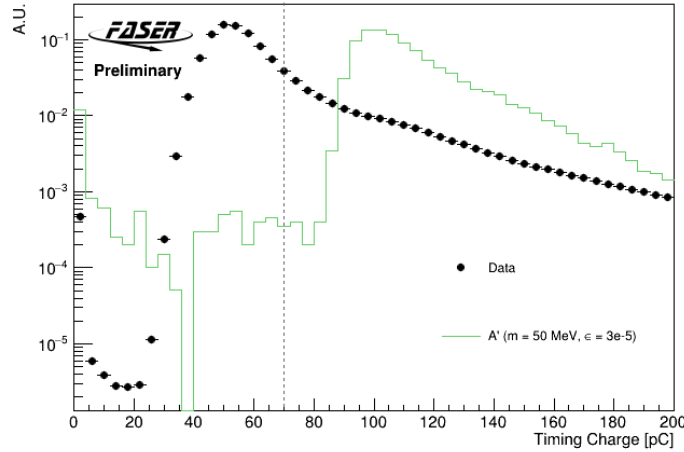


Figure 6.5: Charge deposited in the timing scintillator in data (black), populated mainly by muon events, compared to a representative dark photon MC signal sample (green). The dotted line indicates the 70 pC charge selection used in this analysis.

- Placing a requirement of at least 70 pC deposited in the timing scintillator removes muon events in data whilst retaining dark photon signal, motivation for this requirement is shown in Figure 6.5
- The event has two reconstructed tracks of good quality and opposite charge
 - A good quality track is defined as having a momentum of at least 20 GeV, a χ^2/NDF of less than 25, and at least 12 hits on track
- The event has two fiducial reconstructed tracks throughout the entire tracking spectrometer
 - A track position within a 95 mm radius in all three stations in the tracking spectrometer and extrapolated back to the scintillator stations
- The event has a total calorimeter energy greater than 500 GeV
 - Significant deposits in the calorimeter ensures that events with EM-like behaviour are selected and neutrino background is rejected

Table 6.1 shows the efficiency of each of the selections used in this analysis for two dark photon MC signal points at different mass and coupling in the parameter space. The event selection retains between 40 and 50% of signal events decaying in the decay volume, with the largest inefficiency

Table 6.1: MC cutflow for representative dark photon signal points with mass 25.1 MeV and coupling $\epsilon = 3 \times 10^{-5}$ and mass 50.1 MeV and coupling $\epsilon = 1 \times 10^{-5}$, showing number of signal events entering and passing each selection, along with the efficiency of that selection and the cumulative efficiency to that point. The signal yield is scaled for 27.0 fb^{-1} .

| Selection | Input | Pass | Effic. | Cum. Effic. |
|----------------------------------------------------------|-------|------|--------|-------------|
| $m_{A'} = 25.1 \text{ MeV}, \epsilon = 3 \times 10^{-5}$ | | | | |
| No VetoNu Signal | 95.3 | 95.3 | 100.0% | 100.0% |
| No Veto Signal | 95.3 | 95.0 | 99.7% | 99.7% |
| Timing Signal | 95.0 | 93.3 | 98.2% | 97.9% |
| Preshower Signal | 93.3 | 93.0 | 99.7% | 97.6% |
| ≥ 1 good track | 93.0 | 85.2 | 91.6% | 89.4% |
| $\Rightarrow 2$ good tracks | 85.2 | 52.4 | 61.5% | 55.0% |
| Track Radius $< 95 \text{ mm}$ | 52.4 | 47.6 | 90.9% | 50.0% |
| Calo E $> 500 \text{ GeV}$ | 46.9 | 46.8 | 99.8% | 49.0% |
| $m_{A'} = 50.1 \text{ MeV}, \epsilon = 1 \times 10^{-5}$ | | | | |
| No VetoNu Signal | 16.9 | 16.9 | 100.0% | 100.0% |
| No Veto Signal | 16.9 | 16.8 | 99.8% | 99.8% |
| Timing Signal | 16.8 | 16.5 | 98.1% | 97.9% |
| Preshower Signal | 16.5 | 16.5 | 99.6% | 97.6% |
| ≥ 1 good track | 16.5 | 14.9 | 90.5% | 88.3% |
| $\Rightarrow 2$ good tracks | 14.9 | 8.99 | 60.3% | 53.2% |
| Track radius $< 95 \text{ mm}$ | 8.99 | 8.07 | 89.8% | 47.8% |
| Calo E $> 500 \text{ GeV}$ | 7.39 | 7.26 | 98.2% | 43.0% |

coming from the strict tracking requirements. In order to replicate realistic two-track efficiency, the MC in Table 6.1 would also need to be scaled down by 7% following data-driven estimation of this efficiency, detailed in Section 6.4.2.3.

6.3 Background Estimation

Multiple sources of background that can potentially contaminate the selected signal are described in this section. The largest source of background in this analysis is due to neutrino interactions, followed by background from neutral hadrons that may enter FASER. Muons are a potential source of background, there could be muons that pass the veto scintillator charge requirements due to inefficiency, and large-angle muons that may miss the veto scintillator but still leave a signal in the timing scintillator when they travel through the tracking spectrometer. Other sources of background

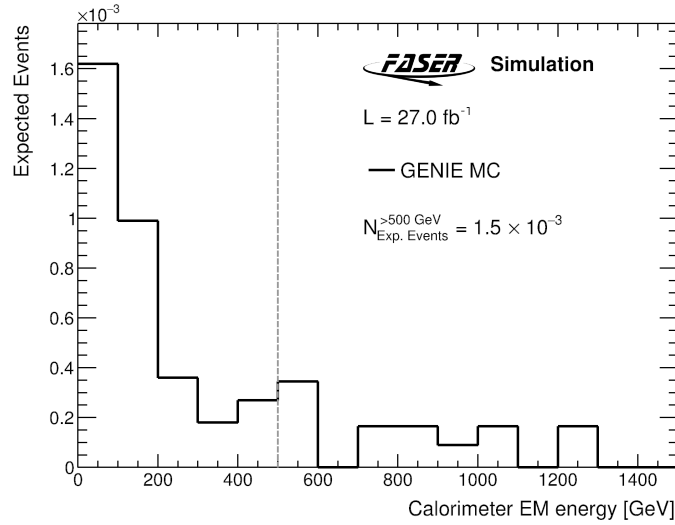


Figure 6.6: The calorimeter EM energy distribution of the GENIE neutrino MC sample after the signal region selections have been applied. The dashed line indicates the calorimeter energy requirement above 500 GeV, above this point there are 1.5×10^{-3} expected neutrino events.

considered are non-collision backgrounds from LHC beam 1 and cosmic-ray interactions.

6.3.1 Neutrino Background

Neutrinos produced upstream of FASER will pass the charge selections placed on the five veto scintillators. In addition, interactions of the neutrinos with detector material downstream of the veto stations can produce charged and neutral particles that may leave tracks in the spectrometer and significant energy deposits in the calorimeter, similar to the dark photon signature. In order to estimate this background, the 300 ab^{-1} MC sample described in Chapter 5 is used. Once scaled to the luminosity of the dataset, 1.5×10^{-3} events passed the signal region selection, consisting of $1.2 \times 10^{-3} \nu_e$ events and $3 \times 10^{-4} \nu_\mu$ events. The uncertainty on the incoming neutrino flux is taken to be 100% for electron neutrinos and 25% for muon neutrinos due to the theoretical uncertainties [1] according to Ref. [157]. An additional 100% uncertainty is applied to account for the effect of uncertainties in the modelling of neutrino interactions in MC, this is a conservative estimate chosen due to known mismodelling. This approach was updated for the ALP analysis, which followed recommendations from Ref. [23] and uses updated MC for neutrino background estimation.

Figure 6.6 shows the calorimeter energy distribution of the neutrino MC sample. The 500 GeV

Table 6.2: Summary of the MC estimate for the neutrino background for 27.0 fb^{-1} in the signal region. Included are uncertainties from flux variations, and those derived from MC statistics, respectively. The total estimate is $(1.5 \pm 1.9(\text{syst.})) \pm 0.5(\text{stat.}) \times 10^3$ events.

| Signal Region | |
|---------------|---------------------------------------------------------|
| ν_e | 0.0012 |
| ν_μ | 0.0003 |
| Total | $(1.5 \pm 1.9 \pm 0.5) \times 10^{-3}$ |
| Total | $(1.5 \pm 2.0) \times 10^{-3}$ (130%) |

requirement used in the event selection is indicated by the dashed line, chosen to reject the majority of this background whilst keeping significant dark photon signal. An almost negligible amount of very high energy neutrino interactions are capable of passing the selections applied in this analysis. Due to the requirement of a large EM shower in FASER’s ECAL, more electron neutrinos are expected in the signal region than muon neutrinos. The total neutrino background estimate, in terms of neutrino type and with sources of systematic and statistical error, is presented in Table 6.2.

6.3.2 Neutral Hadrons

Neutral hadrons could be a possible source of background in this analysis if the parent muon of a neutral hadron passes through the veto scintillator system undetected and goes on to decay to particles producing two charged particles that leave tracks in the spectrometer and deposit a significant amount of calorimeter energy, mimicking an e^+e^- pair in the detector. This type of background is highly suppressed by a number of factors: the parent muon must be stopped or scattered before reaching the VetoNu scintillator, otherwise the event would be discarded as muon signal; the neutral hadron would have to travel through the eight interaction lengths that make up the FASER ν emulsion detector; the decay products would have to have very high calorimeter energy.

In order to investigate the fraction of neutral hadron events that do produce this signal-like topology and deposit at least 500 GeV in the calorimeter, a three-track control region is used. This is due to low statistics in the case of signal-like two-track events.

Three-track events are studied where a parent muon enters FASER, interacts to produce a neutral hadron which then decays to two daughter particles. The ratio of events with a calorimeter

Table 6.3: Summary of the neutral hadron estimate method targeting two and three-track events.

| Selection | Nevents $E < 100$ GeV | Nevents $E > 500$ GeV |
|-----------------------------|-----------------------|-----------------------|
| 3 tracks (VetoNu signal) | 404 | 19 |
| 2 tracks (No VetoNu signal) | 1 | Predicted: 0.047 |

energy below 100 GeV to the number of events with a calorimeter energy above 500 GeV is used to scale the number of events with two reconstructed tracks at low energy ($E < 100$ GeV), where the parent muon does not enter the detector, in order to estimate the expected number of such two-track events originating from neutral hadrons in the signal region ($E > 500$ GeV).

To further improve statistics in the low-energy two-track control region, the veto scintillator requirements used in the main analysis are relaxed such that no signal is required in VetoNu but no requirements are placed on the other Veto scintillators.

A large fraction of three-track events are made up of photon conversions, which must be removed from the dataset. This is achieved by placing a requirement on the E/p ratio, the calorimeter energy divided by the z -momentum of the two lowest momentum tracks. A requirement of $E/p < 0.7$ separates the hadrons from the conversion events. After the removal of these photon conversion events, the number of three-track events is 404 and 19 in the low and high calorimeter energy bins, as shown in Table 6.3. This ratio of 19/404 is used to scale the 1 event in the low energy two-track region to the high energy signal-like region, resulting in a prediction of 0.047 neutral hadron events in this region. Further scaling to obtain the actual signal region estimate must be performed to account for the relaxed requirement on the veto scintillators. The fraction of 3-track events in which 1 track goes through the veto system is 0.0184. This results in a final neutral hadron estimate in the signal region of $(0.8 \pm 1.2) \times 10^{-3}$ events. An uncertainty of 100% comes from the single event in the low-energy 2-track control region. The additional uncertainty is due to the uncertainty associated with assumptions made in this method.

6.3.3 Inefficiency of the Veto Scintillators

The expected number of muons crossing through the FASER volume in the dataset considered for this analysis is of the order of 10^8 . The efficiency of the five individual veto scintillators is described in Chapter 3.3.2 and is greater than 99.99%, resulting in a combined inefficiency of 10^{-27} . The

Table 6.4: Cutflow for large-angle muon background in the case of a veto signal (top) and no veto signal (bottom).

| Selection | Input | Pass | Effic. | Cum. Effic. |
|----------------------|--------|--------|--------|-------------|
| Veto Signal | | | | |
| No timing saturation | 800000 | 799877 | 99.9% | 99.9% |
| Veto/VetoNu Signal | 799877 | 195651 | 24.5% | 24.5% |
| Timing Signal | 195651 | 24946 | 12.8% | 3.12% |
| Preshower Signal | 24946 | 9878 | 39.6% | 1.24% |
| ≥ 1 good track | 9878 | 1258 | 12.7% | 0.157% |
| $= 2$ good tracks | 1258 | 0 | 0.00% | 0.00% |
| No Veto Signal | | | | |
| No timing saturation | 800000 | 799877 | 99.9% | 99.9% |
| No VetoNu Signal | 799877 | 655829 | 81.9% | 82.0% |
| No Veto Signal | 655829 | 604226 | 92.1% | 75.5% |
| Timing Signal | 604226 | 26519 | 4.39% | 3.32% |
| Preshower Signal | 26519 | 8893 | 33.5% | 1.11% |
| ≥ 1 good track | 8893 | 96 | 1.08% | 0.012% |
| $= 2$ good tracks | 96 | 0 | 0.000% | 0.00% |

expected background of muons crossing FASER without being vetoed by any of the scintillator stations is therefore below 10^{-18} , showing this component of background to be negligible.

6.3.4 Large-angle Muons

As discussed above, one of the potential sources of background arises from muons coming from the IP that miss the veto stations but still enter FASER, depositing charge in the timing scintillator and tracks in the spectrometer. Such muons with an angle of around 40 mrad can miss both veto scintillator stations.

Dedicated MC samples are used to confirm that there is no component of background arising from large-angle muons. The resulting sample consists of 800k muons and is described in Chapter 5.3.2, of which no events have two good tracks either with or without a veto signal, see Table 6.4. When requiring no veto signal, only 96 events have even 1 track with none passing the fiducial requirements. Before any signal selection requirements, the reconstructed calorimeter energy spectrum shows no events above 50 GeV, suggesting that the background from large-angle muons is negligible.

To avoid relying on an approach based on purely MC prediction, a data-driven method conventionally referred to as an ABCD method, can be used to validate the estimation of large-angle muon background. The ABCD method [166] relies on the assumption that the distribution of background events can be factorised in the plane of two uncorrelated variables so that it is divided into four regions: A (the signal region, SR), B, C, and D (control regions, CRs). The number of background events in the SR can be evaluated as $N_A = N_C \times N_B/N_D$. To define the various regions, the two variables used are the calorimeter EM energy and the requirement that there is or is not a signal in the veto stations above 40 pC.

Data events categorised in both the signal region and control regions defined in Figure 6.7 are selected with the following requirements:

- Preshower signal selection: The charge in each preshower layer > 2.5 pC
- At least one good track (1+ track) selection
- Timing signal selection: The signal in the timing scintillator is consistent with 1 MIP

The ABCD plane is defined considering a 1+ good track selection rather than a 2-track selection as in the final analysis, this is to overcome a substantial lack in statistics in the control regions. In addition, events are required to have a track with extrapolated radius at the first veto station greater than 90 mm, and extrapolated track angles θ_X and θ_Y at veto station 1 greater than 10 mrad. Such strict requirements on track angle and radius lead to selected events with a deposited energy in the calorimeter that is most likely to be equivalent to what would be expected from the background muon events of interest, whilst excluding regions populated by other sources of background.

The ABCD plane is divided to include intermediate regions to be used as validation regions (A^* , B^*). In this case, given that the Veto signal/No Veto signal variable cannot be split, additional regions are defined in terms of the calorimeter EM energy.

Events in the “No Signal in Veto Station” (SR A, VR A^* , CR C in Figure 6.7), are referred to as NoVeto and are required to pass the No VetoNu signal and No Veto signal selections defined in the event selection for this analysis. On the other hand, events in the “Signal in Veto Station” (SR B, VR B^* , CR D in Figure 6.7) are referred as Veto and are required to have charges in all veto stations > 40 pC.

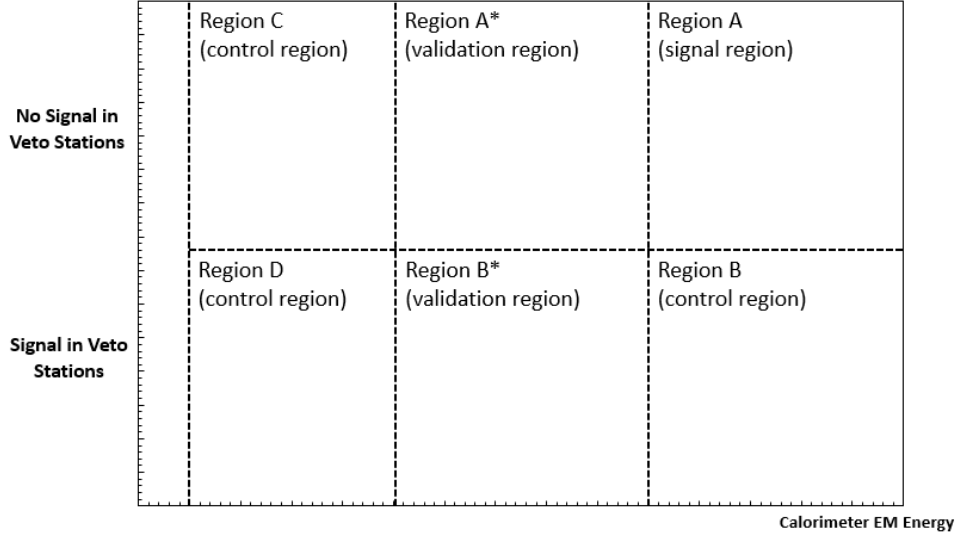


Figure 6.7: The ABCD background estimation method showing the control regions, validation regions and signal regions used to validate the large-angle muon estimate in the dark photon analysis.

The basic assumption that motivates the use of the VetoNu and Veto scintillator charge as variables in this method is that a muon that misses the veto stations but still creates a signal-like topology will resemble a signal which is within FASER's acceptance and does not fire the veto stations.

Multiple thresholds are used to define regions in term of the calorimeter EM energy that are considered as control and validation regions following the logic below:

- The range 10-25 GeV is used to define the initial control regions C and D;
- The range 25-50 GeV is first used as validation region and then merged to be used as a control region in the range 10-50 GeV (initial validation regions A* and B*);
- The range 50-100 GeV is first used as validation region and then merged to be used as a control region in the range 10-100 GeV (extended validation regions A* and B*);
- The range 100-500 GeV is used as a validation region post-unblinding and then merged to be used as a control region

Table 6.5 shows the number of events for each of the regions considered above before any scaling. The statistical uncertainty of the prediction will be driven by the statistics of the Veto

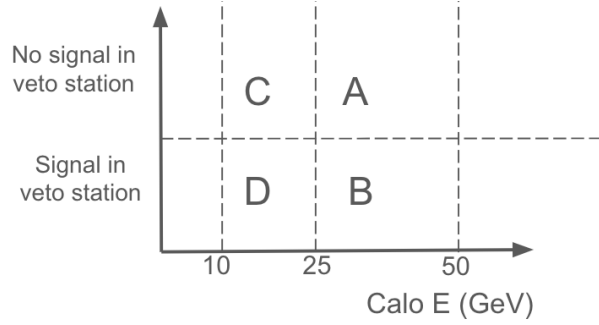


Figure 6.8: An example of the regions considered for the ABCD configuration carried out in the first entry in Table 6.6.

region corresponding to the same energy range of the SR. As there is only 1 event in this region, the uncertainty is 100%¹. It is still useful to calculate the various cases and compare the predictions obtained depending on the range used for the control regions C and D.

The scaling from the 1+ to the 2-track selection used in the main event selection is evaluated by scaling the ABCD-method prediction by the ratio between the number of events found in a Veto-region with EM energy between 10-50 GeV and two tracks, and the yields in the 1+ Veto region in the same EM energy range. The 2-track selection is the same as in the signal region of this analysis, but it also requires that at least one track has radius above 90 mm and angle greater than 10 mrad.

The scaling factor for 1+ to 2-track selection is calculated by dividing the 3 events in the corresponding 2-track Veto region by the 798 events in the 10-50 GeV 1+ track Veto region. Resulting in a scaling factor of 0.00376.

Table 6.6 shows the expected and observed yields for various signal-like regions (25-50, 50-100 and 100-500 GeV) and the signal region, calculated either using the lowest ranges for C, D regions, or using an intermediate or extended validation region that incorporates the previous one(s). Figure 6.8 shows an example sketch of regions used in the first line of Table 6.6. This table shows the calculated predictions after scaling has been applied.

The predicted number of events for the fully unblinded validation region, taken as the one with calorimeter EM energy between 25 and 50 GeV, is 3.2 ± 0.5 , compared with 1 observed event. For the following range (50-100 GeV), the prediction for the fully unblinded validation region is between

¹Asymmetric errors calculated according to the Clopper-Pearson approach [167] for small numbers of events were considered, however, a more conservative symmetric approach was chosen for this validation method.

Table 6.5: Event yields in the various regions. Note: number of events as found using a 30 pC charge requirement for a single track.

| Regions | Energy Range | | | | |
|---------|--------------|-----------|------------|-------------|----------|
| | 10-25 GeV | 25-50 GeV | 50-100 GeV | 100-500 GeV | 500 GeV |
| NoVeto | 31 | 1 | 0 | 0 | 0 |
| Veto | 724 | 74 | 2 | 1 | 1 |

Table 6.6: Calculations and predictions for intermediate validation regions and for the final signal regions. In the former case, various ranges are used as test. For the SR, only the integrated 10-500 GeV region is used for the predictions. The uncertainty in 100% due to the Veto region in the range 100-500 GeV having only 1 event. **Post-unblinding**: in bold, the observed events (0) in both validation and signal regions.

| ABCD region/method | Predicted | Observed |
|------------------------------------------------------------------------------------------|-----------------|----------|
| $N_{25-50,noVeto} = N_{25-50,Veto} \times \frac{N_{10-25,NoVeto}}{N_{10-25,Veto}}$ | 3.2 ± 0.5 | 1 |
| $N_{50-100,noVeto} = N_{50-100,Veto} \times \frac{N_{10-25,NoVeto}}{N_{10-25,Veto}}$ | 0.09 ± 0.06 | 0 |
| $N_{50-100,noVeto} = N_{50-100,Veto} \times \frac{N_{25-50,NoVeto}}{N_{25-50,Veto}}$ | 0.03 ± 0.02 | 0 |
| $N_{50-100,noVeto} = N_{50-100,Veto} \times \frac{N_{10-50,NoVeto}}{N_{10-50,Veto}}$ | 0.08 ± 0.06 | 0 |
| $N_{100-500,noVeto} = N_{100-500,Veto} \times \frac{N_{10-25,NoVeto}}{N_{10-25,Veto}}$ | 0.04 ± 0.04 | 0 |
| $N_{100-500,noVeto} = N_{100-500,Veto} \times \frac{N_{25-50,NoVeto}}{N_{25-50,Veto}}$ | 0.01 ± 0.01 | 0 |
| $N_{100-500,noVeto} = N_{100-500,Veto} \times \frac{N_{10-50,NoVeto}}{N_{10-50,Veto}}$ | 0.04 ± 0.04 | 0 |
| $N_{100-500,noVeto} = N_{100-500,Veto} \times \frac{N_{50-100,NoVeto}}{N_{50-100,Veto}}$ | 0 | 0 |
| $N_{100-500,noVeto} = N_{100-500,Veto} \times \frac{N_{10-100,NoVeto}}{N_{10-100,Veto}}$ | 0.04 ± 0.04 | 0 |

0.03 ± 0.02 and 0.09 ± 0.06 , depending on the regions taken as control regions. This is consistent with the observation of no events. The predictions for the 100-500 GeV region is 0.04 ± 0.04 . The same prediction is found for the SR when considering the whole range below 100 GeV as regions C and D: this can be considered a conservative upper bound for this source of background.

The background prediction for the 2-track signal region therefore takes the control region prediction of 0.04 and scales it to 1.5×10^{-4} , with an uncertainty up to 100%. This is consistent with the above estimation from MC, therefore, this study can be used to validate the above method of estimation and confirm that this source of background is negligible.

6.3.5 Non-collision Backgrounds

Due to FASER's location in TI12, background can arise due to interactions of the nearby LHC beam. In addition, despite being 100 m underground, the interactions of cosmic ray muons must

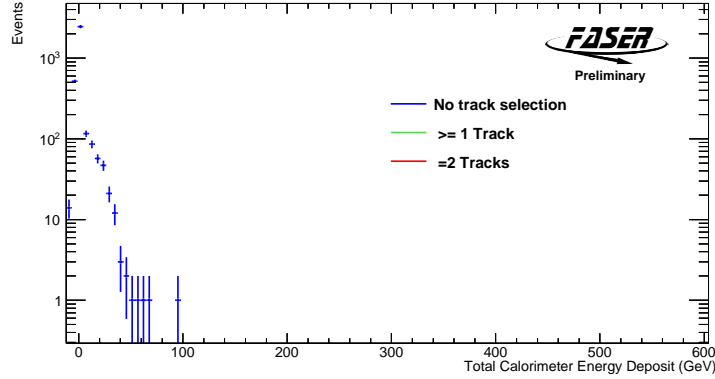


Figure 6.9: The calorimeter energy distribution of cosmic muon events with various track requirements. Zero events with tracks survive selections. No events survive the requirement of at least one good track.

be considered. The following sections demonstrate that all non-collision background is negligible in this analysis.

6.3.5.1 Background due to cosmic ray muons

Most high-energy cosmic ray muons will have been absorbed by the surrounding rock and concrete before reaching FASER, however, it is possible that these particles could survive the selections used in this analysis. Cosmic ray muon events are recorded during time with no beam in the LHC to ensure no physics events are collected. The cosmic ray data is collected over a period that is roughly equivalent to the length of physics data-taking used in this analysis, around 300 hours. In the collected cosmic ray dataset, no events with a good track were found. In addition, Figure 6.9 shows that none of the events without a track had a calorimeter energy deposit greater than 100 GeV or had any tracks, and so are far removed from the signal region for the dark photon analysis. This cosmic ray background can therefore be considered negligible.

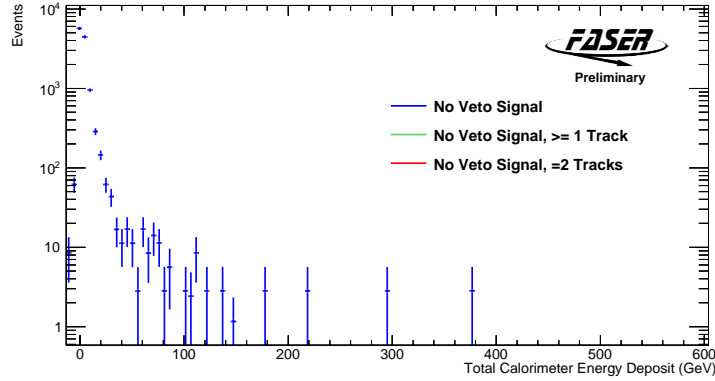


Figure 6.10: The calorimeter energy distribution of beam 1 background events with various track requirements. Zero events with tracks survive the veto scintillator selection.

6.3.5.2 Beam 1 Background

Background from LHC beam 1 is the result of secondary particles produced when beam 1, passing FASER towards the ATLAS IP, interacts with beampipe material, such as an LHC quadrupole magnet located close to FASER. The data to evaluate this background is collected by taking events with colliding BCIDs that overlap with BCID timings of the inbound LHC beam 1 passing FASER.

Figure 6.10 shows that none of the events that survive the veto scintillator selection have at least one good track. Furthermore, zero of these events without tracks have a calorimeter energy above 400 GeV. Therefore, this component of background can be considered negligible.

6.3.6 Summary of Total Expected Background

A summary of the total background estimate in this analysis is shown in Table 6.7. Components from large-angle muons, inefficiencies from the veto scintillators, and non-collision backgrounds are considered to be negligible. Therefore, the background estimate in the signal region is due to neutral hadrons and interactions from neutrinos. When combined, the total background estimate is $(2.3 \pm 2.3) \times 10^{-3}$ (100%).

Table 6.7: Summary of the different sources of background considered in this analysis and the total estimate, with uncertainty.

| Source | Background | Uncertainty |
|---------------------------|----------------------------------------|-----------------------------------------------|
| Neutrino | 1.5×10^{-3} | 2.0×10^{-3} (130%) |
| Neutral Hadrons | 0.8×10^{-3} | 1.2×10^{-3} (140%) |
| Veto Inefficiency | 0 | 0 |
| Large-angle Muons | 0 | 0 |
| Non-collision Backgrounds | 0 | 0 |
| Total | 2.3×10^{-3} | 2.3×10^{-3} (100%) |

6.4 Systematic Uncertainties

This section describes the various sources of systematic uncertainties that are relevant to the signal. The systematic uncertainties in this analysis are related to the signal yield, rather than shape uncertainty. These systematic uncertainties are implemented as nuisance parameters in the model-dependent fit performed in the statistical interpretation of the results of this analysis, this is discussed in Chapter 5.4.1. The main sources of systematic uncertainty are categorised into theory and experimental uncertainties. The theory uncertainty is the uncertainty associated with the MC generators used to simulate signal and background processes. The experimental uncertainties include those which arise due to MC modelling, tracking efficiency and measurement uncertainties. There is also a statistical uncertainty derived from MC statistics, calculated from the standard deviation of the sum of the weights of each MC sample.

6.4.1 Signal Theory Uncertainties

Theory uncertainties arise due to the systematic uncertainties from the differences in the MC generator predictions used to simulate the signal in this analysis. The systematic uncertainty associated with the generation of the dark photon signal is derived by comparing the signal yields from the central MC prediction provided by the EPOS-LHC generator with the signal yields from QGSJET and SIBYLL. The envelope provides an uncertainty on the number of signal events and also on the uncertainty on the signal prediction due to the modelling of the cutoff in transverse momentum for dark bremsstrahlung with the different generators. Such uncertainty on the signal

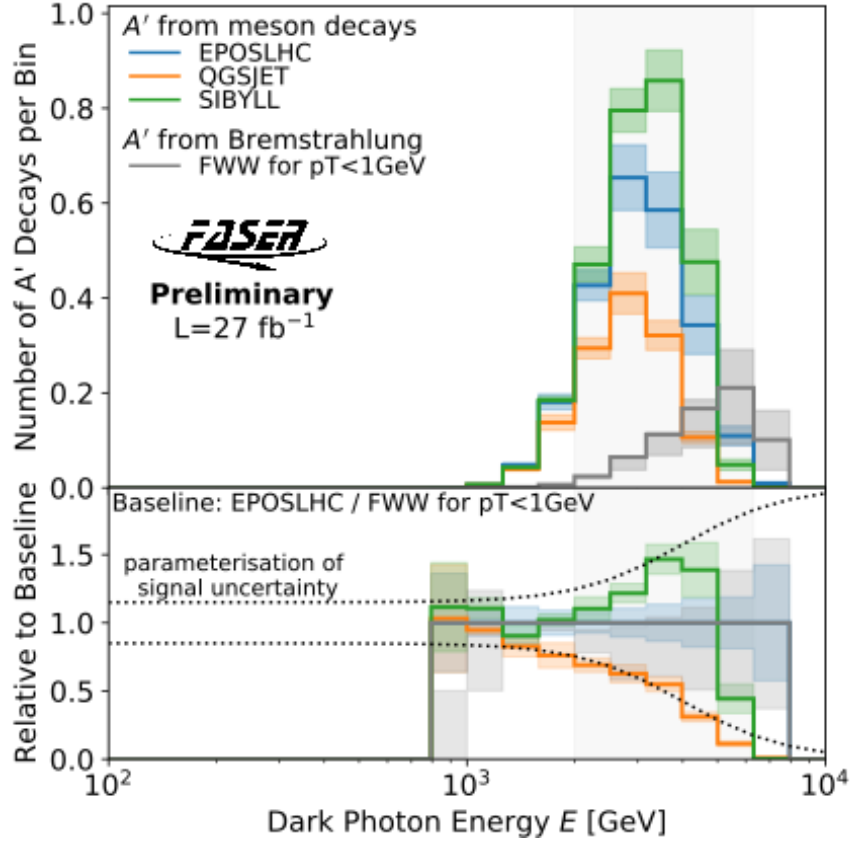


Figure 6.11: The energy spectrum of a dark photon signal with mass 50 MeV and coupling $\epsilon = 3 \times 10^{-5}$ produced in meson decays whose production is modelled by the EPOS-LHC (blue), QGSJET (orange) and SIBYLL (green) generators. The production due to bremsstrahlung is shown in grey, with a factor of two variation in the p_T cutoff. The bottom panel shows the ratio of the different generator estimates with the parameterisation of the uncertainty as a function of signal energy. Figure from Ref. [1].

is parameterised as:

$$\frac{\Delta N}{N} = \frac{0.15 + (E_{A'}/4 \text{ TeV})^3}{1 + (E_{A'}/4 \text{ TeV})^3}, \quad (6.1)$$

where $E_{A'}$ is the energy of the dark photon. Figure 6.11 [1] shows the energy spectrum of a dark photon with mass 50 MeV and coupling $\epsilon = 3 \times 10^{-5}$ produced in meson decays whose production is modelled by the three different generators. The production due to bremsstrahlung is shown, with a factor of two variation in the p_T cutoff. The parameterisation of this uncertainty has been tested for signal samples encompassing the entire phase space that is relevant to this analysis.

6.4.2 Experimental Uncertainties

The experimental uncertainties in this analysis are the systematic uncertainties related to the modelling of the detector response in MC simulation. This includes the uncertainty associated with the scintillators, the calorimeter and the tracker. Another experimental uncertainty is the 2.2% uncertainty on the luminosity measurement from ATLAS [164, 109].

6.4.2.1 Scintillator Systematic Uncertainty

The systematic uncertainties associated with the veto scintillators are considered negligible due to the almost 100% efficiency of the five individual scintillator layers upstream of the decay volume.

In order to evaluate the systematic uncertainty associated with the remaining scintillators (timing scintillator and preshower scintillators), the fraction of two-track events that are rejected by the requirements on these scintillators is measured. The timing and preshower scintillator efficiencies were found to be greater than 99.7% in both data and MC. The effect on the signal yield is less than 1%, therefore, it is not necessary to place an uncertainty on these scintillator charge requirements.

6.4.2.2 Calorimeter Systematic Uncertainty

The uncertainty associated with the threshold applied to the EM calorimeter energy as part of the event selection in this analysis is calculated from the individual uncertainties in the various stages of the energy calibration process, for both data and MC. Uncertainties arise from the MIP MPV Landau fit, the PMT HV gain dependence, the drift in the PMTs over time, the corrections in data and MC calibration, the difference in the average calibrated energy in test beam data and MC, and other components from energy loss at the calorimeter module edges and position dependence. A breakdown of all of these measured uncertainties, which result in the total uncertainty associated with the calorimeter, are shown in Table A.1 in Appendix A.2. The total uncertainty associated with the calorimeter energy measurement is estimated to be 6%.

The uncertainty on the calorimeter energy selection is validated in TI12 data by comparing the calorimeter response in data and FLUKA MC in the case of photon conversion events. Photon conversions are isolated from three-track high-energy muon events in which the muon traverses FASER and the resulting photon converts to a e^+e^- pair. The ratio E/p of photon conversions

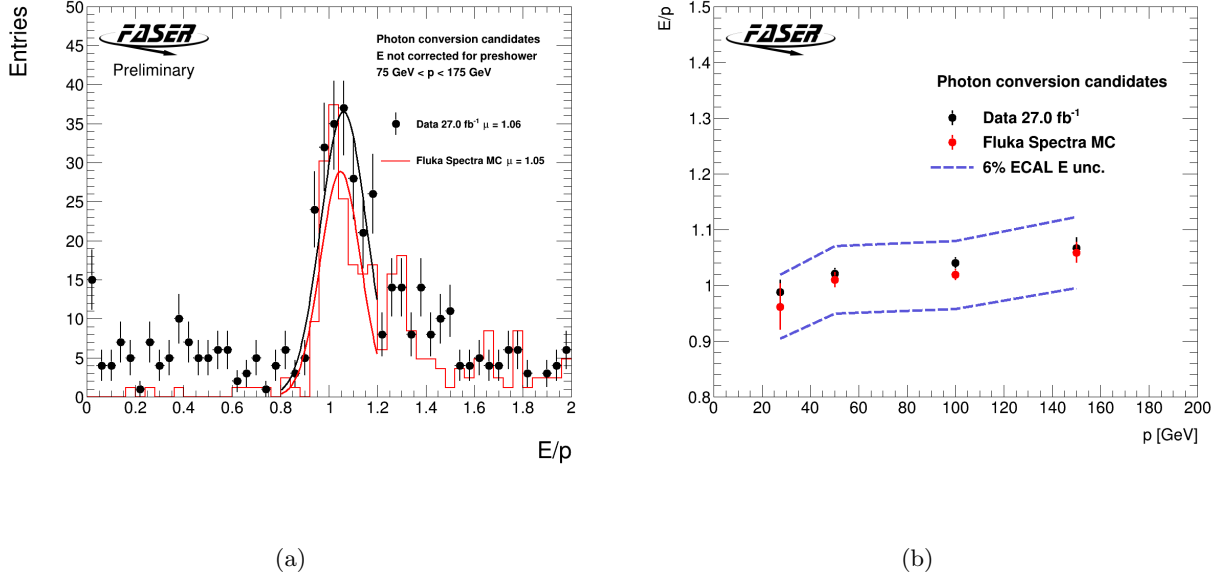


Figure 6.12: (a) The E/p distribution for photon conversion events with $75 \text{ GeV} < p < 175 \text{ GeV}$ for data and FLUKA MC. (b) The fitted E/p peak values for various momentum ranges: $20 \text{ GeV} < p < 30 \text{ GeV}$, $35 \text{ GeV} < p < 75 \text{ GeV}$, $75 \text{ GeV} < p < 125 \text{ GeV}$, $125 \text{ GeV} < p < 175 \text{ GeV}$. The E/p ratio is centred around one, and the agreement between data and MC is well within the 6.06% uncertainty across the momentum range.

is measured in data and compared to MC, where E is the EM energy in the calorimeter, and p is the measured track momentum of these e^+e^- candidates. The selection applied in order to isolate these photon conversion events in data is as follows:

- Require 3 good tracks
- Require that the two lowest momentum tracks were oppositely charged (to target e^+e^- events)
- Require a ratio in the preshower scintillator layers of greater than 2 (removes 90% of non-conversion events with $E/p < 0.5$)

Ideally, the E/p distribution should be centred around one, indicating that the selection correctly targets EM events, and that the calorimeter calibration is as expected. The relative difference in the E/p ratio in data and MC is well within the 6% uncertainty across a range of track momentum, this is shown in Figure 6.12.

6.4.2.3 Tracking Systematic Uncertainty

The uncertainty associated with single-track efficiency is evaluated by investigating events with at least one good track segment in each of the spectrometer's three tracking stations. Comparing the single-track efficiency in data and MC leads to an uncertainty of 1.5% per track.

The process of reconstructing tracks in two-track events is more complex, particularly in the case of two closely-spaced tracks, as is likely given the dark photon decay. It is possible that tracks from different events could share common hits in the tracking stations making reconstruction difficult. To measure the uncertainty associated with the reconstruction of two-track events, the raw strip data from two high momentum single track events is overlaid to mimic a reconstructed closely-spaced two-track event. This mimics signal-like events with real data and this process can be carried out in MC with single muon events for direct comparison. Since the single tracks in the individual events can be reconstructed by definition, additional inefficiency is due to the two track environment. The reconstruction efficiency as a function of track separation in data and MC is shown in Figure 6.13. The ratio of the efficiency between data and MC, as a function of the distance between the two tracks, is used to assess the uncertainty. At track separations equivalent to what is expected in a typical dark photon decay, the efficiency in data is up to 7% less than in MC simulation. A 7% correction is, therefore, applied to the two-track reconstruction efficiency, and this value is taken as the overall uncertainty.

The uncertainty associated with the momentum resolution and momentum scale is estimated with a conservative assumption of 5% uncertainty. By comparing the mass peak in photon conversion events in data and MC, a shift of 5% more than accounts for the difference in the position of the photon conversion peak in data and MC. The shift in the mass peak and resolution due to a 5% and 10% smearing of the momentum in MC, compared to data is shown in Table 6.8. It can therefore be concluded that this conservative uncertainty of 5% is sufficient for both track momentum resolution and track momentum scale.

6.4.3 A Summary of Systematic Uncertainties

A comprehensive overview of the various sources of systematic uncertainty in the search for dark photons is given in Table 6.9. The effect of each systematic uncertainty on the signal yield is shown,

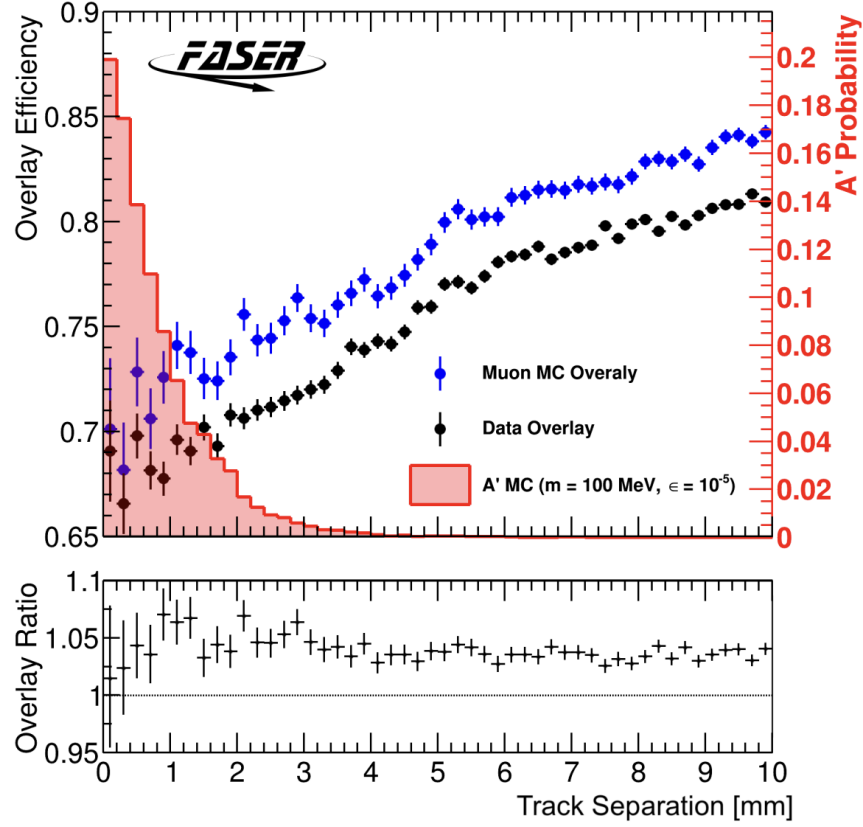


Figure 6.13: Top panel: The two track reconstruction efficiency as a function of track separation for single, overlaid tracks in both data and FLUKA MC. Shown in red is the track separation of e^+e^- tracks in a representative A' signal sample. Bottom panel: The ratio of the reconstruction efficiency of these overlaid events in data and MC.

Table 6.8: Summary of the track scale, and resolution variations in MC and compared to data.

| Sample | Scale | Resolution |
|--------------------|-----------------|------------------|
| | Mass peak (MeV) | Peak width (MeV) |
| Data | 503 | 51 |
| MC | 514 | 39 |
| MC (5% variation) | 489 | 57 |
| MC (10% variation) | 463 | 88 |

Table 6.9: Summary of the various sources of signal uncertainty, the size of the uncertainty and the range of the effect of this uncertainty on the signal yield across the parameter space. For the latter, the numbers in parenthesis indicate the effect on signals in the new exclusion reach with this analysis. The error on the MC statistics is calculated using the standard deviation of the sum of the weights (W) of each sample. The systematic uncertainty is dominated by the uncertainty on the signal generators.

| Source | Value | Effect on signal yield |
|---------------------------|----------------------------------------------------------------|------------------------|
| A' Signal Generator | $\frac{0.15+(E_{A'}/4\text{TeV})^3}{1+(E_{A'}/4\text{TeV})^3}$ | 15-65% (15-45%) |
| Luminosity | 2.2% | 2.2% |
| MC Statistics | $\sqrt{\sum W^2}$ | 1-3% (1-2%) |
| Single track efficiency | 3% | 3% |
| Two-track efficiency | 7% | 7% |
| Track Momentum Scale | 5% | <5% |
| Track Momentum Resolution | 5% | <5% |
| Calorimeter Energy scale | 6% | 0-8% (<1%) |

the dominant source of systematic uncertainty is the parameterised uncertainty associated with the dark photon signal event generator.

6.5 Results

Once the signal efficiency and background estimates with uncertainties were evaluated, data were unblinded and no events were found to pass the event selection. This is consistent with the total expected background of 2.3×10^{-3} events expected in the signal region, with an uncertainty of 100%. Figure 6.14 shows the calorimeter energy distribution of events with at least one track, with no selection applied to data (left) and the case where the veto scintillator charge requirement of <40 pC is applied (right). This selection drastically reduces the number of data events, and comparison with three representative A' MC signal points demonstrates that the energy of the data events that survive the selection is far below the signal region. Figure 6.15 shows the same distribution in data but with the application of all signal region selections, including the two-track requirement.

Since no events are observed in the signal region, exclusion limits on FASER's sensitivity to this model can be set. The statistical interpretation of the results produces the exclusion limit shown in Figure 6.16. The HistFitter framework used to produce this limits plot is discussed in Chapter 5. The results are shown at a 90% confidence level [161], in accordance with previous searches

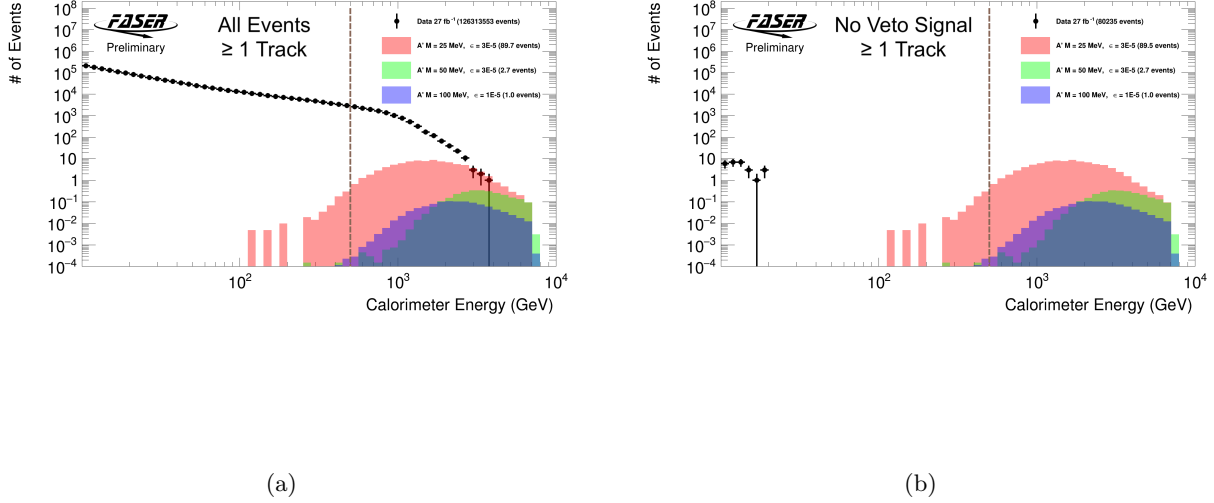


Figure 6.14: Calorimeter EM energy distributions showing three representative A' signal samples with (a) all data events with at least one good track (b) data events with at least one good track which also survive the veto scintillator selections outlined in the selection.

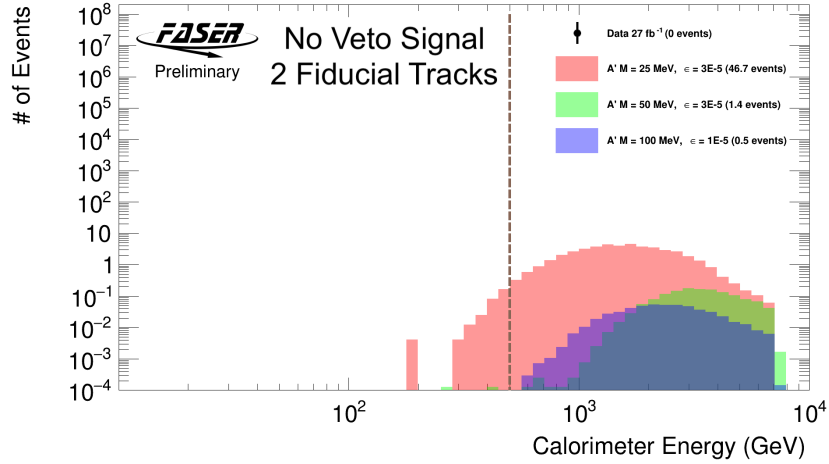


Figure 6.15: Calorimeter EM energy distributions showing three representative A' signal samples showing data events with 2 good tracks that pass all the signal selections. Zero events survive these requirements.

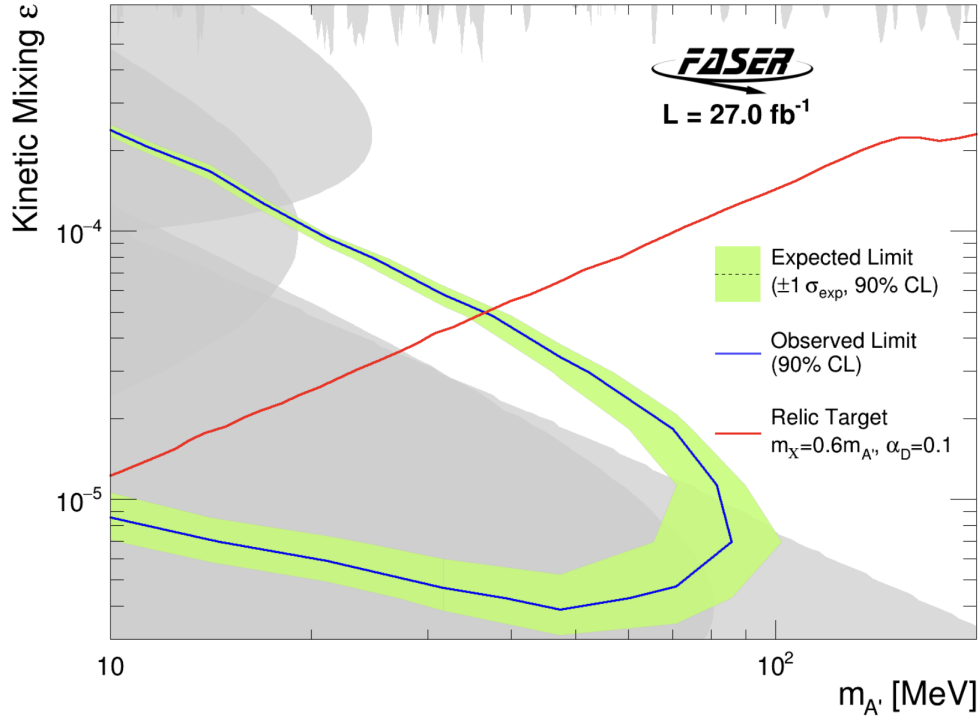


Figure 6.16: Interpretation of the signal region yield as A' exclusion limits with the assumption of 2×10^{-3} background events and zero data events. The expected limit with 90% CL is shown by the dashed line and yellow uncertainty band. The observed limit is shown by the blue line. Existing constraints are shown in grey. The thermal relic density target is shown in red,

performed by other experiments with sensitivity in the same parameter space. The grey regions indicate previous constraints, the details of which are given in Chapter 2. In the dark photon parameter space that is probed by this analysis, signal models with mass $10 \text{ MeV} < m_{A'} < 80 \text{ MeV}$ and coupling $4 \times 10^{-6} < \epsilon < 2 \times 10^{-4}$ are excluded. World-leading constraints are set by FASER for signal models in the mass range $17\text{--}70 \text{ MeV}$ and coupling $2 \times 10^{-5} - 1 \times 10^{-4}$. This can be seen in the region of Figure 6.16 where no previous limits have been set. Of particular interest in this dark photon search is the thermal relic density probed; the contour, indicated by the red line in Figure 6.16, is obtained by assuming a mass ratio of $m_{\chi}/m_{A'} = 0.6$ between the dark matter candidate and the dark photon, leading the dark photon in this model to decay to SM final states. The thermal relic density is discussed further in Chapter 2; the region below the contour would be populated by an over-abundance of dark matter and thus is ruled out cosmologically. FASER, therefore, probes a significant amount of phase space in this cosmologically-allowed region [1].

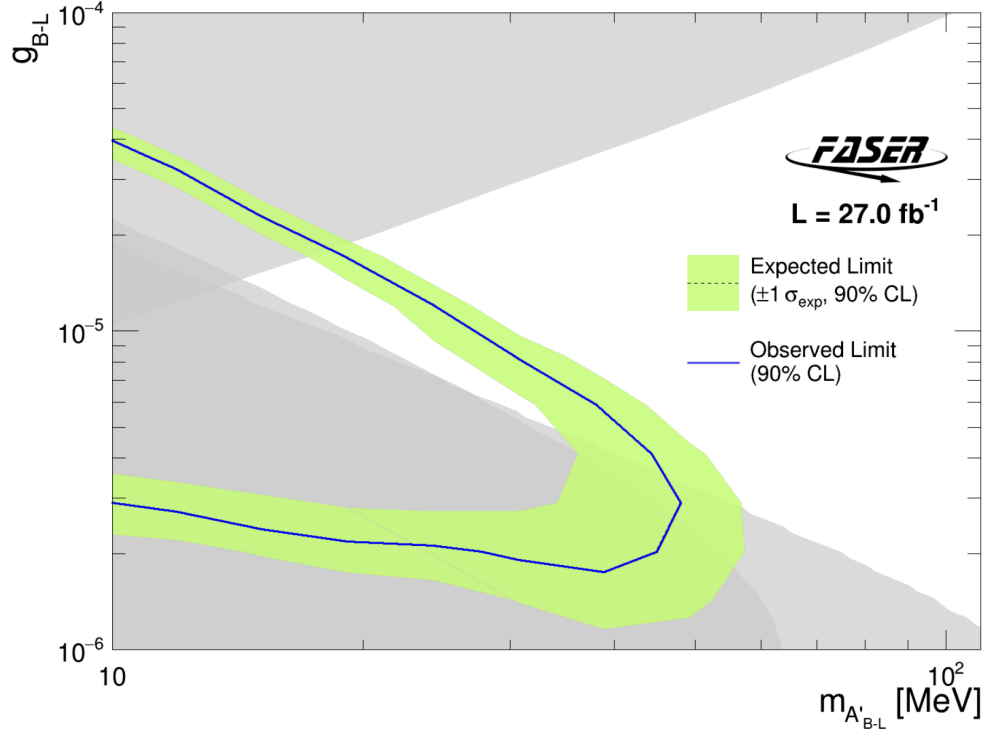


Figure 6.17: Interpretation of the signal region yield as $B - L$ gauge boson exclusion limits. The expected limit with 90% CL is shown by the dashed line and green uncertainty band. The observed limit is shown by the blue line. Existing constraints are shown in grey.

6.5.1 Reinterpretation: The $B - L$ Gauge Boson

The dark photon analysis can be reinterpreted for the $B - L$ gauge boson [7], a well-motivated model that is similar to the dark photon, linked to the SM with a local $U(1)_{B-L}$ gauge symmetry [1]. The contour from evaluating the CLs values at a 90% confidence level for the $B - L$ gauge boson model is shown in Figure 6.17. The analysis probes unconstrained parameter space in the region of $B - L$ gauge boson mass around $m_{A'_{B-L}} \sim 15 - 40$ MeV and coupling $g_{B-L} \sim 5 \times 10^{-6} - 2 \times 10^{-5}$.

Chapter 7

The Search for Axion-like Particles

This chapter describes FASER’s search for axion-like particles with 57.7 fb^{-1} of the 2022 and 2023 Run 3 dataset. This analysis searches for a highly energetic di-photon signal characteristic of an ALP decay within FASER’s decay volume. The parameter space explored in this analysis includes ALPs with couplings $g_{aWW} \sim 10^{-5} - 10^{-3} \text{ GeV}^{-1}$ and masses $m_a \sim 60 \text{ MeV} - 500 \text{ MeV}$. This analysis has been optimised for the ALP-W signal model, described in Chapter 2. This is a blinded analysis that uses signal and background yields in the defined signal region.

This chapter will describe: the dataset and signal MC simulation samples used in the analysis; the event selection applied to data and MC in order to identify the ALP signal; the methods of SM background estimation, including a prediction of the total background processes present in the dataset; the evaluation of various systematic uncertainties; the statistical interpretation of the results of the analysis. The author led analysis efforts, covering numerous aspects including the definition and optimisation of the signal selection, the estimation of the SM background using both MC and data-driven approaches, the estimation of signal systematic uncertainties related to the MC generation, the estimation of the experimental systematic uncertainties related to the calorimeter, and the statistical interpretation of the final results.

7.1 Dataset and Simulation Samples

This analysis uses Run 3 data at a centre of mass energy of $\sqrt{s} = 13.6 \text{ TeV}$ corresponding to an integrated luminosity of 57.7 fb^{-1} collected by the FASER experiment during 2022 and 2023

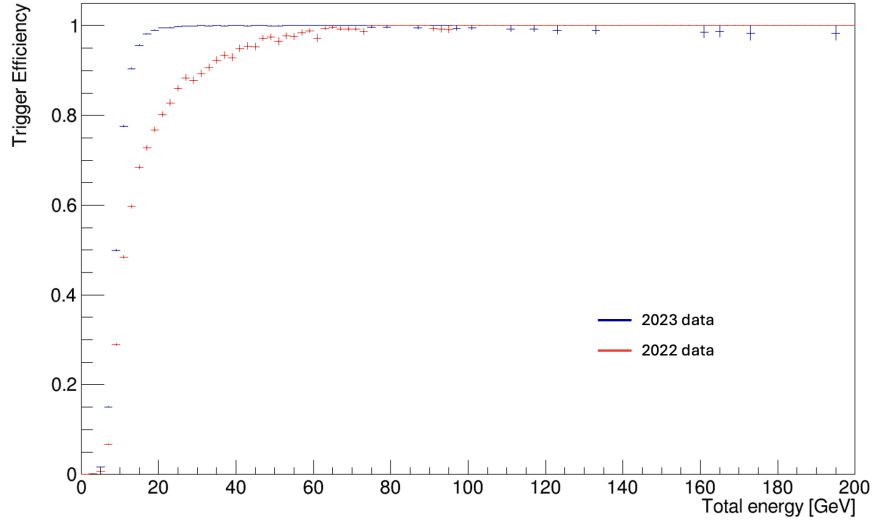


Figure 7.1: Calorimeter trigger efficiency in 2022 vs 2023 data. The calo turn-on curve vs total energy for a large run in 2022 (red) and 2023 (blue).

physics running. The 2022 ALP dataset contains an additional run compared to the A' dataset, this is due to a slight change in the determination of recorded luminosity, which pushed a single run above the 10 pb^{-1} data quality threshold. The luminosity values are taken from ATLAS, this has an associated uncertainty of 2.2% [164, 109, 165], for 2022 and an uncertainty of 2.04% in the 2023 dataset. This is a small uncertainty compared to other systematic uncertainties associated with the signal (see Chapter 7.4), it therefore has a small impact on the final results.

An important note on the differences in the 2022 and 2023 dataset is the change in calorimeter trigger efficiency turn-on. There is a clear improvement in the 2023 data due to better trigger timing of the calorimeter, resulting in fewer late triggers and a much improved trigger efficiency. This is illustrated in Figure 7.1. It can be seen that the trigger efficiency has no impact above 100 GeV, where both the 2022 and 2023 datasets have very high (close to 100%) trigger efficiency. As part of data quality checks, and to confirm that the data and luminosity have been reconstructed correctly in the offline processing, the number of events per run that pass the calo trigger (see Table 3.3) and are in a colliding BCID, with at least 100 GeV in the calorimeter for the 2022 and 2023 dataset are studied. Figures 7.2 and 7.3 show the number of events per unit luminosity for each run that passes these data quality requirements for 2022 and 2023, respectively. The yield plots show a stable data yield within 15% for both 2022 and 2023 datasets.

It is required that data is recorded during periods in which the LHC is running in stable beams.

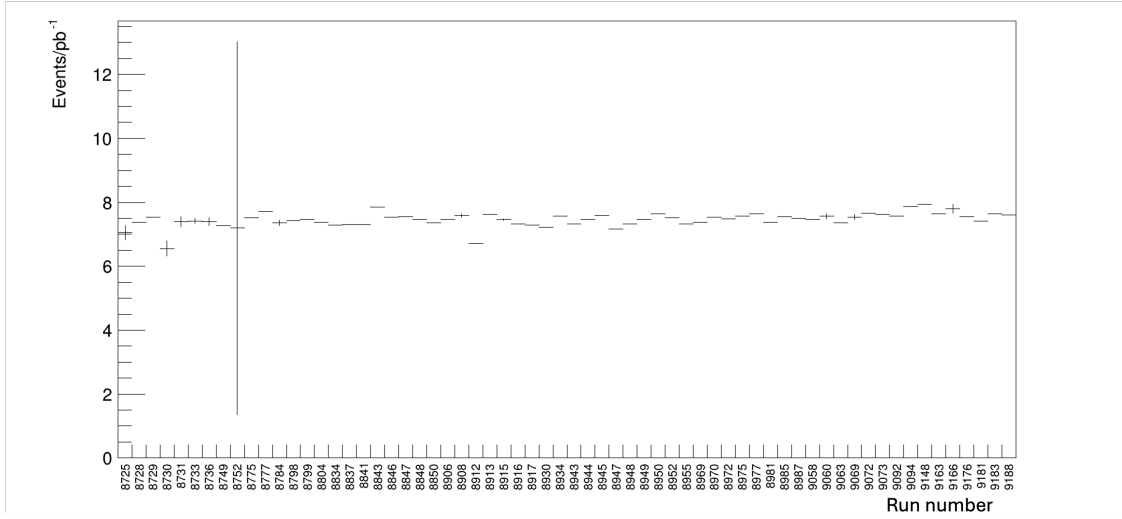


Figure 7.2: Reconstructed events per unit luminosity that pass data quality requirements in the 2022 dataset. Plot shows the total yield of events with calorimeter energy greater than 100 GeV. The large error band seen in run 8752 is due to low statistics for this run (10.3 pb^{-1} recorded).

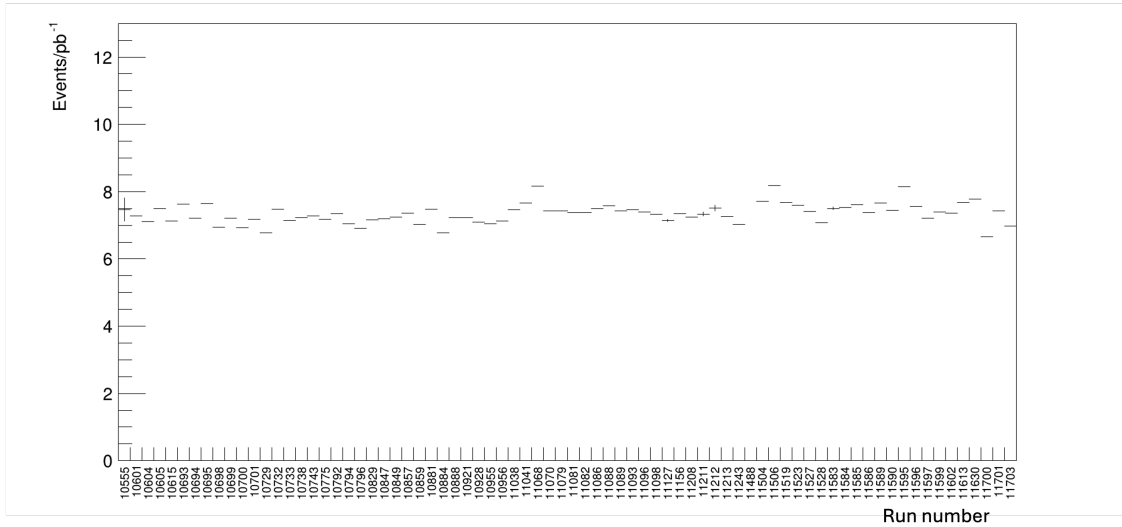


Figure 7.3: Reconstructed events per unit luminosity that pass data quality requirements in the 2023 dataset. Plot shows the total yield of events with calorimeter energy greater than 100 GeV.

Table 7.1: Requirements on data to target physics events and ensure good quality data.

| Selection | Description |
|--------------------|-----------------------------------------------------------------------|
| Stable Beams | Require period of stable beam delivered to LHC |
| Excluded Times | Remove time regions with potential issues |
| Colliding BCID | Event corresponds to a colliding bunch |
| Calo Trigger | Triggers the calorimeter |
| Calorimeter Timing | Timing in the calorimeter between $> -5\text{ns}$ and $< 10\text{ns}$ |

The removal of certain time regions is performed for a number of reasons. Notable to this dataset are periods when ATLAS stopped their physics running and so did not report the delivered luminosity to FASER. An excluded times criteria is also applied to two runs during which FASER experienced operational issues related to storage space for raw data. As stated above, for data quality purposes, events are required to belong to a colliding BCID and to pass the calo trigger. In addition, the timing in each calorimeter module with respect to the expected bunch collision time is required to be larger than -5ns and smaller than 10ns in order to remove non-collision background. This requirement has no impact on physics signal, but removes non-collision background from beam 1 with 100% efficiency. Motivation for this requirement can be seen in Figure 7.20 in Section 7.3.5.2. A summary of all requirements applied to data to ensure good quality physics events are targeted is shown in Table 7.1.

The ALP-W signal points are generated spanning a 2D parameter space across a range of couplings $g_{aWW} \sim 10^{-5} - 10^{-3} \text{ GeV}^{-1}$ and masses $m_a \sim 60 \text{ MeV} - 500 \text{ MeV}$. The modelled parameter space covers the expected region of sensitivity and is shown as a function of mass and coupling in Figure 7.4. The grey regions indicate previous constraints, the details of which are given in Chapter 2. The ALP MC signal samples are modelled in FORESEE and scaled points generated in FORESEE and scaled to 57.7 fb^{-1} . Additional simulation samples are used in background estimation and studies of the systematic uncertainties, more details are given in Chapter 5.

7.2 Event Selection

A typical ALP signature is shown in Figure 7.5 [3] in which a neutral ALP particle enters the detector and deposits no charge in any of the veto scintillator stations. It decays within the FASER

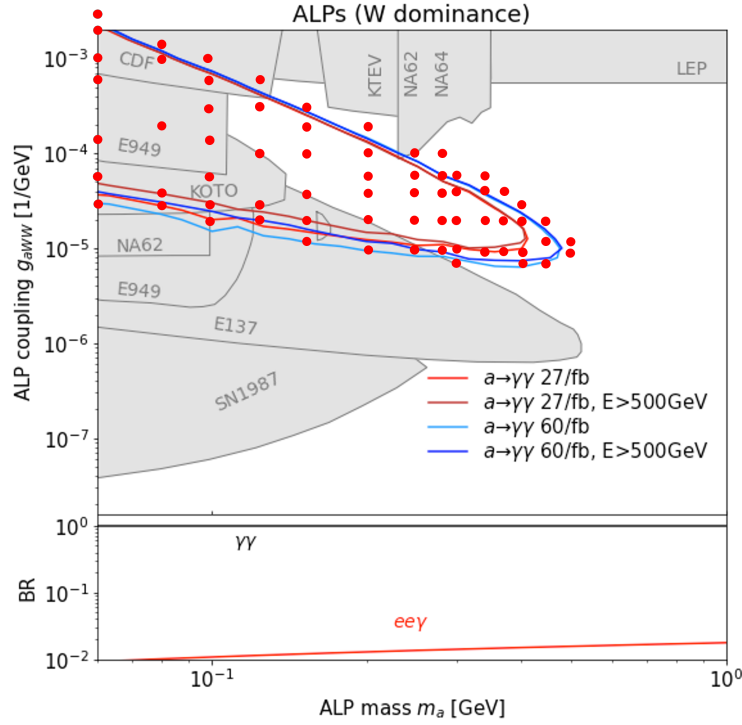


Figure 7.4: ALP-W signal points generated across the parameter space that FASER is sensitive to. Previous limits set by existing experiments are indicated in grey. The projected expected limits in red and blue were produced for 27 fb^{-1} , which is equivalent to the dataset used in the dark photon analysis, and 60 fb^{-1} , which was the initial prediction for the combined 2022 and 2023 dataset used in the ALP search, and close to the final 57.7 fb^{-1} that was recorded. These projections are shown for a zero-background case with a 500 GeV calorimeter energy selection. This is not the case for this analysis, which has a non-zero background expectation and applies a stricter calorimeter energy requirement.

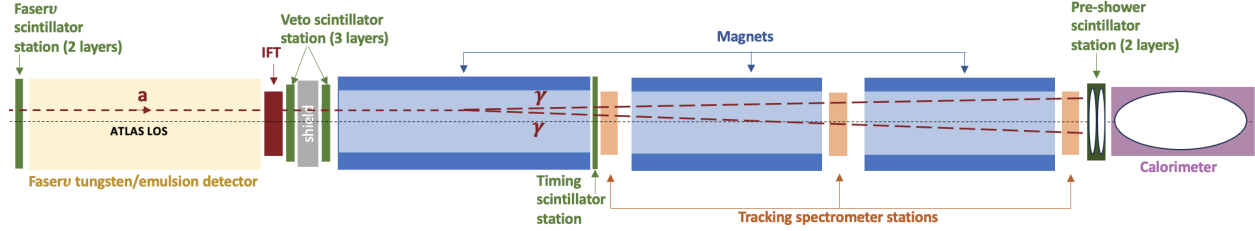


Figure 7.5: A typical ALP signal event traversing FASER. The neutral ALP (dotted line) enters the detector from the left and deposits no charge in any of the veto scintillator stations. It decays within FASER’s decay volume to two highly energetic photons (dashed lines) which also do not leave any charge deposits in the timing scintillator. However, energy deposits will be seen in both preshower layers and in the calorimeter, as the EM shower develops. Figure from Ref. [3].

decay volume to a highly-energetic di-photon pair, depositing no charge in the timing scintillator but significant deposits in the preshower and calorimeter consistent with an EM shower. The dominant background in this analysis is high energy neutrinos, variables related to the preshower station are vital to distinguish ALP signal with neutrino background.

To avoid any bias affecting the outcome of the analysis, a blinding strategy is initially applied to avoid looking at any event with the equivalent of less than a MIP deposited in each of the veto scintillators, and with more than 100 GeV EM energy deposited in the calorimeter. During the analysis, in order to validate background predictions, this was relaxed to 500 GeV calorimeter energy.

The event selection applied to the signal region in this analysis, in addition to the data quality requirements already discussed and defined in Table 7.1, is as follows:

- No charge is deposited in any of the five veto scintillator stations
 - Placing a requirement at a threshold of 40 pC is roughly equivalent to half a MIP signal. This requirement removes over 99% of the muon background in this analysis
- No charge is deposited in the timing scintillator
 - In the absence of tracking variable selections in this analysis, the decision was made to place a requirement that less than 20 pC charge is deposited in the timing scintillator station that sits at the beginning of FASER’s tracking spectrometer. The idea is that any event depositing more than 20 pC at this stage is very likely to be a charged muon or similar unwanted background. A selection at 20 pC lies below the expected MIP signal,

as shown in Figure 7.6a for the 2022 data and Figure 7.6b for the 2023 data. Specifically, it is required that the raw charge deposit in the top scintillator layer and the bottom scintillator layer be less than 20 pC

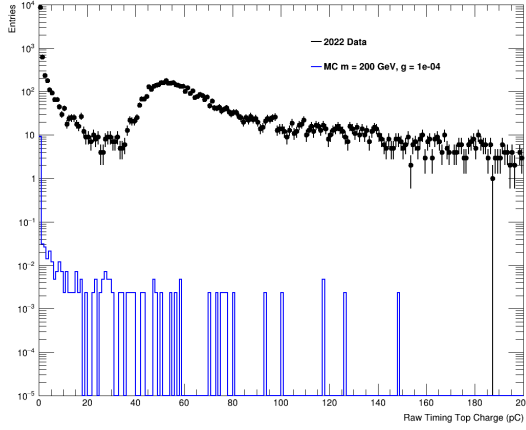
- The event has a ratio of charge deposited in the second and first preshower layers that is greater than 4.5 (PS ratio > 4.5)
 - The preshower detector plays an important role in distinguishing between the photon signatures of the ALP and any potential background. The ratio of charge deposited in the preshower layers is used to target the EM behaviour in the preshower
- The event has greater than the equivalent of 10 MIP signals deposited in the second preshower layer (PS1 nMIP > 10)
 - ALP signal events have large deposits in the second preshower layer (PS 1) relative to the first layer (PS 0), as a result of the showering photons
- The event has a total calorimeter energy greater than 1.5 TeV
 - The ALP signal is expected to have very large deposits in the calorimeter, as shown in Figure 7.7, significant deposits in the calorimeter also ensures that events with EM-like behaviour are selected and neutrino background is rejected

The ALP event selection is summarised in Table 7.2. Table 7.3 shows two MC ALP signal points at different mass and coupling in the parameter space and the efficiency of each of the selections used in this analysis. The same cutflow is shown in Table 7.4 for the neutrino background MC prediction.

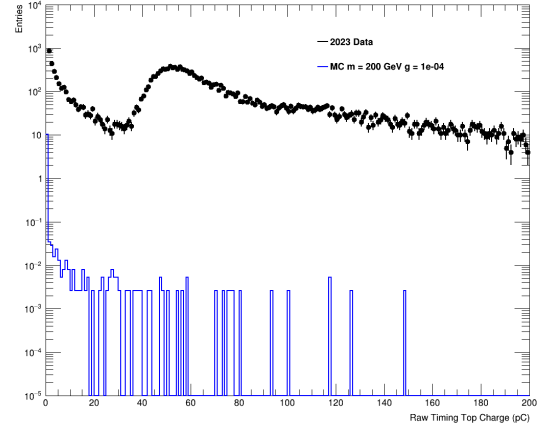
Initial signal optimisation studies were done to investigate the significance of applying a selection to the calorimeter EM energy. The definition of significance (Z) used in these studies is given by:

$$Z = \frac{s}{\sqrt{b + \sigma_b^2}}, \quad (7.1)$$

where s is the number of signal events, b is the corresponding number of background events, σ_b is the uncertainty associated with the background (studies were done for 20%, 50% and 100% background uncertainty). This form of significance was chosen in preliminary investigations before any

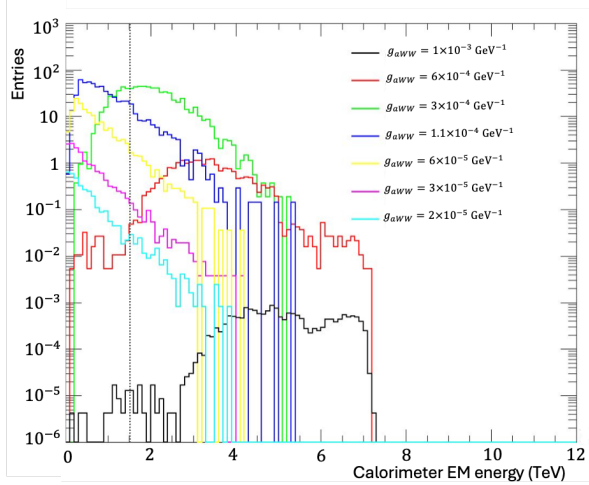


(a)

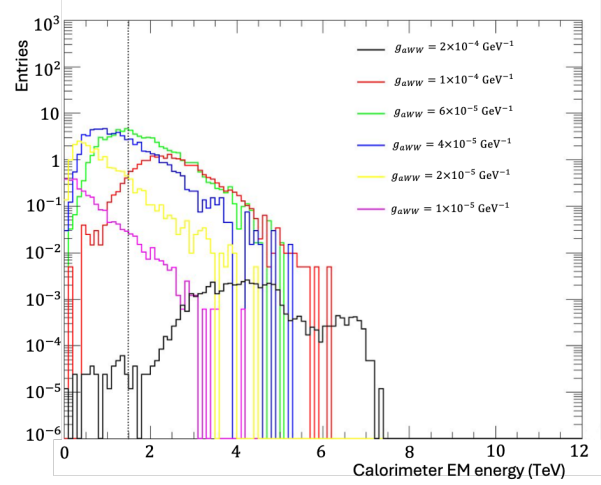


(b)

Figure 7.6: Charge deposited in the top timing scintillator layer. Comparison between data (black) and a representative ALP signal point (blue) with mass 200 GeV and coupling 1×10^{-4} . Shown for (a) the 2022 dataset and (b) the 2023 dataset.



(a)



(b)

Figure 7.7: Calorimeter EM energy distributions for ALP signal models with (a) $m_a = 100$ MeV (b) $m_a = 200$ MeV for a range of different couplings. The calorimeter EM energy threshold of 1.5 TeV is indicated by the dashed line.

Table 7.2: Event selection for the ALPs analysis signal region.

| Selection | Description |
|-----------------------|---------------------------------------------|
| Baseline Selection | |
| Veto Signal < 40 pC | Veto and VetoNu Scintillator Charge < 40 pC |
| Timing Signal < 20 pC | Timing Scintillator Charge < 20 pC |
| Signal Region | |
| PS Ratio > 4.5 | Preshower Ratio (Layer 1/Layer 0) > 4.5 |
| PS1 nMIP > 10 | Preshower Layer 1 nMIP > 10 |
| Calo E > 1.5 TeV | Calorimeter EM energy > 1500 GeV |

Table 7.3: MC cutflow for representative ALP-W signal points with mass 120 MeV and coupling $g_{aWW} = 3 \times 10^{-4} \text{ GeV}^{-1}$ and mass 100 MeV and coupling $g_{aWW} = 6 \times 10^{-5} \text{ GeV}^{-1}$, showing number of signal events entering and passing each selection, along with the efficiency and the cumulative efficiency to that point. The signal yield is scaled for 57.7 fb^{-1} .

| Selection | Input | Pass | Effic. | Cum. Effic. |
|----------------------------------------------------------------------|-------|-------|--------|-------------|
| $m_a = 120 \text{ MeV}, g_{aWW} = 3 \times 10^{-4} \text{ GeV}^{-1}$ | | | | |
| Veto Signal < 40 pC | 115.7 | 115.4 | 99.7% | 99.7% |
| Timing Signal < 20 pC | 115.4 | 111.1 | 96.2% | 96.0% |
| PS Ratio > 4.5 | 111.1 | 94.4 | 85.0% | 81.6% |
| PS1 nMIP > 10 | 94.4 | 93.4 | 98.9% | 80.7% |
| Calo E > 1.5 TeV | 93.4 | 88.3 | 94.5% | 76.3% |
| $m_a = 100 \text{ MeV}, g_{aWW} = 6 \times 10^{-5} \text{ GeV}^{-1}$ | | | | |
| Veto Signal < 40 pC | 147.8 | 147.6 | 99.9% | 99.9% |
| Timing Signal < 20 pC | 147.6 | 144.8 | 98.1% | 97.9% |
| PS Ratio > 4.5 | 144.8 | 114.4 | 79.0% | 77.4% |
| PS1 nMIP > 10 | 114.4 | 108.3 | 94.7% | 73.3% |
| Calo E > 1.5 TeV | 108.3 | 8.72 | 8.09% | 5.90% |

Table 7.4: MC cutflow for the neutrino background MC prediction. The background yield is scaled for 57.7 fb^{-1} .

| Selection | Input | Pass | Effic. | Cum. Effic. |
|-----------------------|---------|--------|--------|-------------------------|
| Veto Signal < 40 pC | 16075.9 | 7478.0 | 46.5% | 46.5% |
| Timing Signal < 20 pC | 7478.0 | 5060.1 | 67.7% | 31.5% |
| PS Ratio > 4.5 | 5060.1 | 278.4 | 5.50% | 1.73% |
| PS1 nMIP > 10 | 278.4 | 84.5 | 30.4% | 0.526% |
| Calo E > 1.5 TeV | 84.5 | 0.415 | 0.491% | $2.58 \times 10^{-3}\%$ |

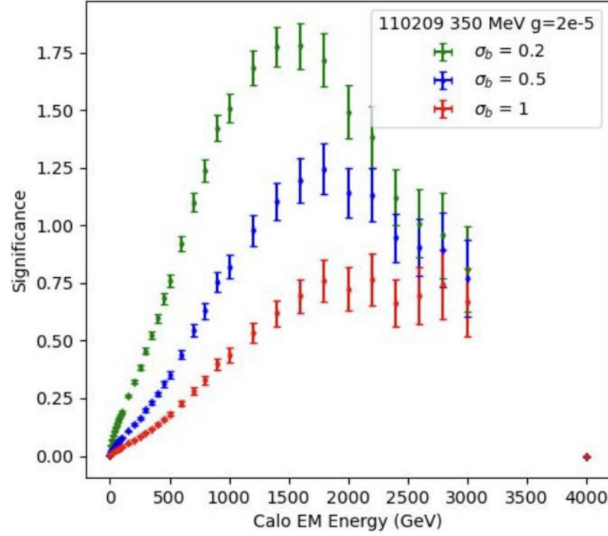


Figure 7.8: Significance studies on initial ALP-W signal sample. The significance of selections on the calorimeter EM energy (left) assuming 100% (red), 50% (blue) and 20% (green) background uncertainty. For two different ALP MC samples.

background estimation, to give initial indications of useful energy values for a selection. The distribution is shown for an ALP signal sample in Figure 7.8 for three values of background uncertainty. These studies motivated the decision to place a strict requirement on the calorimeter EM energy. Motivations for the preshower selections are discussed in the next section (see Chapter 7.3.1) where ALP signal MC is compared to neutrino background MC, defined in terms of where in FASER the neutrino interactions take place.

7.3 Background Estimation

Multiple sources of background that can potentially contaminate the selected signal are described in this section. The primary source of background in this analysis is due to neutrino produced upstream of FASER and further neutrino interactions in the FASER volume. Also considered are large-angle muons that could miss the FASER veto scintillators, the component of background that may arise due to inefficiency of the veto scintillators themselves, and interactions of neutral hadrons. Beam-related background and background from cosmic rays are also taken into consideration.

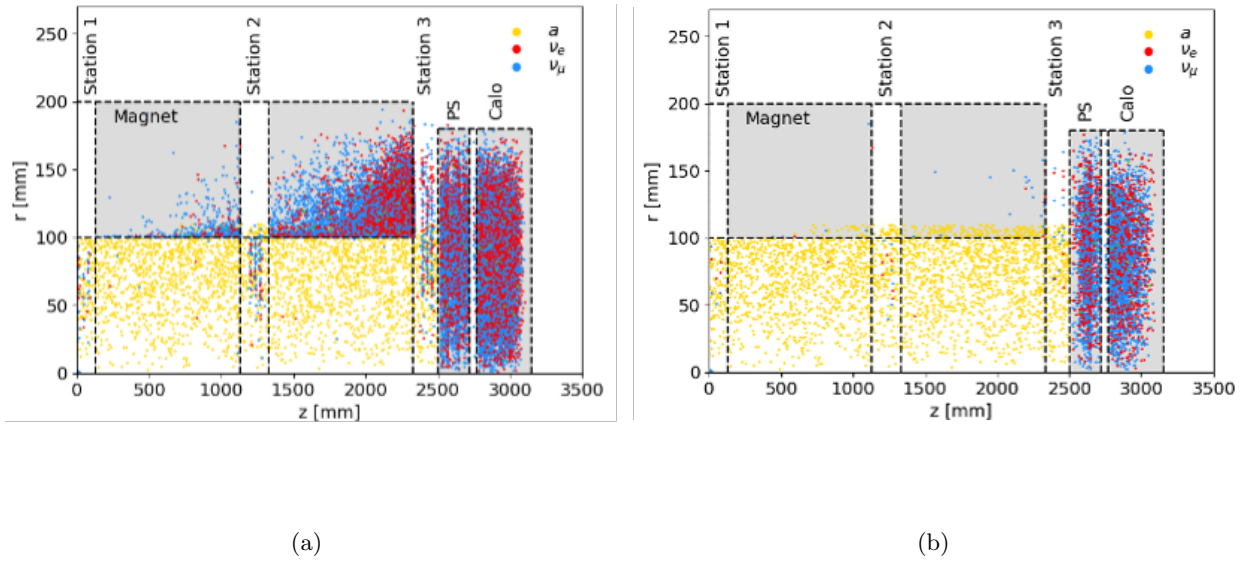


Figure 7.9: Distributions in r - z of the neutrino interaction vertex (blue/red) and ALP decay vertex (yellow) within the FASER detector with (a) calorimeter energy above 100 GeV (b) calorimeter energy above 100 GeV and preshower ratio > 4.5 .

7.3.1 Neutrino Background

Neutrinos produced upstream of FASER will pass the charge requirements placed on the five veto scintillators. In addition, interactions of the neutrinos [168] with detector material downstream of the veto stations can produce charged and neutral particles that may leave significant energy deposits in the calorimeter, with a signature that appears similar to that of the ALP signal. The lack of material in the tracking stations means that most of the neutrino interactions are expected to happen in the magnets, preshower and calorimeter, resulting in signatures which have little tracker activity, similar to that expected for signal events, and so neutrinos are expected to be a significant background for this analysis. The neutrino background prediction in this analysis is made using MC, this is discussed in Chapter 5. To validate a purely MC approach, neutrino validation regions are constructed; for these validation regions, a lower energy requirement of 100 GeV is applied, but there is no upper energy limit placed on the region definitions.

The most effective way to target this neutrino background is by categorising neutrinos according to where in FASER they interact, resulting in the “Magnet”, “Calorimeter” and “Preshower”

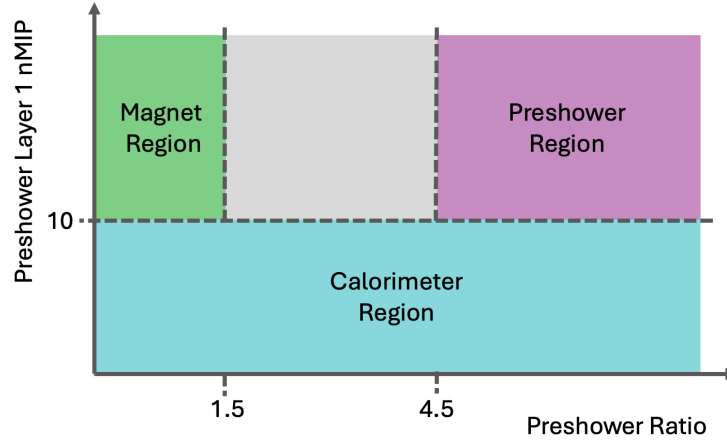


Figure 7.10: Plot showing the magnet region, calorimeter region and preshower region. The three different regions for targeting neutrino interactions, in the plane of the preshower layer 1 and preshower ratio variables. The preshower region becomes the signal region for this analysis at high calorimeter energies.

regions. The difference in location of these interactions can be seen in Figure 7.9. The definitions of the three regions are given below.

- Magnet region: preshower layer 1 nMIP > 10 , preshower ratio < 1.5
- Preshower region: preshower layer 1 nMIP > 10 , preshower ratio > 4.5
- Calorimeter region: preshower layer 1 nMIP < 10

The selections listed are in addition to the baseline selection, and also with Calo E > 100 GeV. Initially, these regions were blinded above a calorimeter energy of 500 GeV, and eventually used as validation regions up to the 1.5 TeV signal region energy selection. Figure 7.10 shows the three different regions for targeting neutrino interactions, in the plane of the preshower layer 1 and preshower ratio selections.

ALP signal could decay in the magnet or calorimeter regions, producing signatures in the detector that pass the selections defining the magnet and calorimeter validation regions. The extent of signal contamination in the validation regions was checked using extended ALP MC signal samples with at larger radius and z position, so that interactions in the full fiducial volume, as well as to the end of the calorimeter, were taken into account. Signal contamination can be very large, particularly in the calorimeter region, however, further investigation into which models provide the largest contamination shows that these models are already well excluded. At the borders of

FASER’s expected reach with this analysis, the signal contamination remains consistent with the systematic uncertainties associated with the neutrino MC prediction.

The efficiency, defined as the percentage of true neutrinos of the desired type found in a particular region, is greater than 80% and 90% in the magnet and calorimeter regions, respectively. The purity of these regions, defined as the percentage of “target” neutrinos kept relative to all neutrinos populating that region, is greater than 90% in both regions. For the preshower/signal region, the efficiency is 47% with a purity of 80%. Signal contamination is not taken into account in these calculations of efficiency and purity; this plays a large role in the low efficiency seen in the preshower region, where signal contamination becomes more significant at large calorimeter energies. These numbers also do not take into account any additional contribution from background. However, due to the calorimeter timing selection, there is no component from beam 1 background. There are two cosmic muon events in the 100 GeV to 500 GeV validation region, but zero above this energy.

The magnet, calorimeter and preshower neutrinos can be effectively distinguished with requirements on number of MIPs in the second preshower layer and the preshower ratio. The power the preshower variable selections have in removing neutrino background from ALP signal is highlighted in Figure 7.11 and Figure 7.12. Figure 7.11 shows that most of the charge deposited by ALP signal (yellow) in the second preshower layer (PS1) is above the equivalent from 10 MIPs. A selection above 10 MIPs is particularly effective at removing neutrinos interacting in the calorimeter. Figure 7.12 shows that the ALP signal lies above a preshower ratio of 4.5. By contrast to the preshower layer 1 selection, this selection mostly targets neutrinos interacting in the magnet.

Neutrinos interacting in the magnet have relatively large charges in the second preshower layer (PS1) as shown in Figure 7.14a, and the PS ratio is centred around one as can be seen in Figure 7.13a. Neutrinos interacting in the calorimeter have low charges in the second preshower layer as most interactions that would produce showering occur at a larger z , this is shown in Figure 7.14b, and a wide range of preshower ratio values shown in Figure 7.13b. In contrast, neutrinos interacting in the preshower look very signal-like, making it difficult to distinguish. Therefore, the majority of neutrinos making up the background in this analysis come from interactions in the preshower.

Figure 7.15 and Figure 7.16 show the distribution of calorimeter energy in the magnet and calorimeter regions, respectively, for the MC neutrino background compared to a representative

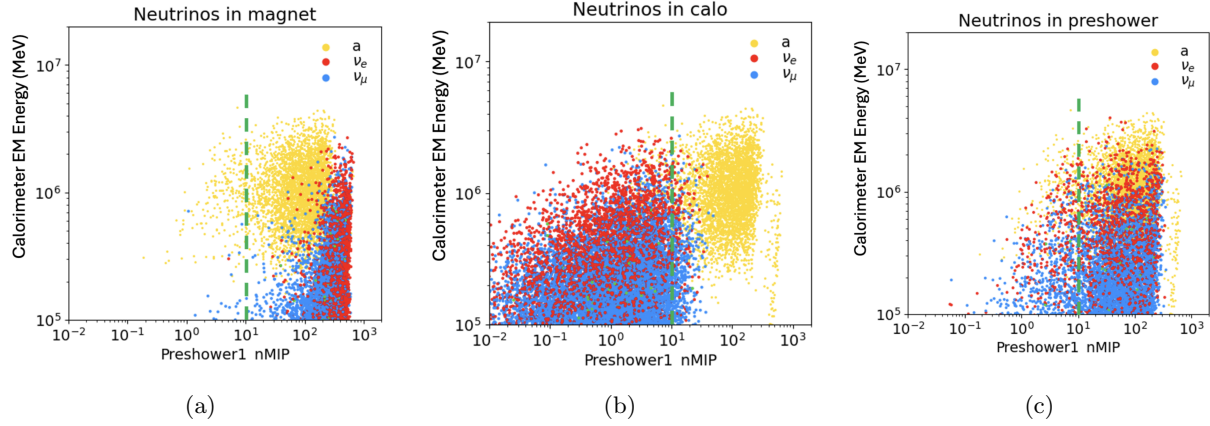


Figure 7.11: Number of MIPs in the second preshower layer against calorimeter energy for electron neutrinos (red) and muon neutrinos (blue) as well as a representative ALP signal (yellow). The neutrinos are categorised in terms of their interaction vertex: (a) neutrinos interacting in the magnet, (b) neutrinos interacting in the calorimeter, (c) neutrinos interacting in the preshower. The green dashed line shows the threshold used in this analysis: PS1 nMIP > 10.

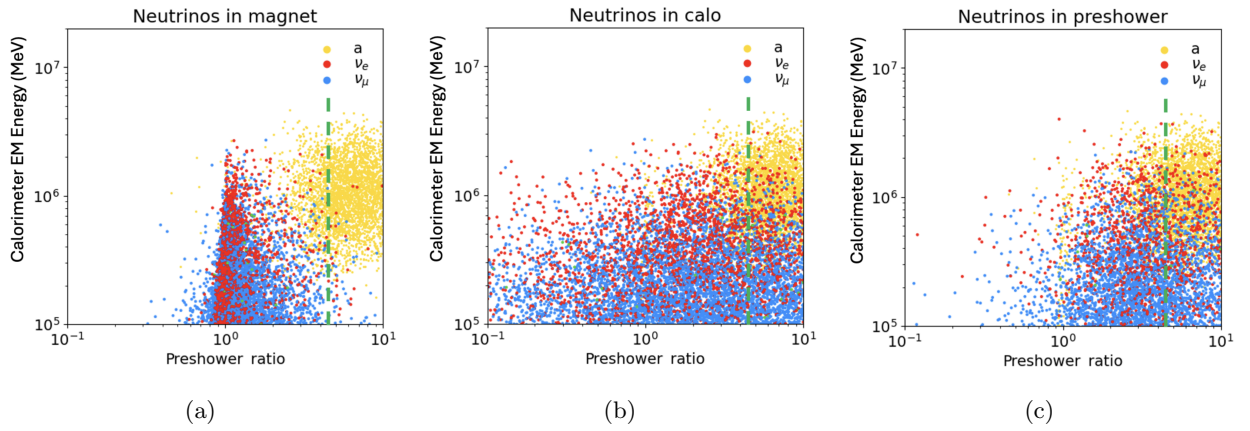
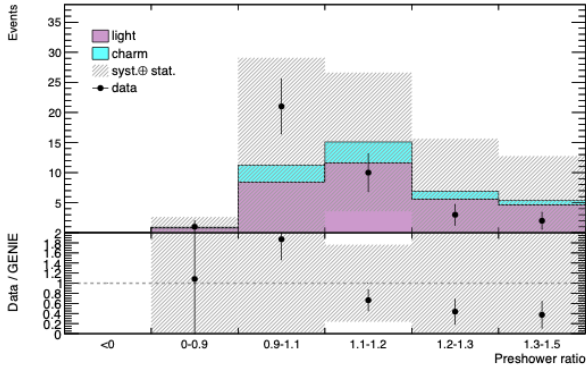
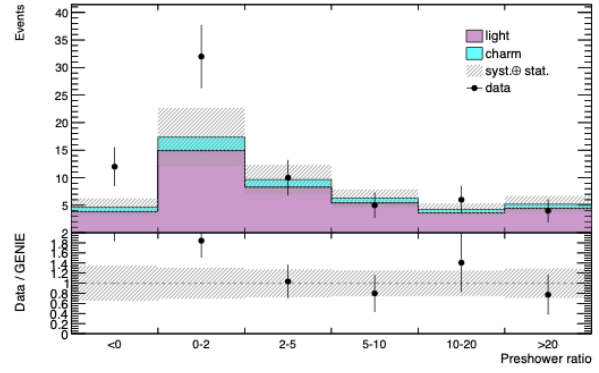


Figure 7.12: Preshower ratio against calorimeter energy for electron neutrinos (red) and muon neutrinos (blue) as well as a representative ALP signal (yellow). The neutrinos are categorised in terms of their interaction vertex: (a) neutrinos interacting in the magnet, (b) neutrinos interacting in the calorimeter, (c) neutrinos interacting in the preshower. The green dashed line shows the threshold used in this analysis: PS ratio > 4.5.

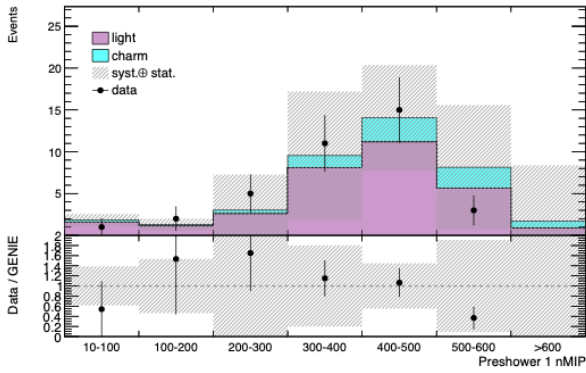


(a)

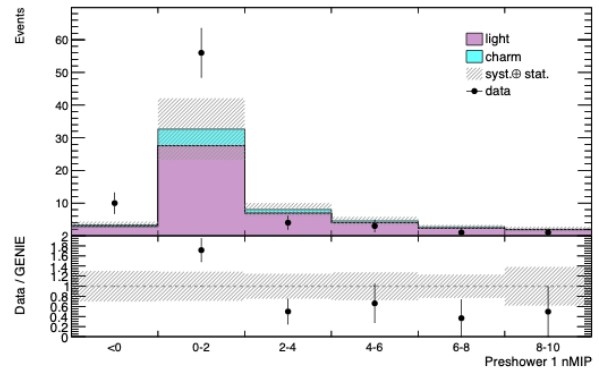


(b)

Figure 7.13: The preshower ratio distribution of the neutrino background MC in (a) the magnet region and (b) the calorimeter region. The neutrino background is shown in terms of light and charm components. The uncertainty band includes MC statistical uncertainties and systematic uncertainties on the neutrino background flux.



(a)



(b)

Figure 7.14: The preshower layer 1 nMIP distribution of the neutrino background MC in (a) the magnet region and (b) the calorimeter region. The neutrino background is shown in terms of light and charm components. The uncertainty band includes MC statistical uncertainties and systematic uncertainties on the neutrino background flux.

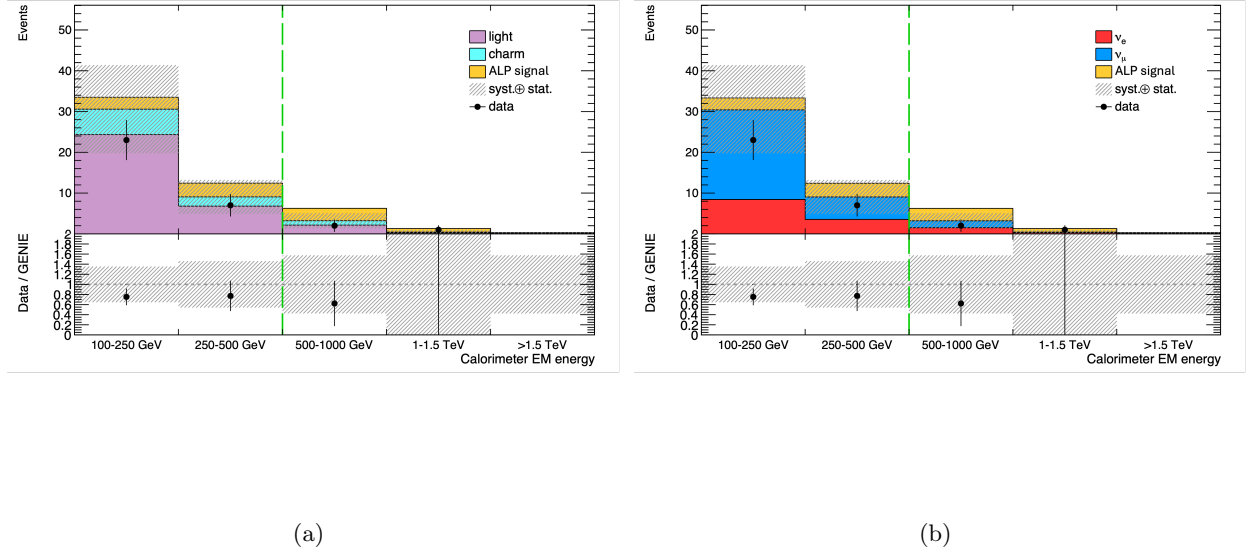


Figure 7.15: The calorimeter energy distribution in the magnet region for a representative ALP signal and the MC neutrino background in terms of (a) light and charm components and (b) neutrino type. The green dashed line indicates the region that was unblinded at the beginning of the unblinding procedure.

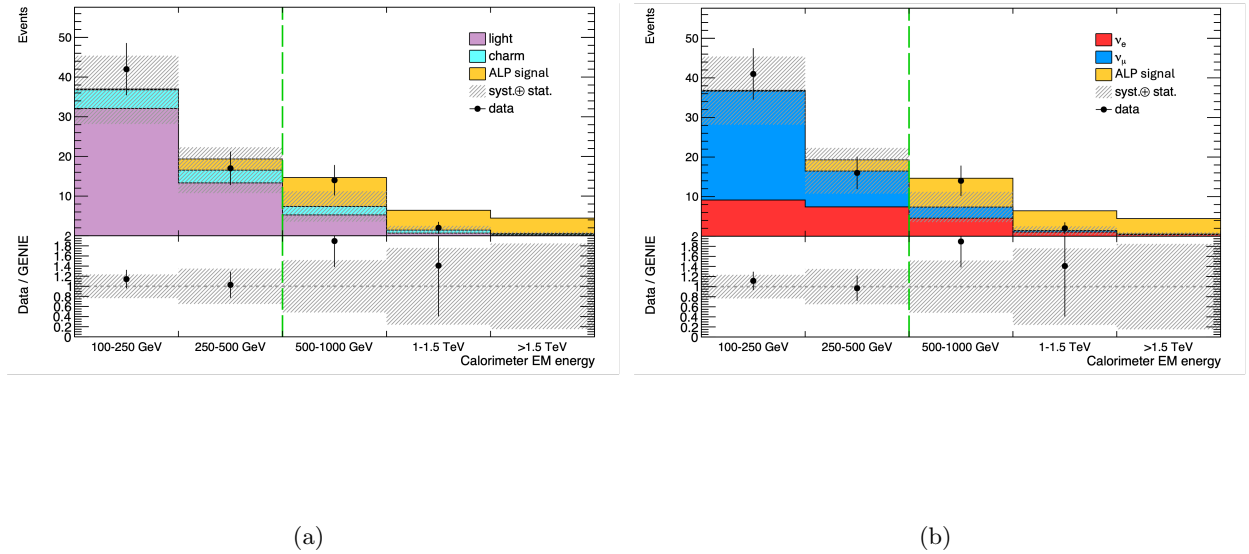


Figure 7.16: The calorimeter energy distribution in the calorimeter region for a representative ALP signal and the MC neutrino background in terms of (a) light and charm components and (b) neutrino type. The green dashed line indicates the region that was unblinded at the beginning of the unblinding procedure.

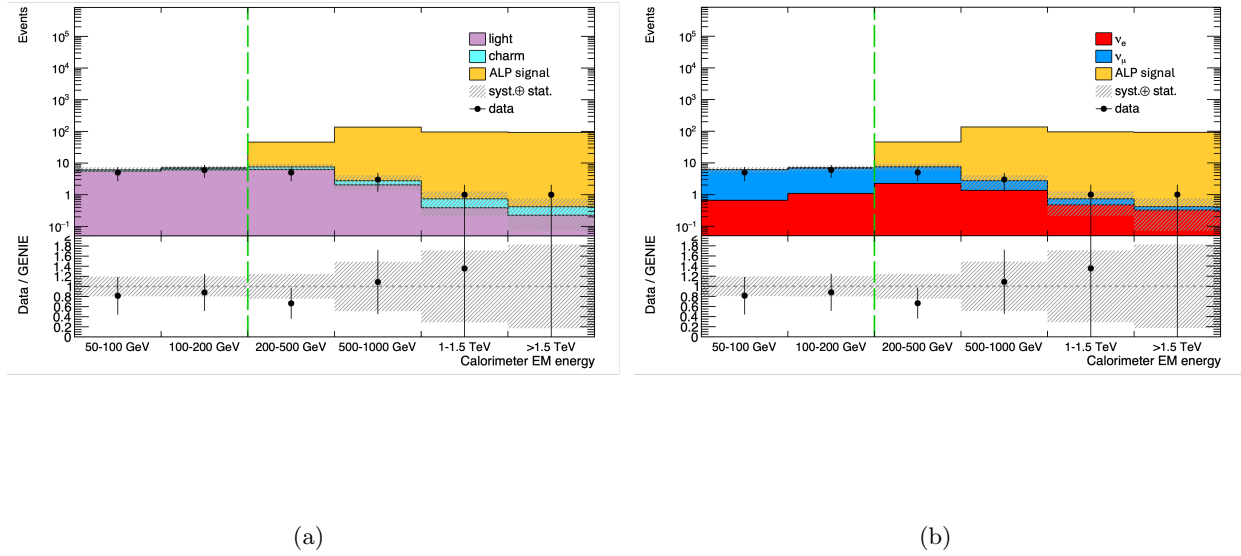


Figure 7.17: The calorimeter energy distribution in the preshower region for a representative ALP signal and the MC neutrino background in terms of (a) light and charm components and (b) neutrino type. The ALP signal has mass 120 GeV and coupling $1 \times 10^{-4} \text{ GeV}^{-1}$. The preshower region becomes the signal region for this analysis at high calorimeter energy. The green dashed line indicates the region that was unblinded at the beginning of the unblinding procedure.

ALP signal. The neutrino background is split in terms of light and charm components, and in terms of neutrino types. The validation regions, particularly at lower calorimeter energy, are largely dominated by neutrino background. Figure 7.17 shows the distribution of calorimeter energy in the preshower region which, at high calorimeter energies, becomes the signal region. Here, the (representative) ALP signal dominates the preshower region at higher energies.

As stated, the neutrino background estimation is based purely on MC predictions. The MC prediction was validated in these neutrino validation regions defined above; good agreement between data and MC in the calorimeter, magnet and preshower neutrino validation regions was found and this is shown in Table 7.5. The number of neutrinos expected in the signal region (the preshower region with a requirement of Calo $E > 1.5$ TeV) corresponding to 57.7 fb^{-1} is 0.44 ± 0.39 events. This is shown in Table 7.6 and broken down in terms of ν_e and ν_μ as well as light and charm components, with the uncertainty arising from generator flux, experimental uncertainties associated with the MC modelling of preshower and calorimeter selections, and the uncertainty due to MC statistics. The uncertainty on the neutrino cross section is negligible, it corresponds to a flat 6% uncertainty [23] across the energy range $100 \text{ GeV} < E < 3 \text{ TeV}$.

7.3.2 Neutral Hadrons

Neutral hadrons could be seen in this analysis if they are generated from muon interactions in the material in front of FASER, and therefore pass through the veto scintillator system undetected. It is possible, through interaction and decay within the magnets and infrastructure of FASER, that such particles could leave significant deposits in the preshower and calorimeter, and therefore be a potential background for an ALP search.

The FLUKA muon MC sample described in Chapter 5.3.2 is used to evaluate this background. The neutral hadrons, and the corresponding PID that are targeted in this study are:

- K_L - PID = 130
- K_S - PID = 310
- Neutrons (and anti-neutrons) - PID = 2112
- Λ_0 (and anti- Λ_0) - PID = 3122

Table 7.5: Neutrino MC predictions in the calorimeter, magnet and preshower validation regions compared to data. Broken down in terms of neutrino flavour and with the uncertainties from flux variations, experimental uncertainties associated with the preshower and calorimeter, and those derived from MC statistics, respectively.

| Calorimeter region | | | |
|--------------------|-------------------------------------------|-------|---------------------------------------|
| ν_e | $22.6 \pm 12.8 \pm 0.7 \pm 0.4$ | Light | $51.6^{+2.0}_{-3.4} \pm 3.1 \pm 0.5$ |
| ν_μ | $39.9 \pm 6.8 \pm 2.8 \pm 0.5$ | Charm | $11.1^{+19.1}_{-5.1} \pm 0.4 \pm 0.3$ |
| MC | 62.7 ± 19.7 (31.4%) | | |
| Data | 74 | | |
| Magnet region | | | |
| ν_e | $13.8 \pm 10.3 \pm 1.4 \pm 0.3$ | Light | $33.6^{+6.7}_{-3.4} \pm 4.3 \pm 0.4$ |
| ν_μ | $29.4 \pm 8.0 \pm 3.8 \pm 0.4$ | Charm | $9.9^{+16.1}_{-4.6} \pm 0.9 \pm 0.2$ |
| MC | 43.5 ± 18.2 (41.9%) | | |
| Data | 34 | | |
| Preshower region | | | |
| ν_e | $5.16 \pm 2.59 \pm 0.51 \pm 0.17$ | Light | $14.8^{+0.9}_{-1.2} \pm 1.8 \pm 0.3$ |
| ν_μ | $12.6 \pm 2.3 \pm 1.61 \pm 0.3$ | Charm | $3.0^{+4.5}_{-1.4} \pm 0.3 \pm 0.1$ |
| MC | 17.8 ± 5.1 (28.8%) | | |
| Data | 15 | | |

Table 7.6: Summary of the MC estimate for the neutrino background for 57.7 fb^{-1} in the signal region. Included are uncertainties from flux variations, experimental uncertainties associated with the preshower and calorimeter, and those derived from MC statistics, respectively.

| Signal Region | | | |
|---------------|-------------------------------------------|-------|------------------------------------------|
| ν_e | $0.34 \pm 0.33 \pm 0.11 \pm 0.05$ | Light | $0.23^{+0.01}_{-0.11} \pm 0.11 \pm 0.04$ |
| ν_μ | $0.10 \pm 0.05 \pm 0.05 \pm 0.02$ | Charm | $0.20^{+0.34}_{-0.09} \pm 0.06 \pm 0.03$ |
| MC | 0.44 ± 0.39 (88.6%) | | |

Table 7.7: MC cutflow for FLUKA muon sample.

| FLUKA Muon MC | | |
|-----------------------|------------|--------|
| Selection | Input | Pass |
| Calo trigger | 5245973878 | 155049 |
| VetoNu Signal < 40 pC | 155049 | 111 |
| Veto Signal < 40 pC | 111 | 0 |
| Timing Signal < 20 pC | 0 | 0 |

It is possible that these neutral hadrons decay to final states with a signal-like topology, by examining the truth information available in the physics ntuples created for this analysis, it was found that none of these events survived calorimeter energy requirements above 200 GeV which is far below the signal region. This confirms that neutral hadrons are negligible in this analysis.

7.3.3 Inefficiency of the Veto Scintillators

As shown in Chapter 6.3.3, the expected background of muons crossing FASER without being vetoed by any of the scintillator stations is below 10^{-18} , due to the very high efficiency of each veto layer. Therefore, this component of background is considered to be negligible.

7.3.4 Large-angle Muons

A potential background that must be considered in this analysis arises due to large-angle muons that enter FASER at such an angle that they miss the veto scintillators but potentially leave a large enough energy deposit in the calorimeter to be mistaken for signal. Two MC samples are used in this analysis to investigate this background component and are defined in Section 5.3.2. The resulting cutflow for the FLUKA MC sample is shown in Table 7.7, scaled to 57.7 fb^{-1} . Zero muon events pass the veto requirements in the ALPs baseline selection, additionally, a second MC sample, designed to specifically generate this type of muons was tested and shows zero events passing the selection. This is summarised in Table 7.8.

The two MC samples give confidence in a negligible component of large-angle muons but are limited by statistics. Additional methods are applied in order to validate and confirm that this background is negligible.

Table 7.8: MC cutflow specifically for studying ALP large-angle muon background.

| Large-angle Muon MC | | |
|-----------------------|--------|------|
| Selection | Input | Pass |
| Calo trigger | 400000 | 431 |
| VetoNu Signal < 40 pC | 431 | 4 |
| Veto Signal < 40 pC | 4 | 2 |
| Timing Signal < 20 pC | 2 | 0 |

7.3.4.1 The ABCD Method

Various data-driven ABCD methods are explored, with the aim of trying to capture and target this large-angle muon component, should it be present in the dataset, in order to place a conservative upper limit on this background. The definition of an ABCD method is given in Chapter 6.3.4 in the context of a validation method for the dark photon analysis background estimate. Here the basic idea is similar, with the aim to take two uncorrelated variables: energy in the calorimeter, and charge deposited in scintillators, to construct an ABCD validation of the signal region such that a prediction can be calculated:

$$A(\text{pred.}) = B \times \frac{C}{D}. \quad (7.2)$$

A number of differently constructed ABCD regions are investigated in the plane of calorimeter energy and either timing scintillator charge or veto scintillator charge. Investigations were carried out with various combinations of baseline selections in order to find the best method for targeting this type of background, whilst also minimising the necessary extrapolation to the signal region.

7.3.4.2 Constructing regions based on the timing scintillator

The first ABCD configuration to be tested is based on the assumption that these muons could plausibly deposit significant charge in the timing scintillator, which has a larger area than either of the veto scintillator stations, and go on to leave deposits in the calorimeter. Modelling this background and using an ABCD method to extrapolate to the signal region, should give a clear idea of the size of this background.

The four regions are constructed in terms of calorimeter energy and the inversion of the timing

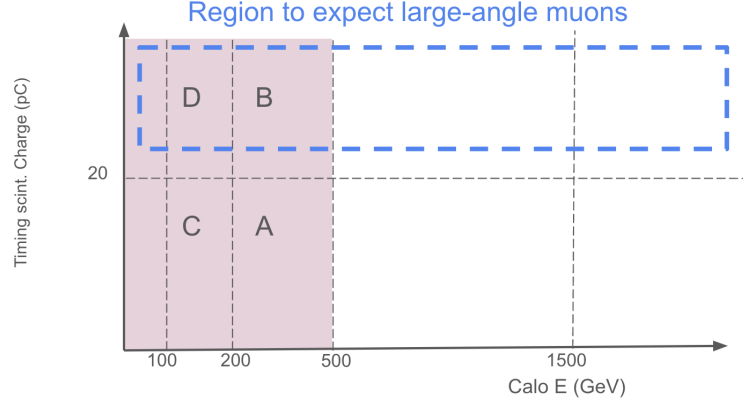


Figure 7.18: The first ABCD configuration considered to target large-angle muons. Using an inversion of the timing scintillator charge selection used in this analysis, and the calorimeter energy. The unblinded regions are indicated in pink. The regions where the timing charge requirement is inverted are indicated by the dashed blue lines to show where large-angle muons would be expected to populate data.

scintillator charge requirement used in the analysis, Figure 7.18 shows the ABCD regions. The baseline selection is applied and the region definitions are:

- Region A - Calorimeter energy 200 GeV – 500 GeV, Timing scintillator charge < 20 pC.
- Region B - Calorimeter energy 200 GeV – 500 GeV, Timing scintillator charge > 20 pC.
- Region C - Calorimeter energy 100 GeV – 200 GeV, Timing scintillator charge < 20 pC.
- Region D - Calorimeter energy 100 GeV – 200 GeV, Timing scintillator charge > 20 pC.

With this logic, control regions D and B would be populated by large-angle muons and, using C as shown in Equation 7.2, would provide an estimate of the component of this background present in the signal region, A, once scaling had been applied to extrapolate to higher calorimeter energy.

Issues arise with this configuration because once the neutrino estimate in these regions is taken into account, the remaining component argued to be large-angle muons is negative. Therefore, no meaningful scaling can be applied to extrapolate to the signal region. The population of these regions, in terms of data and neutrino MC prediction, and the resulting large-angle muon component is shown in Table 7.9.

This problem becomes even more apparent when the requirements on the preshower variables used in this analysis are applied (PS ratio > 4.5, PS1 nMIP > 10), this is shown in Table 7.10.

Table 7.9: The events in ABCD regions defined above, after the baseline selection. The central MC neutrino estimate in the different regions is subtracted from data events to give a picture of the component of large-angle muons captured by this method. In bold is the negative large-angle muon estimate which proves this method unsuitable for targeting this background.

| Events in ABCD Region | | | |
|-----------------------|----------------|-----------------|------------------------------------|
| Region | Data | Neutrino MC | Large-angle Muon |
| A | 43.0 ± 6.6 | 54.0 ± 18.3 | -11.0 ± 19.5 |
| B | 5.0 ± 2.2 | 3.7 ± 1.5 | 1.1 ± 2.7 |
| C | 71.0 ± 8.4 | 70.8 ± 17.3 | $0.19. \pm 19.3$ |
| D | 11.0 ± 3.3 | 8.2 ± 2.8 | 2.8 ± 4.37 |

Table 7.10: The events in ABCD regions defined above, after the baseline selection and the preshower requirements used in this analysis (PS ratio > 4.5 , PS1 nMIP > 10). The central MC neutrino estimate in the different regions is subtracted from data events to give a picture of the component of large-angle muons captured by this method. In bold is the negative large-angle muon estimates which proves this method unsuitable for targeting this background.

| Events in ABCD Region + Preshower Selections | | | |
|----------------------------------------------|---------------|-----------------|------------------------------------|
| Region | Data | Neutrino MC | Large-angle Muon |
| A | 5.0 ± 2.2 | 7.5 ± 1.8 | -2.5 ± 2.9 |
| B | 1.0 ± 1.0 | 0.12 ± 0.08 | 0.88 ± 1.0 |
| C | 6.0 ± 2.5 | 6.8 ± 1.4 | -0.81 ± 2.80 |
| D | 0.0 ± 0.0 | 0.19 ± 0.07 | -0.19 ± 0.08 |

The negative large-angle muon estimate, and the lack of statistics particularly in region D, proves that this method, in the current configuration, is unsuitable for targeting this type of background.

7.3.4.3 Constructing regions based on the veto scintillator

In each of the ABCD configurations using the timing scintillator charge and calorimeter energy, it was found that the regions were dominated by neutrino background. It is, therefore, impossible to use this method to place an upper limit on the number of large-angle muons expected in the signal region, the reason being that there are so little of such events to capture. Therefore, in order to validate that the large-angle muon component of background in this analysis is negligible, a final ABCD method is constructed using the veto scintillator charge requirement and calorimeter energy, the relaxation of the veto charge requirement improves statistics and allows more muon events to be captured by this method.

This ABCD method is used to estimate the large-angle muon background in two separate control regions. Both require charge deposits in the timing scintillator of greater than 20 pC but less than 40 pC in the veto scintillators. The first control region requires a preshower ratio less than 4.5, whereas the second control region requires a preshower ratio greater than 4.5 and a charge in the second preshower layer of greater than the 10 MIP equivalent. The construction of the first control region, with the requirement of PS ratio < 4.5 should target large-angle muons, which are unlikely to have a large preshower ratio. The second control region has the same selection as the preshower/signal region, but with the charge requirement in the timing scintillator inverted.

To summarise, the following combination of preshower requirements are applied to the two ABCD configurations:

- Configuration 1:
 - PS Ratio > 4.5
- Configuration 2:
 - PS Ratio > 4.5
 - PS1 nMIP > 10

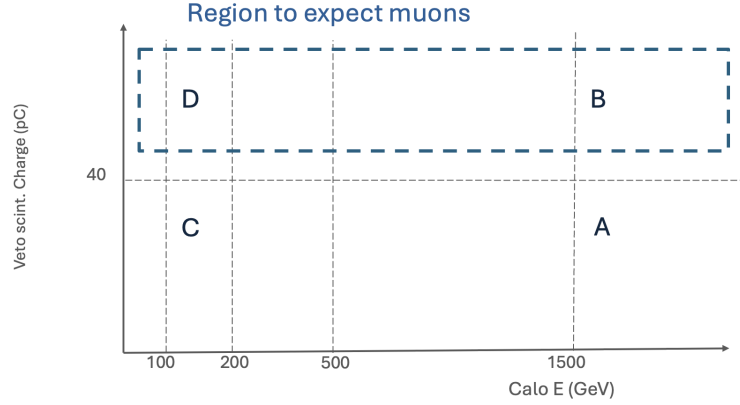


Figure 7.19: ABCD configuration of the two configurations considered to target muons. Using an inversion of the veto scintillator charge requirement used in this analysis, and the calorimeter energy as the ABCD variables. The regions where the veto charge requirement is inverted are highlighted in blue to show where forward-going muons are expected to populate data.

The four ABCD regions in each of the two configurations are defined in terms of calorimeter energy and the inversion of the veto scintillator charge requirement used in this analysis. The regions are visualised in Figure 7.19. In addition to the above preshower selections, the baseline selection is applied and all of the ABCD regions require a timing scintillator charge > 20 pC, this is the opposite of the selection used in the signal region. The ABCD region definitions are:

- Region A - Calorimeter energy > 1.5 TeV, Veto scintillator charge < 40 pC.
- Region B - Calorimeter energy > 1.5 TeV, Veto scintillator charge > 40 pC.
- Region C - Calorimeter energy $100 \text{ GeV} - 200/500 \text{ GeV}$, Veto scintillator charge < 40 pC.
- Region D - Calorimeter energy $100 \text{ GeV} - 200/500 \text{ GeV}$, Veto scintillator charge > 40 pC.

This ABCD method was investigated after the initial unblinding of this analysis, therefore, the regions could be extended to higher calorimeter energy compared with the previous approach. The two values considered for the upper limit on calorimeter energy in regions C and D depends on which control region is considered. The higher threshold is used for the second configuration, to provide sufficient statistics for this method.

The estimate in region A is shown in Table 7.11, as with the previous method, the component of neutrino background (inclusive of uncertainties) is subtracted from the data. The final prediction in

Table 7.11: Data and neutrino yields in the different ABCD regions and the prediction for the large-angle muon estimate for the two preshower selections. To calculate the prediction in region A, the expected MC neutrino background is first subtracted from the data in region C. The uncertainty on the neutrino MC includes flux and experimental sources and is propagated to the final estimate.

| Preshower selection | A | B | C | C (ν MC) | D | A (pred.) $\times 10^{-3}$ |
|-------------------------------------------------------------|---|------|----|---------------|--------|---------------------------------------------------|
| PS ratio < 4.5 (Configuration 1) | 0 | 1211 | 11 | 7.9 ± 2.9 | 199506 | 19.1 ± 20.1 (stat.) ± 17.7 (ν syst.) |
| PS ratio > 4.5 , PS 1 nMIP > 10 (Configuration 2) | 0 | 143 | 1 | 0.3 ± 0.2 | 24130 | 4.1 ± 5.9 (stat.) ± 1.0 (ν syst.) |

Table 7.12: Final estimates of the large-angle muon background in the two configurations.

| Preshower selection | A (pred.) $\times 10^{-3}$ |
|----------------------------------------------------------|-------------------------------------------------------------------------------------------------------------------------|
| PS ratio < 4.5 (Configuration 1) | 19.1 ± 20.1 (stat.) ± 17.7 (ν syst.) ± 5.2 (track syst.) $= 19.1 \pm 27.3$ (143%) |
| PS ratio > 4.5 , PS 1 nMIP > 10 (Configuration 2) | 4.1 ± 5.9 (stat.) ± 1.0 (ν syst.) ± 1.1 (track syst.) $= 4.1 \pm 6.1$ (148%) |

the two configurations, inclusive of tracking systematics and uncertainties associated with studying the muon events, is shown in Table 7.12.

The neutrino background in the signal region is estimated to be 0.44 ± 0.39 , taking the more conservative upper limit of $(19.1 \pm 27.3) \times 10^{-3}$ is an order of magnitude below this estimate. The estimate derived from the second configuration, $(4.1 \pm 6.1) \times 10^{-3}$, requires the least scaling to the signal region since both preshower requirements are applied. For example, the timing scintillator charge requirement would have to be inverted, which is very likely to suppress this estimate further. The large-angle muon estimate is several orders of magnitude below the neutrino estimate, as a result, the large-angle muon background can be considered negligible in this analysis.

7.3.5 Non-collision Backgrounds

As with the dark photon analysis, it is necessary to consider the component of background that arises due nearby LHC beam interactions and the interactions of cosmic ray muons. The following sections demonstrate that all non-collision background is negligible in this analysis.

Table 7.13: Cutflow of events passing selections for the evaluation of cosmic ray muon background.

| Selection | Events | Rel. Acceptance [%] |
|---------------------------------|--------|---------------------|
| Total Events | 98510 | - |
| Calo Trigger and Colliding BCID | 1478 | 1.50 |
| VetoNu Signal < 40 pC | 1478 | 100 |
| Veto Signal < 40 pC | 1478 | 100 |
| Timing Signal < 20 pC | 1478 | 100 |
| PS Ratio > 4.5 | 161 | 10.89 |
| PS1 nMIP > 10 | 9 | 5.59 |
| Calo E > 500 GeV | 0 | 0 |

7.3.5.1 Background due to cosmic ray muons

In order to evaluate the number of cosmic events that could be included in this dataset, data recorded during periods without beam in the LHC is analysed. The total time period of reconstructed data collected in this setup is approximately equivalent to the timeframe in which the physics dataset used in this analysis was collected.

The number of events passing each requirement are shown in Table 7.13. Requiring that the events trigger in the calorimeter removes over 98% of this “cosmics” dataset. The remaining events are completely removed with a relatively low calorimeter energy selection that is far away from the eventual calorimeter energy chosen for the signal region. It is therefore very clear that this component will be negligible.

7.3.5.2 Beam 1 Background

Contributions from beam 1 background come from colliding bunch BCIDs that also correspond with BCID timings of beam 1 passing FASER. This is the result of secondary particles produced when beam 1, passing FASER towards the ATLAS IP, interacts with the LHC Q12 magnet located close to FASER. Unlike cosmic ray muons and general beam background, which display random signal timing, the beam 1 background has a well-defined signal time-of-arrival of roughly -12.5 ns in relation to a collision signal. Timing can be used as an additional and effective handle to reduce beam 1 background.

As with the dark photon analysis, data to evaluate this background is collected by taking events

Table 7.14: Summary of events passing selections and calorimeter timing requirement for the evaluation of beam 1 background.

| Selection | Events | Rel. Acceptance [%] |
|--------------------------|--------|---------------------|
| Calo Trigger and B1 BCID | 54594 | - |
| VetoNu Signal < 40 pC | 54524 | 99.8 |
| Veto Signal < 40 pC | 54359 | 99.7 |
| Timing Signal < 20 pC | 53684 | 98.8 |
| PS Ratio > 4.5 | 6452 | 12.0 |
| PS1 nMIP > 10 | 95 | 1.47 |
| Calorimeter Timing | 0 | 0 |

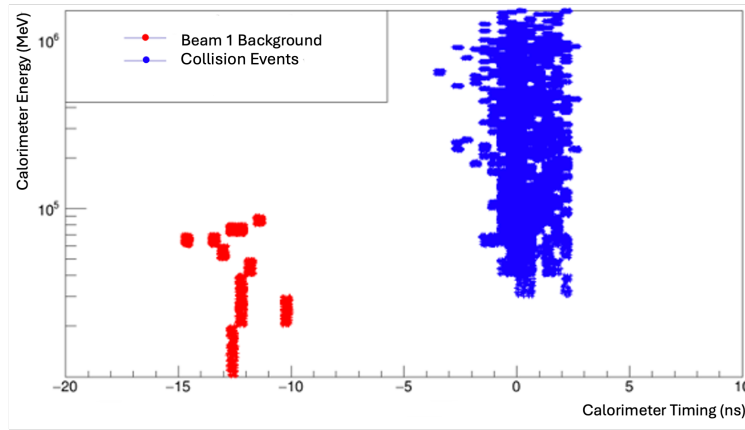


Figure 7.20: Timing in the calorimeter of beam 1 background events (red) and collision events (blue). Placing a threshold at -5 ns removes all components of beam 1 background.

with BCIDs corresponding to collisions in LHC B1 passing FASER, but which do not correspond to colliding bunches at IP1. Although some of these events do pass the scintillator requirements in the baseline selection, the beam 1 background is suppressed to a negligible level once calorimeter timing requirements are applied. Such beam 1 events would arrive 127 bunch-crossings before collisions from when the same bunch would be seen in the detector. Figure 7.20 illustrates the clear distinction that can be made between collision events and beam 1 background. The cutflow in Table 7.14 shows how the calorimeter timing removes all of this background.

7.3.6 Summary of Total Expected Background

A summary of the total background estimate in this analysis is shown in Table 7.15. Components from neutral hadrons, large-angle muons, inefficiencies from the veto scintillators, and non-collision

Table 7.15: Summary of the different sources of background considered in this analysis and the total estimate, with uncertainty.

| Source | Background | Uncertainty |
|---------------------------|-------------|---------------------|
| Neutrino | 0.44 | 0.39 (88.6%) |
| Neutral Hadrons | - | - |
| Veto Inefficiency | - | - |
| Large-angle Muons | - | - |
| Non-collision Backgrounds | - | - |
| Total | 0.44 | 0.39 (88.6%) |

backgrounds are considered to be negligible. Therefore, the background estimate in the signal region is due to interactions from neutrinos. The total background estimate is 0.44 ± 0.39 events.

7.4 Systematic Uncertainties

This section describes the various sources of systematic uncertainties that are relevant to signal and background. The systematic uncertainties are related to the signal yield, rather than shape uncertainty. These systematic uncertainties are implemented as nuisance parameters in the model-dependent fit performed in the statistical interpretation of the results of this analysis. This is explained in Chapter 5.4.1. The main sources of uncertainty can be categorised into theory uncertainties and experimental uncertainties. The theory uncertainty is the systematic uncertainty associated with the MC generators used to simulate signal and background processes. The experimental uncertainties are the systematic uncertainties associated with the preshower and calorimeter variables used in this analysis and the uncertainty of the measurement of the luminosity that comes from ATLAS. There is also a statistical uncertainty derived from MC statistics, calculated from the standard deviation of the sum of the weights of each MC sample.

7.4.1 Theory Uncertainties

Systematic uncertainties that arise due to the modelling of the MC generators used to simulate the signal and background samples used in this analysis. The flux uncertainties due to the different generators used in the MC is the dominant systematic uncertainty, for both signal and background.

7.4.1.1 Signal Systematic Uncertainties

As discussed in Chapter 5, the type of generators used for the ALP signal can be separated into light and charm hadron components. The uncertainty on the light hadron component comes from the spread of the generator predictions provided by SIBYLL, QGSJET and Pythia (forward). The uncertainty associated with the charm hadron component comes from the POWHEG+Pythia minimum and maximum predictions which use central factorisation and resummation scales defined in Ref. [22].

The net shift in the yield, either up or down, was taken for each generator and added in quadrature, along with an additional 20% uncertainty recommended for the modelling of the B hadron component, in order to obtain a total uncertainty up and down. This is shown as a percentage of the total yield in Table 7.16. The uncertainty on the signal is by far the dominant systematic uncertainty involved in this analysis, equal to between 30 and 60% uncertainty depending on the mass and coupling of the signal.

7.4.1.2 Background Systematic Uncertainties

As detailed in Chapter 5, the component of neutrino flux coming from light hadrons is based on the EPOS-LHC generator and the charm hadron component uses the POWHEG+Pythia prediction. The theory systematic uncertainty associated with the neutrino background comes from the spread of the flux predictions from the different MC generators used. Particularly, there is a large uncertainty due to the modeling of the charm hadron component. A breakdown of the uncertainties associated with the neutrino background in terms of: theory uncertainty due to the spread of the generator predictions, experimental uncertainty due to the preshower and calorimeter selections, and the uncertainty due to MC statistics is shown in Table 7.6.

7.4.2 Experimental Uncertainties

This section deals with the experimental uncertainties: the systematic uncertainties related to the scintillator, preshower and calorimeter selections used in this analysis, in addition to the 2.2% (2022 data) and 2.04% (2023 data) uncertainty on the luminosity measurement from ATLAS.

Table 7.16: The percentage change in yield up and down due to systematic uncertainty on generator type. Uncertainty from each generator are added in quadrature, including the additional 20% uncertainty arising from modeling of B hadrons in the ALP-W model.

| ALP Signal | Generator unc shift up | Generator unc shift down |
|---------------------------------------------------------------------------|------------------------|--------------------------|
| $m_a = 80 \text{ MeV}$ $g_{aWW} = 1 \times 10^{-3} \text{ GeV}^{-1}$ | 63.3% | 34.5% |
| $m_a = 60 \text{ MeV}$ $g_{aWW} = 1.1 \times 10^{-4} \text{ GeV}^{-1}$ | 57.9% | 33.3% |
| $m_a = 120 \text{ MeV}$ $g_{aWW} = 3 \times 10^{-4} \text{ GeV}^{-1}$ | 59.9% | 33.7% |
| $m_a = 100 \text{ MeV}$ $g_{aWW} = 6 \times 10^{-5} \text{ GeV}^{-1}$ | 57.4% | 33.2% |
| $m_a = 140 \text{ MeV}$ $g_{aWW} = 2 \times 10^{-4} \text{ GeV}^{-1}$ | 59.4% | 33.6% |
| $m_a = 140 \text{ MeV}$ $g_{aWW} = 4 \times 10^{-5} \text{ GeV}^{-1}$ | 56.6% | 32.9% |
| $m_a = 200 \text{ MeV}$ $g_{aWW} = 1 \times 10^{-4} \text{ GeV}^{-1}$ | 59.7% | 33.7% |
| $m_a = 200 \text{ MeV}$ $g_{aWW} = 4 \times 10^{-5} \text{ GeV}^{-1}$ | 57.7% | 33.2% |
| $m_a = 230 \text{ MeV}$ $g_{aWW} = 6 \times 10^{-5} \text{ GeV}^{-1}$ | 58.8% | 33.5% |
| $m_a = 230 \text{ MeV}$ $g_{aWW} = 4 \times 10^{-5} \text{ GeV}^{-1}$ | 57.4% | 33.1% |

7.4.2.1 Scintillator Systematic Uncertainty

The approach to the systematic uncertainty on the veto scintillator selections in this analysis is based on the treatment of this uncertainty in the A' analysis, detailed in Chapter 6.4.2.1. The same 40 pC threshold in both the VetoNu scintillator and the veto scintillator stations is used in the selection. Given that the veto scintillators are very efficient, the uncertainty on the signal yield is considered to be negligible.

The systematic uncertainty associated with the timing scintillator in this analysis is driven by the low threshold. Any signal greater than 20 pC in either the top or bottom timing scintillators is rejected. When data (2022 and 2023) are compared to a representative MC ALP-W signal sample, the difference between data and signal is clear, this was shown in Figure 7.6. The need to place a large uncertainty on this threshold is not necessary.

7.4.2.2 Preshower Systematic Uncertainty

The systematic uncertainty related to the two preshower variables used in this analysis is evaluated by looking at the discrepancy between data and MC for the charge distributions in the preshower scintillator layers using both test beam (TB) and TI12 data.

The difference between MC and photon conversion events in TI12 data, shown in Figure 7.21a, is used to derive a correction factor. The difference in test beam data and MC, shown in Figure 7.21b, is used to determine the uncertainty.

A correction factor is applied in MC to the value of the preshower layer 1 nMIP (PS1 nMIP) of 1.20, with a 20% uncertainty applied to the variable. A correction factor of 1.13 is applied to the MC preshower ratio (PS Ratio), with an uncertainty of 13%. Derivation of this correction factor comes from the fits shown in Figure 7.22, where the agreement between data and MC is measured as a function of momentum. The percentage shifts in the yield are shown in Table 7.17 and Table 7.18, respectively. These uncertainties, particularly those associated with the PS1 nMIP variable, have a small overall impact on the signal.

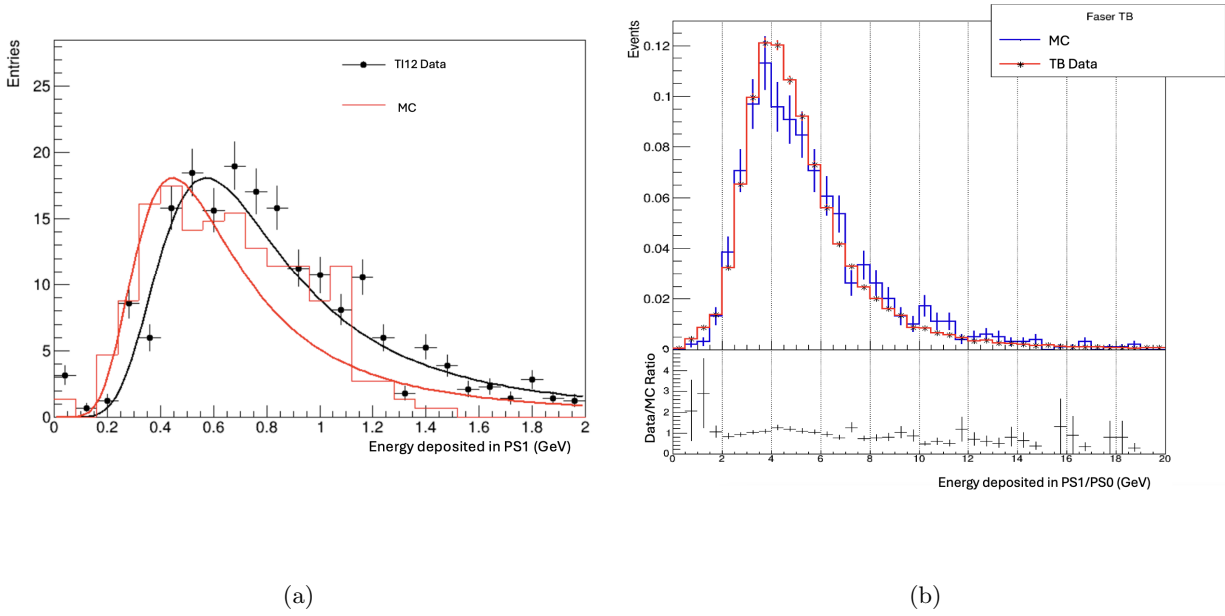


Figure 7.21: (a) Photon conversion in TI12 data and MC. A correction factor for the preshower variables is derived based on the difference between the two. (b) The difference in test beam data and 100 GeV electron MC in the geometry description matching that used to generate the ALP signal, used to estimate the uncertainty assigned to the preshower variables.

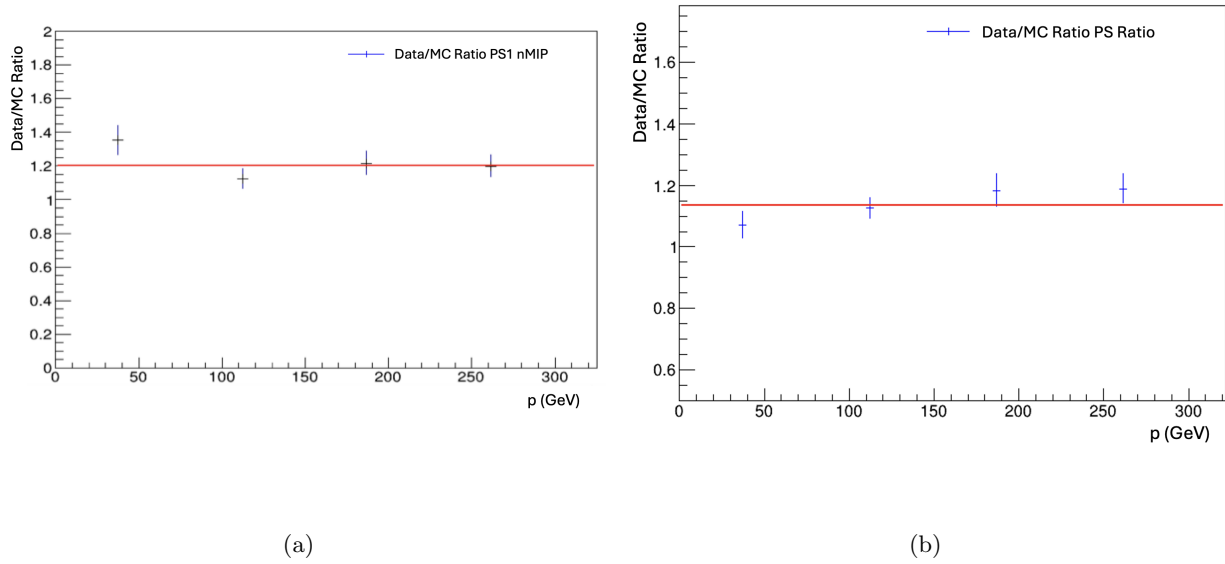


Figure 7.22: The agreement between data and MC measured as a function of momentum in studies of photon conversion events, resulting in correction factors for the preshower variables to be applied in MC for (a) PS1 nMIP (1.20) and (b) PS Ratio (1.13).

Table 7.17: The percentage change in yield up and down due to systematic uncertainty on PS1 nMIP. A correction factor of 1.20 is applied, with an uncertainty of 20%.

| ALP Signal | PS1 nMIP unc. up | PS1 nMIP unc. down |
|---------------------------------------------------------------------------|------------------|--------------------|
| $m_a = 80 \text{ MeV}$ $g_{aWW} = 1 \times 10^{-3} \text{ GeV}^{-1}$ | 0.299% | 0.454% |
| $m_a = 60 \text{ MeV}$ $g_{aWW} = 1.1 \times 10^{-4} \text{ GeV}^{-1}$ | 0.00% | 0.00% |
| $m_a = 120 \text{ MeV}$ $g_{aWW} = 3 \times 10^{-4} \text{ GeV}^{-1}$ | 0.432% | 0.598% |
| $m_a = 100 \text{ MeV}$ $g_{aWW} = 6 \times 10^{-5} \text{ GeV}^{-1}$ | 0.00% | 0.00% |
| $m_a = 140 \text{ MeV}$ $g_{aWW} = 2 \times 10^{-4} \text{ GeV}^{-1}$ | 0.257% | 0.578% |
| $m_a = 140 \text{ MeV}$ $g_{aWW} = 4 \times 10^{-5} \text{ GeV}^{-1}$ | 0.00% | 0.270% |
| $m_a = 200 \text{ MeV}$ $g_{aWW} = 1 \times 10^{-4} \text{ GeV}^{-1}$ | 0.695% | 0.477% |
| $m_a = 200 \text{ MeV}$ $g_{aWW} = 4 \times 10^{-5} \text{ GeV}^{-1}$ | 1.27% | 0.921% |
| $m_a = 230 \text{ MeV}$ $g_{aWW} = 6 \times 10^{-5} \text{ GeV}^{-1}$ | 0.721% | 0.954% |
| $m_a = 230 \text{ MeV}$ $g_{aWW} = 4 \times 10^{-5} \text{ GeV}^{-1}$ | 0.852% | 0.461% |

Table 7.18: The percentage change in yield up and down due to systematic uncertainty on the PS Ratio (preshower1/preshower0). A correction factor of 1.13 was applied, with an uncertainty of 13%.

| ALP Signal | PS Ratio unc. up | PS Ratio unc. down |
|---------------------------------------------------------------------------|------------------|--------------------|
| $m_a = 80 \text{ MeV}$ $g_{aWW} = 1 \times 10^{-3} \text{ GeV}^{-1}$ | 7.0% | 7.6% |
| $m_a = 60 \text{ MeV}$ $g_{aWW} = 1.1 \times 10^{-4} \text{ GeV}^{-1}$ | 4.2% | 5.3% |
| $m_a = 120 \text{ MeV}$ $g_{aWW} = 3 \times 10^{-4} \text{ GeV}^{-1}$ | 6.5% | 8.8% |
| $m_a = 100 \text{ MeV}$ $g_{aWW} = 6 \times 10^{-5} \text{ GeV}^{-1}$ | 4.9% | 4.5% |
| $m_a = 140 \text{ MeV}$ $g_{aWW} = 2 \times 10^{-4} \text{ GeV}^{-1}$ | 6.0% | 7.9% |
| $m_a = 140 \text{ MeV}$ $g_{aWW} = 4 \times 10^{-5} \text{ GeV}^{-1}$ | 6.4% | 8.3% |
| $m_a = 200 \text{ MeV}$ $g_{aWW} = 1 \times 10^{-4} \text{ GeV}^{-1}$ | 6.4% | 8.1% |
| $m_a = 200 \text{ MeV}$ $g_{aWW} = 4 \times 10^{-5} \text{ GeV}^{-1}$ | 5.1% | 7.7% |
| $m_a = 230 \text{ MeV}$ $g_{aWW} = 6 \times 10^{-5} \text{ GeV}^{-1}$ | 6.2% | 7.7% |
| $m_a = 230 \text{ MeV}$ $g_{aWW} = 4 \times 10^{-5} \text{ GeV}^{-1}$ | 5.6% | 7.9% |

7.4.2.3 Calorimeter Systematics

The energy calibration of the calorimeter and the uncertainty in comparing the calibrated energies in data and MC at 500 GeV, is measured to be 6%, the various sources of uncertainty that contribute to this 6% are shown in Table A.1 in Appendix A.2. The percentage change in the signal yield as a result of this uncertainty is shown in Table 7.19. In addition, an 8.8% correction factor is applied to the calorimeter EM energy. This is derived from test beam studies which used a calibrated MC energy to compare to test beam data.

The calorimeter EM energy threshold used in the ALP analysis (1.5 TeV) is considerably higher than the threshold used in the dark photon analysis (500 GeV). In order to study the effect of a much higher calorimeter energy threshold, and whether a 6% uncertainty is still suitable, a 10% and 20% uncertainty is also studied. The percentage change in the signal yield when applying these larger uncertainties to the calorimeter energy are shown in Table 7.20. The increased uncertainty and resulting shift in the signal yield can be large for certain signal points, however, it is still sub-dominant to the uncertainty associated with the generator flux. Furthermore, a calorimeter systematic uncertainty of 20% implemented into the statistical framework has a negligible impact on overall sensitivity and reach. This study shows that the assumption of a 6% uncertainty on the calorimeter energy remains a conservative estimate suitable for this analysis.

7.4.3 A Summary of Systematic Uncertainties

Descriptions of the systematic uncertainties implemented in this analysis are given in Table 7.21. Table 7.22 summarises the sources of uncertainty on the signal, and the effect on the yield. The largest uncertainty, in the case of both signal and background, is due to the different generators used in the production of the MC samples.

Table 7.19: The percentage change in yield for representative signal MC samples in the case of the 6% calorimeter energy systematic uncertainty implemented in this analysis.

| ALP Signal | 6% unc. up | 6% unc. down |
|---------------------------------------------------------------------------|------------|--------------|
| $m_a = 80 \text{ MeV}$ $g_{aWW} = 1 \times 10^{-3} \text{ GeV}^{-1}$ | 0.0% | 0.1% |
| $m_a = 60 \text{ MeV}$ $g_{aWW} = 1.1 \times 10^{-4} \text{ GeV}^{-1}$ | 19.0% | 10.6% |
| $m_a = 120 \text{ MeV}$ $g_{aWW} = 3 \times 10^{-4} \text{ GeV}^{-1}$ | 1.6% | 2.0% |
| $m_a = 100 \text{ MeV}$ $g_{aWW} = 6 \times 10^{-5} \text{ GeV}^{-1}$ | 24.3% | 16.4% |
| $m_a = 140 \text{ MeV}$ $g_{aWW} = 2 \times 10^{-4} \text{ GeV}^{-1}$ | 2.7% | 3.6% |
| $m_a = 140 \text{ MeV}$ $g_{aWW} = 4 \times 10^{-5} \text{ GeV}^{-1}$ | 19.6% | 15.0% |
| $m_a = 200 \text{ MeV}$ $g_{aWW} = 1 \times 10^{-4} \text{ GeV}^{-1}$ | 2.5% | 3.1% |
| $m_a = 200 \text{ MeV}$ $g_{aWW} = 4 \times 10^{-5} \text{ GeV}^{-1}$ | 12.8% | 12.1% |
| $m_a = 230 \text{ MeV}$ $g_{aWW} = 6 \times 10^{-5} \text{ GeV}^{-1}$ | 6.0% | 6.5% |
| $m_a = 230 \text{ MeV}$ $g_{aWW} = 4 \times 10^{-5} \text{ GeV}^{-1}$ | 11.5% | 12.2% |

Table 7.20: An investigation into the percentage change in signal yield for representative signal MC samples with 10% and 20% calorimeter energy systematic uncertainty.

| ALP Signal | 10% unc. up | 10% unc. down | 20% unc. up | 20% unc. down |
|---------------------------------------------------------------------------|-------------|---------------|-------------|---------------|
| $m_a = 80 \text{ MeV}$ $g_{aWW} = 1 \times 10^{-3} \text{ GeV}^{-1}$ | 0.0% | 0.1% | 0.0% | 0.483% |
| $m_a = 60 \text{ MeV}$ $g_{aWW} = 1.1 \times 10^{-4} \text{ GeV}^{-1}$ | 31.7% | 19.0% | 84.7% | 40.2% |
| $m_a = 120 \text{ MeV}$ $g_{aWW} = 3 \times 10^{-4} \text{ GeV}^{-1}$ | 2.5% | 3.7% | 3.6% | 9.108% |
| $m_a = 100 \text{ MeV}$ $g_{aWW} = 6 \times 10^{-5} \text{ GeV}^{-1}$ | 36.9% | 25.0% | 67.6% | 44.3% |
| $m_a = 140 \text{ MeV}$ $g_{aWW} = 2 \times 10^{-4} \text{ GeV}^{-1}$ | 3.8% | 5.6% | 5.8% | 13.2% |
| $m_a = 140 \text{ MeV}$ $g_{aWW} = 4 \times 10^{-5} \text{ GeV}^{-1}$ | 30.0% | 23.9% | 62.7% | 43.4% |
| $m_a = 200 \text{ MeV}$ $g_{aWW} = 1 \times 10^{-4} \text{ GeV}^{-1}$ | 3.8% | 5.5% | 6.4% | 11.4% |
| $m_a = 200 \text{ MeV}$ $g_{aWW} = 4 \times 10^{-5} \text{ GeV}^{-1}$ | 22.8% | 18.1% | 48.3% | 34.5% |
| $m_a = 230 \text{ MeV}$ $g_{aWW} = 6 \times 10^{-5} \text{ GeV}^{-1}$ | 10.0% | 11.0% | 16.3% | 22.4% |
| $m_a = 230 \text{ MeV}$ $g_{aWW} = 4 \times 10^{-5} \text{ GeV}^{-1}$ | 20.3% | 19.3% | 42.1% | 35.3% |

Table 7.21: Systematic uncertainties implemented in the statistical analysis framework.

| Systematic | Description |
|---------------------------------|--------------------------------------------------------------------------------|
| Luminosity uncertainty | 2.2% for 2022 data, 2.04% for 2023 data, from ATLAS. |
| Calorimeter energy uncertainty | A correction factor of 1.088, 6% uncertainty |
| Preshower ratio uncertainty | A correction factor of 1.13, 13% uncertainty |
| Preshower Layer 1 uncertainty | A correction factor of 1.20, 20% uncertainty |
| Generator uncertainty | Different generator weights, additional 20% uncertainty due to the ALP-W model |
| Neutrino background uncertainty | Pure MC estimate uncertainties of 88.6% |

Table 7.22: Summary of the various sources of signal uncertainty, the effect of this uncertainty on the signal yield across the parameter space is shown. Numbers in parenthesis indicate the effect on signals in the new exclusion reach with this analysis. The error on the MC statistics is calculated using the standard deviation of the sum of the weights (W) of each sample.

| Source | Value | Effect on signal yield |
|----------------------|-------------------|------------------------|
| ALP Signal Generator | 30-60% | 30-60% (30-60%) |
| Luminosity | 2.2% | 2.2% |
| MC Statistics | $\sqrt{\sum W^2}$ | 1-7% (1-2%) |
| Preshower Ratio | 13% | 4-8% (4-8%) |
| Preshower Layer 1 | 20% | 0-2% (0-1%) |
| Calo E scale | 6% | 0-30% (0-25%) |

7.5 Results

Once the signal efficiency and background estimates with uncertainties were evaluated, data were unblinded and 1 data event was observed in the signal region. This is consistent with the total expected background of 0.44 background events expected in the signal region, with an uncertainty of 88.6%. The 1 event has a calorimeter energy of 1.6 TeV, a charge deposit in preshower layer 1 equal to 146 MIPs, and a preshower ratio of 9.0. This is consistent with a signal-like electromagnetic shower, however it cannot be ruled out that this event is a background event due to neutrino interactions. In order to claim a discovery with a significance of 3σ , 5 events would need to be observed in the signal region.

Figure 7.23 shows the unblinded results in terms of calorimeter energy in the preshower region and signal region ($\text{Calo } E > 1.5 \text{ TeV}$). The plots are overlaid with the neutrino background expectation from MC, categorised in terms of neutrino type and also in terms of light/charm hadron component. Also overlaid are three representative ALP MC signal points. The final bin showing the 1 event at 1.6 TeV includes overflows and is indicated with a green arrow.

Figure 7.24 shows the event display of the full FASER detector geometry and the reconstructed PMT waveforms from the 1 data event seen in signal region. Characteristics of this event are consistent with a signal-like event: leaving no signal in any of the veto scintillators, a small deposit in the timing scintillator, and large signatures in the preshower and calorimeter. Figure 7.25 shows the reconstructed PMT waveforms for the timing scintillator, preshower scintillator and calorimeter. A small amount of charge, 1.9 pC, is deposited in the timing scintillator, a large signal of 653.3 pC

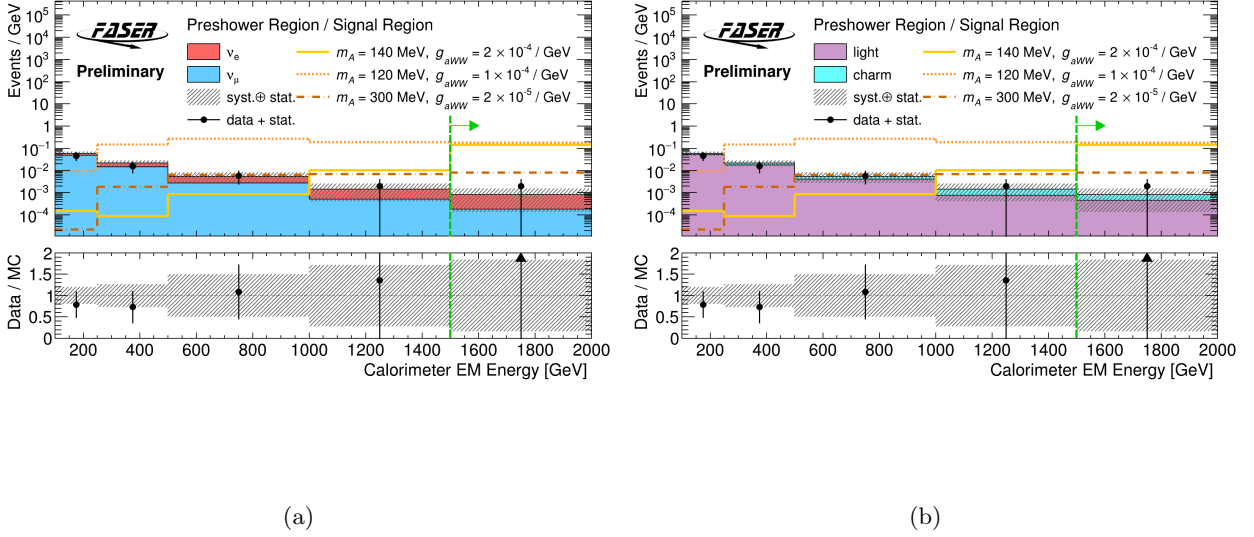


Figure 7.23: Calorimeter EM energy distributions in the preshower and signal regions, showing the composition of the neutrino background expectation separated (a) in terms of neutrino type and (b) in terms of light/charm production. The final energy bin above 1.5 TeV shows the signal region and is indicated by the green arrow.

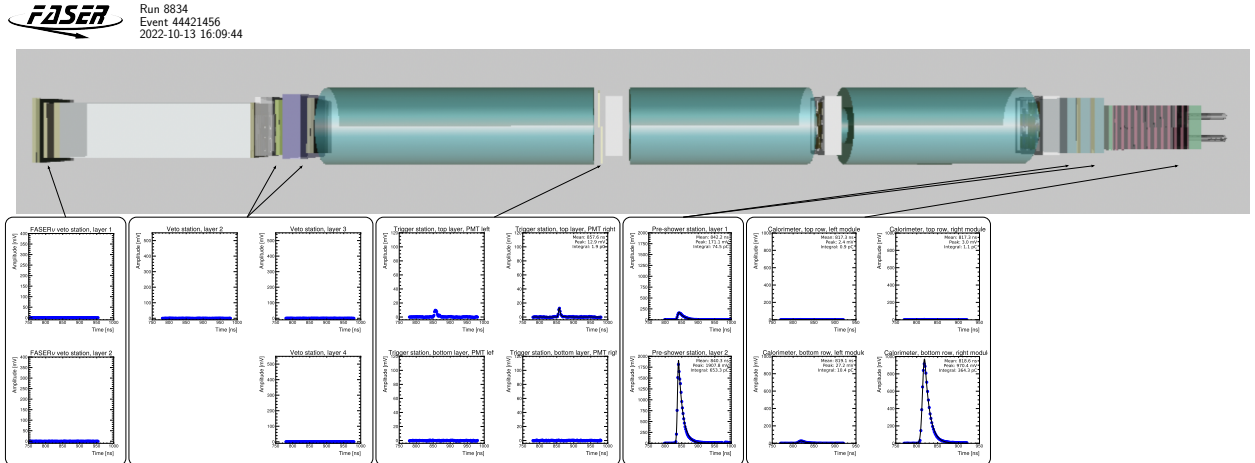


Figure 7.24: An event display of the data event seen in the ALP analysis. Run 8834, eventID 44421456. This event is in time with a collision event and shows signal in the timing scintillator, second preshower layer and the bottom right calorimeter module.

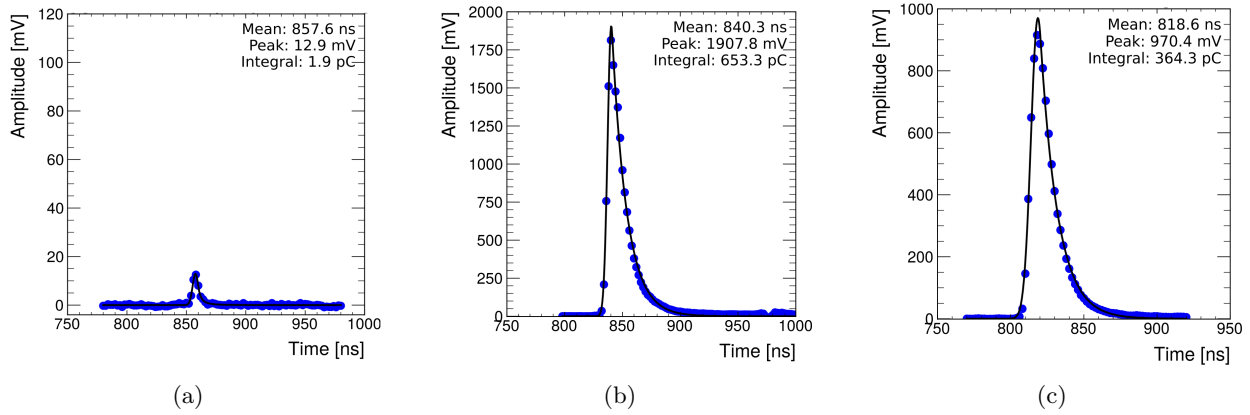


Figure 7.25: Reconstructed PMT waveworms from ALPtrino event (Run 8834, eventID 44421456) in: (a) the top layer of the timing scintillator with a peak of 12.9 mV and an integrated charge of 1.9 pC. (b) the second preshower scintillator layer with a peak of 1907.8 mV and an integrated charge of 653.3 pC. (c) the bottom right calorimeter module with a peak of 970.4 mV and an integrated charge of 364.3 pC.

is deposited in preshower layer 1, an indication of a large EM shower, and 364.3 pC is deposited in the bottom right calorimeter module.

The statistical interpretation of the results of this analysis is performed using the HistFitter statistical framework and described in Chapter 5.4.1. Since no significant excess is observed in the signal region, exclusion limits on FASER’s sensitivity to this model can be set. The expected limits and sensitivity were evaluated using a model-dependent fit which considers the ALP-W signal model and the neutrino background estimate. The sources of systematic uncertainties are implemented in the model as nuisance parameters. This analysis considers the 90% Confidence Level (CL), in line with other similar dark matter searches. The contour from evaluating the CLs values at a 90% confidence level is shown in Figure 7.26. The width of the uncertainty band is driven by the dominant systematic uncertainty, the flux of the MC generators used in signal and background estimation. The grey regions indicate previous constraints, the details of which are given in Chapter 2.

In the case of ALPs coupling to the $SU(2)_L$ gauge boson, FASER probes previously unexplored parameter space with this analysis. ALP masses between 100 and 250 MeV, with coupling between 3×10^{-5} and $5 \times 10^{-4} \text{ GeV}^{-1}$ have been excluded by this search.

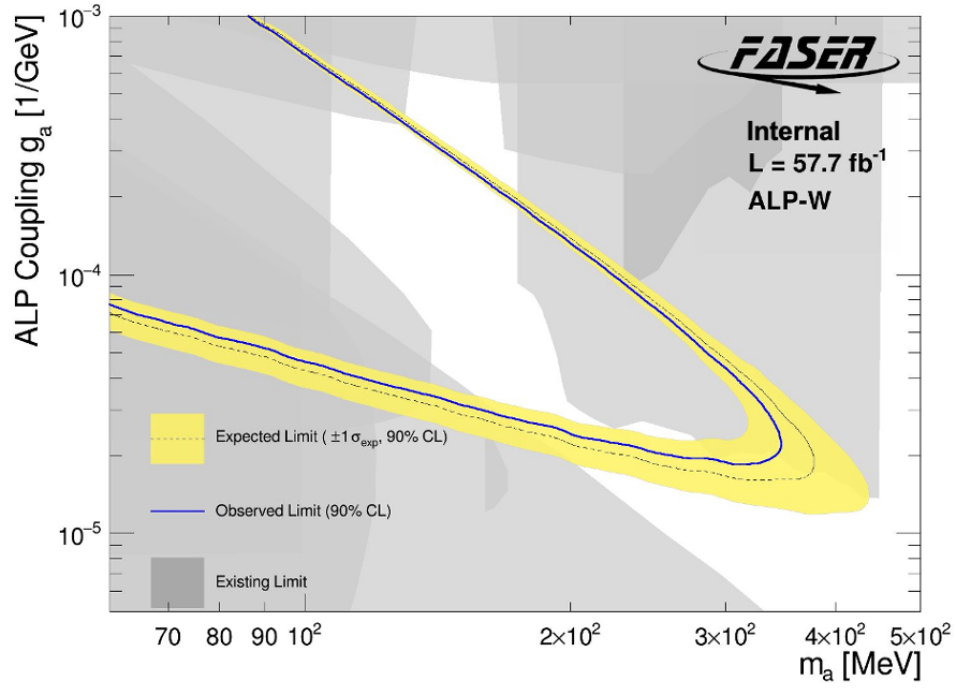


Figure 7.26: Interpretation of the signal region yield as exclusion limits for the ALP with coupling to the $SU(2)_L$ gauge boson (ALP-W), with the assumption of 0.44 neutrino background events. The expected limit with 90% CL is shown by the dashed line and yellow uncertainty band. The observed limit is shown by the blue line. Existing constraints are shown in grey.

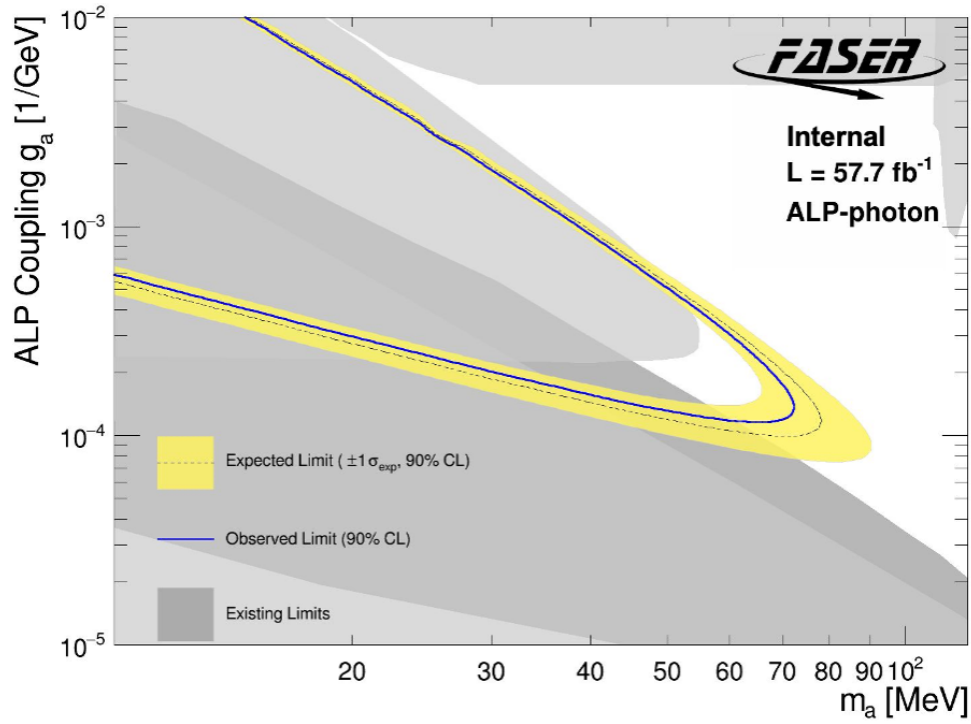


Figure 7.27: Interpretation of the signal region yield as exclusion limits for the ALP with coupling to photon (ALP-photon), with the assumption of 0.44 neutrino background events. The expected limit with 90% CL is shown by the dashed line and yellow uncertainty band. The observed limit is shown by the blue line. Existing constraints are shown in grey.

7.5.1 ALPs Coupling to Photons

The contour from evaluating the CLs values at a 90% confidence level for the ALP-photon model is shown in Figure 7.27. In this search, ALP masses up to $m_a \sim 80$ MeV are excluded and previously unexplored parameter space around $g_{a\gamma\gamma} \sim 10^{-4}$ GeV $^{-1}$ is probed. Existing constraints are set by previous experiments: E141 [169], LEP [170], NA64 [171], CHARM [86], E137 [85], NuCal [172], PrimEx [96], Belle2 [171] and BESIII [173].

7.5.2 ALPs Coupling to Gluons

The contour from evaluating the CLs values at a 90% confidence level for the ALP-gluon model is shown in Figure 7.28. The analysis probes unconstrained parameter space in the region of ALP mass around $m_a \sim 100$ MeV and coupling $g_{agg} \sim 10^{-3}$. There is also a region at higher mass that FASER explores, at mass $m_a \sim 500$ MeV and coupling $g_{agg} \sim 10^{-4}$. The reason FASER has

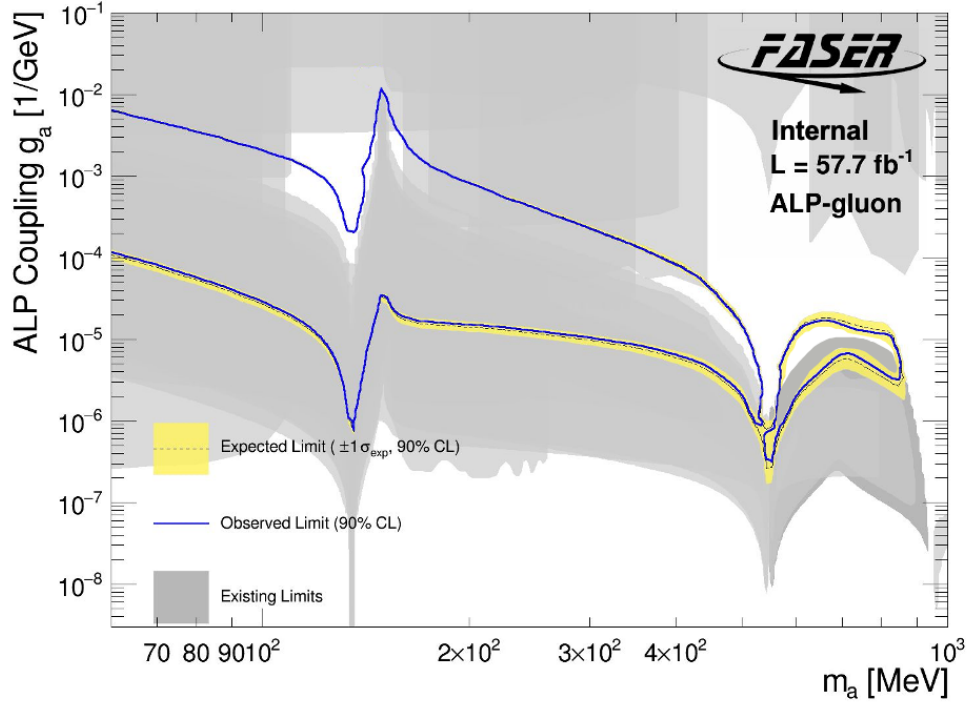


Figure 7.28: Interpretation of the signal region yield as exclusion limits for the ALP with coupling to gluons (ALP-gluon), with the assumption of 0.44 neutrino background events. The expected limit with 90% CL is shown by the dashed line and yellow uncertainty band. The observed limit is shown by the blue line. Existing constraints are shown in grey.

sensitivity in these regions is because of enhanced production rates due to resonant mixing around the π^0 mass ($m_{\pi^0} = 139$ MeV) and the η meson mass ($m_{\eta} = 548$ MeV). Existing constraints from previous experiments include limits from E949 [174], NA48 [97], NA62 [175], NuCal [176], Γ_{K^+} [177] and BaBar [103] .

7.5.3 Reinterpretations

In addition to axion-like particles, the ALP analysis can be reinterpreted for additional models with photonic final states with appropriately long lifetimes. In this section, exclusion limits are presented for: the $U(1)B$ model [178], the up-philic model [179] and the Type-I two-Higgs doublet model (2HDM) [180]. Additionally, the ALP analysis provides sensitivity to the dark photon model discussed in this thesis. A reinterpretation of the results is possible without any tracking requirements, characterising the e^+e^- decay by its EM deposits.

7.5.3.1 $U(1)B$ Gauge Boson

In a similar way that the dark photon can be a mediator to the dark sector by the introduction of an extra $U(1)$ symmetry, the $U(1)B$ gauge boson model explores the case where there is a direct coupling between a new gauge boson, Z_B , and the SM fields. The coupling of a vector boson to baryon number g_B could explain baryon number conservation in the SM [178]. The $U(1)B$ gauge boson is primarily produced in the decays of light mesons and via dark bremsstrahlung. In the mass range of interest, the main decay mode is to a pion and a photon, resulting in a photonic final state within FASER. The contour from evaluating the CLs values at a 90% confidence level for the $U(1)B$ gauge boson model is shown in Figure 7.29. At low masses, where the $U(1)B$ gauge boson mass m_{Z_B} is below that of a pion, Z_B decays radiatively to electrons. As the mass of Z_B increases, the dominant decay channel $Z_B \rightarrow \pi^0 \gamma$ becomes accessible, remaining dominant until $m_{Z_B} \sim 600$ MeV. At $m_{Z_B} > 600$ MeV, decays to $\pi^0 \pi^+ \pi^-$ become dominant, there is a small region of sensitivity in this range due to an enhanced production rate caused by ω and ρ resonance. The $U(1)B$ gauge boson model is anomalous, requiring the introduction of new, heavier fields with implications such as enhanced rare Z , B and K decays to cancel this anomaly [178]. Models related to this anomaly cancellation are indicated in Figure 7.29 by the blue dashed contour, existing constraints are shown in grey from previous experiments including exclusion limits from: NuCal [176, 181], KLOE [182], CHARM [86], E137 [88], NA48 [183], LHCb [184], PS191 [185], and LSND [71].

7.5.3.2 Up-philic scalar

In addition to ALPs there are long-lived pseudoscalars such as the up-philic scalar that can mediate the SM and dark sector. The coupling of the up-philic scalar to up quarks [179] g_u implies symmetry breaking and avoids strict constraints from B meson decays whilst ensuring that production rates in pp collisions remain high [21]. Up-philic scalars are primarily produced in the decays of η and η' mesons, with production via kaon decay and B meson decay being suppressed. The dominant decay mode, if kinematically allowed, is to a pion pair. For lower mass m_S , the lifetime of the up-philic scalar is increased due to loop-induced decays to photons [21], resulting in a photonic final state. The contour from evaluating the CLs values at a 90% confidence level for the up-philic model is shown in Figure 7.30. There is enhanced sensitivity for $m_S > 2m_{\pi^0}$ due to higher LHC energies,

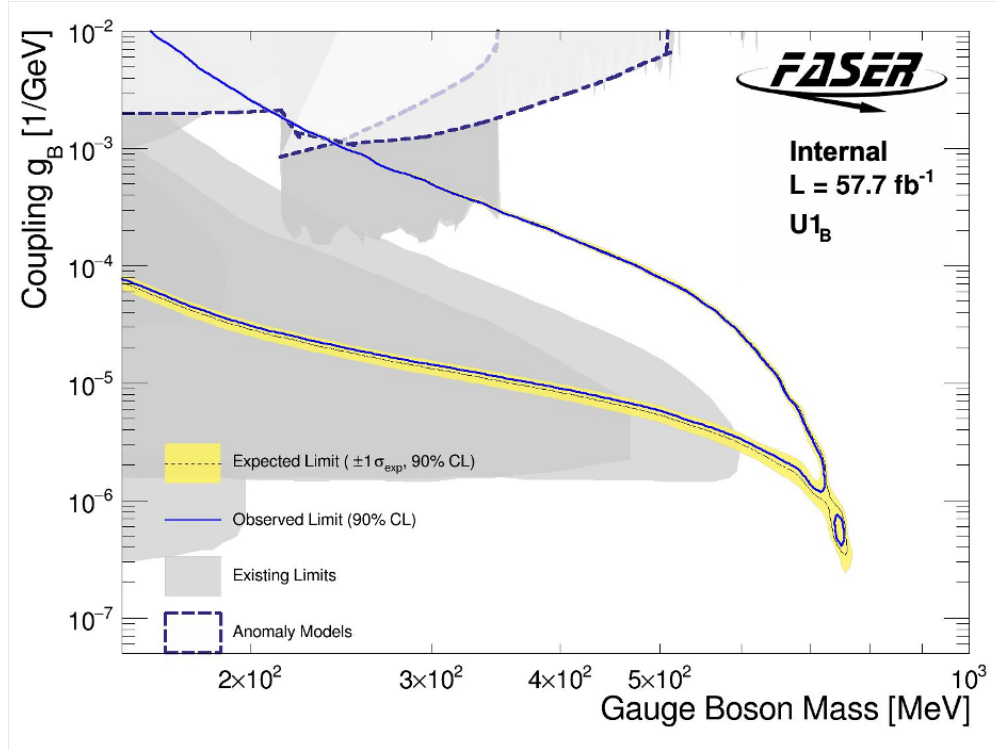


Figure 7.29: Interpretation of the signal region yield as exclusion limits for the $U(1)B$ gauge boson model. The expected limit with 90% CL is shown by the dashed line and yellow uncertainty band. The observed limit is shown by the blue line. Existing constraints are shown in grey. Certain models require the introduction of new, heavier fields which can have phenomenological implications, constraints using such models are indicated by the blue dashed line. The yellow (expected limit) band is not visible in some regions, such as the upper part of the exclusion curves, due to overlap with the blue (observed limit) line and because the expected band is smaller than the thickness of the observed line.

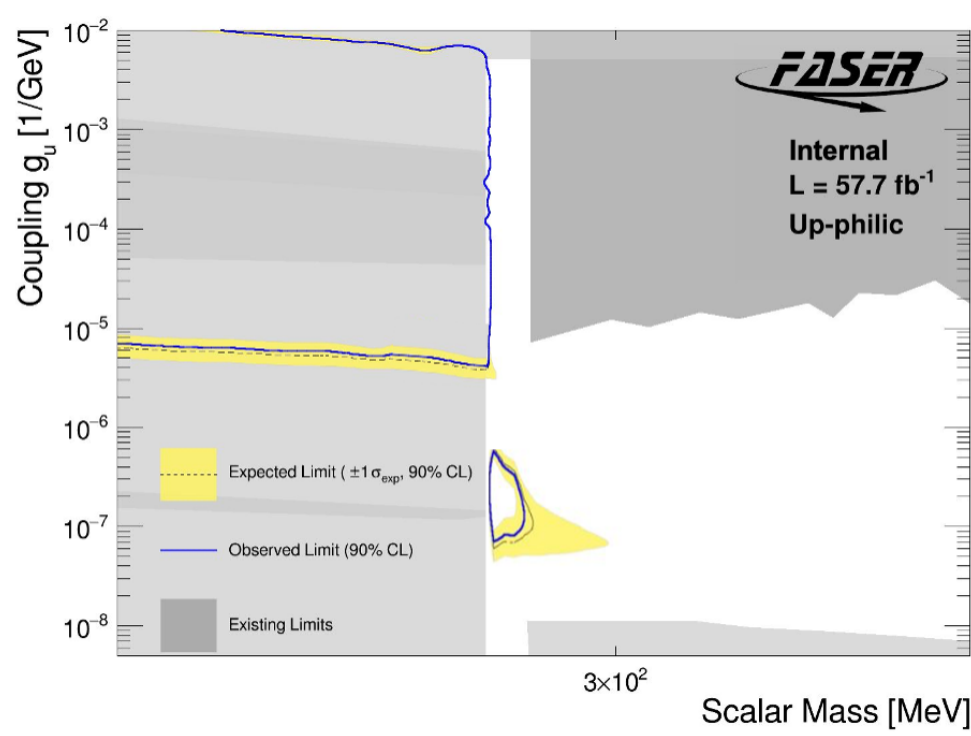


Figure 7.30: Interpretation of the signal region yield as exclusion limits for the up-philic scalar model. The expected limit with 90% CL is shown by the dashed line and yellow uncertainty band. The observed limit is shown by the blue line. Existing constraints are shown in grey.

searches by previous experiments were unable to constrain parameter space in this region [21]. Figure 7.30 contains existing constraints from previous experiments including exclusion limits from: KLOE[186], CHARM [86], E137 [85], SN1987 [104], BBN [179], MAMI [187] and BESIII [188].

7.5.3.3 Type-I two-Higgs doublet model

The Type-I two-Higgs doublet model explores the case where two $SU(2)_L$ scalar doublets Φ_i weakly couple to fermions, leading to a CP-even scalar Higgs H [180] that is long-lived. The H scalar can be produced in FCNC B meson decays and can decay to a pair of photons. The contour from evaluating the CLs values at a 90% confidence level for the 2HDM model is shown in Figure 7.31. FASER has sensitivity up to $m_H \sim 4$ GeV. Figure 7.31 contains existing constraints from previous experiments including exclusion limits from: E949 [101], LEP [189], NA62 [175], SN1986 [104] and CHARM [86].

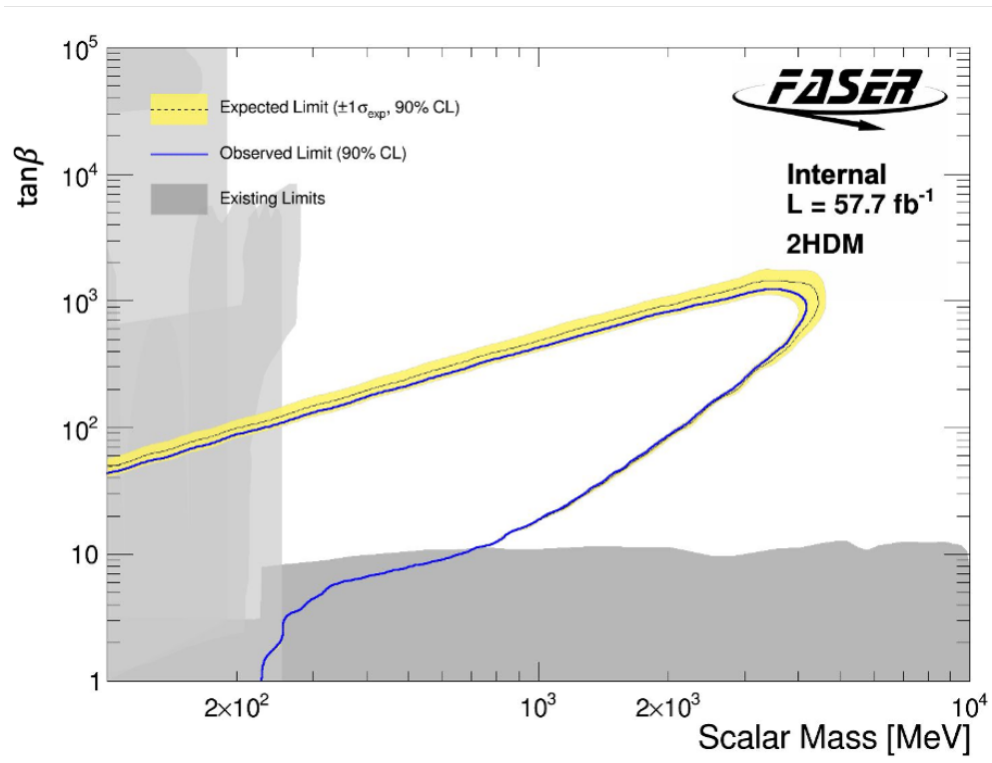


Figure 7.31: Interpretation of the signal region yield as exclusion limits for the Type-I two-Higgs doublet model. The expected limit with 90% CL is shown by the dashed line and yellow uncertainty band. The observed limit is shown by the blue line. Existing constraints are shown in grey.

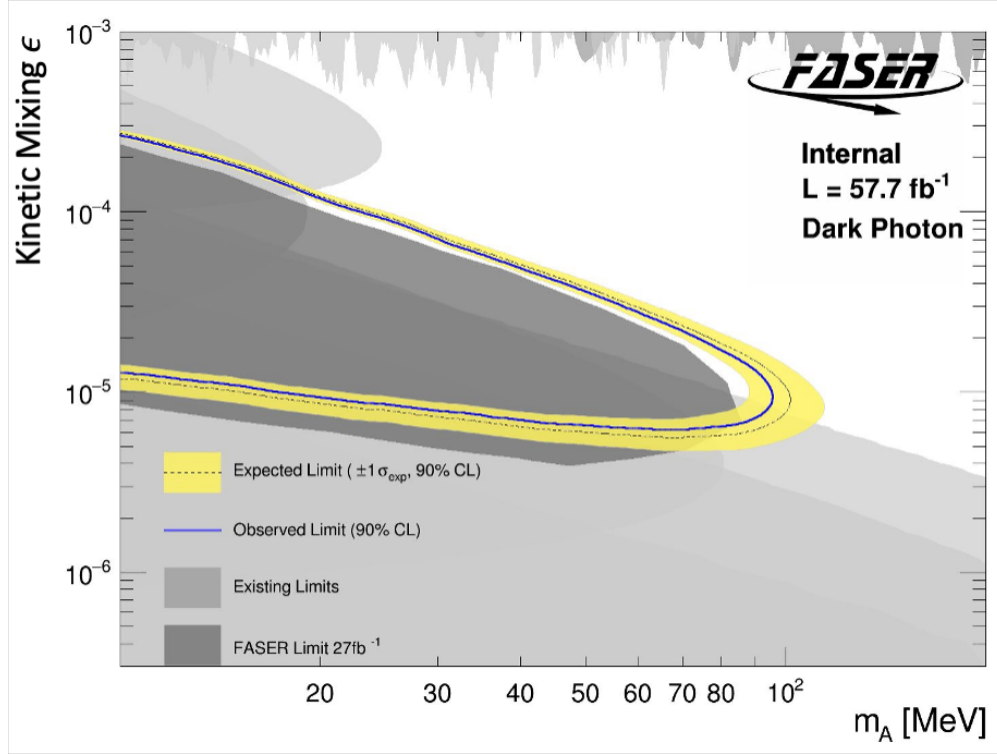


Figure 7.32: Interpretation of the signal region yield as dark photon exclusion limits. The expected limit with 90% CL is shown by the dashed line and yellow uncertainty band. The observed limit is shown by the blue line. Existing constraints are shown in grey, including FASER’s previous results.

7.5.3.4 Dark Photon

Although not a photonic final state, the decay of dark photons with mass between $2m_e$ and $2m_\mu$ to e^+e^- can be seen within FASER using the event selection for the ALP analysis. The contour from evaluating the CLs values at a 90% confidence level for the dark photon model is shown in Figure 7.32. Also shown are the existing limits from previous experiments, discussed in Chapter 2, and the limits set by FASER’s dark photon search using 27.0 fb^{-1} .

Chapter 8

The Preshower Detector Upgrade and Future Outlook

This chapter describes the work carried out in preparation for the planned preshower detector upgrade in YETS 2024. The upgrade will significantly extend FASER’s sensitivity to LLPs, particularly ALPs due to the ability to distinguish individual EM cores from highly-collimated photon pairs. The author was involved in testing the pre-production and production-level readout chips to be used in the upgraded preshower detector. This chapter also explores FASER’s plans for LHC Run 4 and beyond.

8.1 High-Precision Tungsten-Silicon Preshower Detector Upgrade

A limitation of the current preshower detector is its inability to offer any spatial resolution, necessary to identify, for example, the di-photon signature of the ALP-W model. In fact, Chapter 7 demonstrates that there are many LLP models with photons in the final state. An upgraded preshower detector would enable the ability to identify the individual cores of electromagnetic showers, greatly expanding FASER’s current physics reach [25] and ability to reject SM background.

The high-resolution preshower upgrade [25] will be installed in front of the existing calorimeter and will replace the present FASER preshower detector, shown in Figure 3.12. The current preshower contains 2 radiation lengths (χ_0) of tungsten absorbers, which precede the two plastic

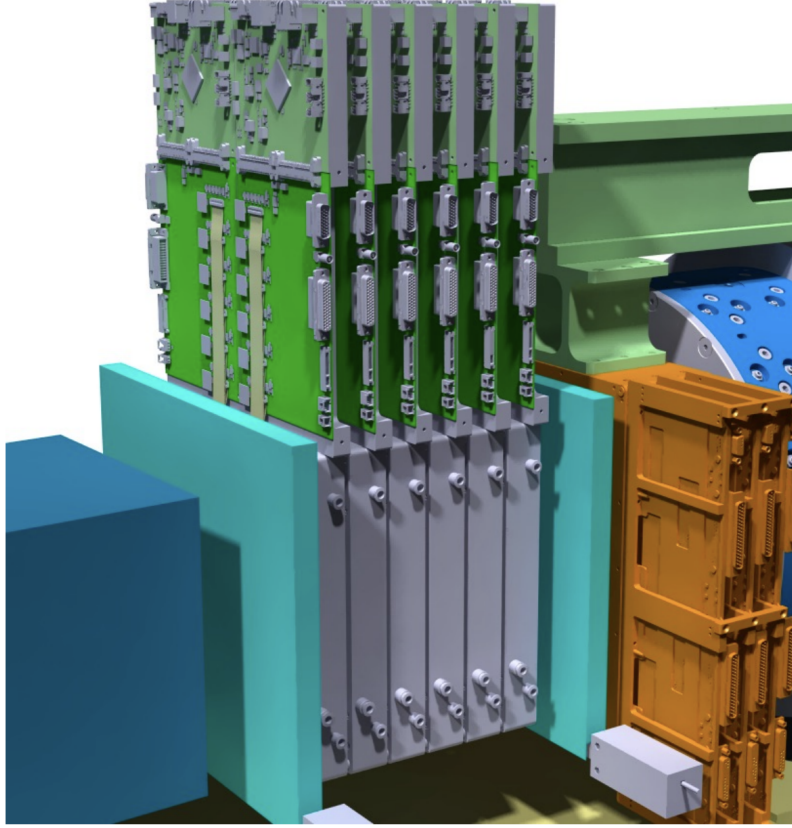


Figure 8.1: CAD view of the preshower detector upgrade, showing the six preshower detector planes.

scintillator layers. In the proposed upgrade, the layout will consist of 6 layers of $1\chi_0$ tungsten absorbers alternated with planes of monolithic silicon pixel detectors which will provide a transverse granularity of $100\mu\text{m}$ [25] needed for the detection of two-photon signatures, while maximising the ability to reject background. The plan is to install the upgrade in the YETS at the end of 2024, with the aim to begin data-taking with the upgraded detector from 2025.

8.1.1 Sub-detector Layout

The new preshower detector will be made up of six preshower detector planes and two scintillators. Figure 8.1 shows a CAD view of the preshower detector upgrade, showing the six preshower detector planes between the two scintillators. Each plane contains 12 modules, a single plane is shown in Figure 8.2a, Figure 8.2b shows a CAD diagram of the components that make up a module. Each module contains 6 ASICs with an array of 208×108 pixels.

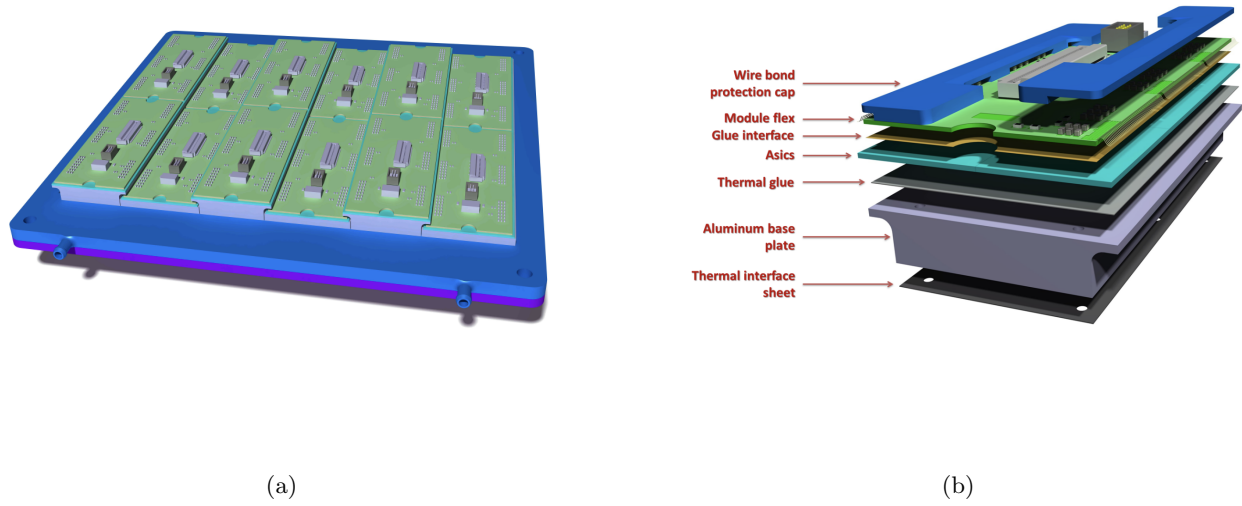


Figure 8.2: (a) A pre-shower planes with 12 modules mounted on a $20 \times 20 \text{ cm}^2$, 5 mm thick cooling plate. (b) CAD diagram of the components that make up each pre-shower module. Figure from Ref. [25].

8.1.2 Monolithic Readout Chip

The monolithic active pixel sensor uses 130 nm SiGe BiCMOS [25] technology. The readout chip will be capable of distinguishing particle showers generated by primary photons with energy 100 GeV to 3 TeV and separation above $200 \mu\text{m}$. The high dynamic range of the readout chips translates to charge measurements from 0.5 up to 65 fC, this corresponds to the huge charges deposited in single pixels at the core of the electromagnetic showers initiated in the tungsten planes by high energy photons.

The ASIC chip is $2.2 \times 1.5 \text{ cm}^2$ and is made up of 13 “super-columns” (SC) subdivided into 8 “super-pixels” (SP) each containing 16 rows of 16 pixels as shown in Figure 8.3, with a $40 \mu\text{m}$ digital column running down the middle of each SP for masking and readout. Masking is the process of excluding readout of pixels from a dataset in order to investigate and isolate the response of individual pixels, this is used to investigate noisy or bad pixels. A slow-control interface which implements an SPI (Serial Peripheral Interface) protocol allows configuration of the chip and the internal DACs (Digital-to-Analogue Converters). During chip configuration and operations testing, probe needles can be aligned with the pads. The pads are the point of contact between the probe

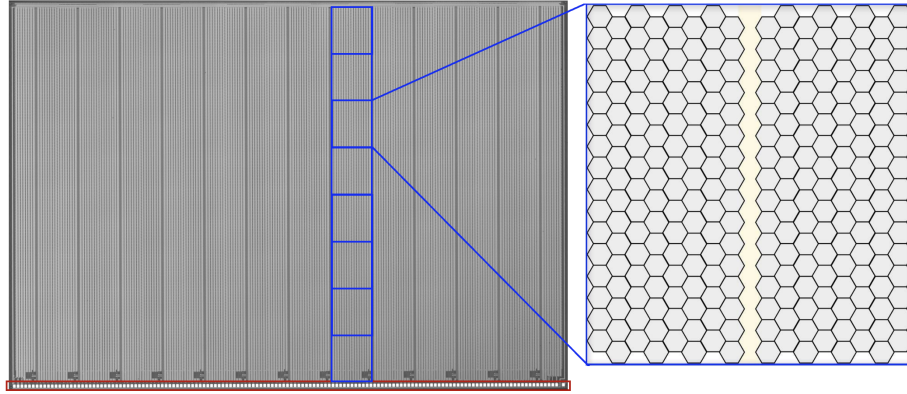


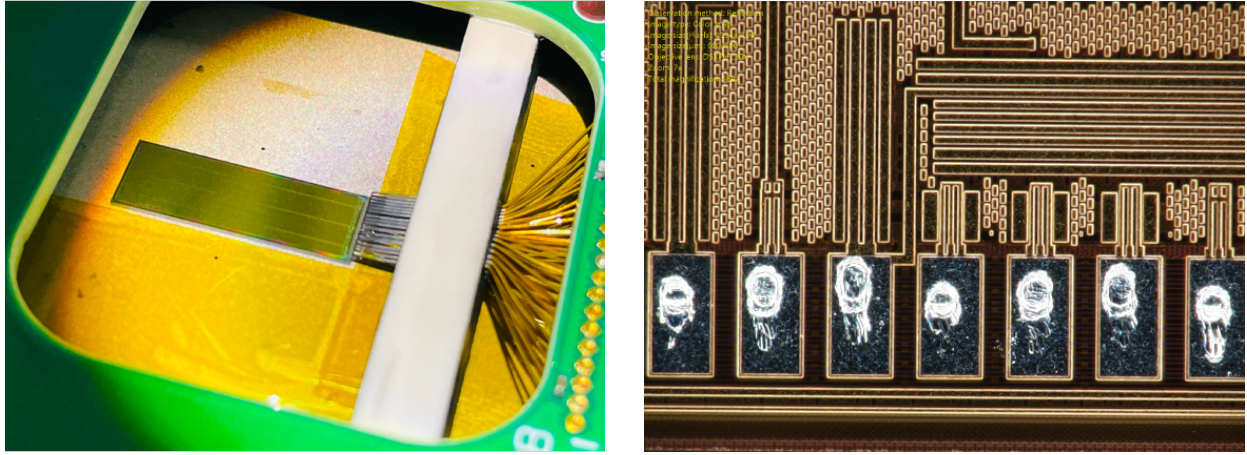
Figure 8.3: An example of one of the ASIC chips, the structure of the super-columns and 13 super pixels are indicated in blue, with a diagram of a single SP on the right-hand side, pads run along the bottom of the chip for probing (red).

needles and the ASIC, marked in red on the bottom of Figure 8.3, in order to deliver test pulses or masking commands.

8.1.3 Prototype Tests for Pre-production

In order to test the electronics and debug software and firmware needed for the preshower detector upgrade, pre-production versions of the ASIC readout chips were designed and produced. These chips contain 3 SCs, rather than the 13 SCs that make up the final production chips. Their behaviour is monitored and tested by mounting the chips into the probe station. A dedicated FASER pre-production probe card with probe needles is inserted into the setup, aligning the pads at the bottom of the chip with the probe needles, as seen in Figure 8.4a. A good contact with the probe needles is required for adequate communication with the chip, Figure 8.4b shows the result of good contact with the pads.

These tests were carried out initially to test the probe card system and to obtain standard measurements of the chips to give an idea of the yield of working chips. The chips are placed on the chuck and loaded into the probe station, whose setup includes a microscope and camera to monitor the position of the chip and to perform alignment with the needles attached to the probe card. The setup is connected to a FPGA (Field Programmable Gate Array) for data acquisition. Figure 8.5 shows the results of a low-voltage (LV) test performed on a pre-production chip. The current delivered to the FPGA board is stable, and the LV and threshold currents become stable



(a)

(b)

Figure 8.4: (a) FASER pre-production probe card used to probe the pre-production chips. (b) Marks from the probe card needles left on the pre-production chip pads after establishing a good contact.

once the configuration command is sent at around 9s into the test. This chip configures well and shows no sign of abnormalities or defects.

Once it is confirmed that the chip is successfully configured through the results of the LV test, a high-voltage (HV) scan is performed between 0 V and -150 V in steps of -100 mV. The results of such a test are shown in Figure 8.6, the chip is configured at -10 V and remains stable from this point, with no sign of breakdown. The current pulled by the HV reaches a minimum of -9.3 nA and the current pulled by the LV is 38.5 mA, which is within the expected range of chip parameters ($\mathcal{O}(10)$ mA). Additional tests are carried out to confirm that the DAQ is responding and data is being sent and readout from the chip, this includes searching for problematic pixels within the pixel matrix. This chip passes all tests and confirms that the probe card system works.

8.1.4 Tests of Production Chips

Before the arrival of the final chips, ready for characterisation and testing in a dedicated test beam, a wafer of the production-level chip was produced for further testing. Figure 8.7 shows the wafer being loaded into the probe station. The ASICs in the test wafer respond to programming commands

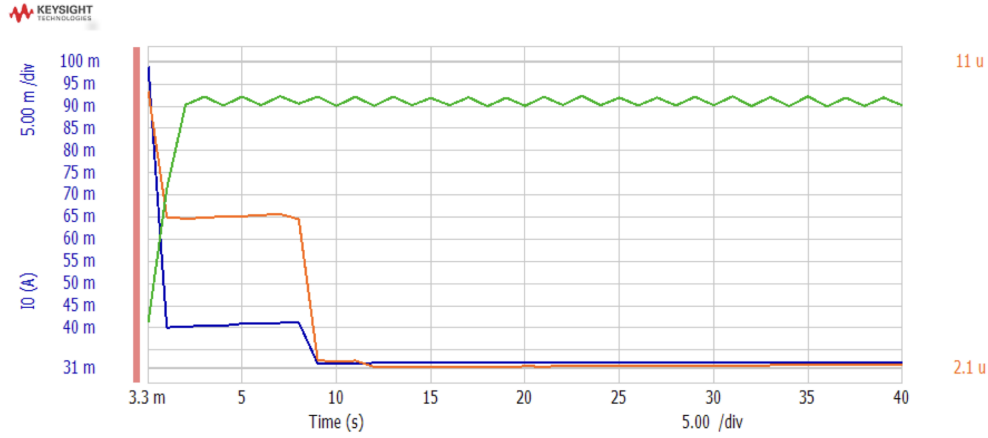


Figure 8.5: LV test to configure pre-production chip. In blue is the LV current I_0 , in orange is the threshold current I_{thr} and green is the current pulled by the FPGA.

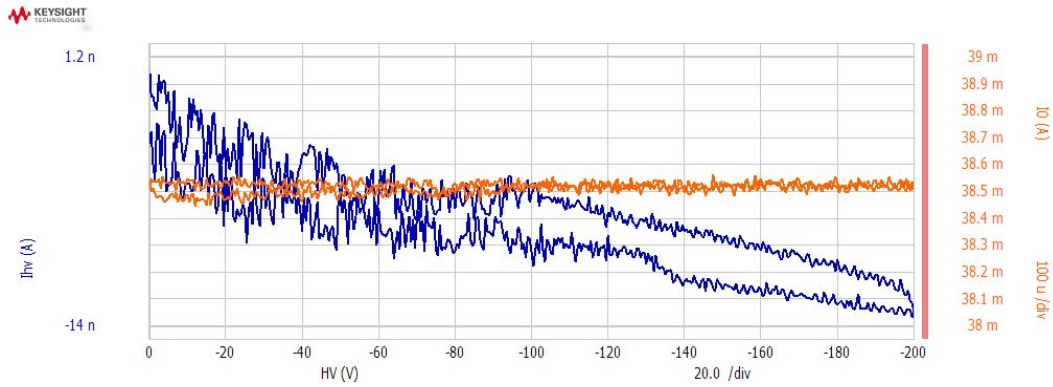


Figure 8.6: HV test to characterise pre-production chip. The current pulled by the HV I_{hv} is shown in blue, the current pulled by the LV I_0 is shown in orange.

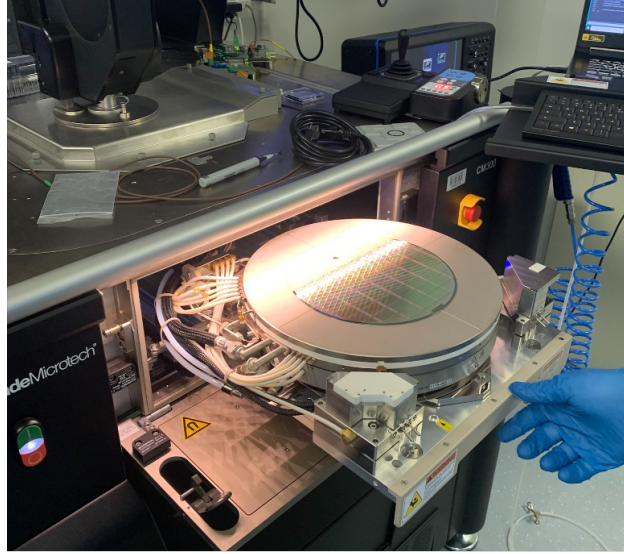


Figure 8.7: A wafer containing multiple chips being loaded into the probe station.

according to expectations. The chip was configured correctly and demonstrated sensitivity to the lowest charge of testpulse sent, which corresponds to 0.5 fC, consistent with having sensitivity to a MIP signal.

The final chips were characterised and assembled over summer, in preparation for the preshower test beam carried out in September 2024. These initial tests show that a high yield of good quality chips will be available.

8.1.5 Implications for Future ALPs Search

The upgraded preshower detector, with its ability to distinguish closely-spaced, highly-energetic di-photon signatures, will have a huge impact on low-background analyses searching for photonic final states. Of particular interest, especially given the focus of this thesis, is the ALP with coupling to the $SU(2)_L$ gauge boson. Assuming the preshower upgrade is operational for data-taking from 2025, the impact on physics reach is substantial.

The ALP-W model discussed in this thesis is the model chosen to characterise the performance of the new preshower detector, the decay signature to two high energy photons makes it the ideal choice for such studies. Figure 8.8 [25] shows the parameter space that could be explored with the improved sensitivity provided by the preshower detector upgrade for the ALP-W model.

The various limits represent the expected reach for particular scenarios, although it is important

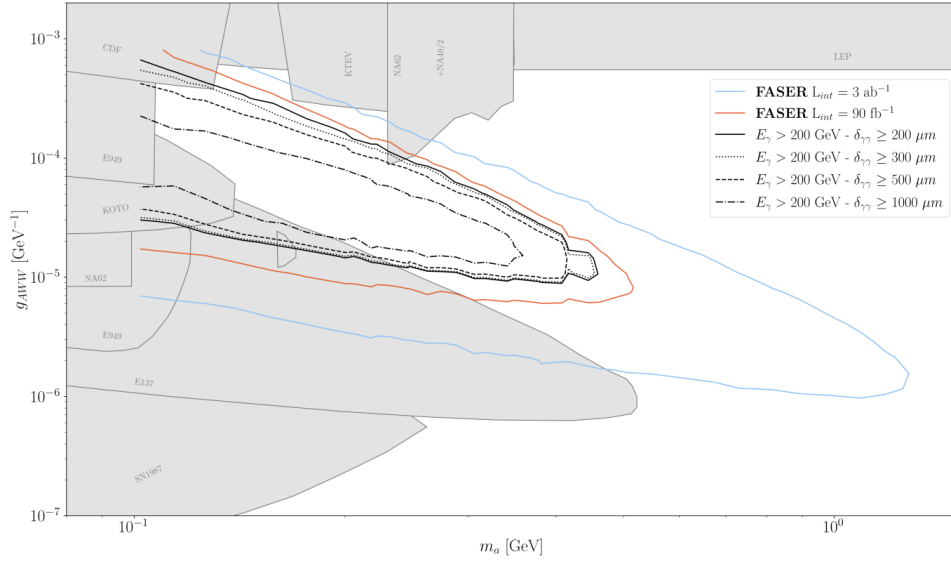


Figure 8.8: The predicted physics reach with the upgraded preshower detector in the ALP-W parameter space. Figure from Ref. [25].

to note that this figure does not show the current reach for the ALP-W analysis presented in this thesis. For comparison, the current ALP-W analysis with 57.7 fb^{-1} probes up to $m_a \sim 250 \text{ MeV}$, whereas the reach expected for an analysis using an upgraded preshower with 90 fb^{-1} , close to what has already been collected with 2022, 2023 and 2024 physics running, probes up to $m_a \sim 500 \text{ MeV}$, this is indicated by the solid red line in Figure 8.8. The blue line shows the reach in the case of an ideal detector performance with 3 ab^{-1} collected, this is the expected luminosity from the High-Luminosity LHC (HL-LHC) era between 2029 and 2042 [190].

The four black lines correspond to the expected reach from a simple photon-reconstruction algorithm, calculating di-photon reconstruction efficiencies for 200 GeV photons with separations of 200, 300, 500 and 1000 μm [25]. The limits correspond to an observation of at least 3 signal events with 100% background rejection for an integrated luminosity of 90 fb^{-1} . These sensitivity curves consider realistic detector effects, the solid black line corresponding to the most realistic expected reach with 90 fb^{-1} . The apparent decrease in reach as photon separation increases is an effect of decreasing statistics in the simulation as the majority of ALP signal is expected to produce highly-collimated photon pairs.

8.2 Outlook

With several months of data-taking left in Run 3, FASER expects to collect a total integrated luminosity of 250 fb^{-1} [26]. FASER has been approved to continue operation in Run 4, which predicts a total integrated luminosity of 680 fb^{-1} . Extending into Run 4 and the HL-LHC era, a total of 3 ab^{-1} is expected. This is a huge increase in recorded luminosity, which has a clear impact on physics reach.

In parallel, FASER has plans for improvements and upgrades to further extend physics potential. This chapter has already highlighted the increased sensitivity to ALP searches that FASER will have following the preshower detector upgrade in YETS 2024. Figure 8.9 [26] shows the projected sensitivity for the predicted Run 3 and Run 4 datasets for the ALP-W model. These estimations were done without the inclusion of the preshower upgrade [25], but still demonstrate the extended reach possible with a larger dataset. Figure 8.10 [26] shows the projected sensitivity for the predicted Run 3 and Run 4 datasets for the dark photon model. The dark photon search will also benefit from improved tracking reconstruction algorithms, leading to better tracking efficiency in identifying highly-collimated particle tracks. In addition to the already large increase in recorded luminosity since the initial dark photon search, these improvements will lead to increased sensitivity in the high mass region, resulting in, if not a discovery, then stricter constraints on this important benchmark model.

Looking even further into the future, a large portion of the FASER collaboration are actively working on the proposal for the Forward Physics Facility (FPF) which plans to include FASER2 and FASER ν 2. A sketch of the possible layout of the facility is shown in Figure 8.11 [27]. These planned experiments will be significantly larger than the current FASER and FASER ν detectors, resulting in a greater physics reach and an extended physics programme.

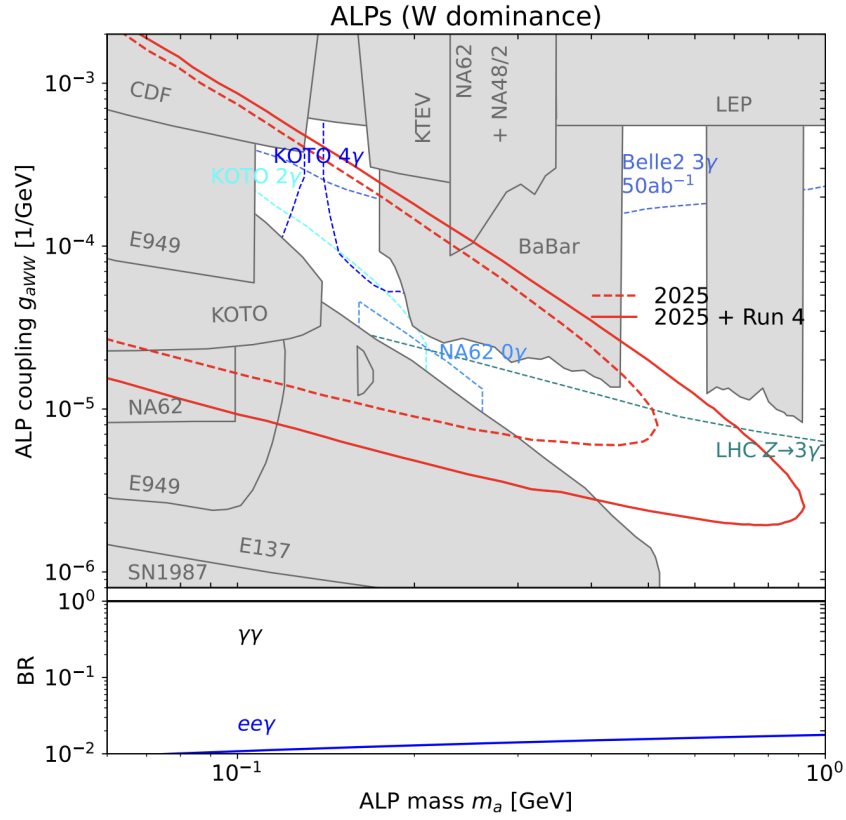


Figure 8.9: FASER's projected sensitivity to the ALP-W model with the combined Run 3 (250 fb⁻¹) and Run 4 (680 fb⁻¹) datasets. The bottom panel shows the branching fraction to the various final states as a function of mass. Figure from Ref. [26].

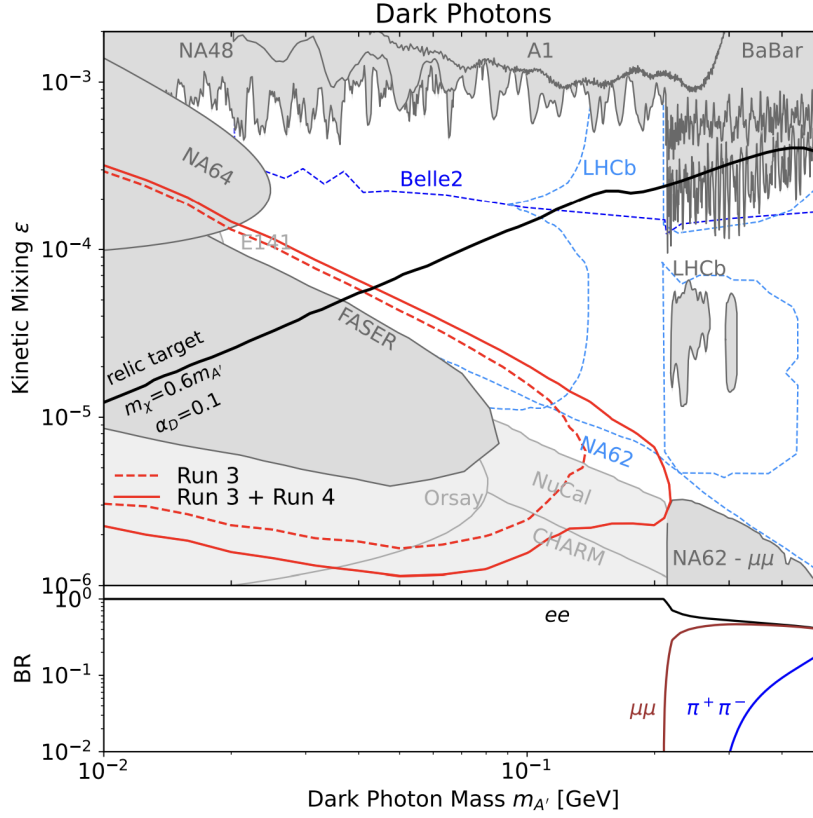


Figure 8.10: FASER’s projected sensitivity to the dark photon model with the combined Run 3 (250 fb^{-1}) and Run 4 (680 fb^{-1}) datasets. The bottom panel shows the branching fraction to the various final states as a function of mass. Figure from Ref. [26].

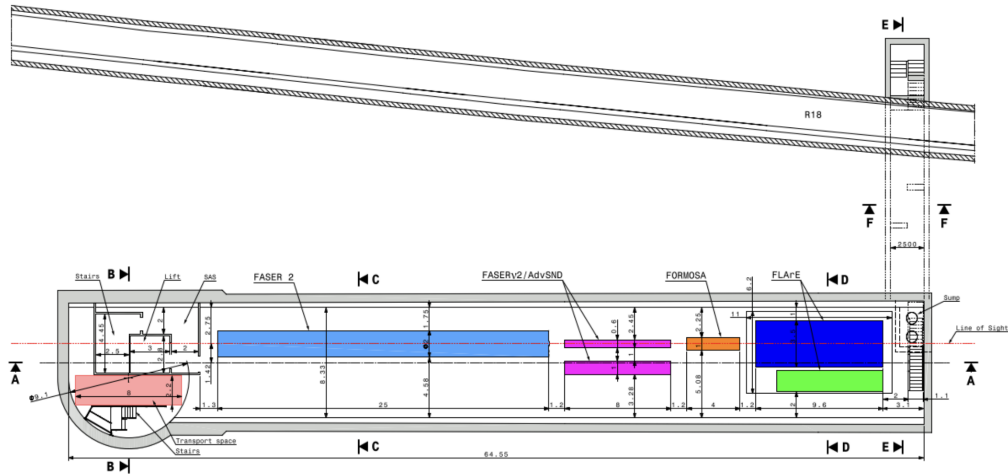


Figure 8.11: Proposed layout of the FPF experimental cavern. The coloured boxes indicated possible experiments and their dimensions. This includes FASER2 for studying LLPs and FASERν2 for studying neutrinos. Figure from Ref. [27].

Chapter 9

Conclusion

FASER has had an extremely successful start to life, with smooth operations and high quality data-taking in Run 3. The procedures in place for detector operations and monitoring have led to reliable data collection and good detector performance. The experiment has undergone multiple test beams, two of which are mentioned in this thesis. Numerous searches for BSM physics have yielded world-leading constraints and explored new parameter space.

Chapter 6 described FASER’s search for dark photons using Run 3 data at a centre of mass energy of $\sqrt{s} = 13.6$ TeV corresponding to an integrated luminosity of 27.0 fb^{-1} collected in 2022. The search sets world-leading exclusion limits for dark photons with mass of $17 \text{ MeV} < m_{A'} < 70 \text{ MeV}$ and coupling of $2 \times 10^{-5} < \epsilon < 1 \times 10^{-4}$. Chapter 7 described FASER’s search for axion-like particles. The analysis also uses Run 3 data, corresponding to an integrated luminosity of 57.7 fb^{-1} collected in 2022 and 2023. This search sets world-leading exclusion limits for ALPs with mass of $100 < m_a < 250 \text{ MeV}$ and coupling of $3 \times 10^{-5} < g_{aWW} < 5 \times 10^{-4} \text{ GeV}^{-1}$. The various reinterpretation models discussed in this thesis, for both the dark photon analysis and the axion-like particle analysis, demonstrate the versatility and breadth of FASER’s physics reach. World-leading exclusion limits have been set for: the $B - L$ gauge boson, the ALP coupling to photons, the ALP coupling to gluons, the $U(1)B$ gauge boson, the up-philic scalar, and the Type-I two Higgs doublet model.

Glossary

2HDM Type-I two-Higgs doublet model. 160, 163

ACTS A Common Tracking Software. 58

ADC Analog-to-digital converter. 59, 60

ALICE A Large Ion Collider Experiment, an LHC experiment located at IP2. 33

ALP Axion-like particle. i, vii, xviii–xxi, xxvii, xxviii, 1–4, 15, 22–25, 27, 30, 56, 76, 80–85, 89, 90, 97, 117, 118, 120, 122–124, 126–130, 132–134, 136, 137, 146–155, 157, 159–161, 165, 166, 173, 174, 177

ASIC Application Specific Integrated Circuit, used for readout in SCT modules and upgraded preshower detector. 47, 167–170

ATLAS A Toroidal LHC Apparatus, an LHC experiment located at IP1. 1, 16, 33–35, 37, 47, 57, 80, 90

BaBar The BaBar Experiment, the name is derived from the nomenclature for $B\bar{B}$. 22, 30

BBN Big Bang Nucleosynthesis. 163

BC Benchmark Case, used to identify PBC benchmark models. 15

BCID Bunch Counter ID, generated by the TLB to indicate the number of clock cycles that have passed between the last BCR and trigger signal. 52, 91, 106, 118, 120, 144

BCR Bunch Counter Reset signal. 52

- BiCMOS** Bipolar Complementary Metal-Oxide-Semiconductor, integrated circuit made up of bipolar junction transistor and CMOS logic gate. 168
- BSM** Beyond Standard Model. 1, 9, 80, 87, 89, 177
- CAD** Computer-aided Design. 167
- CB** Crystal Ball Function. xiv, 60, 63–65, 67
- CC** Charged-Current, usually in the context of neutrino interactions. 41
- CERN** Conseil Européen pour la Recherche Nucléaire, the European Council for Nuclear Research. 15, 31, 69
- CHARM** The CERN High energy Accelerator Mixed field facility. 22
- CKM** Cabibbo-Kobayashi-Maskawa. 11
- CL** Confidence Level. 157
- CMB** Cosmic Microwave Background. 9, 13
- CMS** Compact Muon Solenoid, an LHC experiment located at IP5. 33, 34
- CP** Charge-Parity. 6, 7, 11, 22, 24, 163
- CR** Control Region. 86
- DAC** Digital-to-Analogue Converts, used internally in ASIC chip. 168
- DAQ** Data Acquisition. 53, 170
- DM** Dark matter. 1, 9, 12, 13, 15
- DPMJET** Dual Parton Model (+ Jet), a MC generator for hadronic interactions based on the dual parton model. 79, 83
- ECAL** Electromagnetic Calorimeter. 2, 49, 56, 60, 64–67, 69, 71

EHN1 Experimental Hall North 1, an extension of the Neutrino Platform at the CERN Préessin site. 69, 72

EM Electromagnetic. 2, 49, 60, 62, 67, 71, 92, 122, 123, 126, 152, 157, 160, 166

EPOS-LHC Energy conserving quantum mechanical approach, based on Partons, parton ladders, strings, Off-shell remnants, and Splitting of parton ladders, an event generator. 79–81, 83, 107

EWSB Electroweak Symmetry Breaking. 5, 7, 12, 23, 27

FASER The Forward Search Experiment, an LHC experiment built to search for long-lived particles and to detect collider neutrinos. Located in the forward region 480 m from IP1. i, 1–4, 13, 15, 16, 18, 19, 22–24, 27, 30, 31, 33, 35–38, 40, 41, 43–45, 47, 49, 51, 52, 56–60, 62, 64–67, 69, 80, 83, 85, 96, 100, 106, 113, 117, 120, 157, 159, 161, 163, 165, 166, 174, 177

FCNC Flavour-changing Neutral-current. 25, 27, 81, 163

FLUKA Fluktuierende Kaskade (Fluctuating Cascade), a general purpose tool for calculations of particle transport and interactions with matter. 43, 80, 109, 134, 136

FORESEE Forward Experiment Sensitivity Estimator. 80, 81, 92, 120

FPF Forward Physics Facility. 174

FPGA Field Programmable Gate Arrays, integrated circuits. 169

GENIE Generates Events for Neutrino Interaction Experiments, a neutrino event generator. 79, 83

HERWIG Hadron Emission Reactions With Interfering Gluons, an event generator. xv, 82

HL-LHC High Luminosity LHC. 173, 174

HNL Heavy Neutral Lepton. 15

HV High Voltage. 109, 170

- IFT** Interface Tracker, part of FASER’s tracking system. 38, 45, 69
- IP** Interaction Point, location on the LHC ring where the two proton beams cross. 16, 33–38, 40, 43, 44, 80, 100
- KLOE** The K_L^0 Long Experiment. 22
- KOTO** The K_0 to Tokai Experiment. 30
- LEP** Large Electron-Positron Collider. 30, 36
- LHC** Large Hadron Collider. 1, 2, 16, 31, 33–38, 52, 57, 76, 161, 173
- LHCb** LHC Beauty experiment, an LHC experiment located at IP8. 22, 30, 33, 34, 49, 56, 57, 64–67, 69, 82
- LHCf** LHC Forward experiment, an LHC experiment designed to study the origin of ultra-high-energy cosmic rays. Consists of two independent detectors 140 m either side of IP1. 33
- LINAC** Linear accelerator, used to inject protons and ions into the CERN accelerator complex. 31
- LLP** Long-lived particles. i, 4, 19, 24, 30, 38, 57, 80, 81, 89, 166
- LO** Leading Order. 78
- LOS** Line of Sight. 16, 18, 35, 38, 57
- LS** Long Shutdown, period of shutdown for the LHC machine. 34
- LV** Low Voltage. 169, 170
- LZ** The LUX ZEPLIN Experiment, a dark matter detection experiment. 12
- MC** Monte Carlo simulation, named for the Monico casino. 2, 56, 65, 67, 69, 71, 73, 76, 80, 83–85, 89–91, 96, 97, 101, 109, 111, 117, 120, 123, 126–129, 134, 136, 138, 145, 146, 148, 152, 155, 157
- MIP** Minimum Ionising Particle. 62, 64, 94, 109, 122, 123, 129

MoEDAL Monopole and Exotics Detector at the LHC, an LHC experiment built to search for the magnetic monopole. Located at IP8. 33, 34

MPV Most Probable Value, derived from a Landau fit. 109

NLO Next-to-Leading Order. 78, 79

NuCal The ν -Calorimeter Experiment. 22

PBC CERN Physics Beyond Colliders study group. 15, 24

PDF Parton Distribution Function. 77, 79, 81, 86. Probability Density Function. 86, 87.

PID Particle Identification. 45, 134

PMT Photomultiplier Tube. 41, 43, 44, 49, 51–53, 57–59, 69, 109

POWHEG Positive Weight Hardest Emission Generator, an event generator. 78, 79, 81

PQ Peccei-Quinn. 22

PS 78, 123 Parton Shower. 78. Proton Synchrotron. 31.

QCD Quantum Chromodynamics. 7, 22, 24, 78

QED Quantum Electrodynamics. 6, 7

QGSJET Quark Gluon String (+ Jet), a MC generator for hadronic interactions based on the quark gluon string model. 79, 83, 107

RF Radiofrequency, RF cavities are used for beam acceleration in the LHC. 33

SC Super-column, part of the preshower ASIC substructure. 168

SCT Semiconductor Tracker, ATLAS modules used in the FASER tracking detector. 47, 57, 58

SiGe Silicon-Germanium. 168

SLAC Stanford Linear Accelerator Center. 30

- SM** Standard Model of Particle Physics. 1, 2, 4–9, 11, 12, 15, 17, 18, 20, 22, 23, 30, 81, 87, 91, 115–117, 161, 166
- SND@LHC** Scattering and Neutrino Detector, an LHC experiment built for the detection of collider neutrinos. Located in the forward region 480 m from IP1. 33
- SP** Super-pixel, part of the preshower ASIC substructure. 168
- SPI** Serial Peripheral Interface, a communication protocol. 168
- SPS** Super Proton Synchrotron. 31, 36
- SR** Signal Region. 86, 89
- TAN** Target Absorber for Neutral particles. 37
- TAS** Target Absorber for Secondary particles. 37
- TB** Test Beam. 148
- TDAQ** Trigger and Data Acquisition System. 51–53
- TI12** Location of the FASER experiment, a former service tunnel connecting the SPS to LEP. 38, 69, 109, 148
- TLB** Trigger Logic Board. 52, 53
- TOTEM** Total Elastic and diffractive cross section Measurement, an LHC experiment aimed at measuring total cross section, elastic scattering and diffraction processes. Located at IP5. 33, 34
- TPC** Time Projection Chamber. 12
- TRB** Tracker Readout Board. 52
- UV** Ultraviolet. 7, 15, 25
- WIMP** Weakly interacting massive particle. 13

WLS Wavelength shifting fibres or rods. 41, 66, 204

YETS Year End Technical Stop. 34, 45, 166, 167, 174

Bibliography

- [1] **FASER** Collaboration, H. Abreu *et al.*, “Search for dark photons with the FASER detector at the LHC,” *Phys. Lett. B* **848** (2024) 138378, [arXiv:2308.05587 \[hep-ex\]](#).
- [2] **FASER** Collaboration, , “Search for Axion-Like Particles in Photonic Final States with the FASER Detector at the LHC,” (2024) . <https://cds.cern.ch/record/2892328?ln=en>.
- [3] **FASER** Collaboration, R. Mammen Abraham *et al.*, “Shining Light on the Dark Sector: Search for Axion-like Particles and Other New Physics in Photonic Final States with FASER,” *JHEP* **01** (2025) 199, [arXiv:2410.10363 \[hep-ex\]](#).
- [4] E. Corbelli and P. Salucci, “The Extended Rotation Curve and the Dark Matter Halo of M33,” *Monthly Notices of the Royal Astronomical Society* **311** (2000) no. 2, 441–447. <http://dx.doi.org/10.1046/j.1365-8711.2000.03075.x>.
- [5] Chandra X-ray Observatory Center, “1E 0657-56: Site of a collision between two large galaxy clusters about 3.4 billion light years from Earth,” 2006. https://chandra.harvard.edu/photo/2006/1e0657/1e0657_hand.html.
- [6] J. L. Feng, “Dark matter candidates from particle physics and methods of detection,” *Annual Review of Astronomy and Astrophysics* **48** (2010) no. 1, 495–545. <http://dx.doi.org/10.1146/annurev-astro-082708-101659>.
- [7] **FASER** Collaboration, A. Ariga *et al.*, “FASER’s Physics Reach for Long-lived Particles,” *Phys. Rev. D* **99** (2019) no. 9, 095011, [arXiv:1811.12522 \[hep-ph\]](#).

- [8] A. Berlin and F. Kling, “Inelastic dark matter at the LHC lifetime frontier: ATLAS, CMS, LHCb, CODEX-b, FASER, and MATHUSLA,” *Physical Review D* **99** (2019) no. 1, .
<http://dx.doi.org/10.1103/PhysRevD.99.015021>.
- [9] R. Vanden Broeck, “THE CERN ACCELERATOR COMPLEX. Complexe des accélérateurs du CERN.” , 2019.
- [10] J. Gareyte, “LHC Main Parameters,” *Part. Accel.* **50** (1995) 61–68.
<https://inspirehep.net/literature/407420>.
- [11] **FASER** Collaboration, , “FASER Public Plots,” 2022.
<https://faser-public-plots.app.cern.ch/>.
- [12] C. Gwilliam, “Hidden Sector Experiments,” in *IOP Joint APP, HEPP and NP Annual Conference 2024*. 04, 2024. <https://indico.cern.ch/event/1388874/>.
- [13] **FASER** Collaboration, A. Ariga *et al.*, “FASER: ForwArd Search ExpeRiment at the LHC,” [arXiv:1901.04468](https://arxiv.org/abs/1901.04468) [hep-ex].
- [14] **FASER** Collaboration, H. Abreu *et al.*, “The FASER Detector,” *Journal of Instrumentation* **19** (2024) no. 05, P05066.
<http://dx.doi.org/10.1088/1748-0221/19/05/P05066>.
- [15] C. Cavanagh, “Faser’s electromagnetic calorimeter test beam studies,” *Instruments* **6** (2022) no. 3, . <https://www.mdpi.com/2410-390X/6/3/31>.
- [16] S. Barsuk *et al.*, “Design and construction of electromagnetic calorimeter for LHCb experiment,”. <https://inspirehep.net/files/cd29a831847b420ac2f4e3eafa777780>.
- [17] **FASER** Collaboration, H. Abreu *et al.*, “The Trigger and Data Acquisition System of the FASER Experiment,” *Journal of Instrumentation* **16** (2021) no. 12, .
<http://dx.doi.org/10.1088/1748-0221/16/12/P12028>.
- [18] **FASER** Collaboration, “PMT Waveform Reconstruction and Calorimeter Energy Calibration,”. <https://cds.cern.ch/record/2851265/>.

- [19] V. Morisbak, “Search for New Physics with ATLAS at LHC - Z’ dilepton resonance at high mass,”. <https://cds.cern.ch/record/1327635>.
- [20] P. Robbe, *Simulation of the LHCb Electromagnetic Calorimeter response with Geant4*. XI International Conference on Calorimetry in High Energy Physics, LHCb Calorimeter Group, (2004). <https://cds.cern.ch/record/1445300>.
- [21] F. Kling and S. Trojanowski, “Forward Experiment Sensitivity Estimator for the LHC and Future Hadron Colliders,” *Physical Review D* **104** (2021) no. 3, .
- [22] L. Buonocore, F. Kling, L. Rottoli, and J. Sominka, “Predictions for Neutrinos and New Physics from Forward Heavy Hadron Production at the LHC,” [arXiv:2309.12793](https://arxiv.org/abs/2309.12793) [hep-ph].
- [23] J. L. Feng, F. Kling, M. Fieg, and R. Mammen Abraham, “Neutrino Rate Predictions for FASER,” [arXiv:2402.13318](https://arxiv.org/abs/2402.13318) [hep-ex]. <https://arxiv.org/abs/2402.13318>.
- [24] G. Cowan, K. Cranmer, E. Gross, and O. Vitells, “Asymptotic formulae for likelihood-based tests of new physics,” *The European Physical Journal C* **71** (2011) no. 2, .
<http://dx.doi.org/10.1140/epjc/s10052-011-1554-0>.
- [25] **FASER** Collaboration, “The FASER W-Si High Precision Preshower Technical Proposal,”. https://cernbox.cern.ch/pdf-viewer/public/S4N1ULL8HWCRPom/FASERPreshowerUpgradeTechnicalProposal_LHCC_v2.pdf.
- [26] **FASER** Collaboration, “Request to run FASER in Run 4,” tech. rep., CERN, Geneva, 2023. <https://cds.cern.ch/record/2882503>.
- [27] J. L. Feng *et al.*, “The Forward Physics Facility at the High-Luminosity LHC,” *Journal of Physics G: Nuclear and Particle Physics* **50** (Jan., 2023) 030501.
<http://dx.doi.org/10.1088/1361-6471/ac865e>.
- [28] **Planck** Collaboration, N. Aghanim *et al.*, “Planck 2018 results. VI. Cosmological parameters,” *Astron. Astrophys.* **641** (2020) A6, [arXiv:1807.06209](https://arxiv.org/abs/1807.06209) [astro-ph.CO].
[Erratum: *Astron.Astrophys.* 652, C4 (2021)].

- [29] M. Cacciari and G. Hamel de Monchenault, “Standard Model Theory Calculations and Experimental Tests,” *Comptes Rendus Physique* **16** (2015) no. 4, 368–378.
<https://doi.org/10.1016/j.crhy.2015.04.004>.
- [30] **Particle Data Group** Collaboration, S. Navas *et al.*, “Review of Particle Physics,” *Phys. Rev. D* **110** (2024) .
- [31] **Katrin** Collaboration, , “Direct neutrino-mass measurement with sub-electronvolt sensitivity,” *Nat. Phys.* **18** (2022) 160–166.
- [32] C. Rovelli, “Notes for a brief history of quantum gravity,” 2001.
<https://arxiv.org/abs/gr-qc/0006061>.
- [33] **ATLAS** Collaboration, , “Observation of a New Particle in the Search for the Standard Model Higgs Boson with the ATLAS Detector at the LHC,” *Phys. Lett. B* **716** (2012) no. 1, 1–29. <https://doi.org/10.1016/j.physletb.2012.08.020>.
- [34] **CMS** Collaboration, , “Observation of a New Boson at a Mass of 125 GeV with the CMS Experiment at the LHC,” *Phys. Lett. B* **716** (2012) no. 1, 30–61.
<https://doi.org/10.48550/arXiv.1207.7235>.
- [35] J. Ellis, “Outstanding Questions: Physics Beyond the Standard Model,” *Phil. Trans. R. Soc. A* **370** (2012) 818–830.
- [36] M. C. Gonzalez-Garcia, “Neutrino Masses and Mixing: Evidence and Implications,” *Rev. Mod. Phys.* **75** (2003) no. 345, . <http://dx.doi.org/10.1103/RevModPhys.75.345>.
- [37] R. Alkofer and H. Reinhardt, *Chiral Quark Dynamics*. Springer-Verlag Berlin Heidelberg, Germany, 1995.
- [38] M. Gell-Mann, “A Schematic Model of Baryons and Mesons,” *Phys. Lett.* **8** (1964) 214–215.
- [39] D. Johnson, I. Polyakov, T. Skwarnicki, and M. Wang, “Exotic Hadrons at LHCb,”
[arXiv:2403.04051](https://arxiv.org/abs/2403.04051) [hep-ex].
- [40] D. Wu, “A brief introduction to the strong CP problem,” *Zeitschrift für Naturforschung A* **52** (1997) no. 1-2, 179–182. <https://doi.org/10.1515/zna-1997-1-245>.

- [41] M. Thomson, *Modern Particle Physics*. Cambridge University Press, 2013.
- [42] J. Fröhlich, G. Morchio, and F. Strocchi, “Higgs phenomenon without symmetry breaking order parameter,” *Nuclear Physics B* **190** (1981) no. 3, 553–582.
<https://www.sciencedirect.com/science/article/pii/055032138190448X>.
- [43] P. Nason, “Introduction to QCD,” *Conf. Proc. C* **9705251** (1997) 94–149.
- [44] A. Hoecker and Z. Ligeti, “CP Violation and the CKM Matrix,” *Annual Review of Nuclear and Particle Science* **56** (2006) no. 1, 501–567.
- [45] R. D. Peccei and H. R. Quinn, “CP Conservation in the Presence of Pseudoparticles,” *Phys. Rev. Lett.* **38** (1977) 1440–1443.
- [46] F. Wilczek, “Problem of Strong P and T Invariance in the Presence of Instantons,” *Phys. Rev. Lett.* **40** (1978) 279–282.
- [47] E. Babichev *et al.*, “Gravitational Origin of Dark Matter,” *Phys. Rev. D* **94** (2016) no. 8, .
<https://doi.org/10.48550/arXiv.1604.08564>.
- [48] **Planck** Collaboration, , “Planck 2018 Results. IV. Diffuse Component Separation,” *Astron. Astrophys.f* **641** (2020) . <https://doi.org/10.48550/arXiv.1807.06208>.
- [49] R. H. Wechsler and J. L. Tinker, “The Connection Between Galaxies and Their Dark Matter Halos,” *Annual Review of Astronomy and Astrophysics* **56** (2018) no. 1, 435–487.
<http://dx.doi.org/10.1146/annurev-astro-081817-051756>.
- [50] M. C. Weisskopf, H. D. Tananbaum, L. P. van Speybroeck, and S. L. O’Dell, “Chandra x-ray observatory (cxo):overview,” *Proc. SPIE Int. Soc. Opt. Eng.* **4012** (2000) 2,
[arXiv:astro-ph/0004127](https://arxiv.org/abs/astro-ph/0004127).
- [51] R. Massey, T. Kitching, and J. Richard, “The dark matter of gravitational lensing,” *Reports on Progress in Physics* **73** (2010) no. 8, 086901.
<http://dx.doi.org/10.1088/0034-4885/73/8/086901>.

- [52] G. White, “The sakharov conditions,” in *Electroweak Baryogenesis (Second Edition)*, 2053-2563, pp. 2–1 to 2–2. IOP Publishing, 2022.
<https://dx.doi.org/10.1088/978-0-7503-3571-3ch2>.
- [53] I. Esteban, M. C. Gonzalez-Garcia, and M. Maltoni, “On the determination of leptonic cp violation and neutrino mass ordering in presence of non-standard interactions: present status,” *Journal of High Energy Physics* **2019** (2019) no. 6, .
[http://dx.doi.org/10.1007/JHEP06\(2019\)055](http://dx.doi.org/10.1007/JHEP06(2019)055).
- [54] M. Battaglieri *et al.*, “US Cosmic Visions: New Ideas in Dark Matter 2017: Community Report,” (2017) , [arXiv:1707.04591 \[hep-ph\]](https://arxiv.org/abs/1707.04591). <https://arxiv.org/abs/1707.04591>.
- [55] F. S. Queiroz, “Dark Matter Overview: Collider, Direct and Indirect Detection Searches,” 2016. <https://arxiv.org/abs/1605.08788>.
- [56] Pieri, Lidia and Lavalle, Julien and Bertone, Gianfranco and Branchini, Enzo, “Implications of High-Resolution Simulations on Indirect Dark Matter Searches,” *Phys. Rev. D* **83** (2011) 023518, [arXiv:0908.0195 \[astro-ph.HE\]](https://arxiv.org/abs/0908.0195).
- [57] T. M. Undagoitia and L. Rauch, “Dark matter direct-detection experiments,” *Journal of Physics G: Nuclear and Particle Physics* **43** (2015) no. 1, 013001.
<http://dx.doi.org/10.1088/0954-3899/43/1/013001>.
- [58] **LZ** Collaboration, J. Aalbers *et al.*, “First Dark Matter Search Results from the LUX-ZEPLIN (LZ) Experiment,” *Phys. Rev. Lett.* **131** (2023) no. 4, 041002, [arXiv:2207.03764 \[hep-ex\]](https://arxiv.org/abs/2207.03764).
- [59] **DarkSide-20k** Collaboration, I. Manthos, “DarkSide-20k: Next generation Direct Dark Matter searches with liquid Argon,” *PoS EPS-HEP2023* (2024) 113, [arXiv:2312.03597 \[hep-ex\]](https://arxiv.org/abs/2312.03597).
- [60] A. Boveia and C. Doglioni, “Dark Matter Searches at Colliders,” *Annual Review of Nuclear and Particle Science* **68** (2018) no. 1, 429–459.
<http://dx.doi.org/10.1146/annurev-nucl-101917-021008>.

- [61] R. J. Scherrer and M. S. Turner, “On the Relic, Cosmic Abundance of Stable Weakly Interacting Massive Particles,” *Phys. Rev. D* **33** (1986) 1585. [Erratum: Phys.Rev.D 34, 3263 (1986)].
- [62] T. Bringmann, T. Edsjö, P. Gondolo, P. Ullio, and L. Bergström, “DarkSUSY 6: An advanced tool to compute dark matter properties numerically,” *Journal of Cosmology and Astroparticle Physics* **2018** (2018) no. 07, 033–033.
<http://dx.doi.org/10.1088/1475-7516/2018/07/033>.
- [63] M. Strassler and K. Zurek, “Echoes of a Hidden Valley at Hadron Colliders,” (2006) .
<https://arxiv.org/pdf/hep-ph/0604261.pdf>.
- [64] J. Beacham *et al.*, “Physics beyond colliders at CERN: beyond the Standard Model working group report,” *Journal of Physics G: Nuclear and Particle Physics* **47** (2019) no. 1, 010501.
<http://dx.doi.org/10.1088/1361-6471/ab4cd2>.
- [65] J. L. Feng, I. Galon, F. Kling, and S. Trojanowski, “ForwArd Search ExpeRiment at the LHC,” *Phys. Rev. D* **97** (2018) no. 3, 035001, [arXiv:1708.09389](https://arxiv.org/abs/1708.09389) [hep-ph].
- [66] J. L. Feng, I. Galon, F. Kling and S. Trojanowski, “ALPs at FASER: The LHC as a Photon Beam Dump,” *Physical Review D* **98** (2021) no. 5, .
<http://dx.doi.org/10.1103/PhysRevD.98.055021>.
- [67] F. Kling and S. Trojanowski, “Looking forward to test the KOTO anomaly with FASER,” *Phys. Rev. D* **102** (2020) no. 1, 015032, [arXiv:2006.10630](https://arxiv.org/abs/2006.10630) [hep-ph].
- [68] E. Izaguirre, T. Lin and B. Shuve, “A New Flavor of Searches for Axion-Like Particles,” *Physical Review Letters* **118** (2017) no. 11, .
<http://dx.doi.org/10.1103/PhysRevLett.118.111802>.
- [69] **FASER** Collaboration, , “Technical Proposal for FASER: ForwArd Search ExpeRiment at the LHC,” (2018) , [arXiv:1812.09139](https://arxiv.org/abs/1812.09139).
- [70] S. Biswas *et al.*, “Searching for Massless Dark Photons at the LHC via Higgs Boson Production,” *PoS EPS-HEP2017* (2017) 315.

- [71] M. Bauer, P. Foldenauer, and J. Jaeckel, “Hunting All the Hidden Photons,” *JHEP* **07** (2018) 094, [arXiv:1803.05466 \[hep-ph\]](#).
- [72] **Particle Data Group** Collaboration, P. A. Zyla *et al.*, “Review of Particle Physics,” *Progress of Theoretical and Experimental Physics* **2020** (2020) .
<https://doi.org/10.1093/ptep/ptaa104>.
- [73] **FASER** Collaboration, A. Ariga *et al.*, “FASER’s physics reach for long-lived particles,” *Phys. Rev. D* **99** (2019) no. 9, 095011, [arXiv:1811.12522 \[hep-ph\]](#).
- [74] D. Curtin, R. Essig, S. Gori, and J. Shelton, “Illuminating dark photons with high-energy colliders,” *Journal of High Energy Physics* **2015** (2015) no. 2, .
[http://dx.doi.org/10.1007/JHEP02\(2015\)157](http://dx.doi.org/10.1007/JHEP02(2015)157).
- [75] **BaBar** Collaboration, J. P. Lees *et al.*, “Search for a Dark Photon in e^+e^- Collisions at BaBar,” *Phys. Rev. Lett.* **113** (2014) no. 20, 201801, [arXiv:1406.2980 \[hep-ex\]](#).
- [76] F. Archilli, D. Babusci, D. Badoni, *et al.*, “Search for a Vector Gauge Boson in ϕ Meson Decays with the KLOE Detector,” *Physics Letters B* **706** (2012) no. 4–5, 251–255.
<http://dx.doi.org/10.1016/j.physletb.2011.11.033>.
- [77] **LHCb** Collaboration, , “Search for Dark Photons Produced in 13 TeV Collisions,” *Physical Review Letters* **120** (2018) no. 6, .
<http://dx.doi.org/10.1103/PhysRevLett.120.061801>.
- [78] **NA62** Collaboration, , “Search for Leptonic Decays of the Dark Photon at NA62,” [arXiv:2312.12055 \[hep-ex\]](#). <https://arxiv.org/abs/2312.12055>.
- [79] **NA62** Collaboration, , “Search for Dark Photon Decays to $\mu^+\mu^-$ at NA62,” [arXiv:2303.08666 \[hep-ex\]](#). <https://arxiv.org/abs/2303.08666>.
- [80] **NA64** Collaboration, , “Search for a Hypothetical 16.7 MeV Gauge Boson and Dark Photons in the NA64 Experiment at CERN,” *Physical Review Letters* **120** (2018) no. 23, .
<http://dx.doi.org/10.1103/PhysRevLett.120.231802>.

- [81] **NA48/2** Collaboration, , “Search for the Dark Photon in π^0 Decays,” [arXiv:1504.00607 \[hep-ex\]](#). <https://arxiv.org/abs/1504.00607>.
- [82] E. M. Riordan *et al.*, “Search for Short-lived Axions in an Electron-Beam-Dump Experiment,” *Phys. Rev. Lett.* **59** (1987) 755–758.
<https://link.aps.org/doi/10.1103/PhysRevLett.59.755>.
- [83] M. Davier and H. Nguyen Ngoc, “An Unambiguous Search for a Light Higgs Boson,” *Physics Letters B* **229** (1989) no. 1, 150–155.
<https://www.sciencedirect.com/science/article/pii/0370269389901743>.
- [84] J. Blumlein *et al.*, “Limits on the mass of light (pseudo)scalar particles from Bethe-Heitler e^+e^- and $\mu^+\mu^-$ pair production in a proton - iron beam dump experiment,” *Int. J. Mod. Phys. A* **7** (1992) 3835–3850.
- [85] J. D. Bjorken *et al.*, “Search for neutral metastable penetrating particles produced in the slac beam dump,” *Phys. Rev. D* **38** (1988) 3375–3386.
<https://link.aps.org/doi/10.1103/PhysRevD.38.3375>.
- [86] **CHARM** Collaboration, F. Bergsma *et al.*, “Search for Axion Like Particle Production in 400–GeV Proton - Copper Interactions,” *Phys. Lett. B* **157** (1985) 458–462.
- [87] S. Andreas, C. Niebuhr, and A. Ringwald, “New Limits on Hidden Photons from Past Electron Beam Dumps,” *Phys. Rev. D* **86** (2012) 095019, [arXiv:1209.6083 \[hep-ph\]](#).
- [88] J. D. Bjorken, R. Essig, P. Schuster, and N. Toro, “New Fixed-Target Experiments to Search for Dark Gauge Forces,” *Phys. Rev. D* **80** (2009) 075018, [arXiv:0906.0580 \[hep-ph\]](#).
- [89] P. Ilten, Y. Soreq, M. Williams, and W. Xue, “Serendipity in dark photon searches,” *JHEP* **06** (2018) 004, [arXiv:1801.04847 \[hep-ph\]](#).
- [90] Y. Tsai, P. deNiverville, and M. X. Liu, “Dark Photon and Muon $g - 2$ Inspired Inelastic Dark Matter Models at the High-Energy Intensity Frontier,” *Phys. Rev. Lett.* **126** (2021) no. 18, 181801, [arXiv:1908.07525 \[hep-ph\]](#).

- [91] P. Hansson Adrian et al., “Dark Sectors and New, Light, Weakly-Coupled Particles,” (2013) , [arXiv:1311.0029 \[hep-ph\]](#). <https://arxiv.org/abs/1311.0029>.
- [92] T. Banks, Y. Nir and N. Seiberg, “Missing (up) Mass, Accidental Anomalous Symmetries, and the Strong CP Problem,” (1994) , [arXiv:hep-ph/9403203 \[hep-ph\]](#).
- [93] H. Fukuda, M. Ibe, M. Suzuki, and T. T. Yanagida, “A ”gauged” $U(1)$ Peccei–Quinn symmetry,” *Phys. Lett. B* **771** (2017) 327–331, [arXiv:1703.01112 \[hep-ph\]](#).
- [94] B. Döbrich, J. Jaeckel, F. Kahlhoefer, A. Ringwald, and K. Schmidt-Hoberg, “ALPtraum: ALP production in proton beam dump experiments,” *JHEP* **02** (2016) 018, [arXiv:1512.03069 \[hep-ph\]](#).
- [95] S. Weinberg, “A New Light Boson?,” *Phys. Rev. Lett.* **40** (1978) 223–226.
- [96] D. Aloni, Y. Soreq, and M. Williams, “Coupling QCD-Scale Axionlike Particles to Gluons,” *Phys. Rev. Lett.* **123** (2019) no. 3, 031803, [arXiv:1811.03474 \[hep-ph\]](#).
- [97] **NA62** Collaboration, C. Lazzeroni *et al.*, “Study of the $K^\pm \rightarrow \pi^\pm \gamma \gamma$ decay by the NA62 experiment,” *Phys. Lett. B* **732** (2014) 65–74, [arXiv:1402.4334 \[hep-ex\]](#).
- [98] **KTeV** Collaboration, E. Abouzaid *et al.*, “Final Results from the KTeV Experiment on the Decay $K_L \rightarrow \pi^0 \gamma \gamma$,” *Phys. Rev. D* **77** (2008) 112004, [arXiv:0805.0031 \[hep-ex\]](#).
- [99] **KOTO** Collaboration, J. K. Ahn *et al.*, “Search for the $K_L \rightarrow \pi^0 \nu \bar{\nu}$ and $K_L \rightarrow \pi^0 X^0$ decays at the J-PARC KOTO experiment,” *Phys. Rev. Lett.* **122** (2019) no. 2, 021802, [arXiv:1810.09655 \[hep-ex\]](#).
- [100] **E949** Collaboration, A. V. Artamonov *et al.*, “Search for the decay K^+ to $\pi^+ \gamma \gamma$ in the π^+ momentum region $P > 213$ MeV/c,” *Phys. Lett. B* **623** (2005) 192–199, [arXiv:hep-ex/0505069](#).
- [101] **E949** Collaboration, A. V. Artamonov *et al.*, “Study of the decay $K^+ \rightarrow \pi^+ \nu \bar{\nu}$ in the momentum region $140 < P_\pi < 199$ MeV/c,” *Phys. Rev. D* **79** (2009) 092004, [arXiv:0903.0030 \[hep-ex\]](#).

- [102] M. Bauer, M. Neubert, and A. Thamm, “Collider Probes of Axion-Like Particles,” *JHEP* **12** (2017) 044, [arXiv:1708.00443 \[hep-ph\]](#).
- [103] **BaBar** Collaboration, , “Search for an Axion-Like Particle in B Meson Decays,” [arXiv:2111.01800 \[hep-ex\]](#).
- [104] J. Jaeckel, P. C. Malta, and J. Redondo, “Decay Photons from the Axion-like Particles Burst of Type II Supernovae,” *Phys. Rev. D* **98** (2018) no. 5, 055032, [arXiv:1702.02964 \[hep-ph\]](#).
- [105] S. Gori, G. Perez, and K. Tobioka, “KOTO vs. NA62 Dark Scalar Searches,” *JHEP* **08** (2020) 110, [arXiv:2005.05170 \[hep-ph\]](#).
- [106] J. Jaeckel and M. Spannowsky, “Probing MeV to 90 GeV axion-like particles with LEP and LHC,” *Phys. Lett. B* **753** (2016) 482–487, [arXiv:1509.00476 \[hep-ph\]](#).
- [107] CERN, “Linear accelerator 4,” 2024. <https://home.cern/science/accelerators/linear-accelerator-4>.
- [108] O. S. Bruning, P. Collier, P. Lebrum et al., *LHC Design Report Vol. 1: The LHC Main Ring*, , 2004. <https://cds.cern.ch/record/782076/files/>.
- [109] **ATLAS** Collaboration, G. Aad *et al.*, “Luminosity determination in pp collisions at $\sqrt{s} = 13$ TeV using the ATLAS detector at the LHC,” *Eur. Phys. J. C* **83** (2023) no. 10, 982, [arXiv:2212.09379 \[hep-ex\]](#).
- [110] Large Hadron Collider Committee, “Large Hadron Collider Committee: Minutes of the one-hundredth-and-fifty-fifth meeting held on Wednesday and Thursday, 13-14 September 2023,” (2023) . <https://cds.cern.ch/record/2873699/files/LHCC-156.pdf>.
- [111] **ATLAS** Collaboration, , “Characterisation and mitigation of beam-induced backgrounds observed in the ATLAS detector during the 2011 proton-proton run,” *Journal of Instrumentation* (2013) no. 07, P07004–P07004.
- [112] **FASTER** Collaboration, “First neutrino interaction candidates at the LHC,” *Phys. Rev. D* **104** (2021) no. 9, L091101, [arXiv:2105.06197 \[hep-ex\]](#).

- [113] **FASER** Collaboration, , “First Measurement of the ν_e and ν_μ Interaction Cross Sections at the LHC with FASER’s Emulsion Detector,” (2024) , [arXiv:2403.12520 \[hep-ex\]](#).
- [114] Eljen Technology, “General purpose ej-200, ej-204, ej-208, ej-212,”
<https://eljentechnology.com/products/plastic-scintillators/ej-200-ej-204-ej-208-ej-212>.
- [115] Hamamatsu, “Photomultiplier tube assembly h11934,” <https://www.hamamatsu.com/eu/en/product/optical-sensors/pmt/pmt-assembly/head-on-type/H11934-100.html>.
- [116] Hamamatsu, “Photomultiplier tube assembly h6410,” <https://www.hamamatsu.com/eu/en/product/optical-sensors/pmt/pmt-assembly/head-on-type/H6410.html>.
- [117] G. Battistoni, T. Boehlen, F. Cerutti, P. W. Chin, L. S. Esposito, *et al.*, “Overview of the FLUKA Code,” *Annals of Nuclear Energy* **82** (2015) 10–18.
- [118] **FASER** Collaboration, , “The tracking detector of the FASER experiment,” *Nucl. Instrum. Meth. A* **1034** (2022) 166825, [arXiv:2112.01116 \[physics.ins-det\]](#).
- [119] F. Campabadal *et al.*, “Design and performance of the ABCD3TA ASIC for readout of silicon strip detectors in the ATLAS semiconductor tracker,” *Nucl. Instrum. Meth. A* **552** (2005) 292–328.
- [120] Hamamatsu, “Photomultiplier tube r7899,” https://www.hamamatsu.com/eu/en/product/optical-sensors/pmt/pmt_tube-alone/head-on-type/R7899.html.
- [121] **FASER** Collaboration, , “CALYPSO Software Framework,”
<https://gitlab.cern.ch/faser/calypso>.
- [122] **ATLAS** Collaboration, , “ATLAS ATHENA Software.”
<https://zenodo.org/record/2641997#.XhWRDC2ZPyI>.
- [123] G. Barrand *et al.*, “GAUDI - A software architecture and framework for building HEP data processing applications,” *Comput. Phys. Commun.* **140** (2001) 45–55.
- [124] R. E. Kalman, “A new approach to linear filtering and prediction problems,” *Journal of Basic Engineering* **82** (1960) no. 1, 35 – 45.

- [125] X. Ai, C. Allaire, N. Calace, *et al.*, “A common tracking software project,” *Computing and Software for Big Science* **6** (2022) no. 1, .
<http://dx.doi.org/10.1007/s41781-021-00078-8>.
- [126] D. Fellers, *A Search for Dark Photons with the FASER Detector at the LHC*. PhD thesis, University of Oregon, 2024. <https://cds.cern.ch/record/2897660>.
- [127] Gupta, M., “Calculation of Radiation Length in Materials,” tech. rep., CERN, Geneva, Jul, 2010. <https://cds.cern.ch/record/1279627>.
- [128] J.-H. Cheng, Z. Wang, L. Lebanowski, G.-L. Lin, and S. Chen, “Determination of the total absorption peak in an electromagnetic calorimeter,” *Nucl. Instrum. Meth. A* **827** (2016) 165–170, [arXiv:1603.04433](https://arxiv.org/abs/1603.04433) [physics.ins-det].
- [129] D. H. Wilkinson, “Ionization energy loss by charged particles. I: The Landau distribution,” *Nucl. Instrum. Meth. A* **383** (1996) 513–515.
- [130] S. Nyibule et al, “Birks Scaling of the Particle Light Output Functions for the EJ 299-33 plastic scintillator,” *Nuclear Instruments and Methods in Physics Research Section A: Accelerators, Spectrometers, Detectors and Associated Equipment* **768** (2014) 141–145.
- [131] **LHCb** Collaboration, , *LHCb Calorimeters: Technical Design Report*. CERN, Geneva, 2000. <http://cds.cern.ch/record/494264>.
- [132] Fabjan, C. W. and Gianotti, F., “Calorimetry for Particle Physics,” *Rev. Mod. Phys.* **75** (2003) 1243–1286.
- [133] N. Charitonidis and B. Rae, “The H2 Secondary Beam Line of EHN1/SPS,” 2017.
http://sba.web.cern.ch/sba/BeamsAndAreas/H2/H2_presentation.html.
- [134] S. Agostinelli *et al.*, “Geant4 — A Simulation Toolkit,” *Nuclear Instruments and Methods in Physics Research Section A: Accelerators, Spectrometers, Detectors and Associated Equipment* **506** (2003) no. 3, 250–303.
- [135] **ATLAS** Collaboration, , “The VP1 ATLAS 3D Event Display.”
<http://atlas-vp1.web.cern.ch/>.

- [136] J. M. Campbell *et al.*, “Event Generators for High-Energy Physics Experiments,” (2024) , [arXiv:2203.11110 \[hep-ph\]](https://arxiv.org/abs/2203.11110). <https://arxiv.org/abs/2203.11110>.
- [137] A. Buckley *et al.*, “General-purpose event generators for LHC physics,” *Physics Reports* **504** (2011) no. 5, 145–233. <http://dx.doi.org/10.1016/j.physrep.2011.03.005>.
- [138] S. Höche, “Introduction to parton-shower event generators,” (2015) , [arXiv:1411.4085 \[hep-ph\]](https://arxiv.org/abs/1411.4085). <https://arxiv.org/abs/1411.4085>.
- [139] **Sherpa** Collaboration, E. Bothmann *et al.*, “Event Generation with Sherpa 2.2,” *SciPost Phys.* **7** (2019) no. 3, 034, [arXiv:1905.09127 \[hep-ph\]](https://arxiv.org/abs/1905.09127).
- [140] S. Frixione, P. Nason, and C. Oleari, “Matching NLO QCD computations with Parton Shower simulations: the POWHEG method,” *JHEP* **11** (2007) 070, [arXiv:0709.2092 \[hep-ph\]](https://arxiv.org/abs/0709.2092).
- [141] T. Sjöstrand, S. Ask, J. R. Christiansen, R. Corke, N. Desai, P. Ilten, S. Mrenna, S. Prestel, C. O. Rasmussen, and P. Z. Skands, “An introduction to PYTHIA 8.2,” *Comput. Phys. Commun.* **191** (2015) 159–177, [arXiv:1410.3012 \[hep-ph\]](https://arxiv.org/abs/1410.3012).
- [142] C. Bierlich, S. Chakraborty, N. Desai, L. Gellersen, I. Helenius, *et al.*, “A Comprehensive Guide to the Physics and Usage of PYTHIA 8.3,” [arXiv:2203.11601 \[hep-ph\]](https://arxiv.org/abs/2203.11601).
- [143] P. Skands, S. Carrazza, and J. Rojo, “Tuning PYTHIA 8.1: the Monash 2013 Tune,” *Eur. Phys. J. C* **74** (2014) no. 8, 3024, [arXiv:1404.5630 \[hep-ph\]](https://arxiv.org/abs/1404.5630).
- [144] M. Fieg, F. Kling, H. Schulz, and T. Sjöstrand, “Tuning Pythia for Forward Physics Experiments,” *Phys. Rev. D* **109** (2024) no. 1, 016010, [arXiv:2309.08604 \[hep-ph\]](https://arxiv.org/abs/2309.08604).
- [145] V. Bertone, R. Gauld, and J. Rojo, “Neutrino Telescopes as QCD Microscopes,” *JHEP* **01** (2019) 217, [arXiv:1808.02034 \[hep-ph\]](https://arxiv.org/abs/1808.02034).
- [146] A. Bodek and U. Yang, “Axial and Vector Structure Functions for Electron- and Neutrino-Nucleon Scattering Cross Sections at all Q^2 using Effective Leading order Parton Distribution Functions,” [arXiv:1011.6592 \[hep-ph\]](https://arxiv.org/abs/1011.6592).

- [147] M. Bonvini, S. Marzani, and T. Peraro, “Small- x resummation from HELL,” *Eur. Phys. J. C* **76** (2016) no. 11, 597, [arXiv:1607.02153 \[hep-ph\]](#).
- [148] P. Nason, “A New method for combining NLO QCD with shower Monte Carlo algorithms,” *JHEP* **11** (2004) 040, [arXiv:hep-ph/0409146](#).
- [149] S. Porteboeuf, T. Pierog, and K. Werner, “Producing Hard Processes Regarding the Complete Event: The EPOS Event Generator,” in *45th Rencontres de Moriond on QCD and High Energy Interactions*, pp. 135–140. Gioi Publishers, 2010. [arXiv:1006.2967 \[hep-ph\]](#).
- [150] R. Ulrich, T. Pierog and C. Baus, “Cosmic Ray Monte Carlo Package, CRMC,” 2021. <https://doi.org/10.5281/zenodo>.
- [151] E.-J. Ahn, R. Engel, T. K. Gaisser, P. Lipari, and T. Stanev, “Cosmic ray interaction event generator SIBYLL 2.1,” *Phys. Rev. D* **80** (2009) 094003, [arXiv:0906.4113 \[hep-ph\]](#).
- [152] S. Ostapchenko, “Monte Carlo treatment of hadronic interactions in enhanced Pomeron scheme: I. QGSJET-II model,” *Phys. Rev. D* **83** (2011) 014018, [arXiv:1010.1869 \[hep-ph\]](#).
- [153] S. Roesler, R. Engel, and J. Ranft, “The Monte Carlo event generator DPMJET-III,” in *International Conference on Advanced Monte Carlo for Radiation Physics, Particle Transport Simulation and Applications (MC 2000)*, pp. 1033–1038. 12, 2000. [arXiv:hep-ph/0012252](#).
- [154] C. Andreopoulos *et al.*, “The GENIE Neutrino Monte Carlo Generator,” *Nucl. Instrum. Meth. A* **614** (2010) 87–104, [arXiv:0905.2517 \[hep-ph\]](#).
- [155] M. Dobbs and J. B. Hansen, “The HepMC C++ Monte Carlo event record for High Energy Physics,” *Comput. Phys. Commun.* **134** (2001) 41–46.
- [156] **GEANT4** Collaboration, S. Agostinelli *et al.*, “GEANT4: A Simulation Toolkit,” *Nucl. Instrum. Meth. A* **506** (2003) 250–303.
- [157] F. Kling and L. J. Nevay, “Forward Neutrino Fluxes at the LHC,” *Phys. Rev. D* **104** (2021) no. 11, 113008, [arXiv:2105.08270 \[hep-ph\]](#).

- [158] A. Ferrari, P. R. Sala, A. Fasso, and J. Ranft, *FLUKA: A Multi-particle Transport Code (Program Version 2005)*. CERN Yellow Reports: Monographs. CERN, Geneva, 2005.
<http://cds.cern.ch/record/898301>.
- [159] T. T. Böhlen *et al.*, “The FLUKA Code: Developments and Challenges for High Energy and Medical Applications,” *Nucl. Data Sheets* **120** (2014) 211–214.
- [160] M. Baak, G. J. Besjes, D. Côte, A. Koutsman, J. Lorenz, and D. Short, “HistFitter Software Framework for Statistical Data Analysis,” *Eur. Phys. J. C* **75** (2015) 153,
[arXiv:1410.1280 \[hep-ex\]](https://arxiv.org/abs/1410.1280).
- [161] A. L. Read, “Modified frequentist analysis of search results (The CL(s) method),” in *Workshop on Confidence Limits*, pp. 81–101. 8, 2000.
- [162] A. L. Read, “Presentation of search results: The CL_s technique,” *J. Phys. G* **28** (2002) 2693–2704.
- [163] **FASER** Collaboration, “First Results from the Search for Dark Photons with the FASER Detector at the LHC,” <https://cds.cern.ch/record/2853210>.
- [164] **ATLAS** Collaboration, “Preliminary Analysis of the Luminosity Calibration of the ATLAS 13.6 TeV Data Recorded in 2022.” ATL-DAPR-PUB-2023-001, 2023.
<https://cds.cern.ch/record/2853525>.
- [165] G. Avoni *et al.*, “The new LUCID-2 detector for luminosity measurement and monitoring in ATLAS,” *JINST* **13** (2018) no. 07, P07017.
- [166] W. Buttinger, “Background Estimation with the ABCD Method: Featuring the TRooFit Toolkit,” 2018.
https://twiki.cern.ch/twiki/pub/Main/ABCDMethod/ABCDGuide_draft18Oct18.pdf.
- [167] F. James and M. Roos, “Errors on Ratios of Small Numbers of Events,” *Nucl. Phys. B* **172** (1980) 475–480.

- [168] **FASER** Collaboration, H. Abreu *et al.*, “First Direct Observation of Collider Neutrinos with FASER at the LHC,” *Phys. Rev. Lett.* **131** (2023) no. 3, 031801, [arXiv:2303.14185 \[hep-ex\]](#).
- [169] B. Döbrich, “Axion-like Particles from Primakov production in beam-dumps,” *CERN Proc.* **1** (2018) 253, [arXiv:1708.05776 \[hep-ph\]](#).
- [170] **OPAL** Collaboration, G. Abbiendi *et al.*, “Multiphoton production in e^+e^- collisions at $\sqrt{s} = 181\text{--}209$ GeV,” *Eur. Phys. J. C* **26** (2003) 331–344, [arXiv:hep-ex/0210016](#).
- [171] **NA64** Collaboration, D. Banerjee *et al.*, “Search for Axionlike and Scalar Particles with the NA64 Experiment,” *Phys. Rev. Lett.* **125** (2020) no. 8, 081801, [arXiv:2005.02710 \[hep-ex\]](#).
- [172] B. Döbrich, J. Jaeckel, and T. Spadaro, “Erratum to: Light in the beam dump. axion-like particle production from decay photons in proton beam-dumps,” *Journal of High Energy Physics* **2020** Oct. . [http://dx.doi.org/10.1007/JHEP10\(2020\)046](http://dx.doi.org/10.1007/JHEP10(2020)046).
- [173] **BESIII** Collaboration, M. Ablikim *et al.*, “Search for an axion-like particle in radiative J/ψ decays,” *Phys. Lett. B* **838** (2023) 137698, [arXiv:2211.12699 \[hep-ex\]](#).
- [174] Y. Afik, B. Döbrich, J. Jerhot, Y. Soreq, and K. Tobioka, “Probing long-lived axions at the KOTO experiment,” *Phys. Rev. D* **108** (2023) no. 5, 055007, [arXiv:2303.01521 \[hep-ph\]](#).
- [175] **NA62** Collaboration, E. Cortina Gil *et al.*, “Measurement of the very rare $K^+ \rightarrow \pi^+ \nu \bar{\nu}$ decay,” *JHEP* **06** (2021) 093, [arXiv:2103.15389 \[hep-ex\]](#).
- [176] J. Blumlein *et al.*, “Limits on neutral light scalar and pseudoscalar particles in a proton beam dump experiment,” *Z. Phys. C* **51** (1991) 341–350.
- [177] E. Goudzovski *et al.*, “New physics searches at kaon and hyperon factories,” *Rept. Prog. Phys.* **86** (2023) no. 1, 016201, [arXiv:2201.07805 \[hep-ph\]](#).
- [178] S. Tulin, “New weakly-coupled forces hidden in low-energy QCD,” *Phys. Rev. D* **89** (2014) no. 11, 114008, [arXiv:1404.4370 \[hep-ph\]](#).

- [179] B. Batell, A. Freitas, A. Ismail, and D. Mckeen, “Probing Light Dark Matter with a Hadrophilic Scalar Mediator,” *Phys. Rev. D* **100** (2019) no. 9, 095020, [arXiv:1812.05103 \[hep-ph\]](#).
- [180] F. Kling, S. Li, H. Song, S. Su, and W. Su, “Light Scalars at FASER,” *JHEP* **08** (2023) 001, [arXiv:2212.06186 \[hep-ph\]](#).
- [181] J. Blumlein *et al.*, “Limits on the mass of light (pseudo)scalar particles from Bethe-Heitler e^+e^- and $\mu^+\mu^-$ pair production in a proton - iron beam dump experiment,” *Int. J. Mod. Phys. A* **7** (1992) 3835–3850.
- [182] A. Anastasi *et al.*, “Limit on the production of a low-mass vector boson in $e^+e^- \rightarrow U\gamma$, $U \rightarrow e^+e^-$ with the KLOE experiment,” *Phys. Lett. B* **750** (2015) 633–637, [arXiv:1509.00740 \[hep-ex\]](#).
- [183] **NA48/2** Collaboration, J. R. Batley *et al.*, “Search for the dark photon in π^0 decays,” *Phys. Lett. B* **746** (2015) 178–185, [arXiv:1504.00607 \[hep-ex\]](#).
- [184] **LHCb** Collaboration, R. Aaij *et al.*, “Search for $A' \rightarrow \mu^+\mu^-$ Decays,” *Phys. Rev. Lett.* **124** (2020) no. 4, 041801, [arXiv:1910.06926 \[hep-ex\]](#).
- [185] G. Bernardi *et al.*, “Search for Neutrino Decay,” *Phys. Lett. B* **166** (1986) 479–483.
- [186] **KLOE-2** Collaboration, A. Anastasi *et al.*, “Precision measurement of the $\eta \rightarrow \pi^+\pi^-\pi^0$ Dalitz plot distribution with the KLOE detector,” *JHEP* **05** (2016) 019, [arXiv:1601.06985 \[hep-ex\]](#).
- [187] B. Nefkens *et al.*, “New measurement of the rare decay $\eta \rightarrow \pi^0\gamma\gamma$ with the Crystal Ball/TAPS detectors at the Mainz Microtron,” *Physical Review C* **90** (05, 2014) .
- [188] **BESIII** Collaboration, M. Ablikim *et al.*, “Amplitude Analysis of the Decays $\eta' \rightarrow \pi^+\pi^-\pi^0$ and $\eta' \rightarrow \pi^0\pi^0\pi^0$,” *Phys. Rev. Lett.* **118** (2017) no. 1, 012001, [arXiv:1606.03847 \[hep-ex\]](#).

-
- [189] A. Arbey, F. Mahmoudi, O. Stal, and T. Stefaniak, “Status of the Charged Higgs Boson in Two Higgs Doublet Models,” *Eur. Phys. J. C* **78** (2018) no. 3, 182, [arXiv:1706.07414 \[hep-ph\]](#).
- [190] “LHC Long Term Schedule.”
<https://lhc-commissioning.web.cern.ch/schedule/LHC-long-term.htm>.

Appendix A

FASER's EM Calorimeter

A.1 Calorimeter Corrections

Figure A.1a shows the difference in deposited energy in the calorimeter with and without the implementation of Birks' Law correction to the energy loss of a charged particle in the simulation of FASER's ECAL modules. Figure A.1b shows the difference in energy response when the local non-uniformity correction is applied, which accounts for variation at the cell edges and variation in response close to WLS fibres in the ECAL module. The implementation of Tyvek into the simulation geometry for the calorimeter also impacts the energy loss, shown in Figure A.2.

The addition of the Birks' law correction decreases the energy deposited in the calorimeter by around 3%. The non-uniformity corrections increase the energy deposited by a similar amount, this effect also reduces energy resolution. The larger density of Tyvek was chosen and implemented into the simulation, decreasing the deposited energy by around 6%.

A.2 Calorimeter Energy Uncertainty

A 6% uncertainty is assigned to the calorimeter energy threshold used in both the dark photon and the ALP analysis. This overall uncertainty is calculated by including the individual uncertainties in the various stages of calibration of both data and MC. The correction of the MC using the test beam data as calibration also needs to be taken into account in this step. A summary and description of each of these components that leads to the determination of the total uncertainty on

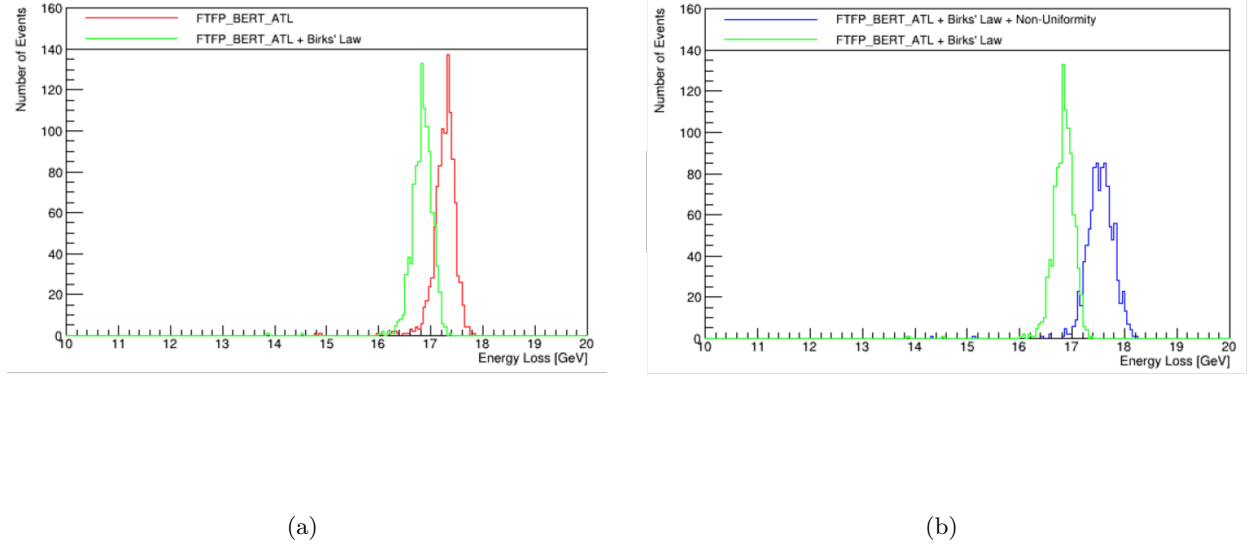


Figure A.1: The change in energy loss in the calorimeter due to the implementation of (a) Birks' Law correction (red) and (b) non-uniformity correction (blue). The green represents the simulation setup without the correction, FTFP BERT ATL refers to the physics list used in the simulation.

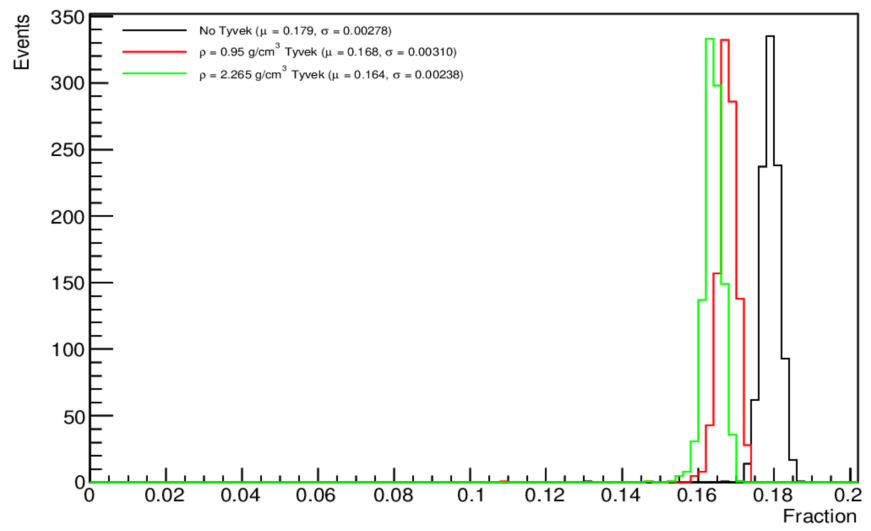


Figure A.2: The change in fraction of deposited energy due to the addition of Tyvek paper into the ECAL simulation, compared to the setup without Tyvek (black). Two different Tyvek densities were investigated 0.95 g/cm^3 (red) and 2.265 g/cm^3 (green).

Table A.1: Summary and description of each of the sources of uncertainty on the calorimeter energy threshold, leading to a total uncertainty of 6%.

| Source | Uncertainty | Description |
|---------------------------------|-------------|-----------------------------------------------------------------------------|
| TI12 MIP fit | 1.90% | Uncertainty associated with MPV fit of MIP data |
| TI12 HV gain | 3.37% | Uncertainty associated with the extrapolation of the HV gain curves in data |
| TI12 PMT drift | 1.45% | Uncertainty due to the drift in the calo PMTs over time |
| TI12 MIP fit (MC) | 1.16% | Uncertainty associated with MPV fit of MIP MC |
| TB data calibration | 0.74% | TB MC energy correction |
| TB MC calibration | 2.35% | TB MC energy correction |
| TB MC calibration extrapolation | 2.46% | TB MC energy correction extrapolated to 500 GeV threshold |
| Local effects | 2.5% | Uncertainty due to energy loss at edges and position dependence |
| Total | 6% | |

this energy selection is given in Table A.1. The process of extrapolating the test beam data, which is at a lower energy, to the higher energy calorimeter energy selection used in analysis is shown in Figure A.3 [126]. The total uncertainty in comparing the calibrated energies at 500 GeV in data and MC is measured to be 6%.

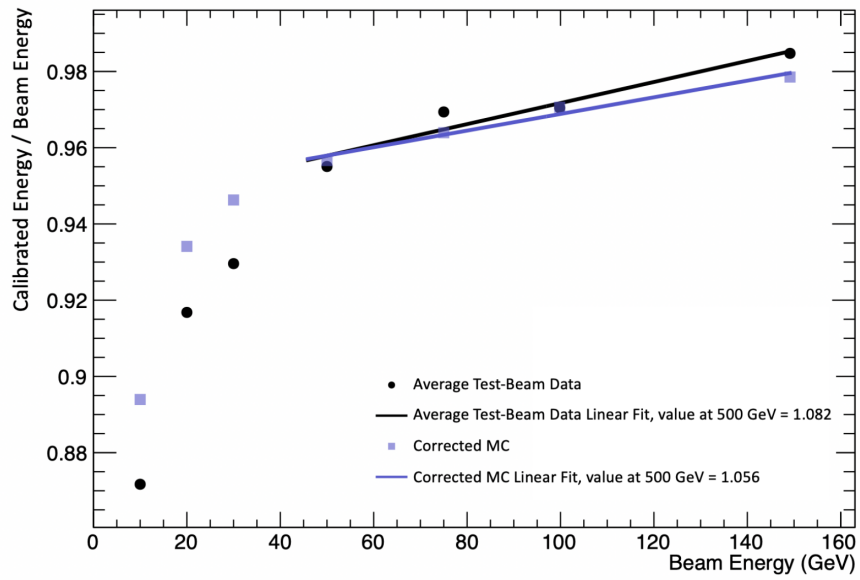


Figure A.3: The average of the calibrated energies of each of the six test beam calorimeter modules as a function of beam energy in data and MC. The average linear fit in each case shows the extrapolation process to higher energy (500 GeV) to evaluate the uncertainty at this point. The fits results in a difference of 2.46% at 500 GeV. Figure from Ref. [18].

Appendix B

ALP Signal Selection: Tracking Variables

The ALP-W analysis does not use a track selection. Various track parameters were investigated to determine whether a tracking cut would further discriminate signal from background. An important factor to note is the lack of tracks present in the ALP-W signal model, which decays to two high energy photons at the mass and coupling to which FASER is sensitive. A small fraction of photons are expected to convert, such that a requirement of zero tracks would impact signal yield. In addition, the main background expected in this analysis is from neutrinos.

The number of spacepoints, number of track segments and number of track clusters in ALP-W MC signal samples with mass = 100 GeV and seven different couplings (g_{aWW}) were compared to a neutrino MC sample (labelled here as 200003).

The number of clusters, defined as adjacent hit strips in the same side of a module in a tracking station layer, is shown in Figure B.1a. The number of spacepoints, defined as the x position of combined clusters from both sides of a module, is shown in Figure B.1b. The number of track segments, defined as 4 or more clusters that could form a possible track, is shown in Figure B.2.

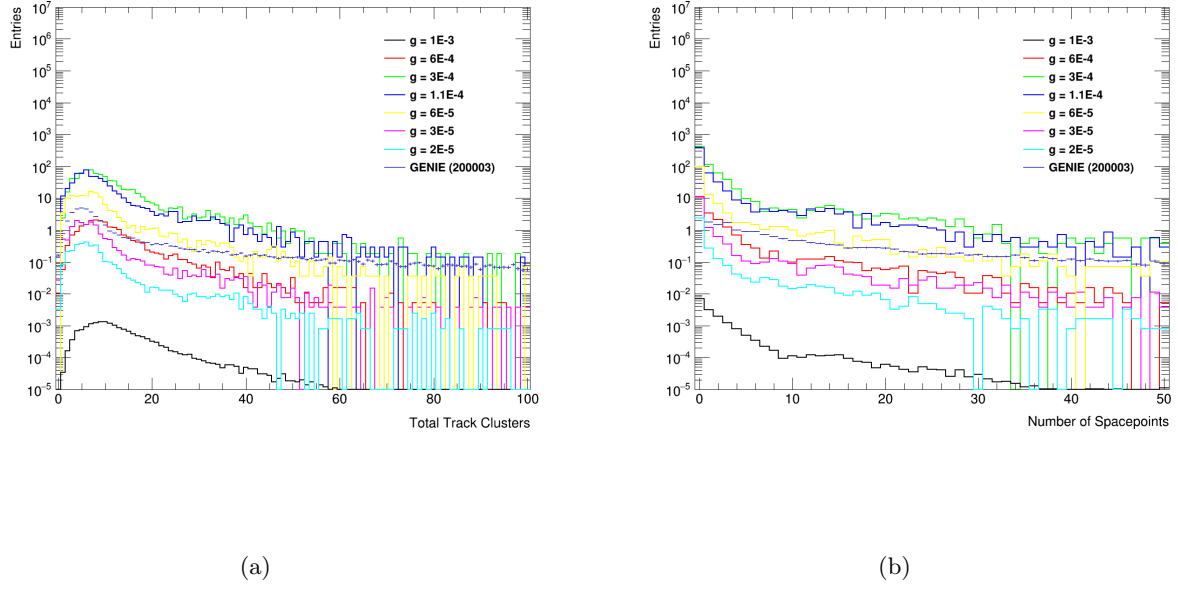


Figure B.1: (a) Number of clusters and (b) Number of spacepoints in 7 ALP-W MC signal samples compared with GENIE neutrino MC. Histograms represent the signal samples, the blue markers show the neutrino MC.

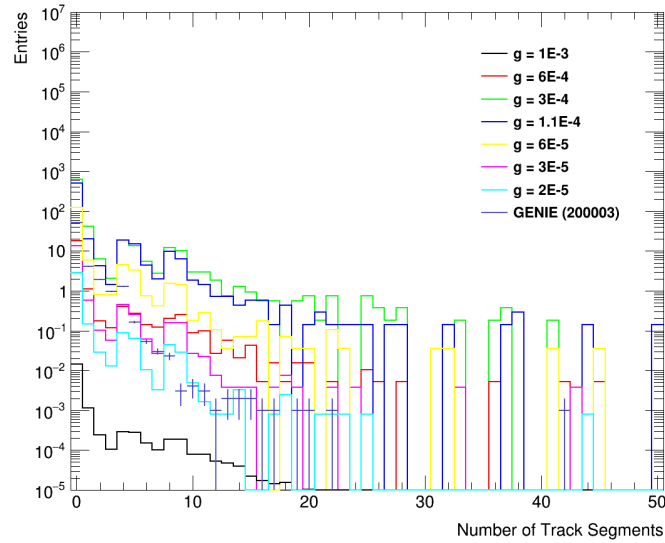


Figure B.2: Number of track segments in 7 ALP-W MC signal samples compared with GENIE neutrino MC. Histograms represent the signal samples, the blue markers show the neutrino MC.